THE UNIVERSITY OF HULL

Empirical Modelling of Turbulence and Wave-current Interaction in Tidal Streams

---

BEING A THESIS SUBMITTED FOR THE DEGREE OF

DOCTOR OF PHILOSOPHY

IN THE UNIVERSITY OF HULL

BY

Ross Jennings

BSc (Hons), PGDip

September 2017

Abstract

The successful development of the tidal stream power industry fundamentally relies on a thorough, quantitative understanding of the available resource. Numerical simulations and laboratory flume experiments have demonstrated that increased turbulence and wave-induced motion can have detrimental effects on the fatigue and performance of prototype tidal stream turbines (TSTs). Knowledge of the relationships between mean current velocity, turbulence and surface waves is limited and presents a significant research gap. This research makes a significant contribution to the field by developing empirical models from *in situ* data collected within the Humber Estuary. These models estimate the turbulence strength and intensity at a point and through depth given a mean current velocity.

An 18-day deployment of bed-mounted directional wave recorders (DWR) at Foul Holme Spit simultaneously recorded two-dimensional flow velocities and surface wave parameters. Static, vessel-mounted, acoustic Doppler current profiler (ADCP) surveys recorded turbulence through depth near St. Andrews Dock.

The analyses revealed distinct relationships between the mean current velocity, turbulence strength and turbulence intensity at a point which are comparable to recently published results. The inter-tidal relationship between streamwise mean current velocity and turbulence strength is modelled at a point using power regression where α is 0.13 and β is 0.72 with an R^2 value of 0.8721. The inter-tidal relationship between streamwise mean current velocity and turbulence intensity is modelled at a point using power regression where γ is 14.315 and δ is -0.2316 with an R^2 value of 0.5482. A newly defined empirical relationship between depth-averaged mean current velocity and turbulence intensity is modelled using power regression where ε is 17.75 and ζ is -0.94 with an R^2 value of 0.7912. The models derived at a point are tested on the data collected through depth and exhibited strong predictive capability within the order of 0.1 ms^{-1}. The exponential approximation of wave-induced velocity, proposed by Soulsby (2006), was tested and shown to be inappropriate for estimating wave-induced velocities at this scale. A comparative spectral analysis between DWR sample bursts determined that spikes in the turbulence spectra can be attributed to surface wave parameters, thus validating the conceptual model proposed by Soulsby and Humphrey (1990).

Acknowledgements

First and foremost, I thank my academic supervisor Prof. Jack Hardisty for his inspiration and encouragement throughout the PhD. I have thoroughly enjoyed working together to develop the thesis and publications. I appreciate every opportunity he has provided me. Thanks also to my second academic supervisor Dr. Graham Ferrier for his invaluable contributions to the direction of the final thesis draft.

Thanks to my industrial supervisor Emma Toulson for giving me an invaluable insight into the industrial sector during my time spent in Newcastle. A special thanks goes to WSP Parsons Brinckerhoff for helping with the research objectives and fieldwork methodology. Thanks to Nick Quarta, Luca Santoni, Leila Tavendale and Geoffrey Bardoux for their individual contributions.

Thanks to the Centre for Adaptive Science and Sustainability (CASS) for generously funding this research and giving me the opportunity to pursue this PhD.

Thanks to the Departmental research assistants Mike Dennett, Kim Rosewell and Mark Anderson for all of their efforts to ensure the fieldwork in the Humber was successful. Many thanks to Xuxu Wu, Hao Hu, Alex Ombler, Nick Quarta and James Wilkinson for assisting me during the fieldwork in challenging conditions.

Thanks to Alex, Charlotte, Lucy, Shona and Hao for all of their support, inspiration and morale boosts whilst sharing our postgraduate office. I wish you all an incredibly successful future and our time together will be sorely missed.

Finally I would like to thank my family and friends for their continued belief and support throughout my career to date. A special thanks to Olivia for her incredible patience and encouragement throughout.

Declaration and Statement of Copyright

I confirm that no part of the material presented in this thesis has previously been submitted by me or any other person for a degree in this or any other university. In all cases, where it is relevant, material from the work of others has been acknowledged.

Ross Jennings

Nomenclature

a	Amplitude (m)
A	Cross-sectional area of moving fluid / Turbine swept area (m^2)
A_{M2}	Amplitude of tidal harmonic (m)
C_A	Aerodynamic force coefficient
C_F	Power flicker (V)
C_P	Power coefficient of tidal stream turbine (%)
C_{Sound}	Speed of sound in water (ms^{-1})
E	Energy (kW)
f	Frequency (Hz)
$F_{Doppler}$	Frequency of sound waves (Hz)
F_{TOT}	Wind force (N)
g	Gravitational acceleration (ms^{-2})
h	Water depth (m)
H	Wave height (m)
H_S	Significant wave height (m)
h_T	Tidal height (m)
I_T	Turbulence intensity (%)
I_{Td}	Depth-averaged Turbulence Intensity (%)
K	Von Karman constant
k	Wave number
K_E	Kinetic energy (J)
m	Mass (kg)
P	Potential power in a fluid (kW)
P_O	Turbine power output (kW)
t	Time (s)
T	Wave period (s)
T_{M2}	Period of tidal harmonic (s)

T_Z	Zero-crossing period (s)
u_*	Friction velocity (ms^{-1})
u, v, w	Streamwise, transverse and vertical flow directions
U	Current velocity (ms^{-1})
$\bar{U}$	Mean current velocity (ms^{-1})
$\bar{U}_d$	Depth-averaged mean current velocity (ms^{-1})
U_{Ti}	Tidal component of flow (ms^{-1})
U_{Tu}	Turbulent component of flow (ms^{-1})
U_W	Wave component of flow (ms^{-1})
U_σ	Turbulence strength (ms^{-1})
U_{MAX}	Maximum wave orbital velocity (ms^{-1})
$V_{Particles}$	Velocity of suspended particles (ms^{-1})
z	Height above the bed (m)
z_0	Hydraulic roughness
η	Surface elevation (m)
λ	Wavelength (m)
ρ	Fluid density (kg/m^3)
ρ_{M2}	Phase shift of tidal harmonic (s)

Acronyms

ABP	Associated British Ports
ABS	Acoustic Backscatter
ADCP	Acoustic Doppler Current Profiler
ADV	Acoustic Doppler Velocimeter
AWAC	Acoustic Wave And Current profiler
CFD	Computational Fluid Dynamics
DWR	Directional Wave Recorder
EIA	Environmental Impact Assessment
EMCM	Electro-Magnetic Current Meter
EMEC	European Marine Energy Centre
EYA	Energy Yield Assessment
FFT	Fast Fourier Transform
GPS	Global Positioning System
O&M	Operations and Maintenance
PIV	Particle Image Velocimetry
RIB	Rigid Inflatable Boat
RMS	Root Mean Square
SSC	Suspended Sediment Concentration
TKE	Turbulent Kinetic Energy
TST	Tidal Stream Turbine
UPS	Uninterruptable Power Supply
USB	Universal Serial Bus
VTG	Vector Track and speed over Ground

Contents

Abstract i

Acknowledgements ii

Declaration and Statement of Copyright iii

Nomenclature iv

Acronyms vi

Contents vii

Figures xi

Tables xix

1 Introduction 1

1.1 Thesis Rationale 1

1.2 Research Aims and Objectives 3

1.3 Thesis Structure 4

1.4 Publications 5

2 Background and Literature Review 6

2.1 Introduction 6

2.2 Tidal Stream Power 6

2.2.1 An Introduction to Renewable Energy and Tidal Stream Power 6

2.2.2 Tidal Stream Turbines 8

2.2.3 Tidal Stream Energy Yield Assessments 11

2.2.4 Predicting the Tidal Stream Resource 15

2.2.5 Summary of Tidal Stream Power 26

2.3 Turbulence in Tidal Streams 27

2.3.1 An Introduction to Turbulence in Tidal Streams 27

2.3.2 Relevant Turbulence Experiments and Methodologies 36

2.3.3 Summary of Relevant Turbulence Experiments 53

2.4 Wave-Current Interaction 54

2.4.1 An Introduction to Wave-Current Interaction 54

2.4.2 An Introduction to Linear Wave Theory 55
2.4.3 Relevant Wave-Current Interaction Experiments and Methodologies 63
2.4.4 Summary of Relevant Wave-Current Interaction Experiments 78
2.5 Conclusion 79
3 Methodology 80
3.1 Introduction 80
3.2 Challenges of Collecting Appropriate Data to Meet the Thesis Objectives 80
3.3 Instrumentation Used 83
3.3.1 Valeport MIDAS DWR 83
3.3.2 Teledyne Workhorse ADCP 88
3.4 Site Selection 96
3.4.1 The Humber Estuary 96
3.4.2 Fieldwork Locations 101
3.5 DWR Fieldwork 107
3.5.1 Introduction 107
3.5.2 Pilot Deployment and Recovery at Spurn Point 107
3.5.3 Foul Holme Spit Deployment and Recovery 112
3.5.4 Data Processing, Validation and Analysis 116
3.6 ADCP Fieldwork 119
3.6.1 Introduction 119
3.6.2 Date Selection 119
3.6.3 ADCP Setup 120
3.6.4 Surveying 122
3.6.5 Data Processing, Analysis and Visualisation 124
3.7 Conclusion 125
4 Results 127
4.1 Introduction 127
4.2 Results of the DWR Fieldwork 129

4.2.1 Meteorological Data from the Port of Immingham 129
4.2.2 Comparison between both Device's Summary Data 131
4.2.3 Foul Holme Spit Summary Files (Device 1) 135
4.2.4 Comparisons between Device 1's Summary Data and TotalTide Predictions of Water Depth and Current Velocity 142
4.2.5 Data Used in the Analysis 145
4.2.6 Summary of the DWR Fieldwork 149
4.3 Results of the ADCP Fieldwork 150
4.3.1 Static Surveys during a Spring Ebb and Flood tide 150
4.3.2 Static Surveys during a Neap Flood and Ebb tide 158
4.3.3 Understanding the Vertical Distribution of Turbulence Intensity 164
4.3.4 Summary of the ADCP Fieldwork 166
4.4 Comparison of Results with the Literature 166
4.5 Conclusion 169
5 Analysis and Discussion 170
5.1 Introduction 170
5.2 Analysis and Discussion of Objective 1: 171
5.2.1 Introduction 171
5.2.2 Modelling the Relationship between Turbulence Strength and Mean Current Velocity at a Point, Ignoring Wave-Current Interaction 171
5.2.3 Modelling the Relationship between Turbulence Intensity and Mean Current Velocity at a Point, Ignoring Wave-Current Interaction 177
5.2.4 Discussion of Objective 1 181
5.3 Analysis and Discussion of Objective 2: 183
5.3.1 Introduction 183
5.3.2 Modelling the Relationship between Turbulence Strength, Intensity and Mean Current Velocity at a Point, Including Wave-Current Interaction. 184
5.3.3 Modelling Wave-Current Interaction in the Turbulence Spectrum 188
5.3.4 Discussion of Objective 2 193

5.4 Analysis and Discussion of Objective 3: 195
5.4.1 Introduction 195
5.4.2 Modelling the Relationship between Turbulence Intensity and Depth-Averaged Current Velocity 196
5.4.3 Modelling the Relationship between Turbulence Strength and Mean Current Velocity through Depth 199
5.4.4 Discussion of Objective 3 203
5.5 Summary of Findings and Implications 204
5.5.1 Comparison of Models to Literature 204
5.5.2 Example Usage of a Model to Predict Turbulence Strength in Tidal Stream Power Energy Yield Assessments 206
5.6 Evaluation and Recommendations for Future Work 207
5.6.1 Evaluation of the DWR Fieldwork Methodology and Recommendations for Improvements 207
5.6.2 Evaluation of the ADCP Fieldwork Methodology and Recommendations for Improvements 208
5.6.3 Recommendations for Measuring Turbulence and Wave-current Interaction Higher in the Water Column 209
5.6.4 Recommendations for Experiments to Analyse the Impact of Bathymetry on Turbulence and TST performance. 212
5.6.5 Recommendation to Analyse the Effect of Increased Fetch on Wave-current Interaction in hyper-tidal Estuaries. 212
6 Conclusion 213
7 Bibliography 216

Figures

Figure 1: Floating turbines; ScotRenewables SR2000, BlueTEC Modular (ScotRenewables, 2016; BlueTEC, 2016). 10

Figure 2: Buoyant turbines; Black Rock Tidal Power's Triton S36, Sustainable Marine Energy's Plat-O and Nautricity's CoRMaT (Black Rock Tidal Power, 2016; Sustainable Marine Energy, 2016; Nautricity, 2016). 10

Figure 3: Bed-mounted turbines; Atlantis' AR1500 and Andritz Hydro Hammerfest's HS 1000 (ATC, 2016; ScottishEnergyNews, 2016). 10

Figure 4: Expected TST interactions with varying flow conditions (Tatum et al., 2016) 13

Figure 5: Mean flow velocity and higher frequency fluctuating component (Duarte et al., 2012) 13

Figure 6: Example of an energy yield assessment timeline emphasising the need for a detailed site characterisation of turbulence (Clark, 2015) 14

Figure 7: Orbital interactions of the Sun and the Moon on the Earth's tides (Kvale, 2006) 17

Figure 8: Major tidal harmonic constituents and their corresponding phase and amplitude (Schwartz, 2006). 18

Figure 9: Global tidal height distribution and location of major amphidromic points (EoEarth, 2011). 19

Figure 10: Relationship in time between tidal heights and tidal currents and the concept of standing and progressive waves (NOAA, 2013). 20

Figure 11: Velocity profiles at a site in the Severn Estuary collected by a vessel-mounted ADCP (Mason-Jones et al., 2013). 21

Figure 12: Global estimated tidal stream power potential by country (Atlantis Resources Ltd., 2015). 23

Figure 13: Tidal stream and wave resource distribution in Europe. (EMEC, 2014). 23

Figure 14: Turbulence energy spectrum curve in a log-log plot of wavenumber (Log(k)) against log(energy) (Davidson, 2012). 29

Figure 15: Review of turbulence intensity measurements (Bouferrouk et al., 2016). 35

Figure 16: Relationship between mean current velocity, (U), and the mean amplitude of short (u1) and long period (u2) fluctuations observed by Bowden and Proudman (1949) in the Mersey Estuary. 41

Figure 17: Relationship between mean flow velocities and streamwise turbulence intensity at Nodule Point, Admiralty Inlet, WA (Thomson et al., 2012). 43

Figure 18: Relationship between mean flow and streamwise turbulence intensity. Anisotropy is scaled in the colour bar and the relationship between mean flow and flow variance is included in the inset (McCaffrey et al., 2015). 45

Figure 19: Relationship between mean velocity, turbulent strength and turbulence intensity over 4 tidal cycles in the Sound of Islay, Scotland (Milne et al., 2013). 46

Figure 20: Turbulence intensity and turbulence strength against mean current velocity in the East River tidal strait, New York. The colour bar represents the fraction of data out of the total number of samples (Gunawan et al., 2014). 47

Figure 21: Tidal current velocity, turbulence strength and turbulence intensity tested against the power flicker of the Seagen TST (MacEnri et al., 2013). 50

Figure 22: Tidal current velocity tested against turbulence strength and turbulence intensity (MacEnri et al., 2013). 50

Figure 23: Turbulence intensity at hub height for varying inflow velocities (Jeffcoate et al., 2015). 51

Figure 24: Characteristics of an idealised sinusoidal linear wave profile (Holthuijsen, 2007). 55

Figure 25: Individual wave harmonics make up the apparently random sea surface from above (Holthuijsen, 2007). 56

Figure 26: Summation of harmonic components to produce observed surface elevation time series (Holthuijsen, 2007). 56

Figure 27: Zero crossing period of a wave (Holthuijsen, 2007). 57

Figure 28: Temporal frequency of various harmonic waves (Holthuijsen, 2007). 59

Figure 29: Time series of surface elevation presented in a frequency spectrum (Holthuijsen, 2007). 59

Figure 30: Orbital motions beneath surface gravity waves upon varying depths (Ahmed et al., 2010). 60

Figure 31: Waverider buoy data showing directional interaction with tidal streams flowing East and West (Lewis et al., 2014). 66

Figure 32: Examples of wave-dominated, mixed and current-dominated time series (Soulsby and Humphrey, 1990). 73

Figure 33: Frequency spectrum of mixed burst (Soulsby and Humphrey, 1990). 74

Figure 34: Wave peak in the turbulence energy spectrum (Hannay et al., 1994). 74

Figure 35: Relationship between turbulence strength (standard deviation) and mean current velocity through depth (Filipot et al., 2015). 76

Figure 36: Comparison between turbulence spectra in calm (red) and stormy (blue) tidal flows (Filipot et al., 2015). 77

Figure 37: Turbulence intensity at three different bin heights in the Bristol Channel (Key: 6.2 m (blue), 21 m (black) and 36 m (red)) (Bouferrouk et al., 2016). 78

Figure 38: Valeport MIDAS DWR (Valeport, 2008) 83

Figure 39: Diagram of the dimensions of the Valeport Midas DWR inside bespoke steel frame (Valeport, 2008). 87

Figure 40: Analogy of Doppler shift observed by a swimmer in waves (Teledyne, 2011). 89

Figure 41: Janus configuration of the Teledyne Workhorse ADCP (Teledyne, 2011). 91

Figure 42: Illustration of depth cell mapping due to instrument rotation (Teledyne, 2011). 93

Figure 43: The ADCP 'trade-off triangle' between Range, Random Noise and Resolution (Teledyne, 2011). 94

Figure 44: Prototype TSTs, Pulse Stream 100 (Top) and Neptune Proteus (Bottom), deployed in the Humber Estuary (HullValley, 2012; PulseTidal, 2016). 99

Figure 45: Map of the Humber Estuary and fieldwork locations. 101

Figure 46: Location of the pilot deployment at Spurn. Bathymetry is illustrated as elevation from chart datum (EFCD). 103

Figure 47: Location of the deployment at Foul Holme Spit. Bathymetry is illustrated as elevation from chart datum (EFCD). 104

Figure 48: Map of survey location based on 2015 admiralty charts. Bathymetry is illustrated as elevation from chart datum (EFCD). 105

Figure 49: Bathymetric survey by ABP at St. Andrews Dock (Edited from ABP, 2012). 106

Figure 50: Diagram of water depth above deployed DWRs during stages of the tide. 108

Figure 51: TotalTide prediction of tidal height throughout the deployment at Spurn Point between 4th and 31st March. 108

Figure 52: Battery configuration of the Valeport MIDAS DWR using 32 1.5 V alkaline D-cells. 109

Figure 53: Photographs of: The RIB being lowered into the Humber Estuary from Hessle Foreshore beneath the Humber Bridge, the DWR deployed at Spurn Point and the device after being successfully recovered. 110

Figure 54: Testing the flow direction output of MIDAS DWR in uni-directional flume. 111

Figure 55: New deployment design laid out on grass incorporating two DWRs and marker buoy 113

Figure 56: Valeport Wavelog Express sampling setup screen displaying deployment criteria used at Foul Holme Spit. 114

Figure 57: Devices deployed at Foul Holme Spit 115

Figure 58: Devices recovered from Foul Holme Spit after 29 days. 115

Figure 59: Summary tidal and wave files viewed in WaveLog Express. 116

Figure 60: Predicted tidal heights at nearby site using TotalTide. 120

Figure 61: Photograph of vessel-mounted ADCP setup in the field. 120

Figure 62: Custom-made power box schematic used to power and control the ADCP from the RIB. 121

Figure 63: TotalTide prediction of Spring tidal heights at Hull (Albert Dock). 123

Figure 64: TotalTide prediction of Neap tidal heights at Hull (Albert Dock). 124

Figure 65: Meteorological data from the Port of Immingham weather station. 130

Figure 66: Comparison of water depth estimates between Devices 1 and 2. 131

Figure 67: Comparison of tidal current velocity estimates between Device 1 and 2. 132

Figure 68: Comparison between tidal current velocity estimates of Device 1 and 2 during the first three Floods. 133

Figure 69: Comparison between tidal current velocity estimates of Device 1 and 2 during the first three Ebbs. 133

Figure 70: Comparison of significant wave height estimates between Device 1 and 2. 134

Figure 71: Comparison of zero-crossing period estimates between Device 1 and 2. 134

Figure 72: Tidal burst summary data from Device 1. 137

Figure 73: Wave burst summary files from Device 1. 140

Figure 74: Comparison of significant wave height, zero-crossing period and wave direction at Foul Holme Spit throughout deployment 141

Figure 75: Tidal and wave direction occurrence radar overlaying Foul Holme Spit deployment site. 141

Figure 76: Comparison between wave and tide direction in the style of Lewis et al. (2014). 142

Figure 77: Time series comparison between the observed and modelled water depths. 143

Figure 78: Correlation between the observed and modelled water depths. 143

Figure 79: Time series comparison between modelled and observed tidal current velocities. 144

Figure 80: Correlation between modelled and observed tidal current velocities. 145

Figure 81: Time series of tidal and wave data relevant to the analysis from device 1 as well as the modelled values of the Soulsby exponential approximation. 147

Figure 82: Modelled wave-induced URMS values at given significant wave heights, zero-crossing periods and water depths 148

Figure 83: Earth velocity magnitude and direction during the Spring Ebb tide at St. Andrews Dock 152

Figure 84: Earth velocity magnitude and direction during the Spring Flood tide at St. Andrews Dock 152

Figure 85: Streamwise current velocity profiles during Spring Ebb (5 minute averages at 15 min intervals). 153

Figure 86: Spring Ebb streamwise current velocity data through depth and time (using a 5-minute average). 154

Figure 87: Spring Ebb turbulence strength data through depth and time (using a 5-minute average). 154

Figure 88: Spring Ebb turbulence intensity data through depth and time (using a 5-minute average). 154

Figure 89: Spring Flood streamwise current velocity profiles (5-minute averages at 15 min intervals). 156

Figure 90: Peak Spring Flood flow fit to 1/7th power law 156

Figure 91: Spring Flood streamwise current velocity data through depth and time (using a 5-minute average). 157

Figure 92: Spring Flood turbulence strength data through depth and time (using a 5-minute average). 157

Figure 93: Spring Flood turbulence intensity data through depth and time (using a 5-minute average). 157

Figure 94: Earth velocity magnitude and direction during the Neap Flood tide at St. Andrews Dock. 159

Figure 95: Earth velocity magnitude and direction during the Neap Ebb tide at St. Andrews Dock. 159

Figure 96: Streamwise current velocity profiles during Neap Flood (5-minute averages at 15-minute intervals). 160

Figure 97: Neap Flood streamwise current velocity data through depth and time (using a 5-minute average). 161

Figure 98: Neap Flood turbulence strength data through depth and time (using a 5-minute average). 161

Figure 99: Neap Flood turbulence intensity data through depth and time (using a 5-minute average). 161

Figure 100: Streamwise current velocity profiles during Neap Ebb (5-minute averages at 15 minute intervals). 162

Figure 101: Neap Ebb Streamwise current velocity data through depth and time (using a 5-minute average). 163

Figure 102: Neap Ebb turbulence strength data through depth and time (using a 5-minute average). 163

Figure 103: Neap Ebb turbulence intensity data through depth and time (using a 5-minute average). 163

Figure 104: Comparison of simultaneous water depth and current velocity between tidal cycles. 164

Figure 105: Comparison of tidal current velocity, turbulence intensity and depth during the Spring Flood between 15:35 and 19:00. 165

Figure 106: Comparison of tidal current velocity, turbulence intensity and depth during the Neap Flood between 10:15 and 13:15. 165

Figure 107: Relationship between mean current velocity and turbulence strength throughout Flood and Ebb tides. 172

Figure 108: α, β, R2 and α vs β values calculated for every Flood and Ebb tidal cycle during the DWR deployment. 174

Figure 109: Relationship between water depth, significant wave height and zero-crossing period and values of α and β. 175

Figure 110: Relationship between mean current velocity and turbulence intensity throughout Flood and Ebb tides. 177

Figure 111: γ, δ, R2 and γ vs δ values calculated for every tidal cycle during the DWR deployment 179

Figure 112: Relationship between water depth, significant wave height and zero-crossing period and values of γ and δ. 180

Figure 113: Relationship between mean current velocity and turbulence strength with bursts containing significant wave heights greater than 0.2 m highlighted in red. 185

Figure 114: Relationship between mean current velocity and turbulence intensity with bursts containing significant wave heights greater than 0.2 m highlighted in red. 185

Figure 115: The calculated Soulsby exponential approximation at relevant mean current velocities. 186

Figure 116: Comparison of current velocity and surface elevation measured during wave bursts 173 and 284. 191

Figure 117: Comparison of pressure energy and power spectral density calculated during wave bursts 173 and 284. 192

Figure 118: Depth-averaged Flood current velocity against turbulence intensity during Spring and Neap tides. 197

Figure 119: Depth-averaged Ebb current velocity against turbulence intensity during Spring and Neap tides. 197

Figure 120: Power model of combined depth-averaged ADCP results 197

Figure 121: Relationship between mean current velocity and turbulence strength throughout the Spring Flood ADCP survey. 200

Figure 122: Relationship between mean current velocity and turbulence strength throughout the Neap Flood ADCP survey. 200

Figure 123: Difference between observed and modelled turbulence strength during the Spring Flood ADCP transect. 201

Figure 124: Difference between observed and modelled turbulence strength during the Neap Flood ADCP transect. 201

Figure 125: Observed turbulence strength data against modelled turbulence strength data during the Neap Flood ADCP Survey. 202

Figure 126: Comparison of turbulence strength empirical model and power trend between peak flow data presented within the literature. 205

Figure 127: Comparison of turbulence intensity empirical model and power trend between peak flow data presented within the literature. 205

Figure 128: Effect of including turbulence strength within tidal stream power EYA. 206

Figure 129: Diagrams of proposed methodologies to measure turbulence through depth in fast tidal streams by Thomson et al. (2011; 2012). 211

Tables

Table 1: Structure of the thesis objectives 3

Table 2: Tidal resource estimates of the UK. Figures taken from (Black and Veatch and Carbon Trust, 2005; Boyle, 2012; Andrews and Jelley, 2013). 25

Table 3: Tidal resource estimates of the Pentland Firth, North Scotland. Figures taken from (Boyle, 2012; Easton et al., 2012; Draper et al., 2014; Adcock et al., 2014). 25

Table 4: Beaufort wind force scale and estimates of sea state (Met Office, 2016). 58

Table 5: Various equations used to describe propagating monochromatic linear waves analytically in varying depths (Hardisty, 1990; Holmes, 2001; Schwartz, 2006) 61

Table 6: Valeport Midas DWR sensor information (Valeport, 2008). 84

Table 7: Derivation of wave and tidal statistics from Valeport MIDAS DWR and their output locations (Valeport, 2008). 87

Table 8: Technical limitations of the 1200 kHz and 600 KHz models of Teledyne ADCPs (Teledyne, 2011). 95

Table 9: Time and location of each ADCP static survey. 122

Table 10: Ensemble information for the Spring static ADCP surveys. 150

Table 11: Ensemble information for the Neap static ADCP surveys. 158

Table 12: Comparison of relevant literature and thesis results. 168

Table 13: Structure of the analysis chapter 170

Table 14: Linear regression analysis of the whole deployment (All), Flood and Ebb tide between streamwise mean current velocity and turbulence strength. 172

Table 15: Power regression analysis of the whole deployment (All), Flood and Ebb tide between streamwise mean current velocity and turbulence strength. 173

Table 16: Power regression analysis of the whole deployment (All), Flood and Ebb tide between streamwise mean current velocity and turbulence intensity 178

Table 17: Multiple linear regression analysis of the whole deployment (All), Flood and Ebb tide between streamwise mean current velocity, the Soulsby exponential approximation and turbulence strength. 187

Table 18: Tidal and wave parameters of calm and increased wave activity samples. 190

1 Introduction

1.1 Thesis Rationale

In the face of impending climate change, depletion of fossil fuels and energy security vulnerabilities, governments worldwide are adopting innovative technologies to generate clean power from naturally replenishable, 'renewable', energy sources. The tidal stream power sector extracts the kinetic energy within the horizontal motion of tidal currents using tidal stream turbines (TSTs) (Uihlein and Magagna, 2016). The successful development of the tidal stream power industry fundamentally relies on a thorough, quantitative understanding of the available resource. This is important to accurately predict energy yield and potential revenue but also device performance and fatigue. Whilst tidal heights can be accurately predicted at a location, tidal current velocities are more difficult to predict as they vary through depth and time due to a range of dynamic variables; these include turbulence and wave-induced velocities (Hardisty, 2009; Boyle, 2012; Andrews and Jelley, 2013). Over the past decade, numerous energy yield assessments (EYAs) have attempted to predict the power potential of the UK's tidal streams (Black and Veatch and Carbon Trust, 2005; Boyle, 2012; Easton *et al.*, 2012; Andrews and Jelley, 2013; Draper *et al.*, 2014; Adcock *et al.*, 2014) but many ignored the localised effects of turbulence and surface wave activity on velocity time series (Clark *et al.*, 2015a).

At present, there are few published reports of full-scale TST performance in realistic tidal flows (MacEnri *et al.*, 2013; Jeffcoate *et al.*, 2015); though numerous prospective development sites are expected to be turbulent and exposed to significant surface wave activity (EMEC, 2009; Bouferrouk *et al.,* 2016). Within the last decade, research involving numerical modelling (McCann, 2007; Markus *et al.*, 2013) and laboratory flume experiments (Barltrop *et al.*, 2007; Gaurier *et al.*, 2013; Lust *et al.*, 2013; De Jesus Henriques *et al.*, 2014; Galloway *et al.*, 2014; Mycek *et al.*, 2014) has identified that increased levels of turbulence strength, intensity and wave-induced orbital motions can reduce performance and hasten structural fatigue within prototype TSTs. Researchers have measured turbulence strength and intensity at potential tidal stream array sites prior to full-scale deployments of TSTs (Osalusi *et al.*, 2009a and 2009b; Thomson *et al.*, 2010a, 2010b, 2011, 2012; Richards *et al.,* 2013; Gunawan *et al.*, 2014; McCaffrey *et al.*, 2015). Research specifically focusing on modelling turbulence metrics and wave-current interaction using *in situ* data within the context of tidal stream power is limited in scope and relevance thus presenting a significant research gap (Filipot *et al.*, 2015; Bouferrouk *et al.,* 2016). Research

concerning wave-current interaction has instead focused on the implications for sediment transport within tidal flows (Soulsby and Humphrey, 1990; Williams *et al.,* 1996; Wolf and Prandle, 1999; Powell *et al.,* 2000).

Numerous authors have called for an increased understanding of these effects within the context of tidal stream power from empirical data collected *in situ* (EMEC, 2009; Osalusi *et al.*, 2009b; Galloway *et al.*, 2014). Galloway *et al.* (2014) insist that energy yield assessments (EYAs) of the tidal resource are more complex than other renewable sources because of these additional effects and that there is still significant research and development needed before an inclusive methodology for tidal flow prediction can be established. It is, therefore, important to consider that whilst the tidal stream power industry requires an improved knowledge of turbulence and wave-current interaction within strong tidal flows, the environments in question are difficult to observe. Numerous deployment limitations exist and appropriate considerations must be made with regard to what studies are required and what are actually possible in terms of funding and scope. Collecting appropriate measurements from tidal sites is expensive, risky and follows no set methodologies, which makes it a particularly exciting research field in which to work (EMEC, 2015).

For this research, a site with favourable tidal and waves conditions that could be suitably accessed and monitored was desirable. The Humber Estuary, UK, has been dubbed the 'Energy Estuary' because of its surrounding local industries focused on delivering energy to the region (Humber LEP, 2014). Tidal stream power is suggested to be part of the Humber's future energy mix due to the estuary's hyper-tidal characteristics (tidal range >6 m and generally well-mixed (Archer, 2013)). A handful of prototype devices have demonstrated its potential in the past but there has been very limited published data of the estuary's tidal stream current parameters. With the emergence of more economically viable floating TST designs the Humber has again looked a promising development site for tidal stream power and was therefore used as this thesis' primary study site. Whilst sheltered from the very large waves that occur at other prospective tidal stream development sites, such as the Pentland Firth, Scotland, it was envisioned that this work would provide a novel insight into turbulence metrics and wave-current interaction at a considerably lower cost and risk than at more energetic sites. Inevitably, future research must be conducted at more exposed sites but this would require significant funding and innovation beyond the scope of this thesis.

This research utilises directional wave-recorders (DWRs) and acoustic Doppler current profilers (ADCPs) to collect primary datasets from sites within the Humber Estuary. These results are used to empirically model the relationships between mean

current velocity, turbulence strength, intensity and surface waves. The resulting models are shown to be comparable to results present in the literature and could be used to improve tidal stream power energy yield assessments.

1.2 Research Aims and Objectives

The aim of this thesis is to improve tidal stream power EYA models by better understanding the relationships between tidal mean current velocity, turbulence and waves. As the background and literature review chapter explains, the current understanding of these relationships is limited but recent research has determined that turbulence and waves affect tidal stream turbine performance and fatigue. Available instrumentation limits observations of tidal flow velocity to high-frequency measurements at a point in the water column and lower frequency observations through depth. Fieldwork within the Humber Estuary during 2014 and 2015 collected *in situ* data in order to meet the following research objectives:

Objective 1: Model the relationship between turbulence strength, intensity and mean current velocity at a point, ignoring wave-current interaction.

Objective 2: Model the relationship between turbulence strength, intensity and mean current velocity at a point, including wave-current interaction.

Objective 3: Model the relationship between turbulence strength, intensity and mean current velocity through depth, ignoring wave-current interaction.

Table 1 shows how the thesis objectives are divided and in which section they are analysed and discussed. In meeting these objectives, relevant models from the literature are tested against the observed results where possible. The relationship between turbulence strength, intensity and mean current velocity through depth in stormy conditions could neither be observed nor modelled, given the available resources, but recommendations for further work are detailed in section 5.6.

Measure	**Ignoring Wave-Current Interaction**	**Including Wave-Current Interaction**
At a point	Objective 1 (section 5.2)	Objective 2 (section 5.3)
Through depth	Objective 3 (section 5.4)	Recommendations (section 5.6)

Table 1: Structure of the thesis objectives

1.3 Thesis Structure

Beyond this introduction, the thesis is divided into six further chapters. Chapter 2 provides a critical review of relevant literature and theory in order to provide a detailed background to the research aims and objectives. This chapter is divided into three main sections, which include the current trends and challenges of tidal stream power, turbulence research in tidal environments and wave-current interaction. Chapter 3 describes and explains the experimental fieldwork methodology carried out in the Humber Estuary during 2014 and 2015. This involves a detailed description of the instrumentation used, fieldwork sites chosen and the deployment/measurement strategies employed. Chapter 4 presents the results of the fieldwork and is divided into two main sections: the results of the DWR deployments and the results of the ADCP surveys. Chapter 5 reports the analysis and discussion of the results collected during the fieldwork. This section is first divided into the three thesis objectives to explain how the results of the fieldwork were used to meet each objective. This is followed by a summary of findings and implications for tidal stream power energy yield assessments. The methodology is then evaluated and recommendations are made for future work. Chapter 6 provides the concluding remarks of the overall thesis. A comprehensive reference list is provided in Chapter 7.

1.4 Publications

A number of articles were published during this PhD at conferences and within journals:

Jennings, R. (2014). *Storm Wave Interactions with the Tidal Stream Resource*. RGS-IBG Postgraduate Forum Mid-Term Conference, Loughborough University.

Jennings, R. (2015a). *Waves, Tides and Turbulence in an Estuarine Environment: Implications for the Tidal Stream Resource*. PhD Experience Conference, University of Hull.

Jennings, R. (2015b). How Floating Turbines Could Harness the Awesome Power of the Tides. [Online]. Available from: http://theconversation.com/how-floating-turbines-could-harness-the-awesome-power-of-the-tides-46035.

Hardisty, J. and Jennings, R. (2016a). The Parameterisation of Turbulence in the Marine Environment. *Journal of Marine Engineering and Technology*. 16:3, pp. 114-120.

Hardisty, J. and Jennings, R. (2016b). Patterns of Turbulence in Tidal Flows. *Estuarine, Coastal and Shelf Science*. (In review, submitted revised corrections).

Hardisty, J., Martin, J., York, K. and Jennings, R. (2017). Turbulence at an Onshore Windfarm. *Journal of Geography and Earth Sciences*. (Accepted, in press).

2 Background and Literature Review

2.1 Introduction

This background and literature review chapter provides a broad overview of the research area in which this thesis aims to contribute whilst critically analysing relevant studies, methodologies and results in detail to identify research gaps and establish the theoretical framework of the research aim and objectives. The chapter begins by providing an introduction to renewable energy and the tidal stream power industry, which has continued to develop and evolve substantially over the course of the research. Within this section the means by which tidal stream mean current velocities can be predicted are demonstrated and the ways in which turbulence and surface waves may interact with these predictions are discussed. The chapter is then divided into two further sections covering turbulence and wave-current interaction respectively. Within each section, relevant theory and recent research are explored in order to inform the methodologies and analyses used within this thesis. Where necessary, research gaps and methodological limitations are critiqued. It is generally found that research into the prediction of tidal streams, turbulence and wave-current interaction within the context of tidal stream power using *in situ* measurements is increasingly sought after by both researchers and industry. It is also shown that *in situ* data are difficult to obtain considering the harsh environments in question (Easton *et al.*, 2012).

2.2 Tidal Stream Power

2.2.1 An Introduction to Renewable Energy and Tidal Stream Power

The supply and demand of energy is a critical, yet often controversial, global issue (Peake *et al.*, 2012). Energy is required to generate electricity and heat and is, therefore, a fundamental necessity within developed societies (Andrews and Jelley, 2013). As populations increase and aspire to ever-greater standards of living, governments must balance growing energy demand with an appropriate supply. The global energy trilemma is a term used to classify the three main trepidations felt by governments concerning the balance of energy supply and demand (World Energy, 2015). 'Energy security' involves the management of energy supply in order to meet current and future energy demand. 'Energy equity' comprises the accessibility and affordability of energy supply across the global population. 'Environmental sustainability' covers the development and move towards low-carbon resources in order to combat anthropogenically-induced climate change as a result

of the exploitation of fossil fuels. The transition from fossil fuels to renewable sources (primarily wind, solar, hydro, tidal and wave) is an ongoing global shift which aims to meet all three facets of the global energy trilemma (Andrews and Jelley, 2013).

Developed countries with abundant renewable resources, such as the UK, are currently diversifying their generating mix, securing energy supply and reducing carbon emissions effectively and efficiently by increasing their exploitation of renewable sources (RWE, 2015). The UK is at the forefront of many advances in renewable energy science and technologies, particularly onshore/ offshore wind and marine energy, which includes tidal stream power, tidal barrage and wave power. Tidal stream power has the potential to provide a predictable base-load to the national grid thus reducing the dependency on coal and gas power plants.

The tides are, principally, the periodic oscillation of large water bodies because of the gravitational attractions between the Sun, the Moon and the Earth. These forces follow coherent amplitude and phase relationships that vary in both frequency and magnitude over time due to the very precise orbits and rotations of the aforementioned celestial bodies (Hardisty, 2007). This effect is commonly observed as a diurnal (daily) or semi-diurnal vertical rise and fall of oceanic water that is exaggerated in constrained channels and narrow estuaries as well as a semi-diurnal horizontal flow of water observed as the Flood and Ebb tides. The energy within the horizontal flows can be exploited with TSTs, which convert the available kinetic energy flux into electrical power. This process is analogous to the process involved in conventional wind power, albeit with a significant difference in fluid density, which has a large effect on the available energy.

Exploiting the energy contained within tidal streams has a number of advantages in comparison with other renewable sources as it is relatively predictable, energy dense and it's energy conversion requires minimal on-land occupation (Sanchez *et al.,* 2014). Whilst the onshore and offshore wind industries have had exponential growth (in terms of installed capacity) for a number of decades and are now considered mature industries, tidal stream power has taken much longer to mature its technology but is now close to utility-scale development at sites such as Meygen in the Pentland Firth, Scotland (Uihlein and Magagna, 2016).

Exploiting high flow velocities with underwater turbine technologies presents a significant economic, scientific and engineering challenge. Walker (2013) describes the challenges facing array-scale development of tidal stream power in the UK and suggests that the sector is in a similar position to the wind energy industry in the 1980s and as such is 'at the bottom of a very steep yet exciting development curve'. Walker (2013) divides the challenges facing the development of the tidal stream power industry as:

- Scientific - identifying resource, site monitoring and modelling
- Engineering - turbine, foundation, cabling and array design
- Operations and maintenance - servicing and repairing turbines
- Environmental - impact assessments on flora, fauna and sedimentology
- Political - government subsidies, licensing and leasing of sea-bed
- Economic - minimising cost of technology and O&M whilst maximising power output and government subsidies
- Social - Community engagement

Meeting the objectives of this thesis will contribute towards solving scientific, engineering and (O&M) challenges.

2.2.2 Tidal Stream Turbines

This thesis aims to investigate the relationships between mean current velocities, turbulence metrics and surface wave parameters in order to improve tidal stream power energy yield assessments which typically ignore such effects as these relationships are still poorly understood (ORE Catapult, 2015). It is, therefore, important to firstly appreciate and understand the devices available to exploit the resource. This provides a foundation for later sections, which discuss how in-flow velocities interact with these devices and why an improved understanding of these flows at higher frequencies is necessary and is thus a growing research field.

Hardisty (2009) and Khan *et al.* (2009) describe a plethora of different devices designed to extract energy from tidal streams, which include horizontal axis, vertical axis, bed-mounted, floating, unidirectional, bi-directional, helical, direct-drive and hydrofoiled designs. Many TST designs now in development are analogous to the most commonly used wind turbines designs as they are horizontal-axis and 3-bladed. A major difference between wind and tidal turbines is that rotor diameter is limited by water-depth in TSTs and they, therefore, have a smaller aspect ratio (chord/blade length) and are thicker due to high root-bending moments (Fernandez-Rodriguez *et al.,* 2014).

In December 2011, TSTs gained significant exposure because of Siemen's acquisition of pioneering company Marine Current Turbines (MCT), who had developed the Seagen TST (MCT, 2011). With the international reputation and financial backing of Siemens the tidal sector became hopeful that utility-scale developments were just years away. In November 2014, Siemens announced that it had conceded that the 'market and supply chain' had not developed at the speed that they had expected and were to divest

MCT (ReNews, 2014). Nonetheless, the deployment of global marine energy capacity is accelerating and is predicted to increase from 6.8 MW in 2015 to 56.8 MW in 2018 (ReNews, 2016). In August 2016, Nova Innovation installed the first offshore tidal energy array in the world with two Nova M100 TSTs exporting power to the Shetland grid (Nova Innovation, 2016). The Meygen project in the Pentland Firth, Scotland, is the closest to providing utility-scale output at present with ambitious plans to expand to 398 MW installed capacity (Meygen, 2016). Whilst utility-scale developers appear keen to develop very large and robust bed-mounted turbines, smaller, more mobile buoyant and floating designs have recently been developed to exploit the faster flows in the free stream whilst avoiding the high costs of deploying and maintaining devices on the bed.

Below is a general description and comparison of each technology type from surface to bed:

- **Floating Turbines (Figure 1)** – These turbines are positioned near to the surface in the freestream. They are mobile and lightweight thus allowing for relatively easy installations and quick access during routine maintenance. Internal machinery required for electricity generation and transmission can be situated above the water's surface hence reducing waterproofing costs. Near-surface TSTs are likely to be positioned within wave base (see section 2.4.2) which could have negative effects on turbine performance. They are held in place by a tensioned line fixed to the bottom and can freely rotate into the tidal flow due to the shape of the floating hull. Their deployment is unbounded by depth and can, therefore, be located in deep channels or shallow estuaries. Their presence at the surface may affect shipping routes and will have a visual impact as opposed to fully submerged designs. Example designs include ScotRenewable's SR2000, BlueTEC Modular and Evopod.
- **Buoyant Turbines (Figure 2)** – These turbines are also mobile and lightweight and can be positioned in the optimal tidal stream velocities, which occur mid-column, below wave base and above the bottom boundary layer. They are held in place by buoyancy aids and tensioned lines. By submerging the entire device there is a minimised effect on shipping routes and no visual impact. The position of the device could also change with the tidal height in order to extract the fastest flows consistently. Example designs include Black Rock Tidal's Triton S36, Sustainable Marine Energy's PLAT-O and Nautricity's CoRMaT.
- **Bed-mounted Turbines (Figure 3)** – These turbines are often large, heavy and costly, but have large capture areas and robust foundations. Installation costs and routine maintenance are expensive, as specialised vessels are required to transport and

lift them to access internal machinery during operations and maintenance (O&M). Turbine blades are situated well below wave base most of the time but are often situated within the bottom boundary layer where flow velocities are reduced due to shearing with the rough seabed. Example designs include Atlantis' AR1500 and Andritz Hydro Hammerfest's HS 1000.

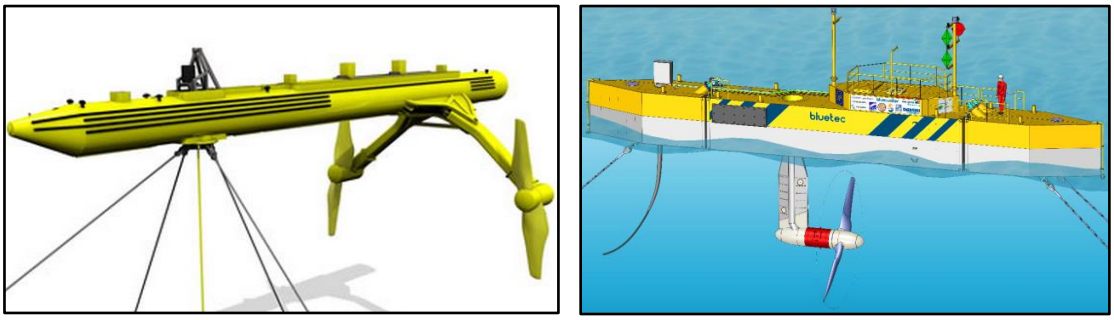

Figure 1: Floating turbines; ScotRenewables SR2000, BlueTEC Modular (ScotRenewables, 2016; BlueTEC, 2016).

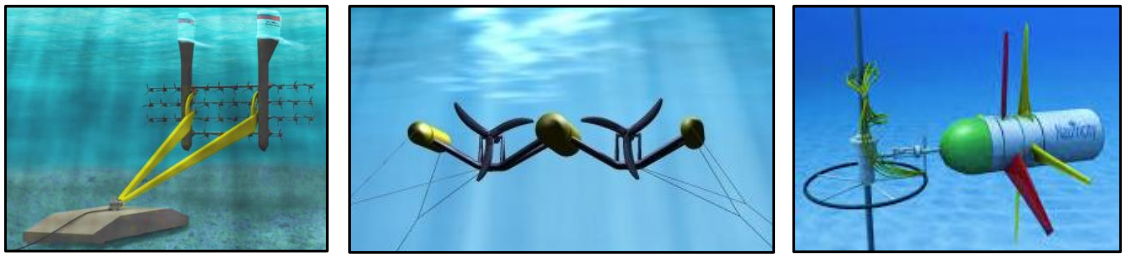

Figure 2: Buoyant turbines; Black Rock Tidal Power's Triton S36, Sustainable Marine Energy's Plat-O and Nautricity's CoRMaT (Black Rock Tidal Power, 2016; Sustainable Marine Energy, 2016; Nautricity, 2016).

Figure 3: Bed-mounted turbines; Atlantis' AR1500 and Andritz Hydro Hammerfest's HS 1000 (ATC, 2016; ScottishEnergyNews, 2016).

2.2.3 Tidal Stream Energy Yield Assessments

EYAs involve identifying and quantifying the available resource at a site to predict energy yields from tidal stream turbines (TSTs). An accurate EYA is crucial to the success of a tidal stream power development as it influences which turbine designs to use and the estimated potential revenue of the project. This process critically relies on accurately understanding the flow velocity through time, *U (t)*.

A typical EYA model calculates the power output of a specific TST through time at a static location based on the predicted flow velocities expected at the site (Hardisty, 2009). The potential power, *P*, in a moving fluid is dependent on the kinetic energy, K_E, within the fluids mass, *m*, and flow velocity, *U*:

$$K_E = \frac{1}{2} m U^2 \quad (1)$$

Mass is determined by the fluid density, ρ, the cross-sectional area of moving fluid, *A*, and the fluid flow velocity, *U*:

$$m = \rho A U \quad (2)$$

The combination of these equations results in the potential power, *P*, in a fluid flow equation:

$$P = \frac{1}{2} \rho A U^3 \quad (3)$$

This equation is commonly used to predict the available power within tidal streams and the wind as both resources are fluid, albeit with significantly different densities (sea water ~1025 kgm^{-3} whereas air ~1.225 kgm^{-3}) (Shapiro, 2010). Limitations including turbine efficiency, drivetrain efficiency, generator efficiency, power conditioning efficiency, cut-in speed and cut-out speed mean that the total potential power in the fluid flow cannot be converted to electrical energy (Gunawan *et al.,* 2014). A power coefficient, C_P, is thus introduced when considering the electrical power output, which is dependent on a turbines average efficiency, the ratio between the power output, P_O, and available power, *P*:

$$C_P = \frac{P_O}{P} \quad (4)$$

C_P does not remain constant at given flow speeds, as both P_O and *P* are dependent on *U*. The power output from a TST is given by:

$$P_O = \frac{1}{2} C_P \rho A U^3 \quad (5)$$

This equation is universally used to predict the instantaneous power output from both wind and tidal turbines. The power coefficient, C_P, is often given as a ratio between P and P_O though it is more appropriate to use a manufacturer's power curve which caters for cut-in and cut-out flow velocities as well as its rated power (Hardisty, 2012). Developers are often keen to increase either the size of the cross-sectional area, A, or the efficiency of the turbine, C_P, to achieve a higher energy yield and thus increased revenue though the most significant component of the equation is the flow velocity, U, because of its cubic relationship with P_O. A small increase in flow velocity can considerably increase power output; therefore, whilst engineering turbines that maximise the extracted energy from a flow field is central to exploiting tidal stream power, understanding the time series of U through various frequencies at a proposed location is of the utmost importance for accurate EYA.

In-flow current velocities passing through a turbine are complex as they accelerate, decelerate and reverse direction over varying depths every tidal cycle and are, therefore, turbulent, unsteady and can exhibit conditions which vary from sub-critical to supra-critical within a few hours (Lu, 2000; Hardisty, 2009). Deterministic mean flows are induced between the rising and falling of the Earths water bodies caused by the gravitational attraction of the Sun and the Moon and can be reasonably well predicted (at low temporal frequencies (tens of minutes)) if the harmonic constituents of tidal height are known at a site (Hardisty, 2009). Using the harmonic method (see section 2.2.4.1), the mean current velocity can be predicted over the 8760 hours in a year using (Hardisty, 2012):

$$E = \sum_{t=0}^{t=8760} P_O(t) \quad (6)$$

As Figure 4 illustrates, tidal current velocities include higher-frequency fluctuations induced by turbulence and surface waves. These fluctuations are poorly understood at development sites and have generally been ignored from previously published EYAs yet can be significant and should be further explored and characterised (EMEC, 2009; Tatum *et al.,* 2016). These fluctuations in velocity about the mean have been experimentally found to have negative impacts on turbine structural fatigue and performance and this thesis, therefore, seeks to investigate these fluctuations further by investigating key relationships from data collected *in situ* (McCann, 2007; Mycek *et al.*, 2014; Jeffcoate *et al.*, 2015).

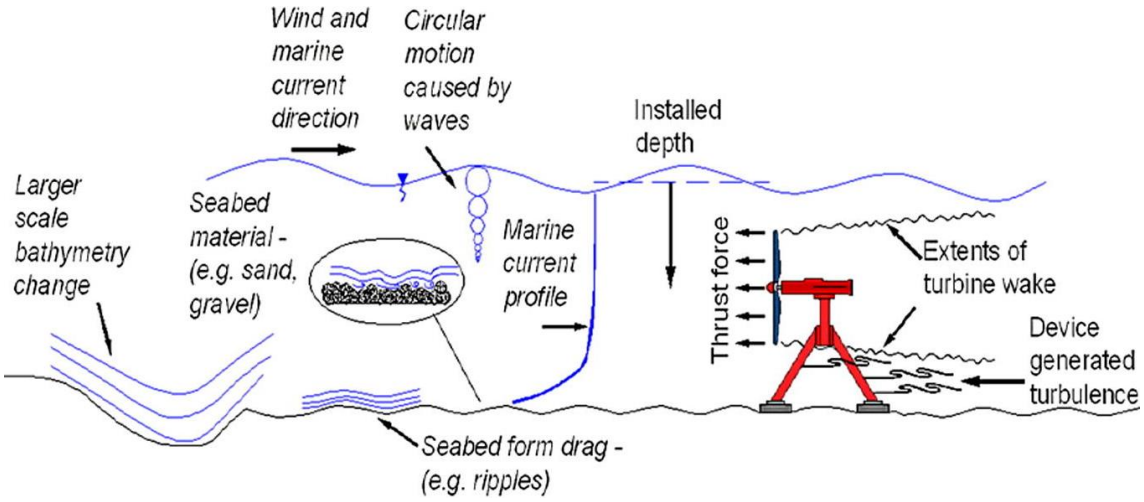

Figure 4: Expected TST interactions with varying flow conditions (Tatum et al., 2016).

The Reynolds decomposition is commonly used to split a high-frequency time series of fluid flow, U, into a steady mean, $\overline{U}$, and fluctuating perturbations, $\acute{U}$ (Duarte *et al.*, 2012; Mycek *et al.*, 2014; Clark *et al.*, 2015a; McCaffrey *et al.*, 2015) (Figure 5):

$$U\,(x,t) = \overline{U}(x) + \acute{U}(x,t) \tag{7}$$

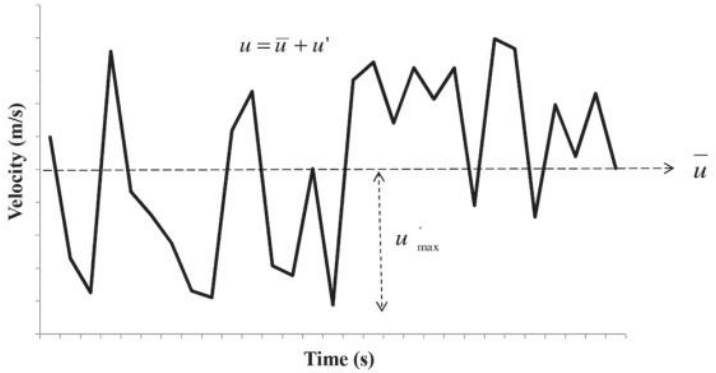

Figure 5: Mean flow velocity and higher frequency fluctuating component (Duarte et al., 2012)

An Eulerian time series of tidally dominant flow can be further divided using a triple decomposition (Soulsby and Humphrey 1990; Thomson *et al.*, 2010a; Suara *et al.*, 2014):

$$U\,(t) = U_{Ti} + U_{Tu} + U_W \tag{8}$$

Where U_{Ti} is the mean current velocity, U_{Tu} is the turbulent velocity fluctuation and U_W is the wave-induced orbital velocity that attenuates with depth from the surface. Each of these variables should also differ with depth/height above the bed. U_{Ti} is affected by frictional forces causing a boundary layer where the average flow is slowest near the bed

and maximum in the 'free flow'. U_{Tu} is dependent on the detailed bathymetry of the channel. U_W is maximised at the surface where wind-waves propagate but forces attenuate exponentially with depth. The theory and literature behind describing, predicting, observing and analysing the fluctuating flow components from turbulence and waves are critically assessed in sections 2.3 and 2.4 respectfully.

The existing international standards for tidal resource assessment and characterisation (IEC 62600-201) state that turbulence will be an important influence on TST performance but no corrections should be made for the effect of turbulence in reported EYAs until further research has adequately quantified its influence (Black *et al.*, 2015). The TiME project (Turbulence in Marine Environments) recently reported on what they considered to be new standards for measuring and interpreting turbulence at tidal stream development sites (Black *et al.*, 2015, Clark *et al.*, 2015a and 2015b). A review of a number of methods and instrumentation was made but many of the papers identified in this thesis and discussed later in this chapter were not acknowledged by TiME but are here considered extremely relevant and important. The Offshore Renewable Energy Catapult recently published a report identifying methods for EYA and addressing areas of losses or uncertainties in tidal stream energy yield estimation (ORE Catapult, 2015). Most important to this thesis is that turbulence and wave-current interaction are identified as being key problems still needed to be researched further within the industry and, therefore, do not yet have standards for *in situ* quantification or characterisation. Clark (2015) presents a timeline of the EYA process, which emphasises the need for inclusion of turbulence monitoring and measuring throughout. A thorough characterisation of turbulence at a development site would be extremely useful for predicting device performance, fatigue and array interaction though at present site characterisation has been mostly concerned with mean velocity estimation (Figure 6).

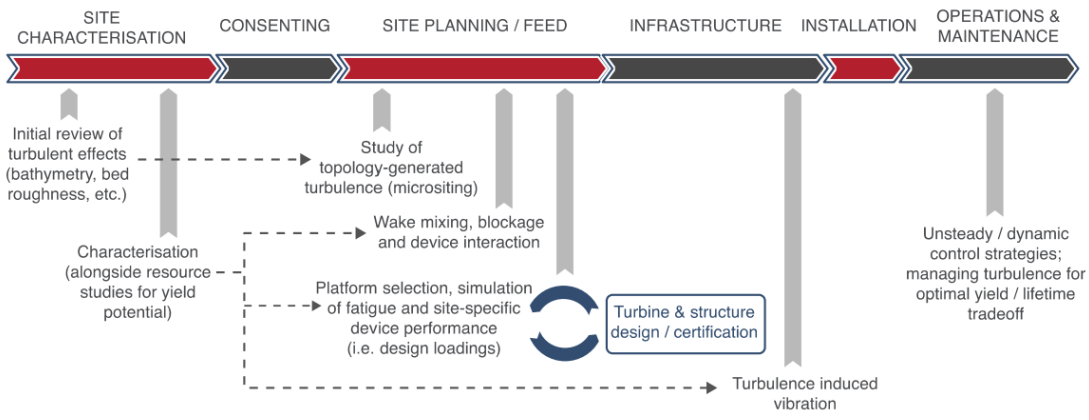

Figure 6: Example of an energy yield assessment timeline emphasising the need for a detailed site characterisation of turbulence (Clark, 2015)

2.2.4 Predicting the Tidal Stream Resource

This section provides a detailed explanation of methods used to predict the tidal stream resource in order to highlight areas that could be improved by meeting the objectives of the thesis.

Barotropic, astronomically forced tidal heights are perhaps the most deterministic phenomena in nature (Thomson and Emery, 2014). Tidal heights can be accurately predicted at a site long into the past or future thanks to our precise understanding of the tides relationship with the exact orbits of the Sun and the Moon relative to Earth (Hardisty, 2009). Two major theories exist for the generation and prediction of tidal heights: equilibrium and dynamic theory (Kvale, 2006). Comparably, tidal currents are far more complex and harder to predict due to their variability with depth because of water column stratification, seafloor topography, basin boundaries and non-deterministic interactions, such as surface wave conditions.

Sir Isaac Newton developed the equilibrium theory of tidal forces, which assumes that the Earth is entirely covered by deep water of uniform depth that instantly responds to tractive forces induced by the orbital motions of the Sun and the Moon (MacMilan, 1966). These movements, along with centrifugal forces, produce oceanic bulges on opposite sides of the Earth (Figure 7 (A)). The bulges height is related to the orientation of the Sun and the Moon but more closely follow the Moon's orbit. Although the Moon has a much smaller mass than the Sun, it is much closer to the Earth and due to the gravitational inverse square law, lunar gravity has a greater gravitational force (and thus influence) on Earth's oceans (Kvale, 2006; Hardisty 2009). The complex perturbations of the Moon's orbit around the Earth have a number of different effects on the tides:

- Figure 7 (B). The Moon's orbit is elongated with respect to the Sun. At New Moon the Moon is directly between the Earth and the Sun (syzygy) combining their respective gravitational forces to produce the Spring tides. The same effect is felt when the Earth is directly between the Moon and the Sun at Full Moon. When the Moon is positioned at a right angle to the Earth and the Sun (during Half Moon), lunar gravitational force is counteracted by the Sun's and a weaker, combined gravitational force is exerted to produce the Neap tides. The time taken between New Moons is referred to as the synodic month, lasting 29.53 days.
- Figure 7 (C). The orbital plane of the Moon is not synchronous with Earth's equator; it is actually inclined at around 5 °. Therefore, there is a variation in tidal forces between hemispheres resulting in the diurnal equality experienced in tidal heights during semi-diurnal tides. The time taken between maximum declinations is known as the tropical month, lasting 27.32 days.
- Figure 7 (D). The Moons orbit is elliptical, meaning that it has a maximum distance from Earth (Apogee, ~405 000 km) and a minimum distance from Earth (perigee, ~360 000 km) which results in stronger and weaker tides respectively. The time between perigees is known as the anomalistic month, lasting 27.55 days.
- Longer period tidal cycles exist such as the lunar-fortnightly, monthly, semi-annual and annual tidal cycles as well as the lunar nodal cycle (18.6 years).
- Concurrently, the Earth is rotating about its axis beneath these bulges, and as there are two bulges either side of the Earth, there are, therefore, two tidal cycles per day, referred to as the semi-diurnal tides. A location on the Earth moving into a bulge experiences a rising tide (Flood) whilst a location moving out of a bulge experiences a falling tide (Ebb).

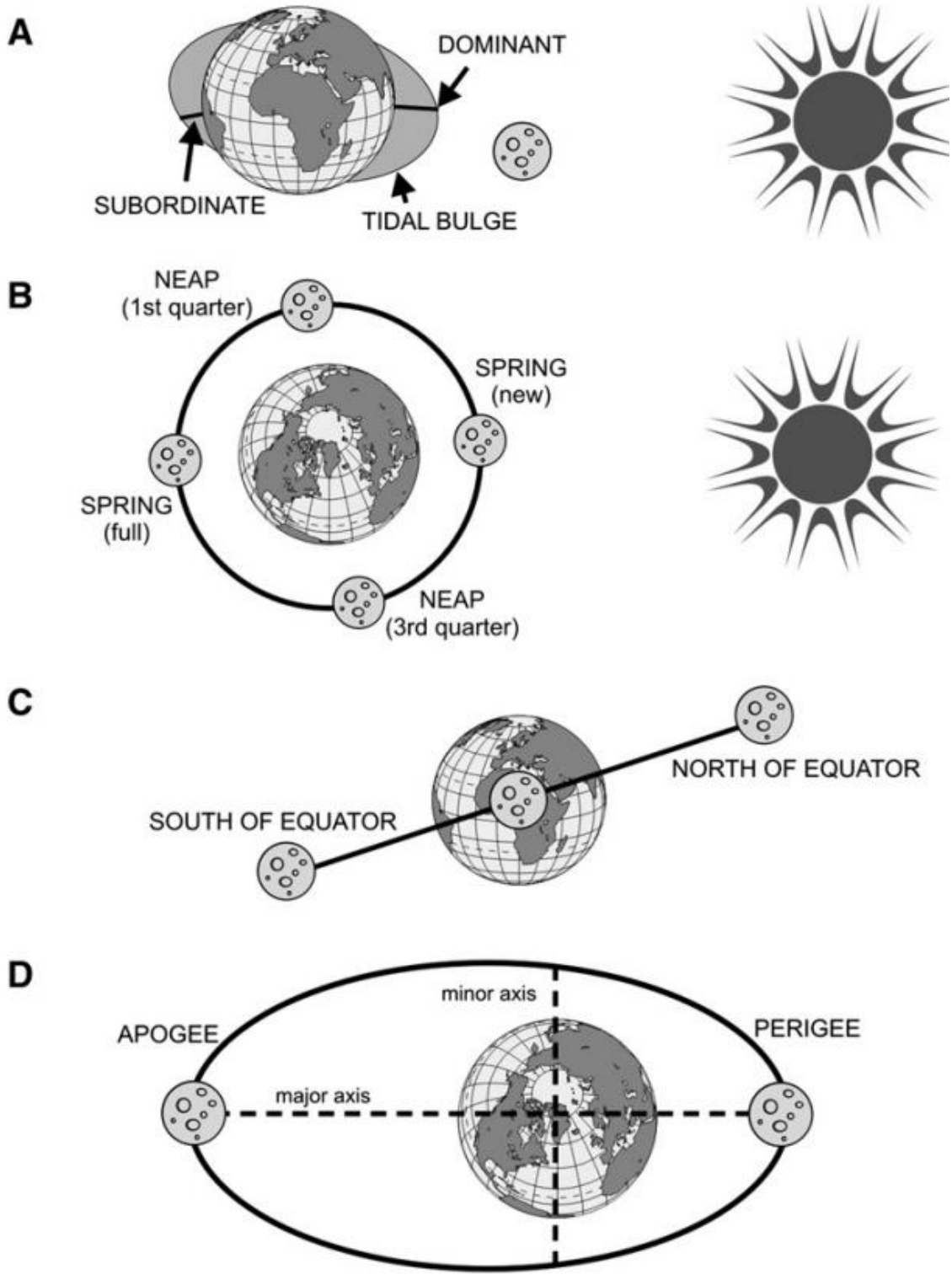

Figure 7: Orbital interactions of the Sun and the Moon on the Earth's tides (Kvale, 2006).

In equilibrium theory, tidal bulges would only be around 30 cm high at their maximum, but real world tidal heights can reach maximum Spring heights of 13 m in places such as the Bay of Fundy, Canada. Dynamic theory explains this amplification by acknowledging the effects of bathymetry on tidal height where large bodies of water are funnelled into narrower channels or estuaries as the tidal wave progresses. Discovered by Lord Kelvin in 1867 and furthered by Doodson and Warburg (1941), tidal heights were

found to be accurately predictable through time at a given site by 'harmonic analyses' of the individual gravitational constituents of the Sun and the Moon (Hardisty, 2009). Kvale (2006) explains that this method essentially combines the effects of 'phantom satellites' which each exert individual tidal forces with their own amplitude, period and phase angle depending on the location. These can be calculated using sinusoidal 'harmonics' once the respective amplitudes and periods of each constituent are known and then summated in a Fourier series to express the resultant tidal height variation at a location (Figure 8). It is the summation of the semi-diurnal lunar and solar harmonics (M_2 and S_2) that generate the simple Spring and Neap tides. The periods of each harmonic species are well known due to the highly predictive orbits of the Sun and the Moon; however, values for amplitudes are entirely site specific because of spatial variations in bathymetry. Only at designated tidal monitoring sites are these harmonics accurately calculated. Therefore, the variation in tidal height through time can be predicted using:

$$h_T(t) = A_{M2}\cos\left(\frac{2\pi t}{T_{M2}} + \rho_{M2}\right) + A_{S2}\cos\left(\frac{2\pi t}{T_{S2}} + \rho_{S2}\right) + A_{M4}\cos\left(\frac{2\pi t}{T_{M4}} + \rho_{M4}\right) + A_{K1}\cos\left(\frac{2\pi t}{T_{K1}} + \rho_{K1}\right) + A_{O1}\cos\left(\frac{2\pi t}{T_{O1}} + \rho_{O1}\right)\ldots \quad (9)$$

Where h_T is tidal height, A is the harmonic amplitude, T is the harmonic period and ρ is the harmonic phase shift. The subscripts refer to the relevant harmonic constituents of the Sun and the Moon (see Figure 8). The accuracy of tidal prediction is reliant on the number of harmonic constituents predicted. With just 15 days of data, harmonic constituents for the major M_2, S_2, K_1 and O_1 tides can be approximately determined (Figure 8) (Schwartz, 2006). The lunar and solar semi-diurnal species (M_2 and S_2) reasonably approximate the distinctive Spring-Neap-Spring cycle.

Constant	Speed (°/h)	Origin	Days needed to separate	From	Amplitude at Trenton, NJ (feet)
M_2	28.984104	Lunar	–	–	3.547
M_4	57.968208	Shallow-water	0.5	M_2	0.517
M_6	86.952313	Shallow-water	0.5	M_4	0.266
M_8	115.936417	Shallow-water	0.5	M_6	0.120
K_1	15.041069	Lunisolar	1.1	M_2	0.349
S_6	90.000000	Shallow-water	4.9	M_6	0.005
S_4	60.000000	Shallow-water	7.4	M_4	0.005
O_1	13.943036	Lunar	13.7	K_1	0.288
MK_3	44.025173	Shallow-water	13.7	$2MK_3$	0.120
$2MK_3$	42.927140	Shallow-water	13.7	MK_3	0.116
OO_1	16.139102	Lunar	13.7	K_1	0.030
$2Q_1$	12.854286	Lunar	13.8	O_1	0.028
S_2	30.000000	Solar	14.8	M_2	0.461
MS_4	58.984104	Shallow-water	14.8	M_4	0.148
$2SM_2$	31.015896	Shallow-water	14.8	S_2	0.025

Figure 8: Major tidal harmonic constituents and their corresponding phase and amplitude (Schwartz, 2006).

Figure 9 identifies the global distribution of tidal heights. A natural phenomenon that occurs due to the rotation of the earth and large oceanic basins is the amphidromic

point about which it appears that tides rotate (Easton *et al.*, 2012). At this point, the tidal height is always 0 m and tidal heights then increase with distance outward. From this, the regions of which developers are most concerned becomes evident as increased tidal height generally implies increased flow velocities and thus greater energy potential.

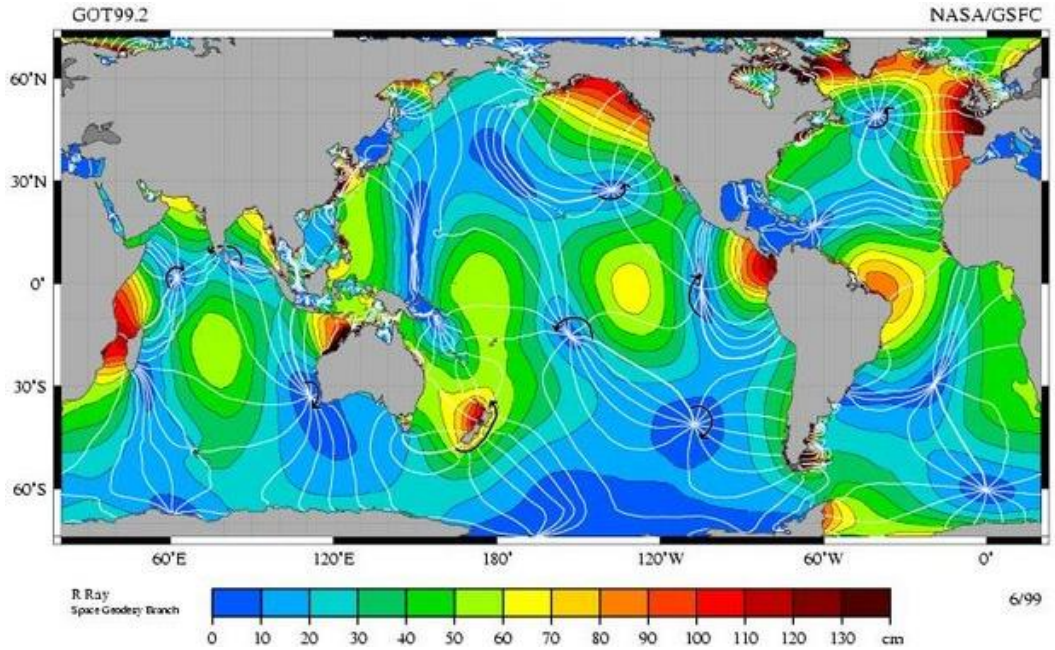

Figure 9: Global tidal height distribution and location of major amphidromic points (EoEarth, 2011).

2.2.4.1 Tidal Stream Mean Current Velocity

When considering that the tidal bulges move as very long period waves, it can be assumed that their accompanying currents are generated similarly to surface gravity waves (these phenomena discussed later in section 2.4.2). The flow velocity induced by the tide is known as the tidal stream, which is said to Flood and Ebb between high and low water. In estuaries, tides behave like that of a standing wave, where peak Flood and Ebb currents generally occur half way between high tide and low tide, whilst in open ocean, tides behave more like a progressive wave, where Flood and Ebb currents occur at the same time as high tide and low tide (Figure 10) (Hardisty, 2009). In the mouth of estuaries, the transition between a standing wave and a progressive wave can cause tidal currents to occur at irregular/asymmetric intervals between high and low water.

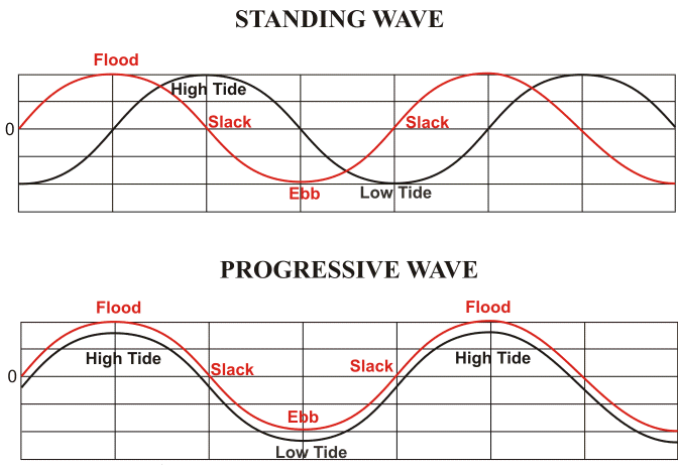

Figure 10: Relationship in time between tidal heights and tidal currents and the concept of standing and progressive waves (NOAA, 2013).

The tidal current velocity can be predicted in a manner similar to the tidal height at a site as a function of the amplitude and phase of sinusoidal harmonic species:

$$U_{Ti}\,(t) = U_0 + \sum \left[U_A \cos \left[\frac{2\pi t}{T_A} + \rho_A \right] \right] \tag{10}$$

This approximation may be reasonable for depth-averaged tidal flows; however, tidal current velocities are not constant through the water column and as TSTs can now be positioned almost anywhere in the water column (due to state of the art advances in technology) the vertical distribution of current velocities is now of significant importance. Any fluid flowing near a solid boundary develops a mean 'velocity profile' whereby the fluid velocity slows to zero at the boundary, or bed in the case of tidal currents. This is a result of the fluids resistance to flowing, or its viscosity, which generates shear stress parallel to the boundary (Clark *et al.*, 2015a). Typical mean velocity profiles through a semi-diurnal tidal cycle are shown in Figure 11 where the x-axis is mean current velocity and the y-axis is depth.

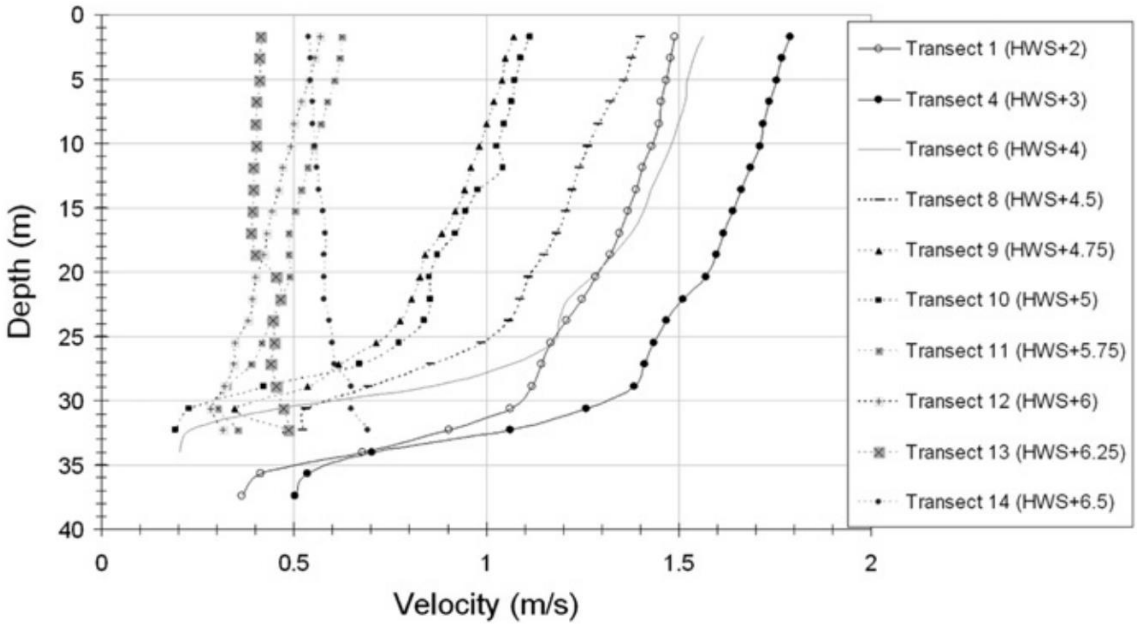

Figure 11: Velocity profiles at a site in the Severn Estuary collected by a vessel-mounted ADCP (Mason-Jones et al., 2013).

The constant velocity observed above the boundary layer is referred to as the free stream velocity, U_∞; this is where TSTs would be ideally situated because it is the fastest part of the flow. The height of the boundary layer, δ, is often defined as the distance above the bed at which $\overline{U} = 0.99\ U_\infty$. Whilst the free stream's mean velocity is considered constant, higher-frequency fluctuating components can be significant and affect the kinetic energy within the flow. The mean shear profile is strongly linked to the turbulent properties of the flow with the greatest region of shear relating to the greatest properties of turbulence (Clark *et al.,* 2015a). Velocity profiles have well-understood shapes; EMEC (2009) demonstrate that tidal stream velocity profiles can be empirically fit to power laws such as the $1/7^{th}$ law:

$$U = U_0 \left(\frac{z}{d}\right)^{\frac{1}{7}} \tag{11}$$

In a fully developed, turbulent boundary flow, the height at which velocity is essentially zero can be determined by Von Karman's law of the wall, which can be used to estimate the roughness of the bed material and the velocity profile (Charnock, 1959; Heathershaw and Langhorne, 1988):

$$\overline{U}(z) = \frac{u_*}{k} \ln\left(\frac{z}{z_0}\right) \tag{12}$$

Where u_* is the friction velocity, k is the Von Karman constant (~0.41), z is the height above the bed, and z_0 is the hydraulic roughness (Holtappels and Lorke, 2011). The

shape of the profile above the boundary and below the free stream is dependent on the bed stress and the bed texture. Antunes do Carmo (2012) describes how over movable beds, the interaction of flow and sediment transport creates a hierarchy of bedforms from small ripples to larger dunes and antidunes. Their presence affects bed roughness, which causes flow separation and recirculation and contributes to turbulence (see section 2.3.1).

2.2.4.2 Global Resource Estimates

The total power available in global tidal streams is estimated to be vast (Boyle, 2012; Andrews and Jelley, 2013). It is simply not feasible to cover the entire world's oceans and inlets in tidal turbines; therefore, other, more realistic methods of estimating the world's best tidal resources have been employed. Boyle (2012) explains how the available resource can be broken down into:

- 'Total Resource' - which corresponds to the total energy delivered by the resource
- 'Technical Potential' - which describes the maximum amount of energy that could be extracted if the area were fully exploited by the current technology
- 'Practical Potential' - which is the most realistic estimate as it takes into account a variety of real world constraints such as uncertainty in resource estimates, supply intermittency and access to the grid as well as socio-economic complications such as planning permission and environmental objection

These three estimates are often defined interchangeably as an instantaneous power (the rate at which energy is generated e.g. GW), or an energy yield (the amount of energy generated over time e.g. TWh). These definitions are crucial when considering any tidal EYA at varying scales. Figure 12 shows the technical potential power of 17 different countries tidal resources. The UK has by far the highest potential with 11.4 TW available, followed by Japan (2.2 TW), China (2 TW) and Canada (2 TW). Some huge countries with long coastlines such as Russia (350 MW), Australia (500 MW) and USA (350 MW) have relatively small potential tidal resources which shows how localised and dense tidal stream resource 'hotspots' can be.

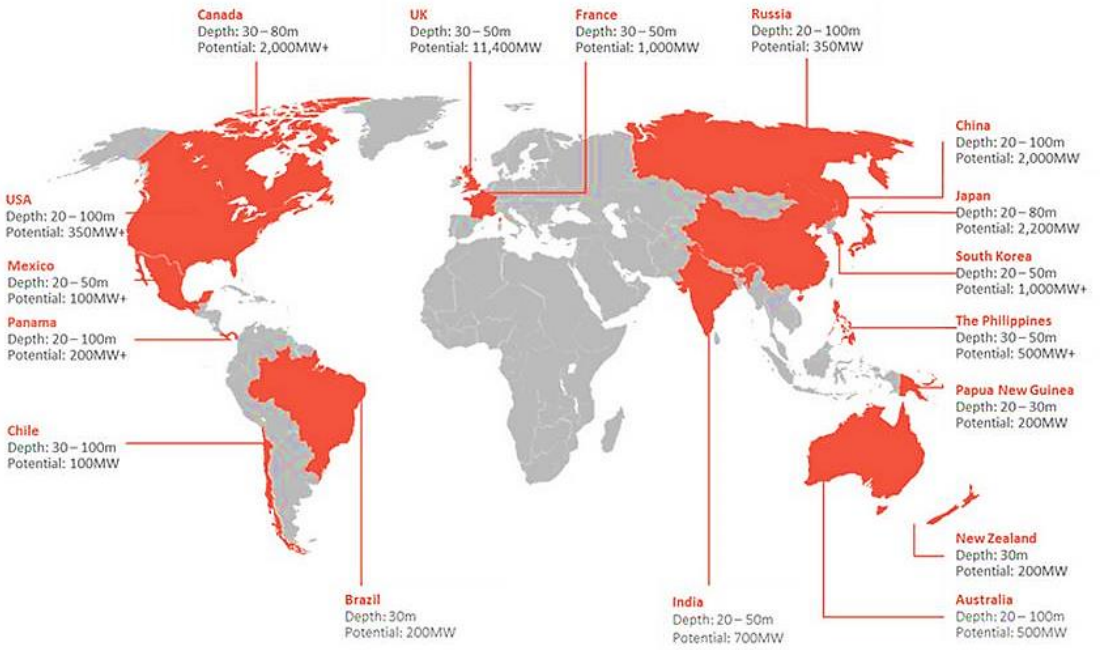

Figure 12: Global estimated tidal stream power potential by country (Atlantis Resources Ltd., 2015).

2.2.4.3 UK Resource Estimates

Figure 13 identifies areas with potential for both tidal stream and wave developments in Europe. The UK coast has some of the greatest potential for tidal stream developments in the world due to numerous channels and estuaries having Spring tidal stream velocities in excess of 2 ms^{-1} (Fairley *et al.*, 2013). The Humber Estuary has been identified here as having a 'low' tidal stream resource due to its maximum flow speeds of around 2 ms^{-1}, relative to other, more energetic, sites such as the Pentland Firth, which has Spring tidal current velocities in excess of 3 ms^{-1}. The figures also show that the wave resource overlaps the tidal resource in the North of Scotland and South-West England, thus suggesting that many tidal stream sites will also undoubtedly experience high wave activity.

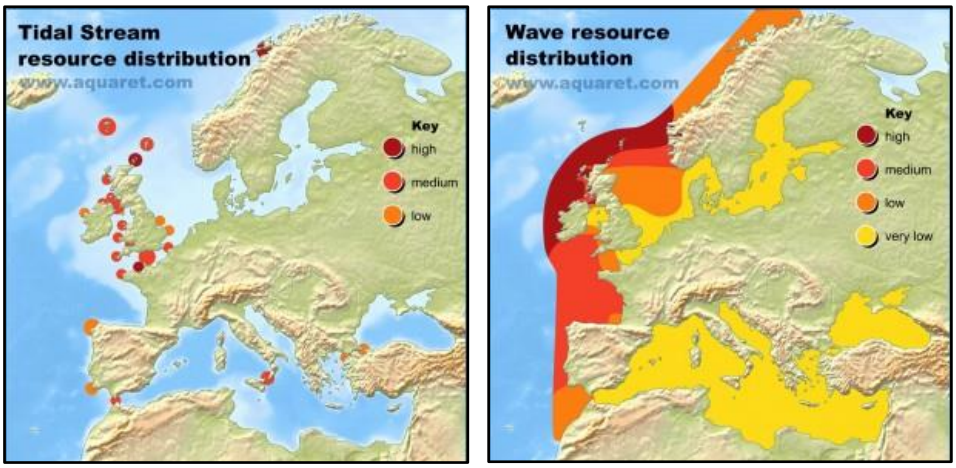

Figure 13: Tidal stream and wave resource distribution in Europe. (EMEC, 2014).

In an attempt to justify investment in tidal stream power within the UK, numerous studies over the last decade have sought to quantify the predicted resource. In particular, the Pentland Firth has been the subject of numerous EYAs as it is generally agreed that this is the most likely site for tidal stream development in the UK due to its impressive Spring currents in excess of 3 ms^{-1}. These extraordinary velocities have led to estimations that this area alone could account for 35 % of the total UK resource (Andrews and Jelley, 2013).

From the examples presented in Tables 2 & 3 it is obvious that there has been little unanimity between estimates of the UK or the Pentland Firth. UK estimates of the technical potential for installed capacity range from 2-4 GW to 36 GW whilst annual yield ranges from 22 TWh to 94 TWh. The estimated technical potential installed capacity of the Pentland Firth ranges from 1.8 to 9 GW whilst the estimated practical potential installed capacity is much lower at 0.6 GW. Garrett and Cummins (2005) acknowledged that there was no universal formula for tidal EYAs, and is likely the reason as to why there has been great variability in tidal power estimates. It is also interesting to note that the majority of previous EYAs focus on two-dimensional depth-averaged mean current velocities and ignore higher frequency flow fluctuation metrics and the vertical velocity distribution of the water column (see Easton *et al.*, 2012). Whilst fast mean flow velocities are the primary concern to tidal stream developers, these other factors must be better understood and included in further estimates, especially now that research has confirmed turbulence and wave-current interaction can have a significant effect on TST power output and thus technical potential (see sections 2.3.2 and 2.4.3) (Gooch, *et al.*, 2009).

Study	Year	Resource Type	Installed Capacity (Power)	Annual Yield (Energy)	Notes
Black and Veatch Phase I	2004	Technical	-	22 TWh	Around 6 % of the UK's energy demand
DTI/ Carbon Trust Renewables Innovation Review	2004	Practical	-	31 TWh	Around 10 % of the UK's energy demand at the time.
Carbon Trust/ Black and Veatch Phase II	2006	Practical	-	18 TWh	Reduced due to economic and non-independent zones
ABPmer	2007	Technical	36 GW	94 TWh	Devices in under 40 m water depth. Could generate 25 % of UK energy demand.
DTI	2011	Technical	2-4 GW	-	For tidal stream, not including tidal barrage
Andrews and Jelley	2013	Practical	50 GW	-	Estimated for 2050

Table 2: Tidal resource estimates of the UK. Figures taken from (Black and Veatch and Carbon Trust, 2005; Boyle, 2012; Andrews and Jelley, 2013).

Study	Year	Resource Type	Installed Capacity (Power)	Annual Yield (Energy)	Notes
Black and Veatch Phase I	2004	Technical	1 GW	8.9 TWh	Potential energy removed before natural currents are significantly reduced.
ABPmer	2007	Technical	1.8 GW	-	-
ABPmer	2007	Practical	0.6 GW	-	-
Salter and Taylor	2008	Technical	18 GW	-	Assumed 3 ms^{-1} tidal currents
Mackay	2008	Technical	9 GW	-	Assumes turbines do not affect natural flows.
Easton *et al.*	2012	Technical	8.97 GW	-	Mean energy flux into channel
Draper *et al.*	2014	Technical	4.19 GW	-	Upper bound
Adcock *et al.*	2014	Technical	~1.9 GW	-	Revised Upper Bound (3.4 GW at Spring tides, 0.47 GW at Neap Tides)

Table 3: Tidal resource estimates of the Pentland Firth, North Scotland. Figures taken from (Boyle, 2012; Easton et al., 2012; Draper et al., 2014; Adcock et al., 2014).

2.2.4.4 Commercial Predictive Software

A variety of commercial software has been developed to predict the tidal characteristics at a site though no known commercial software currently estimates the turbulence, available power or energy yield. TotalTide is the most comprehensive tidal prediction software available, providing tidal height and current predictions for over 7000 ports and 3000 tidal stream stations worldwide based on the harmonic method described in section 2.2.3. It is a digital version of the paper based nautical reference guides produced by the United Kingdom Hydrographic Office. It is relatively useful as a first step for planning tidal energy yield assessments as it provides accurate estimates of tidal height and, to a lesser extent, currents at up to 10-minute intervals at designated tidal stations long into the past or future. Its use is limited to tidal stations close to ports and shipping traffic; areas that are typically avoided for tidal stream power developments. Other numerical models have been developed that can accurately simulate tidal heights over large spatial areas, such as 'Caesar Lisflood'. Skinner *et al.* (2015) recently used Caesar LisFlood to model simultaneously high astronomical tides and storm surges (a rising of the sea due to low atmospheric pressure associated with a storm) in order to predict flooding impact on the Humber Estuary, though current velocity data was proved to be arduous to accurately model in either 2D or 3D.

2.2.5 Summary of Tidal Stream Power

Renewable energy will undoubtedly become a significant portion of the global energy mix in the future as fossil fuels decrease and climate change becomes more prevalent. The tidal stream power sector has the potential to grow dramatically due to its key advantages: predictability and enormous available resource. Large-scale projects, such as Meygen, could provide baseload electricity to the national grid thus competing with GW capacity coal and nuclear power stations. Whilst it has been determined that the tidal stream power industry is continuously advancing in terms of technology, the resource is not yet adequately understood at numerous development sites. Turbulence and wave-current interaction in tidal streams remain poorly understood at present and are key research areas to provide more accurate EYAs. The increasing shift in development towards floating and buoyant turbines undoubtedly means that turbulence and wave-current interaction near the surface and throughout the water column will become of great interest to developers and researchers. However, as the following sections explain, investigating these phenomena can be difficult and complex.

2.3 Turbulence in Tidal Streams

2.3.1 An Introduction to Turbulence in Tidal Streams

Tidal stream developers generally look for strong flow velocities in excess of 2 ms^{-1} at potential development sites in order to generate sufficient electricity to make a project economically viable (Fairley *et al.*, 2013). Most previous EYAs of tidal stream development sites have solely focused on mean velocities to predict installed capacity and annual yields but generally pay little attention to higher frequency flow fluctuations about the mean deterministic tidal stream flow (Clark *et al.*, 2015a; Tsai *et al.*, 2016). At present, tidal energy device manufacturers do not yet have the means to 'understand, predict or model unsteady interactions between their devices and turbulence in the marine environment' (Black *et al.*, 2015). This presents a significant problem as researchers have recently determined relationships between turbulent flow metrics and turbine performance parameters through evidence collected from numerical simulations (McCann, 2007) and scaled flume experiments (Barltrop *et al.*, 2007; Gaurier *et al.,* 2013; Lust *et al.*, 2013; Galloway *et al.*, 2014; De Jesus Henriques *et al.*, 2014). These results suggest that increased fluctuation about the mean flow will have negative impacts on the structural fatigue of the turbine blades and generator, potentially increasing operations and maintenance costs and decreasing revenue through downtime. Therefore, there is a growing demand for an improved knowledge of relationships between mean current velocities and higher frequency flow characteristics from *in situ* measurements at potential tidal stream power development sites (Galloway *et al.*, 2014).

Turbulence studies can be divided into two broad groups (Tatsumi, 2000); research into small-scale properties of turbulence, which are approached as mathematical and physical problems and studies of the large-scale structures of turbulence, which are dealt with as engineering and practical subjects. Tatsumi (2000) critically analyses both approaches stating that most small-scale studies generate 'useless theories' whilst large-scale studies supply a 'large amount of unfounded results' which are increasing as a result of the popularisation of numerical computation studies yet *in situ* studies are comparatively uncommon but increasingly important. Determining length scales (differences in phenomena at varying orders of magnitudes) in tidal stream turbine (TST) focussed turbulence studies is important as, due to the general dimensions of full-scale TSTs and their installed environments, present research is primarily interested in the large-scale structure of turbulence which can significantly affect a TST's performance (Clark *et al.*, 2015a).

Turbulent instabilities in tidal flows are quite different from those that occur in the atmosphere as tidal flows are bounded by the water surface which causes horizontal length scales to be many times the vertical (Fernandez-Rodriguez *et al.*, 2014). Irregularities on the seabed, commonly referred to as bed roughness, generate shear stresses which 'tear the fluid into highly energetic, irregular and three-dimensional eddies, with scales ranging from the size of the flow passage down to unity' depending on the bed type and geomorphology of the area (Osalusi *et al.*, 2009b). However, studies of turbulence in tidal environments are not unique to the emerging tidal stream power sector. For decades, physical geographers have attempted to understand turbulence in estuaries in order to understand its effects on sedimentology, geomorphology and ecology (Bricheno *et al.*, 2015). This has led to some studies being focused on flow-bed interactions at low energy sites, which are largely non-relatable to tidal stream power focused research due to their shallow water depth, low flow velocities and focus on small-scale microstructures of turbulence below the inertial subrange. Tidal stream power developers are, at present, far more interested in understanding the strong horizontal flow velocities, which will flow through a tidal turbine, yet this area contains numerous research gaps.

In situ tidal turbulence data (which of course give the most realistic results compared to flumes and simulations) from potential development sites are not abundant in the literature, thus presenting a distinct knowledge gap. Lu *et al.* (2000) argue that 'turbulence measurements are few compared to the vast pool of mean flow data'. Future research should therefore include additional turbulence measurements to better understand the relationships between mean current velocities and the most important metrics of turbulence used today to characterise potential tidal stream power development sites. However, Osalusi *et al.* (2009b) explain that sites suitable for the placement of a TST are challenging environments to work in as they exhibit large scales of turbulent motion. As there is no fixed point of reference in which to collect rapid measurements of velocity at small spatial scales within the water column, collecting such data presents a significant problem. Harsh met-ocean conditions can delay fieldwork and the instrumentation required to measure turbulence metrics adequately are at risk of being lost or damaged in such conditions (Mycek *et al.*, 2014).

Whilst turbulent flow can appear random in the time domain, turbulent motion and dissipation can be characterised in the frequency domain, which incorporates all components of the flow. At high Reynolds numbers (ratio of inertial forces to viscous forces), turbulent kinetic energy dissipates in an energy cascade from large, dynamically unstable eddies to ever smaller eddies until the remaining energy is eventually dissipated as heat once at the kinematic viscosity limit (Osalusi *et al.*, 2009a; Clark *et al.*, 2015a; Torrens-Spence *et al.,* 2015). The frequency domain representation of a turbulent flow time series allows the observation of portions of the signal that are either not easy to see, or not visible at all, when the signal is represented in the time domain. Fourier analysis is commonly used to convert time series into the frequency domain *via* a sum of sine and cosine terms known as the Fourier series representation (Chatfield, 1984). The Fast Fourier Transform (FFT) is a method used to speed up spectral analysis computation when there are more than 1000 data points (Chatfield, 1984; Torrens-Spence *et al.,* 2015). Spectra can be presented using an arithmetic or logarithmic scale depending on the detail and resolution of the data (Soulsby and Humphrey, 1990). Therefore, turbulence spectra are often generated from time series using the FFT and displayed using log-log plots, as in Figure 14. These graphs plot temporal or spatial frequency against kinetic energy to show which frequencies contain the most kinetic energy from long to short. The frequency at which the spectra can be calculated accurately is limited by the Nyquist frequency, which is half the sampling rate.

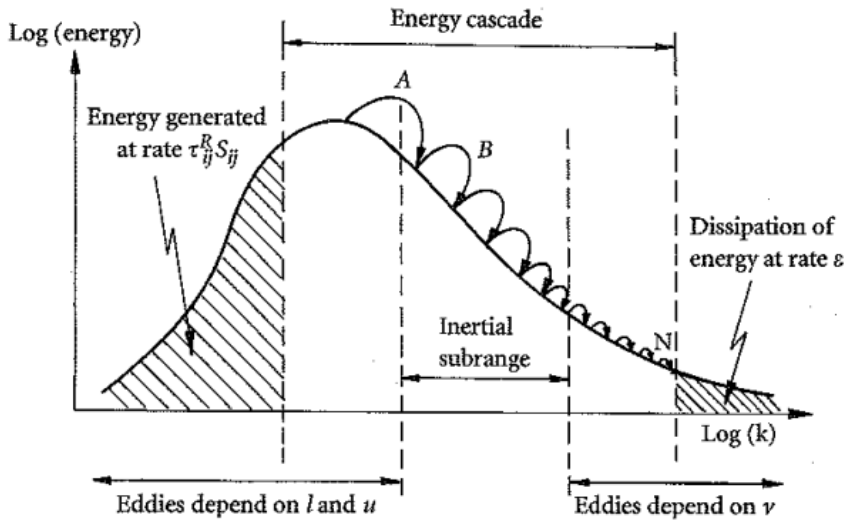

Figure 14: Turbulence energy spectrum curve in a log-log plot of wavenumber (Log(k)) against log(energy) (Davidson, 2012).

A peak in the frequency spectrum of a time series indicates the most important contribution to variance at frequencies in the appropriate region (Chatfield, 1984). The majority of theoretical work on turbulence has been concerned with the high-frequency

part of the energy spectrum where eddies depend on the viscosity of the fluid. At lower wave-numbers, which contain almost all the turbulent energy, the structure of the turbulence is mostly determined by the mean flow upon which it is superimposed and is highly anisotropic which means there is a weak correlation between the three orthogonal directions of flow (*u*, *v* and *w*) (Clark *et al.*, 2015a). This is because, at this scale, turbulent structures are predominantly flowing in a streamwise (*u*) direction; therefore, lateral (*v*) and vertical (*w*) directions are considerably slower. At high wavenumbers, however, the flow is more homogeneous and isotropic with a strong correlation between orthogonal flow directions (Grant *et al.*, 1961). As prospective tidal sites have high Reynolds numbers, the inertial sub-range is often characterised using the $f^{5/3}$ proportion so long as an appropriately high-frequency measurement is made (Durgesh *et al.*, 2014). This rule is governed by:

$$E(f) = C\varepsilon^{2/3} f^{-5/3} \tag{13}$$

Where $C\,\varepsilon^{2/3}$ can be approximated to fit the $f^{5/3}$ law to data in order to determine the inertial sub-range (Filipot *et al.*, 2015). The orbital velocities induced by surface waves oscillate at similar frequencies to the intertial subrange and therefore wave-current interaction is hypothesised to affect such a law. Few studies have observed such interactions at tidal stream power development sites of which this thesis intends to build upon (see sections 2.4.3.3 for case studies of observations and section 5.3 for analysis of these interactions from primary data collected in the Humber Estuary).

Turbulence is generated in tidal environments by a number of sources, as listed by Clark *et al.* (2015a):

- **Inflow:** Any wall-bounded flow at high Reynolds number is turbulent, even if the upstream bathymetry were mirror-smooth. This phenomenon also generates shear profiles and turbulent structures.
- **Bed roughness:** Eddies will have characteristics and length-scales linked to upstream bathymetry. The rougher the bed, the more the flow is torn into progressively complex structures.
- **Channel shape:** The shape of the channel can generate coherent turbulence structures such as vortex sheets proportional to the width of the channel.
- **Stratification:** The stability and buoyancy of the flow is affected by differences in temperature and salinity. This effect is minimal given the high rates of vertical mixing at the majority of tidal stream development sites.

Other physical processes can change the motion of tidal streams but are not strictly defined as being a source of turbulence but instead occur because of a different branch of physics (Clark *et al.*, 2015a). These include the tidal flux (periodic change in speed and direction due to gravity) and unsteady motions caused by surface waves. Waves are known to induce velocity fluctuations throughout the water column affecting turbulent dissipation, isotropy (correlation between velocity vectors *u, v and w*) and structure but wave-current interaction studies at tidal stream development sites are extremely limited at present.

When the turbulence that occurs at tidal stream development sites is insufficiently predicted, TST devices can be considered either over-engineered (increasing capital expenditure (CapEx)) or under-engineered (resulting in more frequent maintenance or device failure thus increasing operational expenditure (OpEx)) (Clark *et al.*, 2015a). In industry, it is generally understood that turbulence in tidal flows affect energy yield and fatigue of TSTs but it is unclear by how much, which results in significant commercial risk (Clark *et al.*, 2015a). It is later shown in sections 5.5.2 that factoring in the turbulence strength to tidal power models can significantly increase power potential at high velocities.

Clark *et al.* (2015b) recently categorised scales of turbulence within the context of tidal stream power. They suggest that different length-scales will have different effects on TSTs depending on their relation to turbine rotor dimensions. A comprehensive list of potential effects of each turbulent scale on TSTs is also presented and explained but are only noted here as the detailed engineering implications are beyond the scope of this thesis.

- **Large-scale eddies:** Having a characteristic length-scale greater than a turbine rotor diameter. Effects involve: Gusting, Downstream wake signature, Induction of distorted wake, Direct hydrodynamic loading, Peak power load, Transient electrical effects, Velocity shear near the bed affected by turbulent mixing, Rapidly changing inflow conditions over ROV or tool, Rapidly changing pressure distribution moves floating hull, Rapidly changing lift distribution on blade creates a noise source.
- **Mid-scale eddies:** Having a characteristic length-scale smaller than a turbine rotor diameter but greater than a turbine rotor blade chord length. Effects involve: Snap loading, Downstream wake signature, Induction of distorted wake, Dynamic stall and cavitation, Direct hydrodynamic loading, Peak power load, Transient electrical effects, Seabed related flow features result in unusual excitation, Velocity shear near the bed affected by turbulent mixing, Rapidly changing inflow conditions over ROV or tool, Rapidly changing pressure distribution moves floating hull, Rapidly changing lift distribution on blade creates a noise source.

- **Small-scale eddies:** Having characteristic length-scales smaller than a turbine rotor blade chord length. Effects involve: Blade-section properties, Downstream wake signature, Altered drag coefficient of bluff bodies, Altered excitation frequency in crossflow, Seabed related flow features result in unusual excitation, Velocity shear near the bed affected by turbulent mixing. Blade singing or 'lock-in' of flow over engineering structure disrupted or excited by turbulent fluctuations, Turbulent wakes and shedding vortices generate broadband noise.

These effects are not equally important and each must be prioritised based on physical significance and cost (Clark *et al.*, 2015b). Whilst some effects appear negligible, Clark *et al.* (2015b) explain that intuition can often be extremely misleading and no intentional prioritisation can be made. They suggest that the most useful turbulence metric at which these affects should be compared also remains unsolved and requires significant further research. It is generally concluded that the effects that are most uncertain should be prioritised but that urgency will shift towards reduced structural load or improved efficiency once the industry matures (Clark *et al.*, 2015b).

Due to the complexity of adequately characterising turbulence at all scales, a number of statistical metrics (uniform measurement scale) are frequently used to describe and model turbulence data in tidal stream research. The turbulence intensity has emerged as a useful metric for quantifying turbulent flows so long as the turbulence strength (square root of the variance) and the mean average of flow is known at a reasonable rate and accuracy. These metrics can more conveniently represent the flow than high-frequency time series are able to. This metric is also regularly used to describe atmospheric turbulence as it is important in a range of applications, for example, aircraft operations, the assessment of dynamic wind loads on structures and wind turbines and the prediction of air pollutant transportation and dispersion (Li *et al.*, 2014). As tidal flows are analogous to wind flows, these metrics are becoming increasingly popular when characterising large-scale tidal turbulence and are, therefore, the focus of the subsequent analysis chapter.

As the instantaneous flow fluctuates about a steady, mean background flow, the distribution of time series data can be considered normal and, therefore, the standard deviation can be used to quantify the variation in the y-axis. Low standard deviations indicate the data are mostly close to the mean value whilst higher standard deviations indicate greater spread. The standard deviation of a flow time series can be referred to as the turbulence strength, U_σ:

$$U_\sigma = \sqrt{\sum_{i=1}^{N} \frac{(U_i - \bar{U})^2}{N}} \quad (14)$$

Where U_i is the i^{th} instantaneous velocity measurement and N is the number of measurements (MacEnri *et al.*, 2013). Sometimes the standard deviation and the root-mean-square (RMS) are used interchangeably in the literature when describing this calculation (MacEnri *et al.*, 2013; Gunawan *et al.,* 2014). Bowden and Proudman (1949) and subsequently Bowden and Howe (1963) identified that the mean and standard deviation of flow are approximately proportional to one another but can vary with depth above the bed and between sites due to the mechanisms that generate such turbulence. This relationship has only recently been explored in the field within the context of tidal stream power and numerous papers have attempted to visualise it yet no effort has been made to model it (MacEnri *et al.,* 2013, Gunawan *et al.,* 2014, McCaffrey *et al.,* 2015).

The streamwise turbulence intensity, I_T *(%)*, is regarded by Milne *et al.* (2016) as being the most important turbulence parameter relevant to unsteady loading on TSTs. It has recently been used as a convenient metric to compare turbulence between tidal development sites (MacEnri *et al.*, 2013; Gunawan *et al.,* 2014; Mycek *et al.*, 2014; McCaffrey *et al.*, 2015; Bouferrouk *et al.,* 2016). Because this field is not yet standardised, recent literature uses a variety of symbols to denote turbulence intensity which is here explained as and when a different nomenclature other than I_T is presented within this review. This metric provides a quantification of the turbulent kinetic energy contained in the flow in a direction in which the angle of attack of the turbine blade is generally most sensitive (Milne *et al.*, 2016). More simply, it describes the ratio of fluctuations about the mean flow to the mean flow and is, therefore, calculated by dividing the standard deviation of flow (U_σ) by the mean flow and presented as a percentage (MacEnri *et al.*, 2013; Gunawan *et al.,* 2014; Mycek *et al.*, 2014, McCaffrey *et al.*, 2015):

$$I_T(\%) = \frac{U_\sigma}{\bar{U}} \quad (15)$$

Essentially, a higher turbulence intensity ratio means that there is greater variability in the flow at a given mean velocity than a lower intensity ratio (MacEnri *et al.*, 2013). The overbar above U represents the mean taken over a specific duration in which the flow can be considered statistically stationary; this interval must be stated. Milne *et al.* (2013), McCaffrey *et al.* (2015) and Bouferrouk *et al.* (2016) explain that the turbulence intensity can be calculated in all three orthogonal directions but *u* (or streamwise) is, of course, the most

important when considering in-flow velocities into TSTs. It is generally found that at lower velocities turbulence intensity is high and at higher velocities turbulence intensity is low; McCaffrey *et al.* (2015) suggest that this distribution in turbulence intensity encourages further analysis into what causes turbulence intensity to peak at differing mean velocities.

Bouferrouk *et al.* (2016) collated and presented published measurements of turbulence intensity, shown here in Figure 15 (denoted by *TI*). Measurements were made by a range of devices, at differing heights above the seabed and at different geographic locations. The table shows that sites generally have varying levels of turbulence intensity measured at different mean velocities, but neglects to include the mean current velocity or the turbulence strength or local wave conditions (which this thesis explores in detail). Measurements of turbulence intensity have been made through depth and time using ADCP (Jeffcoate *et al.*, 2015; Bouferrouk *et al.*, 2016) or at a fixed point using ADV (acoustic Doppler velocimeter) or EMCM (Electro-magnetic Current Meter) at several tidal stream development sites (MacEnri *et al.*, 2013; Milne *et al.*, 2013; McCaffrey *et al.*, 2015). As this is a recent turbulence metric used to characterise fluctuations in tidal flows, and has been measured with a variety of instrumentation, it is considered that a unified methodology for calculating the turbulence intensity has not yet been determined and that other, novel, instrumentation should be used to further the field and contribute and compare to this table. It is important to note that (with the exception of the very recent paper by Bouferrouk *et al.* (2016)) most previous *in situ* studies of turbulence intensity through time at tidal sites have measured in calm wave conditions, below wave-base or inadequately identified local wave conditions during deployment. Therefore, a significant research gap has emerged whereby the study of turbulence intensity in response to wave-current interaction remains limited, yet essential to the tidal stream power industry. Section 2.3.2.3 critically analyses each of these publications in more detail in order to inform the research methodology and analysis employed within this thesis.

Site name and location	Type	Height from seabed (m)	Water depth (m)	TI (%)
Sound of Islay, UK [5]	Tidal	5	55	12–13 (2.5 m/s)
Fall of Warness, UK [3]	Tidal	5	42	10–11 (1.5 m/s)
Puget Sound, USA [6]	Tidal	4.7	22, 56, 65	10–11 (>0.8 m/s)
East River, New York [7]	Tidal	5	~7–9	25–30 (2 m/s)
Orkney Islands, UK [4]	Tidal	25	43	10–11 (1 m/s)
Roosevelt Island, NY [8]	Tidal	4.25	8.8–10.7	12–18 (2 m/s)
Current study, Wave Hub, UK	Wave	6.2	40	10–20 (0.8 m/s)

Figure 15: Review of turbulence intensity measurements (Bouferrouk et al., 2016).

Near the bed, turbulence intensity is generally estimated to be around 10 % during strong flows (>0.8 ms^{-1}) which then decreases away from the 'wall' or bed (Hardisty, 2009). Hardisty (2009) goes on to explain that by factoring in fluctuations about the mean, the hydraulic power density of tidal flow could increase. This increase is proved small, in the order of a single percent. Nevertheless, it is important to consider that during the commercialisation of tidal stream power developments a few percentage points increase in operating efficiency can make or break a project financially. Therefore, an increase in power density could have a similar effect, particularly due to the cubic relationship with power output. Clark *et al.* (2015a) suggest that turbulence can actually increase power performance by around 10 % at sites with mid-large-scale turbulence but that this also coincided with 10 % increase in fatigue loading on the turbine.

Turbulence in tidal flows has been described using a number of other metrics (Clark *et al.*, 2015b). Some metrics such as the turbulent kinetic energy (TKE) and Reynolds stress rely on very high-frequency sampling rates with high accuracy in 3-dimensions which are only truly available from measurements made by instruments such as ADVs, ideally within a controlled laboratory environment. These instruments are ideal for the detailed analysis of flow within a flume (where relationships are scaled) but are mostly too delicate to be used in the field. *In situ* instrumentation deployed near the bed must log its own data within the device and, therefore, sampling strategies are limited by memory and battery size. With the continued advancements in data storage solutions, it is hoped that instrumentation will be able to be adequately deployed for longer durations and sample at a higher rate in the future. Then again, the performance and fatigue of full-scale TSTs is most likely affected by large-scale turbulent fluctuations in the energy containing range. Higher frequency fluctuations in the inertial subrange and dissipation range are unlikely to have any significant influence, thus rendering very high-frequency studies of turbulence at tidal stream development sites relatively futile considering the increased data processing and storage necessary.

2.3.2 Relevant Turbulence Experiments and Methodologies

The relationships between streamwise mean current velocity, turbulence strength and intensity and tidal stream turbine (TST) performance is a contemporary research problem and a key focus of this thesis. There is growing evidence to suggest that increased turbulence may have negative effects on TSTs such as under-performance and accelerated structural fatigue (McCann, 2007, Mycek *et al.*, 2014; Jeffcoate *et al.*, 2015). The literature has been divided thematically into three key research areas; numerical simulations,

laboratory experiments and *in situ* fieldwork. Whilst the best efforts were made to identify relevant turbulence papers for numerical simulations and laboratory work, only a few were identified relating specifically to TSTs whereas more papers are discussed relating turbulence metrics to TSTs using *in situ* measurements. The opposite is found in the following wave section due to the problems involved with collecting simultaneous wave and current data in the field.

2.3.2.1 Numerical Simulations

Full-scale experiments using field measurements of flow interaction with TSTs are both costly and problematic considering the operating environment and the extent of reliable data required (Afghan *et al.*, 2013; Bouferrouk *et al.*, 2016). An alternative method is to use computational fluid dynamics (CFD) to numerically model flows. Such models can give an insight into the physical characteristics of turbulent flow around a turbine, and thus tidal stream array design optimisation. CFD programs use complex, higher-order theories such as Navier-Stokes and Saint-Venant, to model free surface flows accurately in either two or three dimensions (Clark *et al.*, 2015b). This is particularly useful for predicting fluid flow over large spatial areas such as whole seas or estuaries but greater accuracy and resolution requires greater computational power which can be expensive (depending on the application) (Clark *et al.*, 2015b). Clark *et al.* (2015b) estimate that, in order to adequately capture large and mid-scale turbulence motions over a 25 km^2 domain, 80 X 10^9 grid points would be required meaning that calculating these motions for any considerable time would generate impractically vast quantities of data. Smaller scales would inevitably require many magnitudes more data; therefore, it is not practically possible to simulate all scales of turbulent motion over large tidal stream development sites through any meaningful length of time (for example a Spring-Neap cycle). Numerous CFD studies are concerned with TST array design optimisation and the turbulent wake generated behind a TST because of fluid passing through its blades (McNaughton *et al.*, 2013; Edmunds *et al.*, 2014) though this field of study will not be discussed further as this thesis is concerned with in-flow velocities.

Commercial hydrostatic models that are used to model tidal turbines (such as FLUENT) require, as a basic input, measured values for turbulence intensity (Thomson *et al.*, 2012; Bouferrouk *et al.*, 2016); therefore, an improved understanding of turbulence intensity in realistic tidal flows could be especially useful to these models. McCann (2007) presented one of the first comprehensive investigations into the effects of turbulence intensity and sea state severity on the performance and structural fatigue of a TST using a

numerical modelling approach. The paper describes the use of the industrial design tool 'GH Tidal Blade' to numerically model the device and environment behaviour and was divided into two parts. The first focused on the influence of varying turbulence intensities at different mean velocities on the performance and fatigue of a simulated TST under calm surface wave activity (discussed here) whilst the second focused on varying sea state severities under constant turbulence intensity and water depth (discussed in section 2.4.3.1). The simulation tested the power output (MW) and the blade-root out-of-plane bending moment (kNm) (chosen metric for structural fatigue sensitivity) of a typical horizontal axis TST under increasing mean in-flow velocity and with varying levels of turbulence intensity (U = 1, 2 and 3 ms^{-1} and I_T = 0, 5, 7, 10 and 12 %) resulting in 15 separate runs. For each run, a $1/7^{th}$ power law was assumed for current shear. The resulting graphs show that the power output of the simulated TST varied significantly under the different conditions tested. Relatively small fluctuations in P_O and M_Y are observable about the mean for all values of I_T at 1 ms^{-1} whilst larger fluctuations are observed in increased mean flow velocities which increase still as turbulence intensity simultaneously increases. This study, therefore, demonstrates the potential importance of flow turbulence in turbine loading and underlines the requirement for detailed tidal flow measurement studies to better understand the relationships between mean current velocity and turbulence intensity.

More recently, Lloyd *et al.* (2014) investigated the effect of in-flow turbulence on the hydrodynamic noise radiation from a model tidal turbine using a Large Eddy Simulation (LES). Whilst this paper focussed on EIA (environmental impact assessment) rather than EYA (as is this thesis) it is still relevant as they used an input turbulence intensity of 10 % that is isotropic (the same in all directions) and homogenous (does not change temporally or spatially). They acknowledge that more realistic turbulent flows, with anisotropic turbulence intensities, exist in nature and could be inputted but have tried to simplify the turbulence parameters to demonstrate their methodology for testing acoustic responses. Recent authors have demonstrated that the turbulence intensity ratio between u, v and w is often close to 1: 0.7: 0.55 respectively (Milne *et al.*, 2013 and Bouferrouk *et al.,* 2016). What other papers and this thesis later explore is the fact that there is a power relationship between mean current velocity and turbulence intensity and that using the same turbulence intensity at different flow speeds is inaccurate.

Evidence suggests that high turbulence intensity will affect the power output and structural fatigue of a simulated TST and that different intensities of turbulent motion at constant mean flows will have different effects. Papers utilising the turbulence strength as a useful metric of simulated turbulence are not present in the reviewed literature.

2.3.2.2 Laboratory Experiments

Laboratory flumes allow researchers to test controlled, repeatable flow conditions on scaled tidal stream turbine (TST) designs at a fraction of the cost of fieldwork and with greater accuracy than with numerical simulations. Flume experiments are typically used to control flow velocity and other variables being tested such as bed material, surface waves or scaled TSTs. Data from flume experiments can then be used to validate theories by making comparisons with relevant data collected in the field. Flumes are often limited in that they have a very small test section, which is free from underdeveloped flows at either end of the tank, and are restricted to generating uni-directional flow. As the variables can be controlled very precisely, instruments with high temporal frequencies such as EMCMs, Particle Image Velocimetry (PIV), Vectrino and/or ADV are used to collect as much data as possible for the most accurate results, though many of these are delicate and generally unsuitable for field deployments (Babanin and Haus, 2009; Black *et al.*, 2015). Much like in the numerical simulation literature, numerous authors are interested in observing the turbulent wake effects generated beyond arrays of scaled turbines (Stallard *et al.*, 2015) or wind turbine foundations (McGovern *et al.*, 2009) to test flow and geomorphological variations in flumes. Again, these themes shall not be discussed further.

An example of testing turbulence intensity on TST performance in the laboratory is presented in Mycek *et al.* (2014). They tested the effects of two different turbulence intensity rates (3 % and 15 %) on the performances of a model 3-bladed horizontal axis tidal turbine in a simple flume tank. The natural ambient turbulence intensity measured in the flume was reported to be around 15 % at all measured mean velocities and with the aid of a 'honeycomb' could be artificially smoothed to just 3 %. The power coefficient of the TST, C_P, was found not to significantly change when under the higher turbulence intensity flows nor did the thrust coefficient, C_T. However, the standard deviations of C_P (σC_P) and C_T (σC_T) were found to be 2.5 times greater in the higher turbulence intensity flows than the low turbulence intensity flows. These results suggest that the unaffected power coefficient and thrust behaviour enables the deployment of the turbine in environments with a turbulence intensity between 3 and 15 %. The fact that the standard deviation of the power and thrust coefficient increased during the higher turbulence intensity runs means that the turbine blades, gear-box and electrical generators will fatigue at an increased rate. This means the cost of the turbine deployment undoubtedly increases in terms of design (CapEx) and operations and maintenance (OpEx). It is, therefore, crucial to predict turbulence intensity at a site prior to deployment to then estimate the potential effects on the turbine. Surprisingly, other papers testing the effects of turbulence strength and

intensity on the performance of scaled TSTs are relatively uncommon whilst experiments concerning the effects of wave-current interaction are comparatively more common (see section 0).

2.3.2.3 *In Situ* Observations

Experiments conducted *in situ* provide the most realistic results but include many more variables that cannot be controlled or even measured as can be in CFD or flume experiments (Stacey *et al.*, 1999; Nazarenko *et al.*, 2010). Charnock (1959) explains that measuring turbulence in tidal channels (as opposed to flumes) has unique benefits as strong tidal flows provide neutrally stable velocities in which the shearing stress varies linearly from top to bottom and mean velocities naturally vary over time. Correctly determining the mean flow and its fluctuating constituents is fundamental to turbulence characterisation. Recording turbulence in tidal flows presents researchers with a unique challenge whereby the flow must not be disturbed by the instrument and must be recorded at an adequate temporal and spatial frequency to investigate relevant scales of flow. Tidal mean flow and tidal turbulence metrics can be measured in the field at a fixed point using ADVs and/or EMCMs or through depth using ADCPs (Simpson, 2005; Black *et al.*, 2015). The following section reviews early observations of turbulent fluctuations in tidal channels before focusing on more recent publications that report results of turbulence metrics in tidally dominant flows. It is shown that some key findings in these early works could be used to inform and improve future research as mean current and turbulence data from recent publications are often reported but rarely compared or attempted to be modelled, which this thesis attempts to progress.

Some of the earliest *in situ* observations of turbulence in tidal streams were made using mechanical flow meters (Bowden and Proudman, 1949; Gordon and Dohne, 1973; McLean and Smith, 1979; Gross and Nowell, 1983), EMCMs (Bowden and Fairburn, 1952a; 1952b; 1956; 1962 and Bowden and Howe, 1963; West *et al.*, 1986; Shiono and West, 1987; Lueck, 2002 and 2005; Soulsby and Humphrey, 1990) and hot-film flow meters (Grant *et al.*, 1961). Measurements were often made in order to calculate Reynolds stresses and turbulence spectra in which to compare with laboratory observations (Bowden and Howe, 1963; West *et al.*, 1986), to investigate the inertial and dissipation ranges of the turbulence spectrum (Grant *et al.*, 1961) and to investigate the change in turbulent structure over bedforms (McLean and Smith, 1979).

Bowden and Proudman (1949) measured and interpreted, for the first time, the fluctuations about the mean tidal stream velocity near the bed. They used a mechanical

flow meter within the Mersey Estuary to measure flow velocity on photographic paper at a frequency estimated to be around 1 Hz (it is not mentioned in the text and inferred from a figure of results). Their results showed irregular fluctuations in velocity that appeared to increase with mean current velocity. They determined that the amplitudes of these fluctuations could be categorised into two main types; fluctuations with periods of a few seconds (denoted by u_1) and periods of a few minutes (denoted by u_2). Using just 34 records they demonstrated that a positive relationship existed between U and u (Figure 16) that was close to linear but better explained using an empirical formula in the form:

$$u_2 = 0.09\,U^2 \tag{16}$$

Similar relationships are observed in more recent publications (Milne *et al.*, 2013; MacEnri *et al.*, 2013; Gunawan *et al.*, 2014; McCaffrey *et al.*, 2015) between the turbulence strength and mean current velocity but are rarely explained or modelled. Similar relationships are also observed within this thesis (see section 5 for further discussion and comparison).

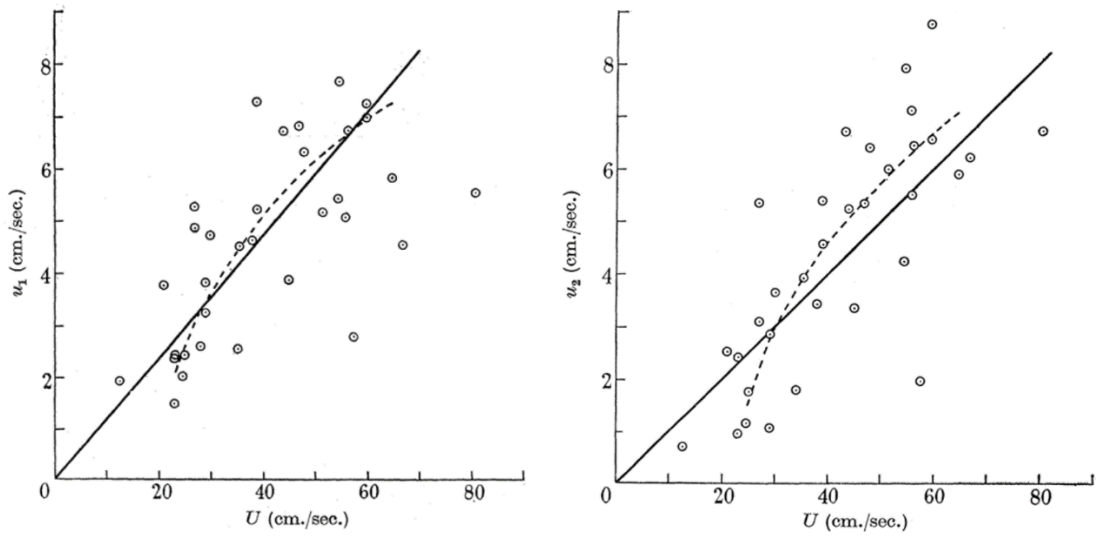

Figure 16: Relationship between mean current velocity, (U), and the mean amplitude of short (u_1) and long period (u_2) fluctuations observed by Bowden and Proudman (1949) in the Mersey Estuary.

Bowden and Fairbairn (1956) attempted to build upon Bowden and Proudman's (1949) results and used a vertically orientated EMCM upon a bed-mounted tripod to gain and compare horizontal and vertical components of the flow, which is typical of many *in situ* methodologies; this was then used to calculate one-dimensional turbulence spectra. Their results were limited as the orientation of the EMCM sensor heads restricted the calculation of the v component of flow, the sampling rate was considered low for a fixed-point instrument (1 Hz) and the tripod was known to have tilted during strong currents

thus resulting in a number of noisy samples being removed from analyses. Samples containing obviously large errors are a common trait of *in situ* data collection using EMCMs, but determining the sources of the errors is often difficult due to the instrumentation being out of the sight of the researcher for long periods (Shiono and West, 1987; Soulsby and Humphrey, 1990). This is relevant as similar problems were encountered and overcome in this thesis' methodology section.

2.3.2.3.1 *In Situ* Observations of Turbulence within the Context of Tidal Stream Power

Recent literature has attempted to observe, *in situ*, the relationships between mean current velocity, turbulence strength and intensity within the context of tidal stream power though within these paper's results are frequently presented without comparison to other relevant literature of which this section explores. Particular attention is paid to numerous figures (Figure 17, Figure 18, Figure 19 and Figure 20) which visualise the relationships between mean current velocity and turbulence, which are rarely modelled (but are directly compared to the thesis results within section 4.4). A number of papers are explored as case studies in that their methodologies and results are critically analysed in detail (Thomson *et al.*, 2012; Milne *et al.*, 2013; Gunawan *et al.*, 2014; McCaffrey *et al.*, 2015). Papers that investigate the interactions of turbulence with TSTs, *in situ*, are explored in the following section.

Acoustic Doppler techniques allow for non-intrusive measurements of mean current velocities and turbulence metrics throughout the water column (Parsons *et al.*, 2012) (see section 3.3.2.2 for more information about the principles of the Doppler Effect). A number of *in situ* investigations using acoustic Doppler techniques have been made within potential tidal stream development sites in the Puget Sound, WA. Thomson *et al.* (2010a, 2010b, 2011, 2012) published a series of progress reports and papers on fieldwork conducted in order to measure the in-flow velocities of TSTs at Admiralty Inlet, WA. For example, in Thomson *et al.* (2012) a tripod was used to mount a Nortek vector ADV (6 MHz) at 4.7 m above the bed to observe turbulent intensities at an expected TST hub height. An RDI Workhorse Sentinel (600 kHz) ADCP was mounted at the foot of the tripod to measure turbulence intensity vertically through the water column for comparison (Figure 17). They identified that turbulence intensities are generally higher and more scattered at mean current velocities (denoted by $<u>$) between 0 and 0.8 ms^{-1} which then drop to around 10 % at higher flow speeds. A relatively small difference was observed in between the ADV and ADCP results at a height above the bed of 4.7 m (denoted by z_{hub}). Whilst this methodology provided detailed information for a fixed location, it did not

consider that hub heights are no longer restricted to the slower flows near the bed due to the development of floating and buoyant TSTs. They suggest that ADCPs can adequately calculate lower-order statistical turbulence metrics such as the turbulence intensity though higher-order metrics such as Reynolds stresses require higher frequency data from an ADV.

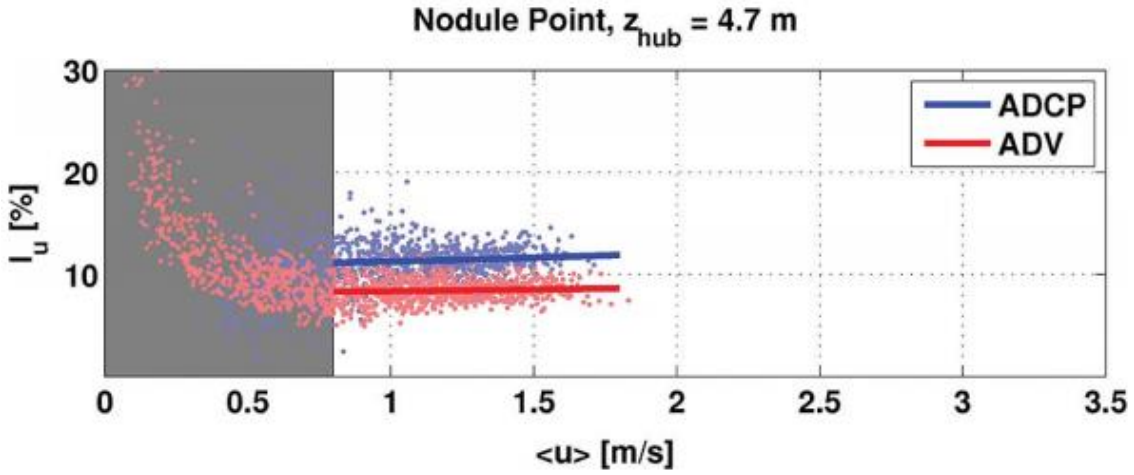

Figure 17: Relationship between mean flow velocities and streamwise turbulence intensity at Nodule Point, Admiralty Inlet, WA (Thomson et al., 2012).

McCaffrey *et al.* (2015) also very recently presented *in situ* observations of tidally induced turbulent intensities from the Puget Sound, WA. A prospective tidal stream development site in a 22 m deep channel was analysed over just four days using an ADV sampling at 32 Hz which was positioned on a 'tidal tripod' at a potential tidal turbine hub height of 4.6 m above the bed, similarly to the earlier papers of Thomson *et al.* (2010a, 2010b, 2011, 2012). The authors suggest that the measuring location will not experience wave-induced motion as it is deeper than the estimated wave base of 7.5 m, based on average wave periods of 3 seconds (and estimated wavelengths of 15 m). Waves 'will introduce coherent structures' into the flows variance above wave base (of which this thesis explores through objective 2). Data were analysed in 10-minute bursts, which was considered long enough to retain the longest timescales of coherent turbulence structures in the flow data whilst still capturing variation in the mean flow through the tidal cycle. Experiments with longer sampling durations in their appendix revealed that all coherent turbulence structures passed by in less than 4 minutes and that longer sampling durations such as 20, 30 or even 60 minutes were too long to statistically analyse whilst assuming stationarity. This was because of the significant linear trend of the deterministic tidal signal, which was not observed in the 5 and 10-minute intervals, meaning that detrending the data would be unnecessary. A number of different turbulence metrics were considered which relied on 3-dimensional flow data available from the ADV though the streamwise, one-

dimensional turbulence intensity was also calculated. The data presented in Figure 18 shows the relationship between $\bar{U}$ and the streamwise turbulence intensity, I_U, for every 10-minute sample throughout the four-day deployment. Here, the turbulence intensity is very high and scattered for low mean velocities, between 20 and 50 % at 0.2 ms^{-1}, which then decreases and becomes less scattered as mean flow velocity increases with values between 7 and 15 % at around 0.8 ms^{-1}. Flow velocities below 0.8 ms^{-1} are considered to have occurred during slack water and have been shaded in grey. Beyond 0.8 ms^{-1} turbulence intensity tends to a constant levelled-off value of 10 % for all mean flow velocities, which is in agreement with Hardisty (2009). As seen in Figure 22 (MacEnri *et al.*, 2013) the turbulence intensity has been observed to drop much further at very high flow speeds (between 6 and 9 % at >2.5 ms^{-1}) and has also been observed to significantly differ between Flood and Ebb tides as shown in Figure 20 (Gunawan *et al.*, 2014). The data are also highlighted by their estimated anisotropy, A, which is a measure of correlation between the orthogonal velocity components of flow (u, v and w dimensions); a clear relationship between increased turbulence intensity at a given velocity and increased anisotropy was defined. In the fastest recorded flows (1.25 to 1.5 ms^{-1}) there is minimal variation in anisotropy suggesting that turbulent flows are more directionally dependent at these mean velocities. The correlation between the mean flow speed and the flow variance (denoted by $\overline{u'^2}$) is inset within Figure 18 which shows a reasonably strong linear relationship with an R^2 of 0.65205 though it is unclear why these data are plotted using lines as opposed to points. Supporting the observations made by Mycek *et al.* (2014), McCaffrey *et al.* (2015) agree that turbulence manifested in gusts, or coherent, anisotropic, and intermittent eddies will put strong and variable stresses on TSTs. As a result, site characterisation methods that quantify the turbulence intensity at a site have the potential to prevent untimely, unexpected, and costly failures of deployed TSTs.

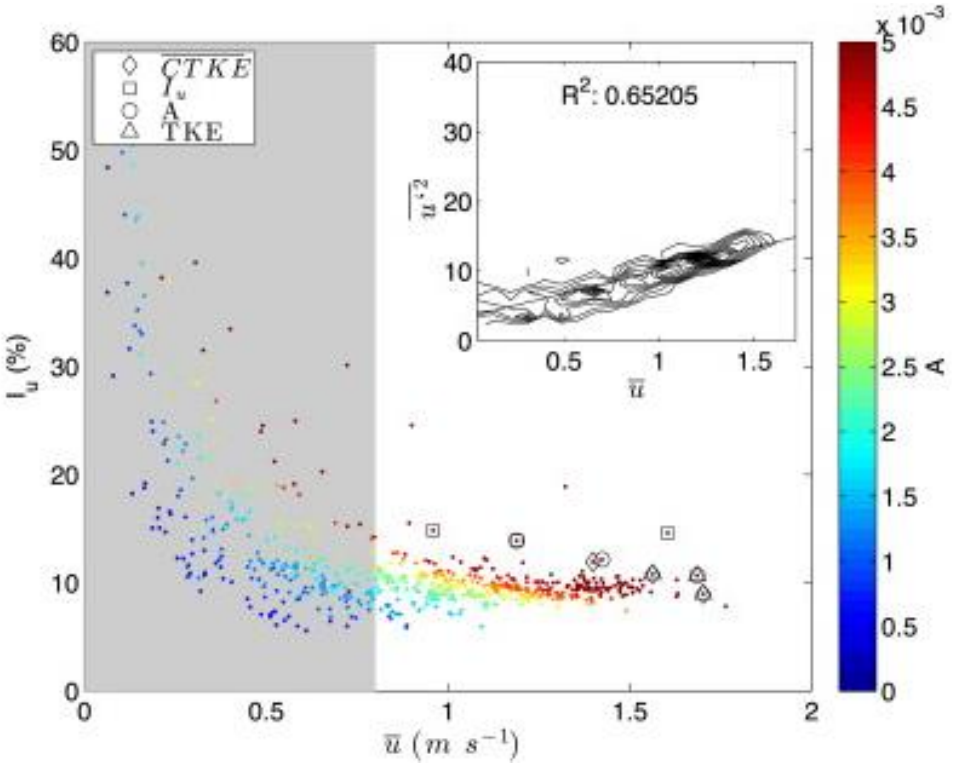

Figure 18: Relationship between mean flow and streamwise turbulence intensity. Anisotropy is scaled in the colour bar and the relationship between mean flow and flow variance is included in the inset (McCaffrey et al., 2015).

Milne *et al.* (2013) used an ADV on a 5 m tall, bed-mounted mast to monitor turbulence intensity in continuous mode at 4 Hz in the bottom boundary layer of the Sound of Islay, Scotland. The continuous data were broken down into 5-minute samples, which was considered long enough to study the dominant turbulence scales at the site. Figure 19 presents the time series of turbulence intensity (denoted by I_u) (a), turbulence strength (denoted by σ_u) (b) and orthogonal mean current velocities in the streamwise, transverse and vertical dimensions (c). The turbulence strength increases at a similar rate in relation to the streamwise mean current velocity and that turbulence intensity is increased at slack tide and generally around 10 % during peak flow. It is also clear that the transverse and vertical velocities are insignificant compared to the streamwise velocity. This paper would have been improved if regression analysis between these measurements were used to quantify and model these relationships in order to compare to other relevant literature.

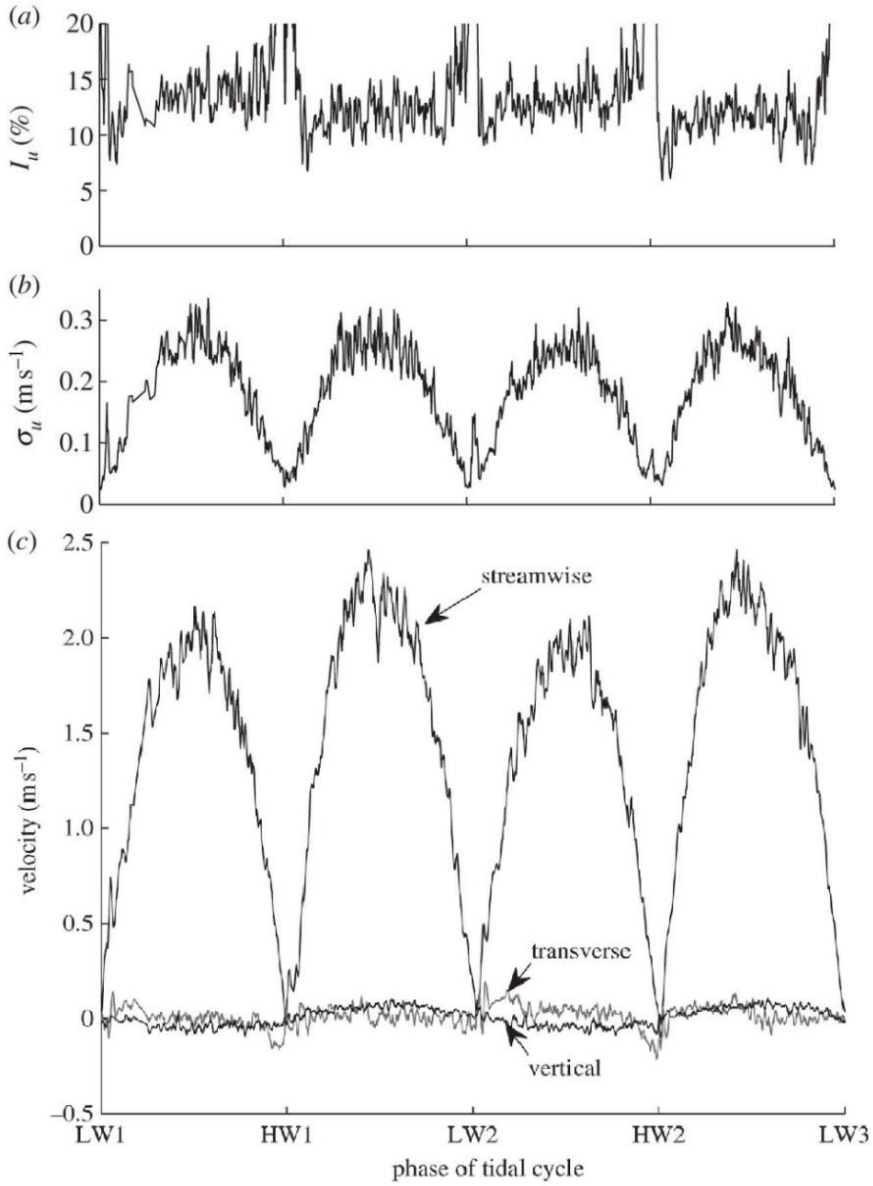

Figure 19: Relationship between mean velocity, turbulent strength and turbulence intensity over 4 tidal cycles in the Sound of Islay, Scotland (Milne et al., 2013).

Gunawan *et al.* (2014) report turbulence intensities from an energetic tidal site near Roosevelt Island, New York, using ADVs positioned on top of a 4.25 m tower. Turbulence intensities were calculated at 5-minute intervals at 10 Hz. The streamwise turbulence intensity (denoted by I_u) and turbulence strength (denoted by $\sqrt{u_c u_c}$) were plotted against mean current velocity in Figure 20. They explain that, generally, the turbulence strength is found to increase with mean current velocity but that turbulence intensity (as it essentially the inverse) decreases with velocity. Differences between turbulence metrics during the Flood and Ebb tides are observed which are said to be indicative of irregular upstream channel roughness generating different intensities of turbulence. The colour bars represent the fraction of the data out of the total number of samples. In graph a the data closely resemble the relationship observed by McCaffrey *et al.* (2015) and Jeffcoate *et al.* (2015) in

which at high flow velocities turbulence intensities tend towards 10 % whereas in low velocities there is a rapid decrease in turbulence intensity as mean current velocity increases. In graph b a near linear relationship between mean current velocity and turbulence strength is observed except from between 0.3 and 0.8 ms^{-1} in which the relationship appears non-linear. A rapid increase in turbulence strength from 0.125 to 0.25 ms^{-1} is observed between 0.3 and 0.5 ms^{-1} which then decreases to 0.22 ms^{-1} between 0.5 and 0.8 ms^{-1} before then increasing again at a steadier rate. The Ebb tide could be considered more turbulent than the Flood tide due to a higher turbulence strength and consequently a higher turbulence intensity at equivalent mean current velocities. It is important to note that none of these relationships were parameterised or modelled.

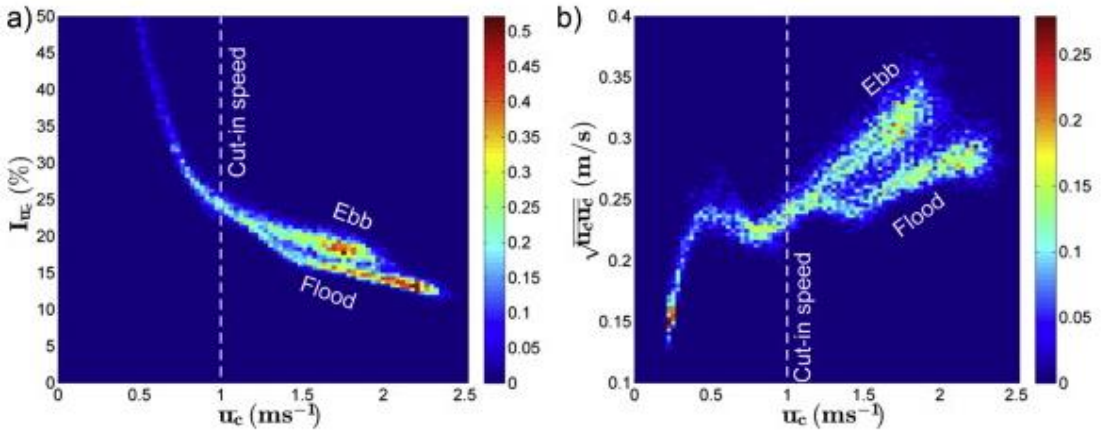

Figure 20: Turbulence intensity and turbulence strength against mean current velocity in the East River tidal strait, New York. The colour bar represents the fraction of data out of the total number of samples (Gunawan et al., 2014).

A number of authors have attempted to derive the turbulence spectra from acoustic instrumentation. Torrens-Spence *et al.* (2015) attempted to derive the turbulence spectra using a fast Fourier transform (FFT) from three closely orientated instruments during the same fieldwork as Jeffcoate *et al.* (2015) (see following section); a TRDI Workhorse Sentinel ADCP, an AquaDopp ADCP and an RSI MicroRider turbulence profiler. They struggled to adequately derive the spectra at a high enough frequency to determine the inertial sub-range or the $f^{5/3}$ slope within the streamwise velocity, *u*, but found a close agreement between devices in the *v* and *w* components. They conclude by suggesting, like many other authors, that the data would be improved with higher frequency sampling for longer durations, but this is not always possible. Bouferrouk *et al.* (2016) very recently used a 5-beam ADCP optimised for wave measurements but, like many others, found that ADCPs could not adequately measure wave-current interaction to a high enough temporal and spatial frequency (discussed in more detail in section 2.4.3.3).

A method that has been utilised by a number of authors to measure turbulence metrics with ADCPs is known as the variance method (Stanley 1999; Simpson *et al.*, 2004; Lu and Lueck, 1999a; 1999b; Nezu and Nakagawa, 1993, Williams and Simpson, 2004; Osalusi *et al.*, 2009b; Bouferrouk *et al.,* 2016). It utilises the difference between opposite beams to calculate 3D estimates of variance in the flow and is, therefore, restricted to ADCPs with at least four beams, as well as to highly energetic systems, such as tidal channels in order to determine signal through Doppler noise (see section 3.3.2.5) (Osalusi *et al.*, 2009b; Bouferrouk *et al.,* 2016). The method is best suited to bed-mounted ADCPs that are securely fastened with 0 ° tilt and orientated directly into the flow as the process relies on the beam coordinates of the ADCP and cannot easily calibrate measurements for changes in ADCP orientation unlike earth coordinates used in vessel mounted methodologies (see section 3.3.2).

ADCPs can collect more information about a tidal flow than just flow velocity. Acoustic backscatter is a parameter derived from the echo intensity of each beam, which has been found to have a strong relationship with the suspended sediment concentration (SSC) present within the water column (Thorne *et al.*, 1993; Wall *et al.,* 2006; Perkey and Pratt, 2010; Ghaffari *et al.*, 2011; Woodward, 2011). SSC (g/ml) has significant implications on water quality, aquatic ecology and sediment transport (Liu *et al.*, 2014) but may also be used as a proxy for turbulence as the higher the turbulence (or the shear stress) the higher the SSC (Gourgue *et al.*, 2013). Perkey and Pratt (2010) and Ashall *et al.* (2016) describe methodologies of converting ADCP acoustic backscatter into an estimate of SSC (and thus a proxy of turbulence). The method requires the knowledge of a sample of SSC and grain size, the water temperature and information collected by the ADCP such as the temperature, water depth and echo intensity of each beam. During the fieldwork of this thesis, sediment concentration was measured throughout the duration of the ADCP surveys in order to estimate SSC though results were extremely limited. Whilst sediment concentration could have an effect on turbulence metrics in tidal streams, this topic is beyond the scope of this thesis but could be interesting to investigate in further research.

2.3.2.3.2 *In Situ* Investigations of Turbulence on TST performance

A handful of papers have reported the direct effect of turbulence on the power performance and structural fatigue of full-scale TSTs, complementing the results of relevant numerical and laboratory studies (MacEnri *et al.*, 2013; Jeffcoate *et al.*, 2015). As in the previous section, these papers are explored as detailed case studies.

The effect of tidal flows and turbulence on the 'power flicker' outputted by the Seagen 1.2 MW TST in Strangford Lough, Ireland, is investigated in MacEnri *et al.* (2013).

Power flicker (denoted by C_F) is described as fluctuations in the output voltage from a turbine, which, for example, can affect the luminescence of an incandescent bulb and is, therefore, an irritation problem to humans. Power flicker emissions are said not to be such a concern from other renewable sources such as hydro-electric where there is a stable input flow; however, it is a key problem in wind turbines and tidal turbines due to unstable input flows which cause uneven power output over a single rotation. As no standards existed for power flicker characterisation in tidal turbines at the time their methodology relied heavily on wind turbine standards, particularly IEC61400-21 (2008) which is an international standard for assessing power quality characteristics of grid connected wind turbines. A range of tidal parameters such as tidal height, tidal current velocity, turbulence strength and turbulence intensity were monitored close to the turbine and tested against power flicker emissions. The authors describe how the turbulence intensity of wind typically relates to the mean velocity and go on to assess this relationship within the context of tidal streams. Flow measurements were made with a Valeport Model 803 electromagnetic current meter positioned at hub height (undefined). This only recorded data when the flow velocity changed at 1 Hz. Tidal current velocities used in the study were arithmetic means calculated in 10-minute intervals consisting of between 200-600 data points due to the sensor only recording new data when the velocity changed (which is an unhelpful sampling method when assessing high-frequency flows). Accelerations in the flow due to the crossbeam of the turbine close to the sensor meant that an ADCP had to be used to calibrate the measured streamwise flow velocity. No filtering or detrending of the raw data was carried out. It was concluded that tidal current velocity had a very strong power relationship with power flicker but also that turbulence strength had a strong positive linear relationship with tidal current velocity, which was thus suggested to be the cause of the power flicker (Figure 21 and Figure 22). There was a weak negative relationship observed between the turbulence intensity and power flicker which was explained by the fact that the turbulence intensity is inversely proportional to the tidal current velocity (which occurs as a 100 % velocity increase results in a 55 % increase in turbulence strength (Figure 21 and Figure 22)). In this case, as the site exhibits very high velocities, only mean current velocities greater than 1 ms^{-1} were tested against turbulence intensity. This paper is useful to the analysis presented in this thesis as it directly tests tidal parameters against performance characteristics of a full-scale TST deployed *in situ* and confirms that an increase in turbulence has negative effects on TST performance, in this case on power flicker. Whilst the site has some of the greatest tidal current velocities in the UK and high values of turbulence strength it is relatively sheltered from the increased wave activity typically associated with coastal sites and thus did not include the effect of surface waves on flow characteristics. They do, however,

suggest that long period waves could 'have a significant adverse effect on flicker levels' and that the effects will not be known until devices are located in these areas. Therefore, improved understanding of the relationships between surface waves and the tidal parameters considered here (which are proved to affect turbine performance) could be extremely insightful and useful to developers.

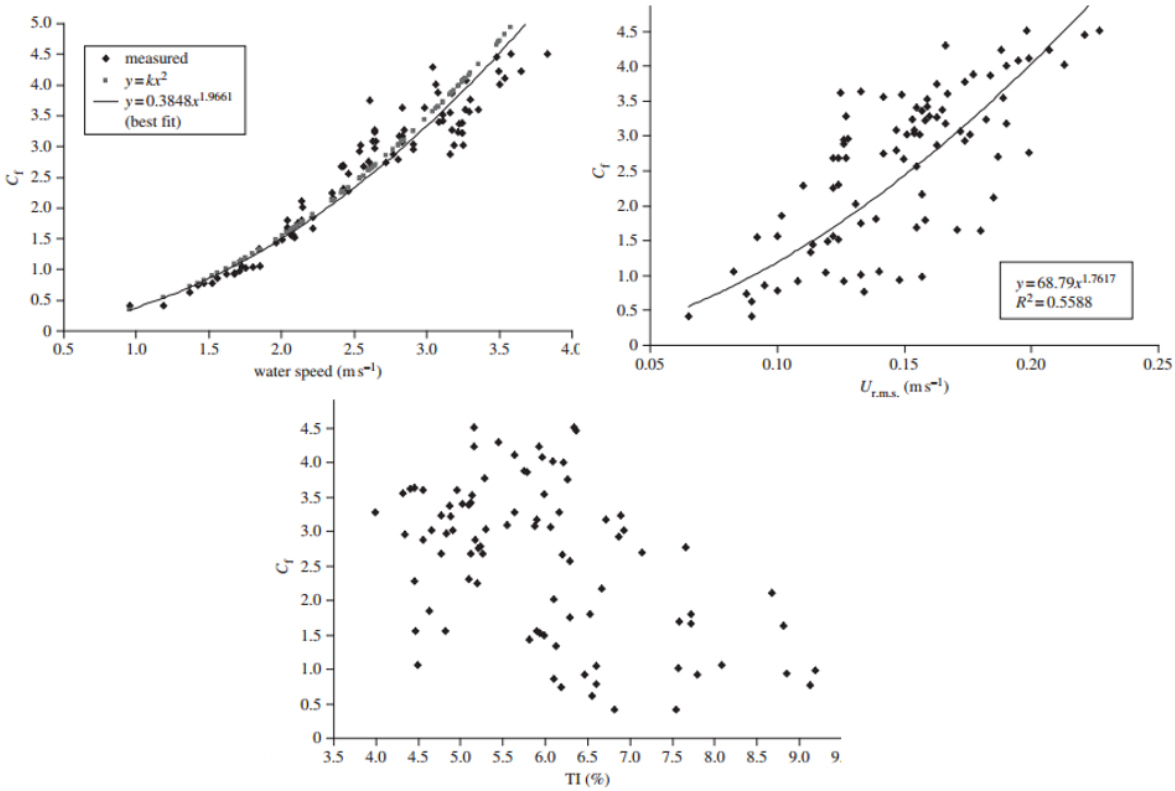

Figure 21: Tidal current velocity, turbulence strength and turbulence intensity tested against the power flicker of the Seagen TST (MacEnri et al., 2013).

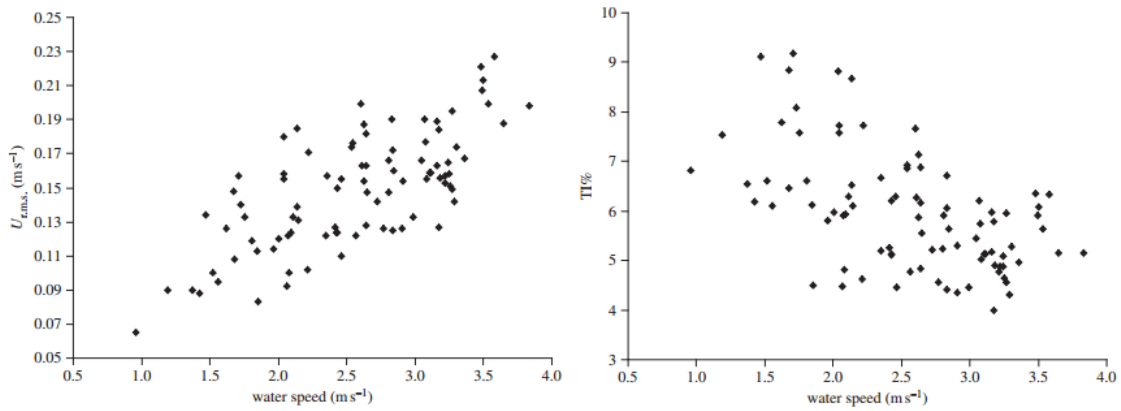

Figure 22: Tidal current velocity tested against turbulence strength and turbulence intensity (MacEnri et al., 2013).

The field-testing of a full-scale Schottel TST is presented within Jeffcoate *et al.* (2015). In order to examine the turbines performance in a variety of in-flow velocities and turbulent intensities a novel instrumentation setup was implemented utilising ADCP, ADV and MicroRider flow sensors. The turbine and instruments were suspended beneath a

floating dump barge in Strangford Lough, Northern Ireland, with the ADCP measuring in-flow velocities in front of the turbine. Mean current velocities during the Ebb tide did not exceed 1 ms^{-1} in this location as an upstream obstruction caused an eddy at the site with backflow; therefore, only the Flood conditions were measured and analysed; these ranged from 0.4 to 2.5 ms^{-1}. Flood flows in daylight hours were monitored over 48 days resulting in 288 hours of data. Local wave conditions were ignored as they were considered minimal due to the sheltering surrounding topography. The most significant wave action occurred due to local ferry wash with estimated wave heights of 0.5 m. Fluctuations in streamwise flow velocity were found to influence the electrical power generated by the TST, which they suggest could result in differences in predicted power output from the mean flow in steady state tests. The turbulence intensity was measured across the hub height using the ADCP data (Figure 23). An undefined parametric relationship between in-flow velocity and turbulence intensity is observed with high values of 50 to 60 % at low velocities of around 0.5 ms^{-1}. Turbulence intensity values then decrease sharply to around 23 % at 1.2 ms^{-1} before decreasing more gradually to around 18 % at higher velocities of around 2 ms^{-1}.

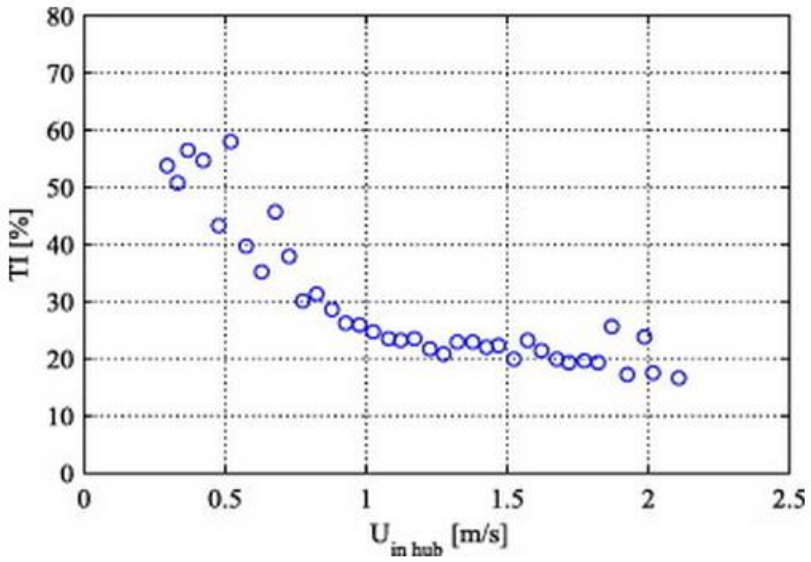

Figure 23: Turbulence intensity at hub height for varying inflow velocities (Jeffcoate et al., 2015).

Further comments are made on the implications of turbulence intensity values on TSTs. They argue that large fluctuations in the incoming flow naturally occur in tidal streams with high velocities and are, therefore, of interest to device developers as higher turbulence intensities at such velocities will cause fatigue to the blades and affect performance. This is likely because long length scale turbulence might affect the angle of attack on the blade whilst smaller scales may only effect the laminar to turbulent flow at the scale of the blade chord. They request further investigation into these relationships to determine which turbulence intensities affect which turbine parameters. They also suggest

in-flow streamwise velocity parameters, such as the turbulence intensity, shear profile and depth-averaged velocity, will change as a result of variation in water depth but do not present an argument for this within this paper and instead suggest that this will be explored in future work. These parameters are explored within this thesis within the later analysis chapters.

2.3.2.3.3 *In Situ* Wind Power Observations

Wind power and tidal stream power share many similarities as they both use turbine technology to exploit the kinetic energy within a moving fluid. Wind, or air, likewise contains turbulent fluctuations within its flow which are generated by surface inhomogeneities, such as bed roughness, sea-surface roughness and temperature transitions, but are not limited vertically (within the atmosphere) (Chamarro and Porte-Agel, 2009; Westerhellweg *et al.,* 2010). As the wind industry is considered more mature than tidal stream power, it is no surprise there has been more substantial research into characterising wind turbulence and understanding its effect on wind turbine performance, power flicker, fatigue and wake recovery (Westerhellweg *et al.*, 2010; MacEnri *et al.*, 2013; Golovanov *et al.*, 2013). As a result, the turbulence intensity is an important and widely used indicator of turbulence in the wind power industry of which the tidal industry and tidal researchers could learn from (Westerhellweg *et al.*, 2010; Belu and Koracin, 2013).

Characterising wind turbulence has long been considered an important factor in site-suitability and EYA studies due to its effects on performance, wake recovery and thus windfarm design (Chamarro and Porte-Agel, 2009; Westerhellweg *et al.*, 2010; Casella, 2015). Chamarro and Porte-Agel (2009) showed that turbulence intensity is increased in the wake of a wind turbine; therefore, downwind turbines would be subject to increased fatigue and reduced performance. Sheinman and Rosen (1992) showed that ignoring turbulent in-flow velocities can result in an overestimation of turbine output by around 10 %. Wharton and Lundquist (2012) determined that increased turbulence intensity at rated speeds affected the power curves of identical wind turbines whilst Westerhellweg *et al.* (2010) and Casella (2015) demonstrated that turbulent intensities are different depending on the direction of the wind. Wind can flow from any direction as opposed to bi-directionally in tidal flows; therefore, surrounding topography is important whilst tidal turbines only have to exploit rectilinear flow. Sea-surface wave heights can increase turbulence intensity in wind due to increasing the roughness of the sea surface (Westerhellweg *et al.*, 2010) which means that bed roughness could affect the turbulence intensity in tidal flows. Binh *et al.* (2008) and Chamarro and Porte-Agel (2009) explain how the turbulence intensity within

the wind's in-flow velocity can affect loading parameters that act on a wind turbine such as the wind force, F_{TOT}. The instantaneous wind force can be derived as:

$$F_{TOT} = \frac{1}{2}\rho C_F A(\bar{U} + u)^2 \quad (17)$$

Where, as in the turbine power output equation, ρ is the density of air, C_A is the aerodynamic force coefficient, A is the swept area, $\bar{U}$ is the mean wind velocity and u is the fluctuating wind velocity. The mean wind force can then be derived as:

$$\overline{F_{TOT}} = \frac{1}{2}\rho C_A A(U^2 + {\sigma_u}^2) = \frac{1}{2}\rho C_A A U^2\left(1 + {I_T}^2\right) \quad (18)$$

Where σ_u is the standard deviation of turbulent fluctuations and I_T is the turbulence intensity. Chamarro and Porte-Agel (2009) note that the equation for F_{TOT} assumes a uniform distribution of U and I_T in in-flow velocity across an area which is only the case in 'free-stream flows'. In boundary layer flows, like onshore wind and tidal, this assumption could lead to important errors, as the in-flow velocity is not homogenous over the turbine area. The F_{TOT} parameter has yet to be tested using *in situ* data collected from a tidal environment but should be equally applicable due to the only significant difference being ρ.

2.3.3 Summary of Relevant Turbulence Experiments

This section explained how turbulence in tidal environments are often described in terms of statistical metrics such as the turbulence strength and intensity. It then demonstrated how these metrics should be important factors in tidal stream power energy yield assessment as they have been experimentally found to be related to TST performance and fatigue within numerical, laboratory and *in situ* experiments. *In situ* studies have typically used ADCP, ADV and/or EMCM instrumentation to monitor turbulence metrics in tidal streams; however, reported relationships with mean current velocities have not been successfully modelled through depth or time. Many papers conclude by stating that *in situ* measurements are limited and further *in situ* investigations in energetic tidal streams are encouraged to improve the understanding of such relationships. The vast majority of these studies have also been located below wave base thus opening up areas of investigation about how these relationships may differ in the presence of increased surface wave activity.

2.4 Wave-Current Interaction

2.4.1 An Introduction to Wave-Current Interaction

Surface gravity waves generated by the wind are considered among the most impressive and complex phenomena that nature can offer (Holthuijsen, 2007). Their formation is directly related to the strength, duration and fetch of the wind meaning that ferocious storms can generate equally ferocious waves. In the field, surface gravity waves are only predictable using a stochastic approach due to insufficient knowledge of surface wind fields and surface momentum transfer (Thomson and Emery, 2014). Beneath the water's surface, orbital velocities are induced by wave propagation, which contribute to fluctuations in any underlying mean flows. Babanin *et al.* (2012) provide a thorough review of literature that has investigated wave-current interaction throughout the last century and explain that the field is now so broad and diverse that they admittedly struggled to account for every branch within their review paper. They did not provide a section on wave-current interaction research within the context of tidal stream power. The following section therefore provides an up to date review of literature relevant to the thesis objectives.

Numerous tidal stream development sites are exposed to storm waves, particularly in the UK, which is, therefore, a major concern for tidal stream developers. However, the interaction between waves and tidal currents and its effect on turbulent characteristics is poorly understood at present (Ojha and Mazumder, 2010; Barman *et al.*, 2016). One of the reasons for this is the distinct lack of simultaneous 'wave-current' data from tidal sites due to the difficulty of measuring the phenomenon *in situ (*Soulsby and Humphrey*,* 1990*)*. The instrumentation required is currently expensive and deployment methodologies risky in the fastest tidal flows but with the acceleration in the development of the tidal stream power sector the data has become increasingly necessary and analyses sought after (EMEC, 2009). Secondary data are not readily available for researchers to analyse, with marine energy test sites such as the European Marine Energy Centre (EMEC) and WaveHub not collecting wave and tidal data simultaneously with appropriate instrumentation at any of their test locations. Tidal stream developers also retain any collected data strictly for themselves or established partners due to the competitive nature of the sector (Mason-Jones *et al.*, 2013; Clark *et al.*, 2015a).

The following sections provide an introduction to linear wave theory in the absence of currents (section 2.4.2) in order to support the subsequent critical analysis of relevant literature which have linked the effect of wave-current interaction to tidal stream turbine (TST) performance (section 2.4.3).

2.4.2 An Introduction to Linear Wave Theory

Wave theories describe the kinematics (position and velocity) and dynamics (physical laws) of propagating waves either analytically or statistically (Sana and Tanaka, 2007). Thomson and Emery (2014) suggest that analytical techniques are unconvincing for determining complex wave signals within time series of flow. Consequently, linear wave theory is considered within this research due to similarities with harmonic tidal analysis, the application of linear wave theory by the chosen instrumentation (directional wave recorder) and because of the novelty of the thesis in terms of application to tidal stream power.

Linear wave theory was developed by George Airy in 1845 and can be used to describe waves in the open ocean, coastal and estuarine environments (Holthuijsen, 2007). Open ocean waves are considered 'fully developed' when they have reached their maximum possible size given the fetch, strength and duration of the wind (Holthuijsen, 2007). Individual, fully developed wave profiles are considered 'monochromatic', consisting of a single sinusoidal frequency and amplitude, which is relatively simple to describe analytically (Figure 24).

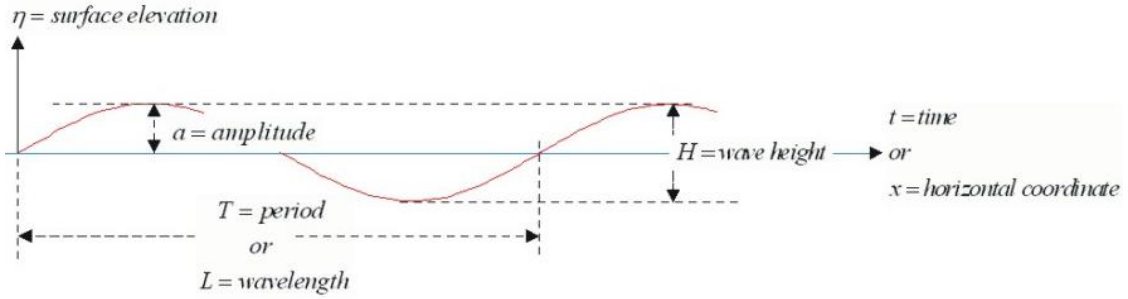

Figure 24: Characteristics of an idealised sinusoidal linear wave profile (Holthuijsen, 2007).

The description of this type of wave thus follows a number of fundamental assumptions:

- The waves surface profile is sinusoidal
- Viscosity and surface tension are ignored
- The Coriolis force is ignored
- The depth is uniform
- The waves are not constrained or deflected by any obstruction
- That 3-D waves behave analogously to 2-D waves
- The waves amplitude is much smaller than its wavelength

These idealistic wave profiles rarely occur in nature but are commonly considered in numerous studies due to their descriptive simplicity and replicability in flumes (Holthuijsen, 2007). Real sea states actually consist of multiple frequency waves propagating in different directions that have been generated from various geographic locations under varying meteorological conditions. When combined, these waves produce the 'random sea' which can only be described statistically due to its complexity and stochastic nature (Figure 25 and Figure 26) (Holthuijsen, 2007).

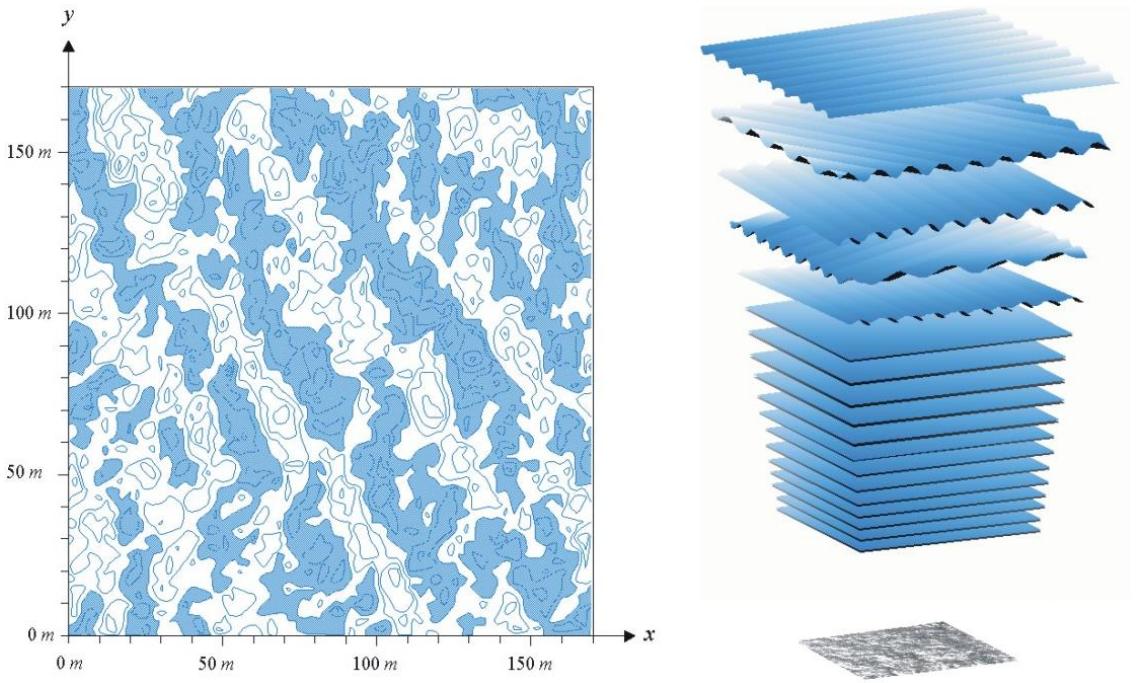

Figure 25: Individual wave harmonics make up the apparently random sea surface from above (Holthuijsen, 2007).

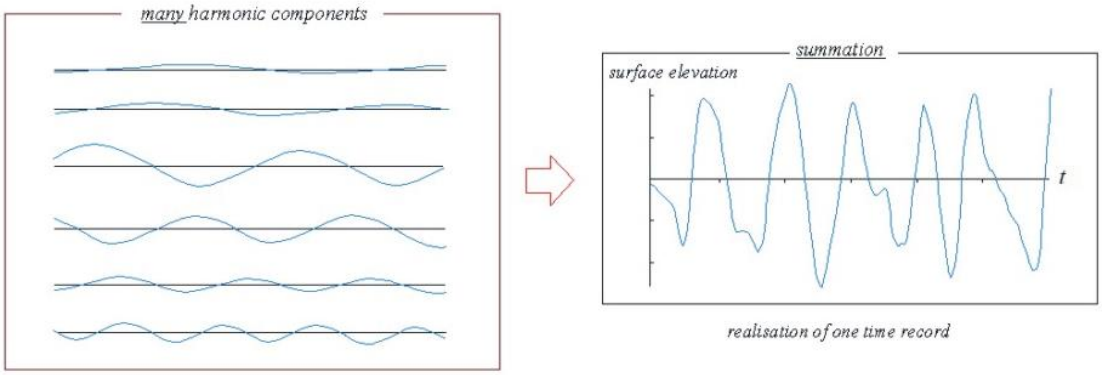

Figure 26: Summation of harmonic components to produce observed surface elevation time series (Holthuijsen, 2007).

Over timescales of around 5 minutes (dozens to hundreds of wavelengths), it is appropriate to describe the water's surface using average statistical characteristics of which the most important is the 'wave spectrum' which describes the probability of a characteristic of a wave occurring within that time frame (Holthuijsen, 2007). This method is typically used to describe *in situ* wave measurements collected from the open ocean, the coast or estuaries. When considered as a time series, the surface elevation at a static point can be used to derive a number of these statistical parameters (Figure 26) (Monbet *et al.*, 2007). Descriptive statistics are often split into wave height and wave period characteristics with the most common being the significant wave height, H_S, and the zero-crossing period T_Z (Holthuijsen, 2007). Significant wave heights are typically determined by calculating the mean of the highest third of wave heights in a wave record, or four standard deviations of a record of surface elevation. Zero-crossing periods are calculated by taking the mean of the separate time intervals between one 'zero-up crossing' and the next (Figure 27).

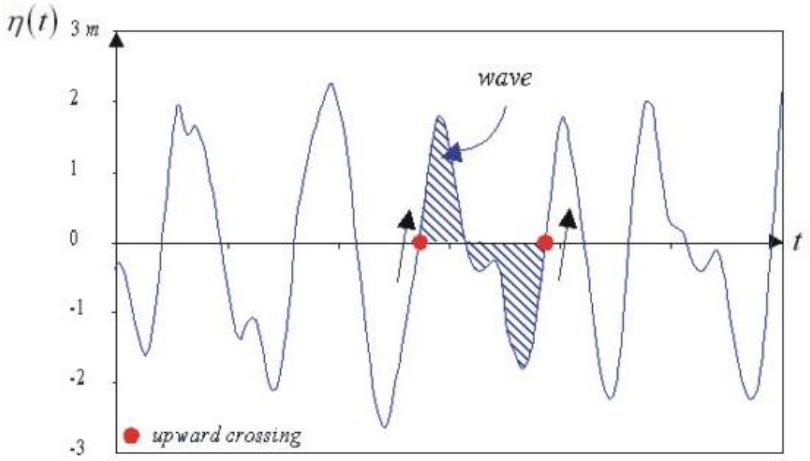

Figure 27: Zero crossing period of a wave (Holthuijsen, 2007).

As surface gravity waves are generated by the wind, their general size and sea state can be estimated given a near-surface wind speed using the Beaufort wind force scale (Met Office, 2016). No use of the fetch is used within these estimates as they are intended for the sea where the fetch is often long enough to generate developed waves. When considering waves in estuaries, areas can be very sheltered given the wind direction and limited fetch, which could have implications for the wave height. In addition, the modification of wave heights in response to currents is not incorporated into the Beaufort scale. Table 4 is included here as reference, which is later used in the methodology to compare measured results to estimations of wave height, based on recorded wind speeds in the Humber Estuary during the DWR deployment.

Beaufort Wind Scale	Wind Speed (kph)	Wind Descriptive Term	Sea Descriptive Term	Estimated Wave Height (m)
0	< 1	Calm	Calm (Glassy)	0
1	1 - 5	Light Air	Calm (Rippled)	0.05 - 0.1
2	6 - 11	Light Breeze	Smooth (Wavelets)	0.1 - 0.3
3	12 - 19	Gentle Breeze	Slight	0.3 - 0.6
4	20 - 28	Moderate Breeze	Slight – Moderate	0.6 - 1.2
5	29 - 38	Fresh Breeze	Moderate	1.2 - 2.4
6	39 - 49	Strong Breeze	Rough	2.4 - 4
7	50 - 61	Moderate Gale	Rough - Very Rough	4 - 6
8	62 - 74	Gale/ Fresh Gale	Very Rough - High	4 - 6
9	75 - 88	Strong Gale	High	4 - 6
10	89 - 102	Whole Gale/ Storm	Very High	6 - 9
11	103 - 117	Storm/ Violent Storm	Very High	9 - 14
12	>117	Hurricane	Phenomenal	>14

Table 4: Beaufort wind force scale and estimates of sea state (Met Office, 2016).

Many different sized waves exist in the ocean, each with a characteristic frequency. Figure 28 shows the typical frequency of different types of ocean waves with an arbitrary energy scale on the y-axis. Wind waves typically occupy the highest frequencies, often between 1 and 0.1 Hz, whilst swell waves dominate a narrower frequency band around 0.1 and 0.05 Hz (Portilla-Yandun *et al.*, 2015). Lower frequency waves in the ocean include tsunamis and of course the tidal constituents of the Sun and the Moon. The point of the wave frequency spectra is to describe the sea-surface as a stochastic process, not just to describe a single observation (Holthuijsen, 2007).

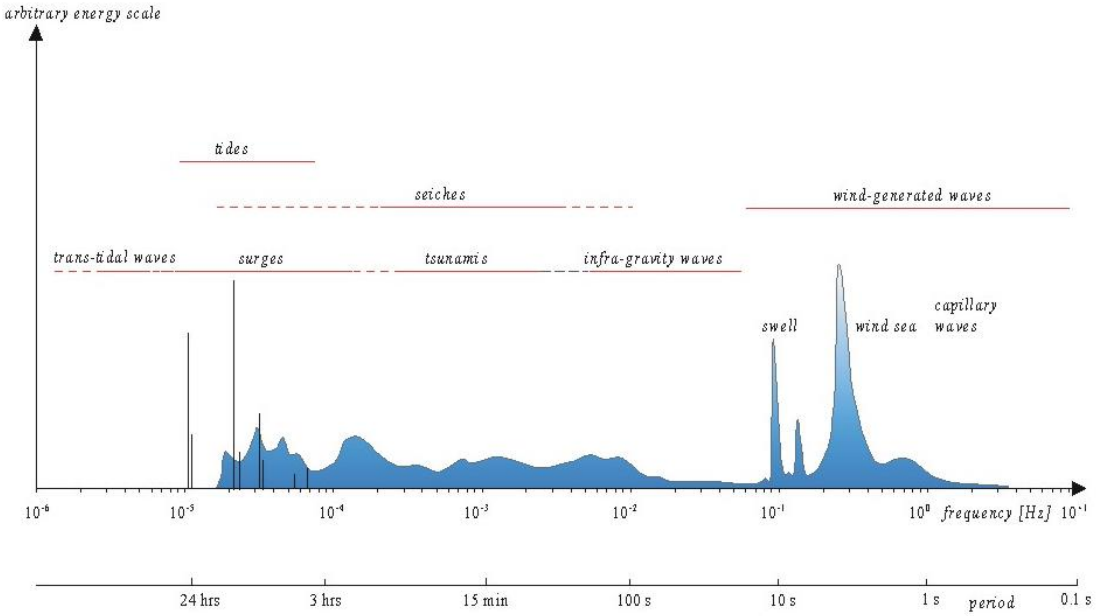

Figure 28: Temporal frequency of various harmonic waves (Holthuijsen, 2007).

A time series of surface elevation can be viewed in the frequency domain using a Fourier Transform. Figure 29 illustrates this process and clearly shows that in most time series of surface elevation a peak frequency can be determined which carries the most energy. This value could be particularly important to TSTs, as this frequency contains the greatest energy. This additional energy to the turbulence spectrum is investigated in Objective 2.

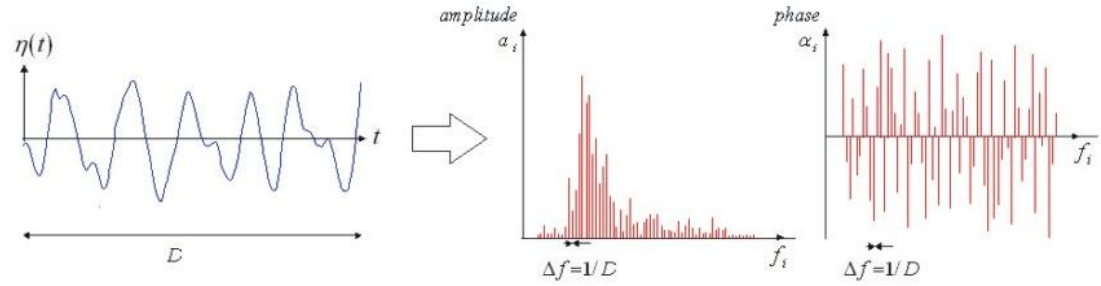

Figure 29: Time series of surface elevation presented in a frequency spectrum (Holthuijsen, 2007).

Understanding the flow velocities induced by propagating waves is critical to understanding and modelling wave-current interaction in tidal streams as additional momentum and energy could increase or decrease the predicted flow velocity or turbulent characteristics of a tidal stream under calm conditions. A propagating wave is dependent on the depth of the homogenous fluid in which it travels meaning that there are different equations for wave properties in 'deep' and 'shallow' waters which are defined by the ratio between the wavelength and the water depth (Table 5). Because of the kinematics and dynamics of dispersion, surface gravity waves induce orbital flows that attenuate with depth as they propagate (Andrews and Jelley, 2013). In deep water, wave-induced motion does not reach the bottom and diminishes at a depth known as wave base. Linear wave theory suggests that these orbitals are closed and circular in deep water and elliptical in shallow water meaning that there is no mass transport of particles (Ahmed *et al.*, 2010). Particle motion at the crest of a surface wave travels in the same direction as its propagation, whereas in the trough of the wave the fluid motion is in the opposite direction (Figure 30) (Ahmed *et al.*, 2010). Whilst the diameters of orbits at the surface are equal to the wave height, the diameters of orbits below attenuate exponentially with depth. Beyond a depth of half a wavelength there is minimal orbital motion; therefore, in water depths shallower than half the wavelength, the wave 'feels the bottom' and begins to transform, producing elliptical orbits. When the depth is shallower than $1/20^{th}$ of the wavelength, orbits no longer have a vertical component (Figure 30). The radius, particle velocity and recorded pressure differences of surface waves' orbital motion are reduced to 4 % when at a depth of half a wavelength in deep water (Knauss, 1978). It is important to consider that this attenuated motion is what will inevitably interact with the in-flow velocities a tidal turbine seeks to exploit beneath the surface therefore understanding wave-current interaction through depth is also a necessary research area.

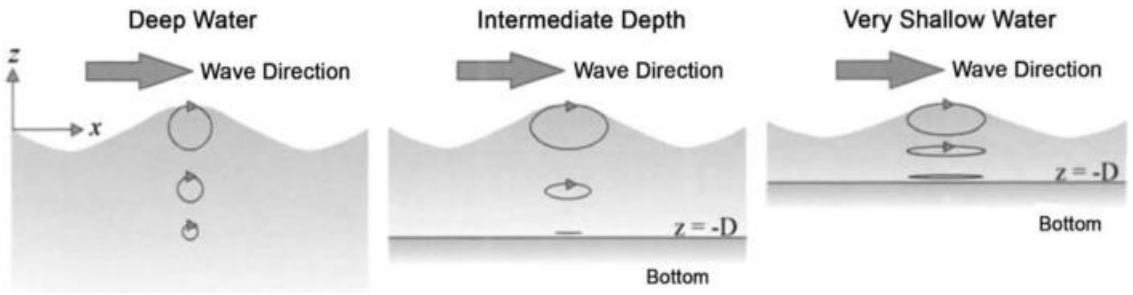

Figure 30: Orbital motions beneath surface gravity waves upon varying depths (Ahmed *et al.*, 2010).

Quantitatively describing surface waves is complicated by the shape of the wave once it 'feels the bottom' (when wave base meets the bed). Table 5 shows the varying equations that can be used to describe the speed, wavelength, period and maximum orbital velocity of a propagating wave in given water depths. Intermediate depths, where water depth is less than half the wavelength but greater than one twentieth of the wavelength, are more difficult to estimate maximum orbital velocities because the wavelength must be known. The wavelength is not commonly recorded by *in situ* instrumentation and is difficult to derive from other parameters such as the wave period as it must be derived iteratively using complex empirical formula if required (Hunt, 1979; Guo, 2002; Holmes, 2001; Soulsby, 2006). It is, therefore, much simpler to use the shallow water linear equations in coastal or estuarine environments at the cost of absolute accuracy in terms of depth.

	Shallow	**Intermediate**	**Deep**
Depth Class	$h < \frac{\lambda}{20}$	$\frac{\lambda}{20} < h < \frac{\lambda}{2}$	$h > \frac{\lambda}{2}$
Wave Speed (*c*)	$c = \frac{\lambda}{T} = \sqrt{gh}$	$c = \frac{\lambda}{T} = \frac{\omega}{k} = \sqrt{\frac{g}{k}}\tanh(kd)$	$c = \frac{\lambda}{T}$ $c = \sqrt{\frac{g\lambda}{2\pi}}$
Wavelength (λ)	$\lambda = T\sqrt{gh}$	$\lambda = \frac{gT^2}{2\pi}\tanh\left(\frac{2\pi h}{\lambda}\right)$	$\lambda = \frac{gT^2}{2\pi}$
Wave Period (*T*)	$T = \frac{\lambda}{\sqrt{gh}}$	-	$T = \sqrt{\frac{2\pi\lambda}{g}}$
Maximum Orbital Velocity (U_{max})	$U_{max} = \frac{H}{2}\sqrt{\frac{g}{h}}$	$U_{max} = a\frac{gT}{\lambda}\left(\frac{\cosh(kz+kh)}{\cosh(kh)}\right)\cos(kx - \omega T)$	-

Table 5: Various equations used to describe propagating monochromatic linear waves analytically in varying depths (Hardisty, 1990; Holmes, 2001; Schwartz, 2006)

Whilst the equations presented in Table 5 are useful for estimating surface parameters of monochromatic linear waves, the wave-induced motions that are likely to

affect tidal stream turbines will be generated by wave spectra and will be at some depth below the surface and above the bed. As mentioned, the orbital velocities induced by wave propagation also decay exponentially with depth meaning that surface estimates are inaccurate when trying to understand flows beneath the surface. Dyer (1995) proposed an analytical solution to determine the maximum orbital motion at the bed within a shallow water wave:

$$U_{max} = \frac{2\pi a}{\mathrm{T}\sinh\frac{2\pi h}{\lambda}} \tag{19}$$

However, this equation requires the accurate estimation of the wavelength, which is difficult to obtain in the field. Soulsby (2006) explains that calculating wave orbital velocity amplitudes at the seabed is problematic and, therefore, a choice must be made between accuracy and simplicity. Soulsby (2006) presents an exponential approximation of wave orbital motion using spectral properties of the surface elevation, as opposed to an analytical solution assuming monochromatic waves. It was developed to describe wave orbital motion in the absence of currents in desk-based applications to give quick and easy estimates within spreadsheets:

$$U_{rms} = \left(\frac{H_s}{4}\right)\left(\frac{g}{h}\right)^{\frac{1}{2}} exp\left\{-\left[\frac{3.65}{T_z}\left(\frac{h}{g}\right)^{\frac{1}{2}}\right]^{2.1}\right\} \tag{20}$$

Relative error:
- < 1.2 % *over*-estimate for $0 \leq t < 0.14$
- < 1 % *under*-estimate for $0.14 \leq t < 0.34$
- < 4 % *over*-estimate for $0.34 \leq t < 0.4$
- < 35 % *under*-estimate for $0.40 \leq t < 0.54$
- > 35 % *under*-estimate for $t > 0.54$

Where:

$$t = \frac{1}{T_Z}\left(\frac{h}{g}\right)^{\frac{1}{2}} \tag{21}$$

The 'Soulsby exponential approximation' (Equation 20) has yet to be tested in the field, though Soulsby (2006) explains that the wave dispersion equation will be modified in the presence of currents. In the field, this would be exceptionally hard to measure as it is impossible to control the wave and current generating processes to determine how a wave's

propagation has actually changed in response to current speed. Nevertheless, if relevant spectral wave parameters and variation about the mean flow are recorded simultaneously the theory should be able to be tested in currents.

Waves simultaneously exhibit a propagating pressure wave into the water column that is in phase with the surface elevation and particle velocity, which concurrently decreases with depth (Andrews and Jelley, 2013). This change in pressure can be measured using very sensitive bed-mounted pressure transducers. Using the concepts of linear wave theory, pressure transducers are often used to measure changes in surface elevation to infer spectral wave parameters. The DWR used within this thesis utilises this concept to measure waves from the bed.

2.4.3 Relevant Wave-Current Interaction Experiments and Methodologies

Waves and currents regularly interact in open oceans, shallow coasts and large estuaries meaning that the amplitude, frequency and direction of waves may change because of shoaling, current-induced refraction and energy transfer (Holthuijsen, 2007). Wave-current interaction is, then, a particularly important phenomenon studied by oceanographers, sedimentologists and geomorphologists due to the associated effects on bedload transport, sediment suspension and bed-ripple formation (Fernando *et al.*, 2011a, 2011b; Soulsby *et al.*, 2012). It has also been studied by civil and structural engineers within coastal engineering due to its effect on offshore structures such as seabed pipelines (Lambrakos *et al.*, 1988), oil-rigs (Wolf and Prandle, 1999) and, more recently, wave converters (Saruwatari *et al.,* 2013) and tidal stream turbines (Barltrop *et al.*, 2007; McCann, 2007; Faudot and Dahlhaug, 2012; Gaurier *et al.*, 2013; Lust *et al.*, 2013; Markus *et al.*, 2013; De Jesus Henriques *et al.*, 2014; Fernandez-Rodriguez *et al.*, 2014; Galloway *et al.*, 2014; Lewis *et al.*, 2014; Hashemi *et al.*, 2015). There is currently a poor understanding of how waves interact with strong current velocities, and particularly how surface wave activity interacts with turbulence metrics and spectra. There is also a poor understanding of how waves interact with TSTs *in situ*. This section critically analyses the literatures current understanding of these areas.

Linear wave theories are still valid within a frame of reference moving with the current so long as the water depth and ambient mean current remain relatively constant (Holthuijsen, 2007). Wave-induced orbital motions will therefore interact with the turbulence present in a fast flowing tidal stream. Due to the relative difficulty of observing this interaction in the field, a large volume of relevant literature has been limited to theoretical studies utilising numerical modelling and computational fluid dynamics (CFD)

or small-scale experimental studies involving laboratory flumes (Dohmen-Janssen *et al.*, 2002). This is widely acknowledged to be because of the cost and risk involved in fieldwork as the areas in which wave-current interaction occurs are very often remote, high-energy sites (Easton *et al.*, 2012). Nevertheless, a handful of papers have collected and reported appropriate *in situ* measurements of wave-current interaction, though for a range of applications not necessarily related to tidal stream power with varying quality and success. There is a distinct gap in the literature concerning reliable *in situ* measurements of wave-current interaction within the context of tidal stream sector, to which this thesis intends to contribute.

2.4.3.1 Numerical Simulations

Due to the large spatial areas available for tidal stream power developments, and the relative difficulty in measuring flows at all possible sites, numerical models and simulations using CFD have been developed to quickly and efficiently predict wave-current flows both spatially and temporally (Blunden and Bahaj, 2005). A combination of bathymetric maps and tidal constituents can give a relatively accurate prediction of the tidal height at any given location; though predicting the tidal flow accurately is more difficult. This is largely because of the 3-dimensional nature of tidal flows, which vary significantly with depth and bathymetry and are potentially influenced by stochastic meteorological effects over varying time-scales.

Recent papers have begun to expand conventional pure-tidal models by including surface wave activity specifically for the benefit of tidal stream sector, though very few have validated their models with appropriate primary *in situ* data collection. Hashemi *et al.* (2015) used a combination of current and wave CFD models to predict the impact of mean and extreme wave scenarios on the tidal stream resource surrounding the Skerries, Anglesey. They suggest that tidal development sites must consider local wave characteristics in order to better understand 'wave-induced hydrodynamic loading, wave-tide interactions, operation and maintenance issues and sediment transport'. Their results show that as a result of wave-current interaction the tidal energy resource at the Skerries tidal stream development site may be reduced by as much as 15 % during mean wave scenarios and up to 20 % during extreme wave scenarios. As a result wave-current interaction effects will be more significant at lower energy sites that are exposed to stronger waves as opposed to high-energy sites exposed to moderate waves. They neglect to explain how the relative direction between tidal flows and wave propagation influenced their results, which other recent papers believe is a fundamental variable to include in a model

(Lewis *et al.*, 2014). Their 2D model only calculated velocities in two orthogonal dimensions, x and y, thus overlooking the modifications to tidal flow as a result of wave orbital motion through depth (at a point) in the x and z dimensions. This is acknowledged by accepting that whilst a 3D version of their model could potentially solve these calculations it would be more computationally exhaustive to consider over such a great spatial area with the necessary accuracy. It is, therefore, evident that without a significant leap in computational power in the near future this issue may not be resolved to an appropriate accuracy using CFD for some time.

An investigation into directional wave-current interaction was carried out by Lewis *et al.* (2014) using a combination of wave and current CFD models to predict changes in theoretical tidal mean velocities as they insist the local wave climate could render some tidal energy sites 'inefficient'. Their main argument proposes that the few previous wave-current interaction studies (within the context of tidal stream power) have only considered the effects of inline wave-current interaction in flumes (defined as waves propagating with or against the tidal current within 20 ° of freedom (see section 0)). However, a significant proportion of the wave spectra interacts with the tidal current at an oblique angle; a phenomenon that is very difficult to simulate within conventional channel flumes. The paper attempts to determine the occurrence of inline wave-current interaction within the Pentland Firth, Scotland. Secondary data taken from a Waverider buoy within the Pentland Firth was used to input a realistic wave climate into the model. Figure 31 shows that the bulk of interactions were oblique and that the majority of 'inline' interactions occurred during periods of relatively low significant wave height and zero-crossing period; thus indicating that the effect could have been minimal during this particular examination. The results provide an indication of when wave-current interaction occurs in the field; however, they do not reveal what the effect was on the tidal mean current velocities or higher frequency turbulence. This is likely due to a lack of freely available, high frequency, simultaneous flow velocity data to feed into the model. They claim that for every metre increase in wave height the theoretical tidal stream resource reduced by as much as 10 %, though the more general effect of direction was not specified. Much like Hashemi *et al.* (2015) the paper stresses the need for high accuracy *in situ* observations throughout a range of wave events in order to validate such simulations and progress the field.

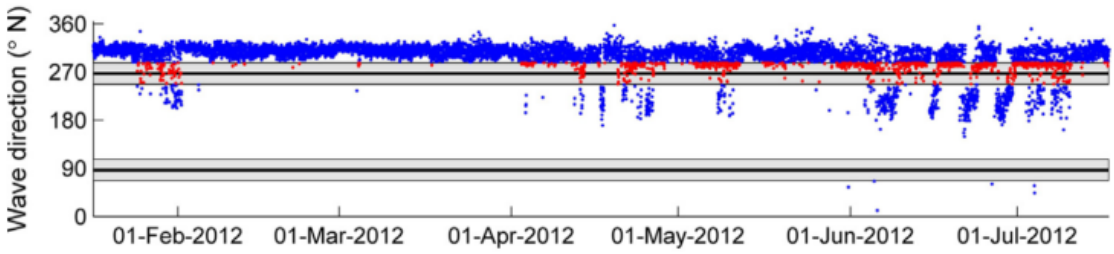

Figure 31: Waverider buoy data showing directional interaction with tidal streams flowing East and West (Lewis et al., 2014).

Some studies have also attempted to model the combined effects of waves and currents on the performance and structural fatigue of simulated TSTs. McCann (2007) investigated the effect of sea-state severity (characterised simply by H_S and T_Z) on the loading of a TST using the 'GH Tidal Bladed' simulation tool. Depth and turbulence intensity were kept constant at 50 m and 10 % respectively whilst H_S and T_Z were increased linearly (i.e. Run 1: H_S = 1.5 m and T_Z = 7 s, Run 2: H_S = 3 m and T_Z = 14 s). Modelled results suggest that the power output (P_O) and structural fatigue (M_Y) of a simulated TST are sensitive to wave action as fluctuations in P_O and M_Y increase with increasing sea state severity. Very recently, Tatum *et al.* (2016) investigated asymmetric loads on TSTs induced by surface gravity waves. It was estimated that thrust loading and bending moments applied to the drive shaft by surface waves can be of the order of hundreds of kN and kNm respectively and that understanding these effects would significantly help developers design durable TSTs. They used linear wave theory to simulate an extreme wave case though the specifics are not detailed. Turbulence effects are generally ignored but the influence of waves on fatigue and performance of a TST were related to the wavelength, amplitude and celerity of the surface waves.

2.4.3.2 Laboratory Experiments

The approach in which the interaction between waves and currents has been studied, measured and applied in the laboratory has evolved considerably over the past few decades. Typically, flumes are used to control flow velocity and wave generation but are limited to uni-directional wave-current interactions. With the increased interest and funding available for marine energy research modern, multi-directional flumes are currently being developed such as the FloWave tank at the University of Edinburgh which could be used in the future to validate the model developed by Lewis *et al.* (2014) (Gyongy *et al.*, 2014). The following section critically analyses relevant literature that has purely investigated wave-current interaction in the laboratory and, more recently, investigated the effects of wave-current interaction on scaled TSTs.

Longuet-Higgins and Stewart (1953; 1960) first observed an alteration in the overall wave kinematics with an exchange of energy between waves and currents near the bed using single-channel, uni-directional laboratory flumes. Kemp and Simons (1982; 1983) furthered this understanding by experimenting with wave-current interaction with both rough and smooth beds in flumes and presented the following qualitative observations:

- Flow reversal was observed near the bed with superpositioned waves propagating with the current.
- Mean velocities at the bed decrease as the wave height increases.
- Waves propagating with the current reduce mean flow velocities in the free stream whilst increasing them as the wave propagates in the opposite direction.
- The superposition of even the smallest wave caused a dramatic increase in turbulence over the values of current flow alone.

Groeneweg and Klopman (1998) later concentrated on free stream velocity profiles providing models that closely matched experimental results that agreed with the findings of Kemp and Simons (1982; 1983). More recently, Mazumder and Ojha (2007) describe a simple experiment over a smooth bed focusing on the change in mean flow, turbulence intensity and shear stress during superpositioned waves and currents in a specialised flume similar to the type used by Kemp and Simons (1982; 1983). Streamwise velocities were measured at three heights above the bed (0.45 cm, 10 cm and 20 cm) at 40 Hz for 5 minutes using an ADV. Runs of the experiment were made keeping mean velocity constant whilst increasing surface wave periods in increments of 0.5 Hz from 0 Hz to 2 Hz. In calm conditions, the mean velocity is greater at around 0.5 ms^{-1} than nearer the bed at around 0.2

ms^{-1} whilst there appears to be greater variation about the mean nearer the bed than higher in the flow. A lower mean velocity with greater variation results in a higher turbulence intensity. As surface wave frequencies increased, orbital fluctuations are clearly visible in the velocity signal, particularly in the measurements made higher above the bed. Whilst the mean streamwise velocity remained constant in the higher measurements, the lower measurements revealed that mean velocity increased by around 0.1 ms^{-1} when wave frequency was ≥1.5 Hz, which suggests there was a positive mass transport of particles induced by the waves. This research was followed by Ojha and Mazumder (2010) in which the turbulent characteristics of flow were measured over dunes when subjected to surface wave activity. They found that surface waves actually increase flow stability on the lee side of bedforms thus reducing turbulence intensities measured in equivalent calm conditions. Tambroni *et al.* (2015) recently researched the interaction between current, waves and a vegetated bottom. Within the paper, they present a state of the art understanding of wave-current interaction over an un-vegetated bottom (which is applicable to the bottom of the Humber):

- When waves and currents coexist, the steady logarithmic profile of longitudinal velocity changes from than that observed in pure-current conditions.
- Wave-current interaction effects are not restricted to the near bottom region and do influence the entire water column. These effects mainly depend on the relative propagation directions of waves and currents.
- Mean streamwise velocities near a smooth bed increase in the presence of waves propagating in the same direction as flow, whereas they reduce near a rough bed.
- When waves propagate in the opposite direction to the current, the longitudinal mean streamwise velocity reduces near to the bed.
- When waves propagate perpendicularly to the current, if the bed is smooth, an increase of the near-bottom velocities occurs whereas the opposite occurs when the bottom is rough.
- Variations of steady current profiles also depend on wave amplitude and water depth.

Whilst surface waves have been experimentally demonstrated to have significant effects on mean current velocities, little empirical work has been carried out on the effect of surface waves on flow variation about the mean, measured in terms of turbulence strength and intensity, which is investigated here in Objective 2.

Over the past decade, a growing number of papers have specifically linked wave-current interaction to the power output and structural fatigue of prototype TSTs in flumes

and tow tanks. Barltrop *et al.* (2007) combined blade element-momentum theory with linear wave theory to test the performance of a horizontal rotor in varying wave-current scenarios within a wave-tank. They showed that wave-induced vertical velocities modify the flow incidence angle into a turbine, varying the lift and drag coefficients thus significantly affecting the thrust and torque of the turbine. Lust *et al.* (2013) also hypothesised that surface gravity waves will have a significant impact on the operating condition of a TST and suggest that sub-surface wave motion could impart unsteady velocities several orders of magnitude larger than the ambient turbulence. This hypothesis was tested in a tow tank with a two-bladed horizontal axis TST subjected to flow with and without surface waves. Whilst average performance characteristics were relatively unchanged, large variations were noticed in the rotational speed, thrust and torque under wave action, thus suggesting that waves are less likely to affect average power output and more likely to affect material fatigue. Similarly, Gaurier *et al.* (2013) measured the influence of both currents and wave-current interactions on the loading of blades of a 3-bladed horizontal axis TST within a uni-directional flume. Mean velocities were kept consistent through depth with a turbulence intensity of 5 %. This was found to increase to around 30 % near the surface when waves were superimposed onto the current. The results indicated that the combination of waves and currents would significantly enhance blade loads compared to currents alone.

Galloway *et al.* (2014) tested the effects that waves and rotor misalignment had on a 1:20th Froude-scaled 3-bladed tidal turbine in a towing tank. They noted that prototype TST devices are over-engineered and have predominantly been deployed at sheltered sites (MCT, 2011; Andritz Hydro Hammerfest HS300, 2012; OpenHydro Group, 2012). Their results suggest that waves are likely to further complicate the power flicker experienced by TSTs (discussed in MacEnri *et al.*, 2013) as they discovered that the largest fluctuations in velocity are observed at the tip of the blade thus the main issue is likely to be an accelerated fatigue to the rotor and blades caused by wave-induced cyclic loading. Operations and maintenance costs for TSTs are already expected to be high due to sub-surface deployment and the increased structural fatigue will likely increase operations and maintenance (O&M) costs further. De Jesus Henriques *et al.* (2014) also investigated power and thrust variations from a three-bladed model horizontal axis turbine under combined, following wave-current conditions within a specialised wave-current flume. The orbital wave velocities generated agreed with linear wave theory and significant cyclic variations in power and thrust were found to occur at the same frequency as the surface waves. The probability density function of thrust and power changed from a normal distribution to a bi-modal distribution under combined waves and currents and the data spread increased as wave

velocities increased. Fernandez-Rodriguez *et al.* (2014) discuss the importance of testing turbulence and wave loads on tidal stream turbines in order to calculate extreme loads. They used the University of Manchester's wide flume, which is 5 m wide with a water depth of 0.46 m; this gave a scale of 1:70 simulating a typical tidal flow of 0.46 ms^{-1} with 30 m depth. A vertical mesh was used to break up turbulence generated by the jets, which created a turbulence intensity of 12 % at the position of the TST. They found that wake velocity profile downstream of a TST was dependent on the wave depth parameter, kh, and that waves helped to increase the rate of recovery of mean velocity to a distance of 10 turbine diameters downstream. However, they did not suggest how waves change the measured turbulence intensity before or after the TST.

In summary, studies have recently been keen to test linear wave theory superimposed upon a mean flow in specialised flumes and tow-tanks in order to test wave-current effects on the power output and structural fatigue of prototype TSTs. The idealised environments created in flumes can only go so far in predicting and modelling nature and *in situ* studies are now required to further understand the relationships between wave-current interaction, turbulence and TSTs.

2.4.3.3 *In Situ* Observations

In situ observations of wave-current interaction in tidal streams are inherently difficult to obtain due to the challenge of deploying expensive and sensitive instrumentation at energetic and potentially hazardous sites where fast tidal flows and large surface waves regularly interact (Bouferrouk *et al.*, 2016). Whilst depth-averaged tidal flow velocities can be reasonably well predicted prior to deployment, surface wave activity is stochastic and comparatively unpredictable. Therefore, long deployments of instrumentation are needed to capture a range of wave-current interactions and sea-state severities. However, the longer the deployment the greater the risk that kit will eventually be lost, damaged or return erroneous data from fouling (Bouferrouk *et al.*, 2016). McCaffrey *et al.* (2015) suggest that a full, *in-situ* characterisation of turbulence in tidal streams would be unrealistic with the current technology available and researchers must instead infer the turbulence characteristics of a tidal site with whatever limited observations can be made. This generally applies to all oceanographic monitoring but is particularly pertinent within wave-current interaction observations due to the constantly changing mean and fluctuating velocities through a typical semi-diurnal tidal cycle. This has resulted in a number of technologies and techniques being employed by researchers with a range of success and failure. This section critically analyses the methodologies and results of relevant case studies and is divided into research using electro-magnetic and acoustic

instrumentation. A current gap in the literature exists, as there has been minimal use of *in situ* data relating specifically to the tidal stream power sector (Bouferrouk *et al.*, 2016).

The seemingly most common method of collecting *in situ* simultaneous wave-current data has been to use a combination of EMCMs and pressure transducers (Lambrakos *et al.*, 1988; Soulsby and Humphrey, 1990; Hannay *et al.*, 1994; Wolf and Prandle, 1999). Aubrey (1989) suggest that EMCMs can adequately measure turbulence metrics, such as the streamwise turbulence intensity, but advises that measurements made in the surf zone will have particularly high levels of turbulence intensity as the shear-generated turbulence combines with velocity fluctuations associated with non-linear breaking waves. Ideally, TSTs would be situated in a location away from breaking waves; therefore, it is reasonable to only observe wave-current interaction in water deep enough to accommodate non-breaking, propagating waves. A number of other papers have identified that wave breaking induces additional near-surface turbulence thus affecting the turbulence spectrum (Jones and Monismith, 2008; Shuiqing and Dongliang, 2016). It is widely acknowledged that measuring turbulence near the surface is difficult, particularly in tidal environments where the water depth constantly changes meaning that fixed instrumentation measures different water depths over the tidal cycle and floating instrumentation rotates due to wave action (Shuiqing and Dongliang, 2016).

The following papers used methods similar to the employed methodology used within this thesis and are therefore critically analysed in detail. Lambrakos *et al.* (1988) recorded 'wave plus current' flow near the bed over 6 months in the Strait of Juan de Fuca, Canada, to predict the effects of waves on pipeline stability. EMCMs at five elevations (0.24, 0.61, 1.22, 1.83 and 3.66 m) recorded flow at 5 Hz whilst pressure, temperature and conductivity sensors were used as support data to validate the flow data. Waves were not directly measured but rather inferred from the standard deviation of flow measurements. Small or no wave action was defined as $U_o < 10$ cms^{-1} whilst large waves were defined as inducing $U_o > 30$ cms^{-1}. This method assumed that fluctuations about the mean flow measurements were solely induced by wave orbital motion and that turbulence fluctuations were ignored. This method is, therefore, flawed as numerous papers such as Soulsby and Humphrey (1990), MacEnri *et al.* (2013) and Milne *et al.* (2013) demonstrated that there is generally an observed increase in turbulent fluctuations with increased mean flow speed in tidal streams in the absence of surface wave activity.

Soulsby and Humphrey (1990) sought to observe and test wave-current theories using a novel methodology involving near-bed mounted EMCM's and pressure transducers. Near-bed measurements were made over eight days in the English Channel, 7.5 km south-west of the Isle of Wight. The site had a mean water depth of 25 m and a tidal range of 2 m

and was, in theory, exposed to large swell waves from the North Atlantic Ocean. Instruments including four electro-magnetic current meters, a pressure transducer and a compass were attached to a STABLE frame (Sediment Transport And Boundary Layer Equipment). The EMCMs were arranged so that two measured horizontal components of flow at 10 and 80 cm from the bed and two measured vertical components at 40 cm. This arrangement meant that flow could only be accurately recorded during Flood tide as Ebb flows were obstructed by the frame. Data were recorded at 4 Hz for a duration of 8.5 minutes in intervals of 3 hours. This sampling setup resulted in 64 bursts of which half occurred during the Ebb tide and a few contained erroneous results meaning that just 28 bursts were available for analysis. The EMCM at 80 cm contained 'noisy' data (the cause and extent of which was not defined) and, therefore, only mean values were analysed. The wave regime at the site approached between a 40 ° sector from the south-west. However, these waves could not be measured at the site due to the failure of the pressure transducer and were instead inferred from a wave-rider buoy positioned 80 km away (a large source of error in terms of accurate surface wave characteristics). Wave heights from the buoy measured relatively low Open-Ocean significant wave heights of between 0.29 and 1.87 m suggesting that this study did not measure particularly large storms or swell. The results contained a wide range of combinations of waves and currents including 'wave-dominated', 'mixed' and 'current-dominated' bursts (Figure 32). Wave-dominated bursts had very low mean currents and clear, regular orbital velocities with evidence of 'groupiness' in the signal. Mixed bursts contained discernible wave signals, which were offset by a mean current velocity and overlain with higher frequency fluctuations. Current-dominated bursts contained large turbulent fluctuations where wave motion was not discernible by eye. From these graphs, it can be seen that the wave orbital flows were similar in velocity to the turbulence-induced fluctuations and that the estimated standard deviation of these flows, and thus the turbulence strength, was in the region of 0.1 ms^{-1}.

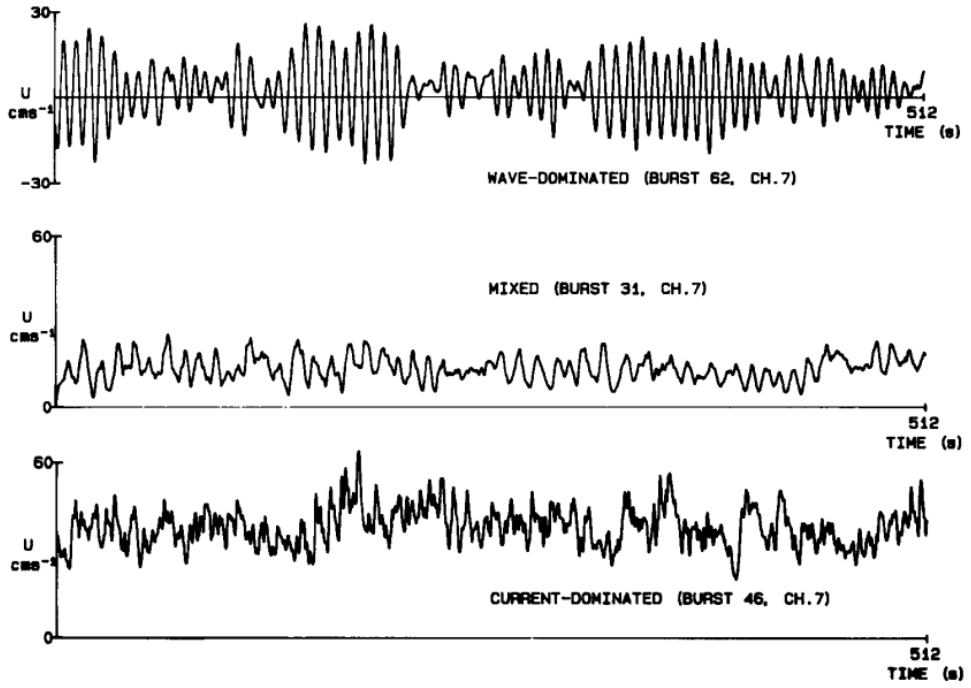

Figure 32: Examples of wave-dominated, mixed and current-dominated time series (Soulsby and Humphrey, 1990).

As many of the bursts were considered 'mixed' the paper goes on to attempt to decompose the signals into their constituent velocities but stress that there is 'no well-established analytical method of separating wave orbital velocities from turbulent fluctuations' and that the problem was exacerbated within the study due to failing to accurately measure local surface wave conditions. By calculating the turbulence energy spectrum of the mixed bursts, a distinct pattern emerged whereby the variance of both wave orbital motion and turbulence are identifiable (Figure 33). By calculating the area under the curve, the variance was split below the peak wave signal. They go on to apply the technique to estimating bed shear stresses, which is not a parameter necessary for implications to in-flow velocities to TSTs, yet they did find that the turbulence kinetic energy and the mean bed shear stress increased strongly with the 'wave-current ratio' and that the detailed structure of the turbulence was unaffected by wave action.

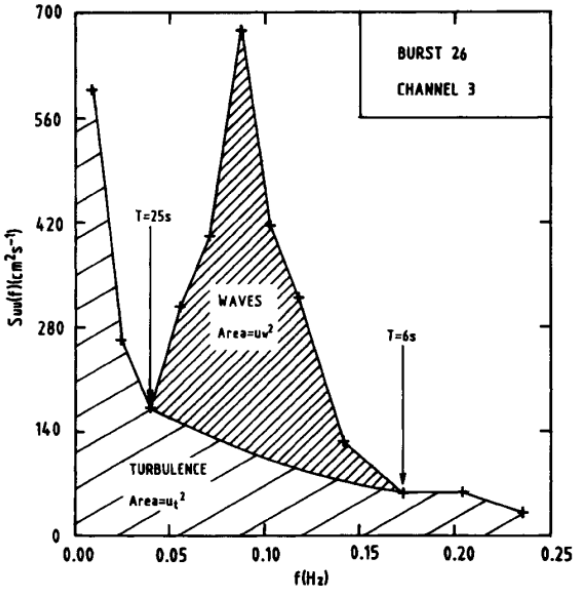

Figure 33: Frequency spectrum of mixed burst (Soulsby and Humphrey, 1990).

Hannay *et al.* (1994) used a very similar methodology and directly compared their results to Soulsby and Humphrey (1990) in the Norfolk sandbanks, UK. They recorded tidal current speeds around 0.2 to 0.9 ms^{-1} and wave-induced velocities of 0.1 to 0.24 ms^{-1} in a water depth of 30 m. They too observed a peak in the turbulence energy spectrum induced by waves (Figure 34).

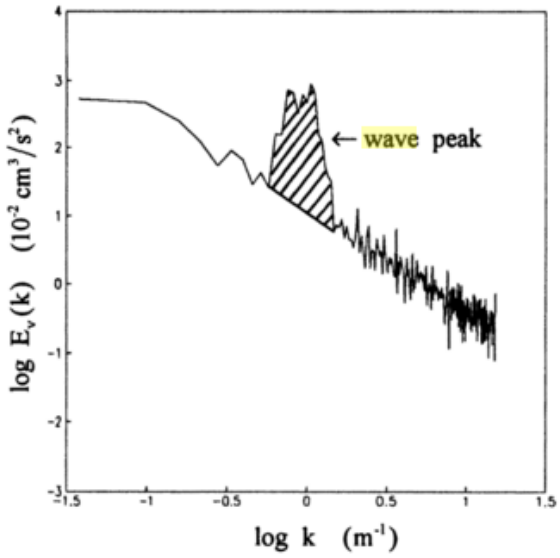

Figure 34: Wave peak in the turbulence energy spectrum (Hannay et al., 1994).

Wolf and Prandle (1999) presented observations of wave-current interaction as part of the SCAWFEX project using a combination of waverider buoys, pressure transducers and EMCMS. Whilst much of the study focused on the effect of currents on waves, a number of conclusions about how waves affected currents were made. They demonstrated that the velocity amplitude of the main tidal constituents, M_2 and S_2, reduced with

increasing significant wave height up to a maximum of 70 % of its undisturbed value. This claim has not been reproduced in subsequent literature and should therefore be further investigated.

Directional wave recorders (DWRs) can collect simultaneous wave and tidal data at high temporal frequencies at a point above the bed by typically combining EMCMs with pressure transducers, but have not yet been used within the literature to analyse wave-current interaction within the context of the tidal stream power industry. Ram *et al.* (2014) used a Valeport MIDAS DWR (identical to the device used within this thesis) to measure the near-shore wave resource of two of sites within the Fiji Islands. Sites were chosen based on visual observations of large waves and on practicality; other sites were available but contained strong rip currents in which the device could not be safely deployed using divers. The device was limited by the fact it had to be resurfaced monthly to swap batteries. Waves during a type 2 tropical cyclone were captured and analysed but no use was made of the measured flow data. It appears that the same Valeport DWR used in this study has not been used in any other published paper but is extremely useful as it combines a number of highly accurate oceanographic sensors into a compact and robust design made for deployment in marine environments. The data collected by MacEnri *et al.* (2013) used a similar Valeport EMCM to analyse their flow and turbulence metrics but could have gained greater knowledge of the effects of waves on flow and TST power outputs had they instead used a DWR.

Another technique used to collect *in situ* wave-current data is to use bed-mounted ADCPs. Work (2008) compares the use of Waverider buoys and ADCPs to measure waves and currents in the Savannah River Channel, Georgia, USA, though does not make good scientific use of recording simultaneous, accurate wave data and current data and rather compares the capabilities of both systems for measuring accurate directional wave data. Rosman *et al.* (2008) used bottom-mounted ADCPs to observe calm conditions and wave conditions at 1 Hz in Moorea, French Polynesia, and Santa Barbara, California. The Moorea site had very low tidal characteristics, for example, the Spring tidal range was just 0.2 m and maximum tidal velocities reached just 0.2 ms^{-1}. The Santa Barbara site had a greater tidal range at 2 m with flows up to 0.3 ms^{-1} and wave statistics were recorded nearby from an unknown source. The study concluded that Reynolds stresses could not be easily computed because of 'instrument tilt' and 'real wave stress associated with the orientation of the principal axes of wave orbital motion'. It is considered that measuring short-period waves at a low frequency such as 1 Hz will not accurately capture wave parameters; however, this method could be useful if measuring longer period surface waves, which develop at higher Beaufort scales.

Filipot *et al.* (2015) investigated wave-current interaction using data from a bed-mounted Workhorse 600 kHz ADCP at the Paimpol Brehat pilot tidal energy farm in the English Channel. The site is exposed to high tidal current velocities (in excess of 3 ms^{-1}) and large swell waves from the Atlantic Ocean. They estimated that with the given wave conditions at the location the average horizontal velocity induced by waves would be 0.17 ms^{-1} and that the maximum could be as high as 1.4 ms^{-1}; therefore, the inclusion of wave-induced variance was considered an important factor to further understand within tidal stream power research. Although a two-month long dataset was collected, just three, 24-hour subsets were used in their analysis, of which two had very long swell waves and one had a very low energy wave field. Figure 35 shows how the turbulence strength of the flow is related to the mean current velocity; these data are presumably from the calm day though it is not confirmed in the text. A parametric relationship close to linear is observed of which higher standard deviations are observed closer to the bed at a given mean velocity; this relationship is less clear at velocities between -0.3 and 0.3 ms^{-1} as this was likely at slack water.

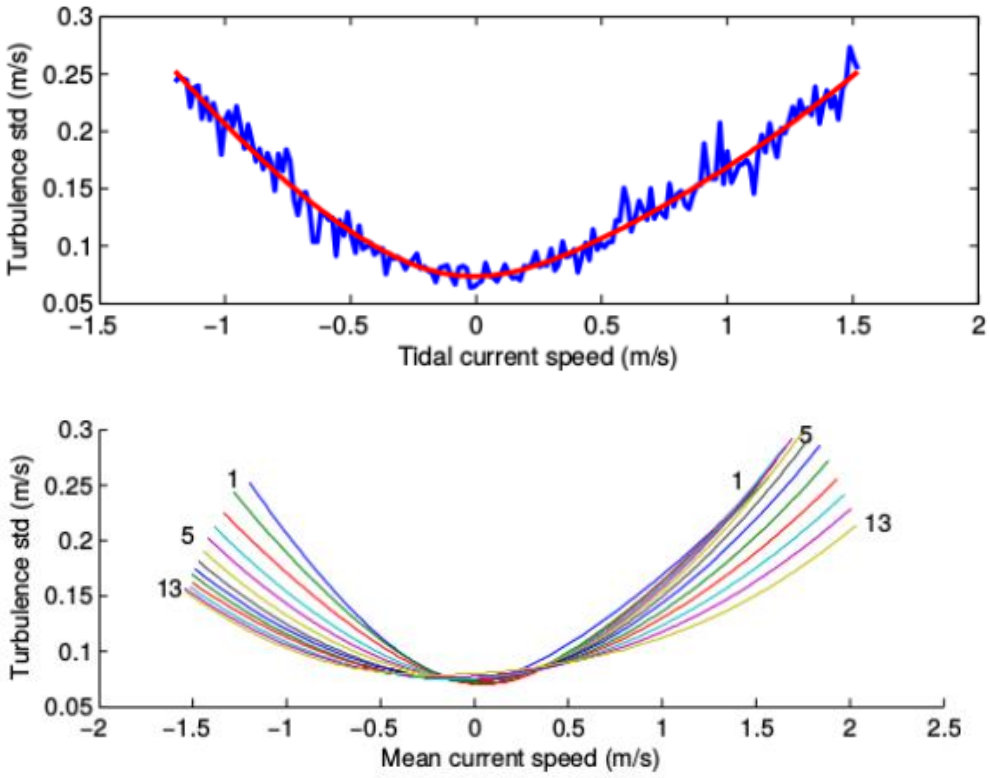

Figure 35: Relationship between turbulence strength (standard deviation) and mean current velocity through depth (Filipot et al., 2015).

The paper goes onto examine the turbulence spectra of current velocities in calm and stormy conditions, though the exact source of these velocities is not given, for example in Figure 36 the time and depth of the spectra are not presented. However, it appears to

show a peak in the turbulence spectrum between 0.04 and 0.3 Hz which is within the frequency range of the recorded surface wave activity. The paper does not relate this effect to TST fatigue but instead focuses on how this effect is likely to increase Doppler noise within the acoustic measurements, especially at higher wave numbers.

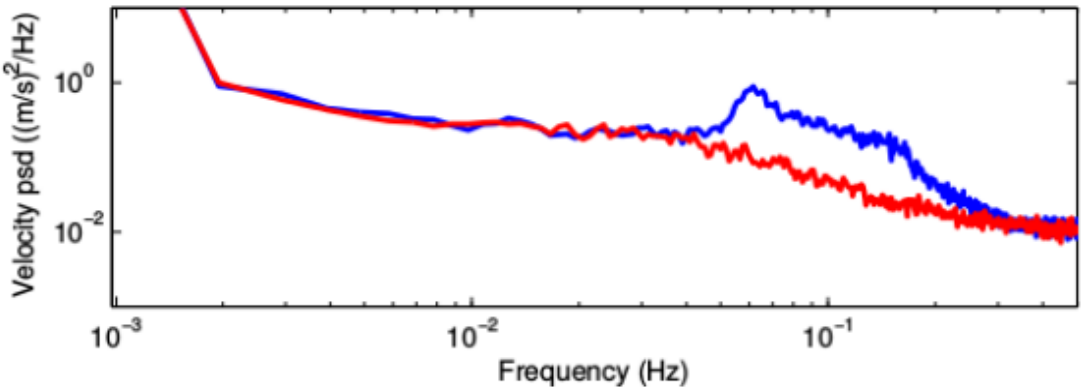

Figure 36: Comparison between turbulence spectra in calm (red) and stormy (blue) tidal flows (Filipot et al., 2015).

Recently, Bouferrouk *et al.* (2016) present results of turbulence intensity through 40 m water depth at a combined wave-current site within the Bristol Channel near the WaveHub site. A bed-mounted, 300 kHz, 5-beam ADCP was used to measure mean and turbulent flow metrics alongside four Waverider buoys to determine wave and current data. Throughout, limitations of the methodology are critically assessed and it is generally concluded that whilst 5-beam ADCPs can measure wave-induced motion and tidal currents separately they struggle to do so simultaneously. They suggest that the fast pinging mode 12 (used by Osalusi *et al.*, 2009b) creates bias in measurements by averaging higher frequency fluctuations into an ensemble average; therefore, the single ping mode 12 (as used in this thesis) is less bias but at the cost of reduced temporal resolution. Spatial resolution over such a depth is low because of the large bin depth required (4 m) and beam spread which increases in height above the bed of which they struggle to generate adequate shear velocity profiles. Figure 37 shows turbulence intensity at three bin depths in relation to the mean current velocity. It can be seen that at the lowest bin heights, turbulence intensity is highly scattered at low velocities and more consistent at high velocities. The turbulence intensities measured close to the surface are highly scattered at most velocities, which is potentially a result of wave-induced orbital velocities or wave breaking increasing the value of turbulence strength and thus the turbulence intensity. As these measurements were made with a bed-mounted ADCP in deep water the accuracy and spatial resolution of turbulence intensity measurements is considered low and probably too low to account for wave-induced velocities. There appears to be no physical reason why turbulence intensity

would increase from the bed as flow velocities should be fastest higher in the water column and turbulence maximised nearer the bed where it is generated. It must also be noted that these measurements were made in relatively low mean current velocities compared to other tidal stream sites. Many other papers describe slack water as <0.8 ms^{-1} of which the majority of these measurements were, thus suggesting that there was likely to be high scatter in turbulence intensity at these velocities, regardless of depth, which is a phenomenon observed in the results of this thesis. The paper stresses that optimum ADCP settings are required to measure turbulence and wave-induced velocities, which include minimum bin size, obstruction to flow and highest instrument frequency. They acknowledge that these settings may not always be at the disposal of the researcher though even a limited characterisation of turbulence from non-optimum ADCP setups could still provide valuable data to support the development of marine energy devices.

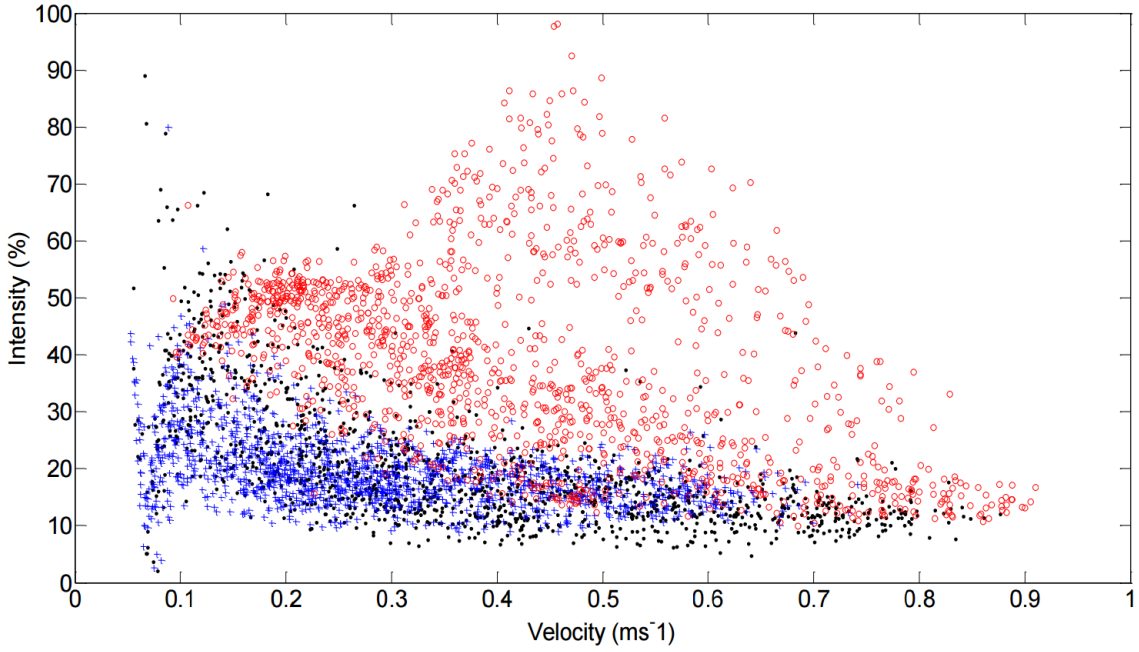

Figure 37: Turbulence intensity at three different bin heights in the Bristol Channel (Key: 6.2 m (blue), 21 m (black) and 36 m (red)) (Bouferrouk et al., 2016).

2.4.4 Summary of Relevant Wave-Current Interaction Experiments

Relevant papers involving the interaction of surface waves and current velocities have been critically analysed to determine research gaps in which to fill. It has generally been determined that the vast majority of wave-current interaction studies over the past 60 years have focused on the impacts of the phenomenon on sedimentology and has only very recently seen studies begin to consider the effect within the context of tidal stream power. Where possible, papers involving *in situ* data collection that are closely related to the

proposed methodology within this thesis have been analysed in more detail in order to determine appropriate instrumentation, sampling duration and rates for comparison.

2.5 Conclusion

The tidal stream power industry is at present nascent and may soon develop at an increased rate with the onset of more economically viable floating and buoyant turbines. Whilst the technology continues to advance towards maturity, the available resource remains poorly understood and *in situ* measurements of mean and higher frequency flow conditions are encouraged within recent literature. Numerous authors have identified the turbulence strength and intensity as useful metrics to characterise turbulent fluctuations in tidal flows and have tested their influence on TST performance and structural fatigue using numerical simulations, laboratory flume experiments and *in situ* observations. Similarly, numerous authors have identified the influence of surface waves on currents and on the performance and structural fatigue of TSTs using numerical simulations and laboratory flume experiments but have not yet tested (or published) this effect on an *in situ* TST. *In situ* observations of turbulence and wave-current interaction at tidally energetic sites are difficult and risky but nonetheless necessary. Of all the literature reviewed, no single methodology stands out as most appropriate for measuring wave-current interaction and this is a result of the limitations of the present day technology. Whilst commercial ADCPs are the only method of observing velocity through the water column (making them the go-to device for mean velocity profile sampling) they have a number of drawbacks when concentrating on turbulence and wave-current interaction. Most operating modes do not capture data at a resolution high enough to measure the whole turbulence spectrum and cannot accurately measure wave-induced velocities. Their beam angle spread and ensemble averaging of separate beams limit their spatial resolution to the measurement of just the largest scales of turbulence. Point sampling instrumentation can sample at higher temporal frequencies allowing characterisation of the turbulence spectra though these are hard to position in the most interesting sections of the flow.

The following chapter describes the methodology employed to model important relationships through depth and time of turbulence and wave-current interaction in the Humber Estuary taking into consideration the reviewed literature.

3 Methodology

3.1 Introduction

The literature review revealed a distinct research gap whereby *in situ* measurements of tidal turbulence and wave-current interaction are extremely limited yet highly sought after, especially within the context of tidal stream power. This chapter details the challenges faced when collecting appropriate data to meet the thesis objectives and explores the chosen methodology employed within the fieldwork in the Humber Estuary using directional wave recorders (DWRs) and acoustic Doppler Current profilers (ADCPs). Novel methodologies were devised to collect primary data by balancing temporal and spatial resolution of instrumentation and site selection with practicality. The instrumentation, site selection, surveying and deployments are described and explained before the results and analysis of each fieldwork is presented in the following chapters.

3.2 Challenges of Collecting Appropriate Data to Meet the Thesis Objectives

The speed of the tidal stream and the short working windows available during slack water means collecting simultaneous *in situ* measurements of turbulence and waves is problematic. Morgan (2014) describes numerous examples of failed surveys, which are of course not available as published literature. Such failures involved moored measurement buoys dragged under the surface or breaking loose and the loss of (or fouling of) deployed sub-surface instrumentation. In addition, flow measurements in energetic tidal environments are limited to just a few points in time and space by practicality. Subsequently, freely available secondary data were found to be extremely limited and often of poor quality in terms of spatial and temporal resolution. Some datasets of tidal and wave data were sourced from the European Marine Energy Centre (EMEC), the British Oceanographic Data Centre (BODC) and the Environment Agency (EA) but collected flow data were often at a low temporal resolution or exclusively contained the mean flow velocity; therefore, turbulence metrics could not be adequately calculated. In addition, tidal and wave measurements were always collected in separate locations and at different times; therefore, precise wave-current interaction could not be investigated.

Soulsby (1979) qualitatively explains the concerns associated with recording turbulence measurements in marine environments, *in situ*. Six factors are identified that must be considered when measuring tidal flows using *in situ* instrumentation:

- **Low-frequency contributions to the spectra:** Too short a record will result in the loss of contributions to the variance from the largest motions whose time scales are longer than the record length.
- **Stationarity:** Statistical methods, such as estimation of the mean and variance, or the production of spectra rely on the data set being 'stationary' (a constant mean). In a tidal flow this is not the case, but if sufficiently short record lengths are considered, the flow can be considered as 'quasi-stationary' at regular intervals (5 – 30 minutes).
- **Sampling variability:** The random error of an estimate of mean or variance depends on the record length. Random error can be reduced to an acceptable level by increasing the record length; however, increasing too long affects the dataset's stationarity.
- **High-frequency contributions to the spectra:** Too slow a digitisation rate will result in the loss of contributions to the variance from the smallest motions, whose frequency is higher than the corresponding Nyquist frequency (half the sampling rate).
- **Sensor response:** The sensor used will have physical limitations both on its frequency response and on the scales of motion it can resolve. This will restrict the maximum digitisation rate that can be used without redundancy. In modern field EMCMs and ADVs this rate is around 8 Hz, whereas laboratory ADVs can measure up to 200 Hz.
- **Size of the dataset:** If the data set is too large, the speed and ease of analysis are restricted by the capabilities of the computer used.

As this summary was presented in the 1970s, the issues of digitisation rates (4) and large datasets (6) have been significantly improved by upgraded instrumentation and computational power. Nonetheless, all six factors remain valid for collecting meaningful datasets of marine turbulence. With the availability of bespoke software, most of these considerations are adequately managed within the instruments default sampling settings (Valeport, 2008; Teledyne, 2011).

The UK has numerous sites that have potential for tidal stream developments (Figure 13) (Boyle, 2012). Of these, many are exposed to severe storm wave activity such as the Pentland Firth, North Scotland. Whilst these sites may seem appropriate locations to collect *in situ* measurements there are a number of reasons why fieldwork at these sites is challenging and why relevant published literature is scarce (Osalusi *et al.*, 2009b):

- Many of the sites are remote and difficult to get to by any means of transportation other than boat.

- Some sites are simply too energetic for relatively delicate instrumentation and, therefore, the risk of successfully deploying and recovering expensive devices is considered high.
- Data collected from marine energy test centres (i.e. EMEC and WaveHub) are not open source and can be expensive to obtain (Osalusi *et al.*, 2009b).
- Some sites are deep and do not dry out during Spring tides, meaning the only method of deployment is via a crane from a vessel.
- Instrumentation such as DWRs are best deployed at slack water under calm wave activity, which limits the deployment window. Vessel-mounted ADCPs are also best used in calm conditions. As storms are relatively unpredictable it could mean that kit and personnel are transported to a site at great expense only to be unable to conduct the fieldwork due to poor weather conditions.
- Some sites are close to shipping lanes, which subsequently means that gaining permission to deploy kit can be difficult.

As a result, relatively sheltered sites away from shipping lanes with strong tidal flows were favoured to meet the thesis objectives. The Humber Estuary was identified as meeting these criteria (see section 3.4.1).

3.3 Instrumentation Used

This section describes the instrumentation used within the fieldwork of this thesis to measure flows at a point (DWR) and through depth (ADCP).

3.3.1 Valeport MIDAS DWR

3.3.1.1 Introduction

The Valeport Midas directional wave recorder (DWR) is a bed-mounted instrument that utilises the PUV method (Pressure, *u* and *v* velocity measurements) by combining a pressure transducer and an EMCM (electro-magnetic current meter) into a small, robust device (Valeport, 2008) (Figure 38). The Midas range of Valeport products are considered to be of the highest quality oceanographic and hydrographic instrumentation available due to their exceptionally accurate burst sampling method and durable design, though there are very few published methodologies of their application (see Ram *et al.*, 2014). The DWR converts high-frequency pressure variations and current oscillations into directional wave data whilst simultaneously recording the tidal current flow's direction and velocity. Burst data are processed and presented by the bespoke WaveLog Express software in separate tidal and wave summary files as well as raw data files for each wave burst. Two identical devices were purchased new at the outset of the project meaning they were both calibrated to Valeport's high standard.

Figure 38: Valeport MIDAS DWR (Valeport, 2008)

3.3.1.2 Principles of DWR Operation

DWRs use EMCMs to measure flow at a single point in the water column. EMCMs come in a range of sizes for a range of applications, which typically results in a trade-off between spatial resolution and robustness. Laboratory-scale EMCM devices normally operate at

small spatial resolution whilst larger and more durable devices are designed for operation in the field. Fulford *et al.* (1994) describe how EMCMs measure flow velocity using Faraday's Law, which states that a conductor (water) moving within a magnetic field (generated by the electrodes) produces a voltage that varies linearly with the flow velocity. Typical EMCMs use four electrodes to measure velocity in two dimensions, u and v when orientated horizontally and u and w when orientated vertically. This, therefore, means that a single EMCM cannot measure three-dimensional flow velocities, though a configuration of two EMCMs in close proximity can. Once the flow velocity is known in the u and v dimensions the magnitude of the flow can be calculated from the resultant velocity, thus providing the one-dimensional streamwise flow, U.

Table 6 provides technical information on the various sensors the DWR device contains. The range of the strain gauge pressure transducer (40 m) and Valeport two-axis EMCM (± 5 ms^{-1}) limit the deployment location due to its inability to accurately operate beyond this depth or current speed (some tidal sites do exceed 40 m depth, though rarely exceed ± 5 ms^{-1}). The device utilises pressure measurements and linear wave theory to generate an accurate statistical summary of the surface wave activity during a sampling period. Peak wave direction is calculated by the direction of high-frequency variations in flow collected by the EMCM in reference to the on-board fluxgate compass. This allows the device to be deployed in an arbitrary orientation (a quantitative description of this process is confidential though according to Valeport). Water temperature is measured with a platinum resistance thermometer whilst salinity is inferred from the waters conductivity, which is measured with inductive coils.

Measure	Sensor	Range	Accuracy	Resolution
Pressure	Strain Gauge	50 dbar (40 m)	± 0.04 %	0.0025 %
Current	Valeport 2 axis EM	±5 ms^{-1}	± 1 %	0.001 ms^{-1}
Compass	Fluxgate	0 - 360 °	± 1 °	0.1 °
Temperature	PRT	-5 - 35 °C	± 0.01 °C	0.005 °C
Conductivity	Inductive Coils	0 - 80 mS/cm	± 0.01 mS/cm	0.004 mS/cm

Table 6: Valeport Midas DWR sensor information (Valeport, 2008).

3.3.1.3 Typical DWR Data Output

The device can operate in two distinct sampling modes: 'self-recording' and 'real-time'. Real-time is used when a computer and cable can be attached to the deployed device to gain real-time data, though this mode is not appropriate when operating in remote locations due to the limitations of cable length and computer proximity. Alternatively, self-

recording mode allows a sampling regime to be applied to a device that is deployed at a location and recovered after the required duration. Due to limited memory (64 MB solid state) and battery life (32 1.5 V alkaline D-cells) the device operates in a strict pattern of 'sample, process, sleep' to allow for longer deployments whilst still giving a good indication of tidal and wave scenarios, which generally do not vary much between 10-20 minute intervals. The sampling rate is controlled by the user prior to deployment using the system-supplied software 'WaveLog Express'. The sample rate must run at a frequency of either 1, 2, 4 or 8 Hz for a number of samples that must be a power of 2 i.e. 128, 256, 512, 1024, 2048 or 4096 as this allows a fast Fourier transform (FFT) to calculate 2D and 3D wave spectra. These samples must start at regular intervals (10, 20, 30 or 60 minutes) where the tide burst interval is a multiple of the wave burst interval. The tidal burst records more frequently than the wave burst but for a shorter duration as it only requires a brief sample of tidal data to produce an average value for tidal height and current velocity. The wave burst, however, requires a greater number of samples to produce accurate directional wave data and the wave frequency spectrum. Unlike the tidal burst data, the wave burst raw data can be accessed and analysed. A post-processing technique within WaveLog Express 'de-trends' the raw pressure data. This removes the tidal variation, thus leaving the realistic surface elevation through time.

In self-recording mode, the device stores the sample bursts internally within a single .bin file that must be downloaded from the device once recovered. This file is then translated from binary to useable data using the Wavelog Express software. This generates raw data files of every wave burst, as well as summary data files for tidal and wave bursts. Within the summary files, a number of useful statistics are calculated. Table 7 describes the output parameters and their relative derivations within the summary files.

Parameter	Derivation of Wave and Tidal Statistics	Output
Conductivity	The conductivity sensor monitors the electrical resistance of the surrounding water in milliSiemens/centimetre ($mScm^{-1}$) thus giving an indication of the waters salinity. The mean average conductivity and standard deviation over the sample are provided.	Wave summary files
Temperature	The platinum resistance thermometer (PRT) recorded the temperature of the surrounding water throughout the deployment in degrees centigrade (°C). The mean average temperature and standard deviation over the sample are provided.	Wave summary files

Pressure	The strain gauge pressure transducer records the pressure above the device, which includes both the water pressure and atmospheric pressure in decibars (dbar). The mean average pressure over the sample is provided.	Tidal + wave summary files
Water Depth	The atmospheric pressure is removed from the pressure data to calculate the water depth above the device in metres (m). As water depth increases the pressure increases linearly; therefore, every successive metre of water depth is equivalent to an increase in pressure of 1 dbar. The atmospheric pressure is approximately 10 dbar; therefore, this was subtracted.	MS Excel
Tidal Current Velocity	The Valeport electro-magnetic current meter measures flow on two axes ('*u*' and '*v*') using electrodes in metres/second (ms^{-1}). The resultant of raw '*u*' and '*v*' vectors calculate the magnitude of flow *U*. The average magnitude current velocity is provided.	Tidal summary files
Tidal Current Direction	The direction of flow over the '*u*' and '*v*' electrodes is made relative to the internal fluxgate compass for each sample thus calculating the average tidal current direction in degrees (°).	Tidal summary files
Surface Elevation	Raw pressure files are post-processed to de-trend tidal variation resulting in the surface elevation and thus the profiles of individual waves in metres (m). These data are used in the calculation of many other wave parameters.	Raw files
Significant Wave Height	Significant wave heights are calculated using the spectral moments of the time series of surface elevation where $H_s=4m_0^{1/2}$ in metres (m) and $m_0^{1/2}$ is the standard deviation of the surface elevation	Wave summary files
Maximum Wave Height	Maximum wave heights are calculated by multiplying the significant wave height by 1.57.	Wave summary files
Wave Energy Density	The wave energy density is calculated by integrating the wave energy over one wavelength and per unit length of wave crest where $E= \rho g H_s^2/16$. As a result, it is presented in joules per metre squared (Jm^{-2})	Wave summary files

Zero-Crossing Period	The zero-crossing period is calculated by measuring the time taken between zero-crossings of the surface elevation data of each individual wave in seconds (s). The average is then taken of every wave in the burst. It can be defined as $T_z = (m_0/m_2)^{1/2}$.	Wave summary files
Peak Frequency	Peak frequency gives the period at the peak of the frequency spectrum in Hertz (Hz)	Wave summary files
Wave Direction	Peak wave direction is calculated using the wave energy spectrum and the on-board compass and is presented in degrees (°). The manual states that the calculations involved are proprietary.	Wave summary files

Table 7: Derivation of wave and tidal statistics from Valeport MIDAS DWR and their output locations (Valeport, 2008).

The device is designed to record from the seabed within a specially designed steel frame. The EMCM sensor head is positioned so that it records flow just above the steel frame meaning that the frame does not obstruct the flow at the measurement height. Due to the nature of the device's calculations, the height above the seabed at which the recording equipment is situated is required. This is set at a default of 0.4 m for bed-mounted deployments but should be altered if the device is to be alternatively located upon a structure within the water column. The steel frame is relatively heavy and designed to prevent accidental trawling from sea-vessels; however, there is no guarantee that it will keep the device in the same position throughout a deployment duration, particularly during storm conditions and fast tidal streams; therefore, other methods of anchoring are encouraged by the manufacturer. It is important to deploy the device on a flat surface to avoid sensor head tilt errors but this is often difficult if deploying in deep water using a crane or upon a dynamic bed.

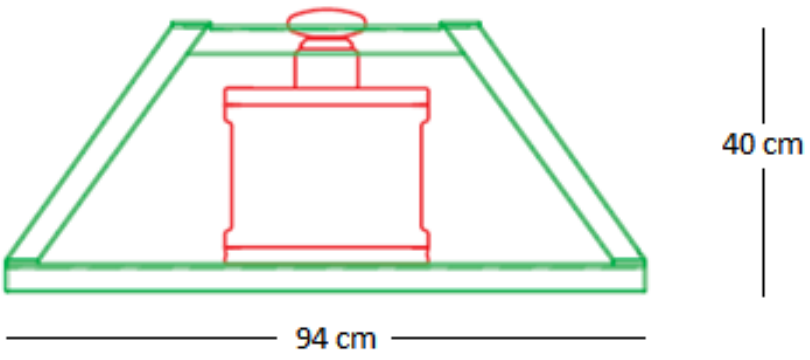

Figure 39: Diagram of the dimensions of the Valeport Midas DWR inside bespoke steel frame (Valeport, 2008).

3.3.1.4 Limitations of DWRs

Unlike acoustic Doppler velocimeters (ADVs), DWRs can only measure tidal streams in two dimensions (*u* and *v*) as opposed to an ADV's three dimensions (*u*, *v* and *w*). ADVs are designed for high temporal frequency studies of turbulent flows though there are expensive, relatively fragile and produce vast amounts of data due to an increased sampling rate. This means ADVs are unsuitable for long deployments in energetic sites, such as estuaries, without considerable computational power. The maximum sampling rate of the DWR is 8 Hz although, for example, this sampling rate halves the battery duration than available at 4 Hz. Typical ADVs are relatively fragile but can measure up to 200 Hz making them more suitable for laboratory studies of turbulence. Some ADVs are made specifically for field deployments but are susceptible to Doppler noise errors, unlike EMCMs (Filipot *et al.*, 2015). McLelland and Nicholas (2000) discuss the potential of ADVs in turbulent flow analysis (mainly in laboratory environments) as opposed to EMCMs due to the much higher sampling frequencies available (up to 100 Hz as opposed to <15 Hz). They acknowledge the many measurement errors associated with ADVs such as hardware sampling errors, Doppler noise and velocity gradients in the sampling volume. It is, however, considered that 4 Hz is a suitable frequency to measure the surface waves and the macro turbulence that occurs at lower frequencies and is arguably the main type of turbulence that is likely to affect the performance and fatigue of a TST.

DWRs require a crane and ideally divers to successfully deploy in deep water below chart datum. Whilst the device combines a number of highly accurate oceanographic sensors, it can only measure tidal streams at a fixed point in the water column close to the bed; this is well below an expected TST hub height. Other studies that have used combinations of EMCMs and pressure transducers have included a vertically orientated EMCM to measure three-dimensional flow velocities as they are interested in bed stresses for sediment transport purposes; however, as TSTs are primarily concerned with the *u* (streamwise in-flow velocity dimension) the DWR can suitably measure such flows.

3.3.2 Teledyne Workhorse ADCP

3.3.2.1 Introduction

ADCPs can accurately measure flow velocities through depth without disturbing the flow, making them the go-to device for tidal stream measuring (Parson *et al.*, 2012; Black *et al.*, 2015). Although primarily designed to improve quality and spatial resolution of mean flow measurements, modern ADCPs are now also able to determine some properties of marine turbulence such as turbulence strength and intensity, though at a much lower temporal

resolution than point measuring devices such as ADVs and EMCMs (Simpson, 2005). The EMEC Tidal Energy Standards (EMEC, 2009) and the TiME project (Black *et al.*, 2015) both suggest ADCPs are to be used to assess the potential of tidal stream site, though most energy yield assessments (EYAs) have only focused on mean current velocities previously and ignored turbulence measurement. The following section provides an overview of how Teledyne RD Workhorse ADCPs, the most commonly used range of ADCP instrumentation, operate as well as critically analysing their advantages and limitations.

3.3.2.2 Principles of ADCP Operation

ADCPs use the principle of the Doppler effect to measure flow velocity through depth by measuring the change in the observed sound pitch that results from relative motion (Teledyne, 2011; Parsons *et al.*, 2012). The Doppler effect is often explained using the analogy of a loud train or emergency service vehicle passing a fixed location. As the vehicle approaches, it's sound has a higher pitch and as it passes it's sound has a lower pitch. The variation in pitch of sound is directly proportional to the speed of the vehicle. When considering how this may translate to water velocity it is useful to compare sound waves to actual surface gravity waves. In the example given in (Figure 40), a person treading water on the surface of the sea may experience 8 waves pass near to them in a given interval (A). However, if they swam towards the waves, more waves would pass them within the same time interval than if they had stayed in the original position (B); this is the Doppler effect whereas Doppler shift is the difference between the frequencies of waves passing them.

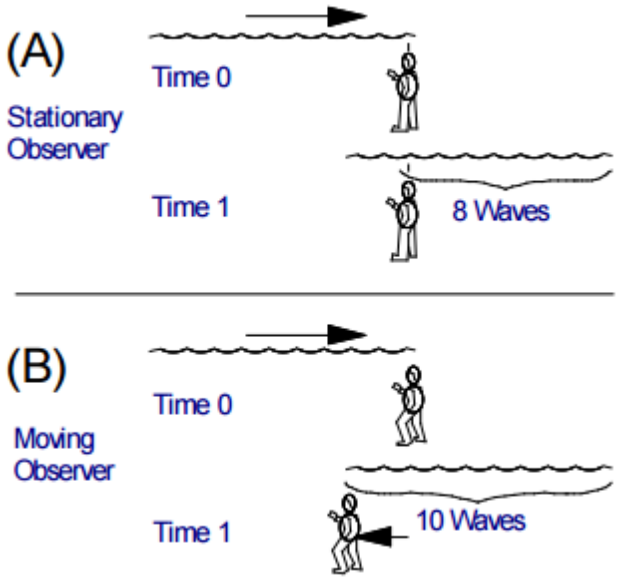

Figure 40: Analogy of Doppler shift observed by a swimmer in waves (Teledyne, 2011).

In terms of flow velocity, the Doppler shift can be calculated using:

$$F_{Doppler} = -2F_{Sound}\frac{V_{Particles}}{C_{Sound}} \quad (22)$$

Where $F_{Doppler}$ is the frequency of sound waves, $V_{Particles}$ is the relative velocity of the suspended water particles and C_{Sound} is the speed of sound in water (Okorie, 2011). Therefore, an ADCP emits a specific pitch of sound into the water column, which reflects off 'sound scatterers' in the water and measures the returning signal to calculate Doppler Shift and thus flow velocity (Parsons *et al.*, 2012; Black *et al.*, 2015). Sound scatterers typically include suspended sediment and zooplankton; therefore, an assumption when using ADCP data is that the sound-scattering material moves at the same velocity as the measured fluid.

The first generation of ADCPs used a narrow-bandwidth, single-pulse, autocorrelation method that computed the first moment of the Doppler frequency spectrum. These primitive systems have since been superseded by broadband signal processing techniques which use around 100 times as much bandwidth and utilise multiple beams, thus reducing variance in velocity estimates by nearly 100 times and making results significantly more accurate. Modern ADCPs use a combination of four beams in a 'Janus' (Roman God who could look forward and backwards) configuration to accurately measure velocity in three dimensions by collecting 'Easting', 'Northing' and 'Up' velocity components (Lu and Luech, 1999a; 1999b; Teledyne, 2011; Black *et al.*, 2015). ADCPs divide the vertical water column using 'range-gating' into uniform segments (bins). This is analogous to how a long string of uniformly spaced point current meters would do but with the added benefit of not obstructing the flow (Parsons *et al.*, 2012). ADCPs must average the velocity observed over the range of the bin, which typically range from 0.1 to 4 m depending on the frequency of the ADCP and the depth of the observed water column. This range, therefore, limits the length scale resolution of turbulence that can be feasibly measured (Black *et al.*, 2015). Figure 41 shows how two pairs of beams measure across East and West velocities whilst the other two beams measure North and South velocities. The resultant of these calculations is the magnitude of horizontal current velocity, of which tidal stream power is most concerned for power extraction and will be the focus of this thesis' analysis.

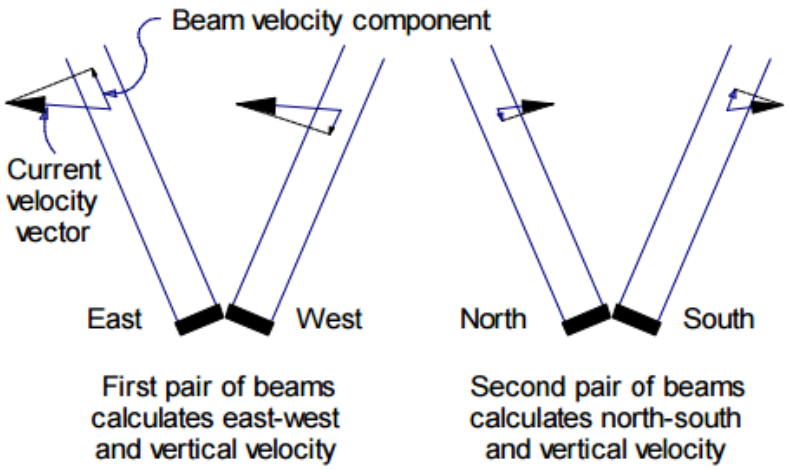

Figure 41: Janus configuration of the Teledyne Workhorse ADCP (Teledyne, 2011).

This method, therefore, follows an assumption of horizontal current homogeneity (the extent to which all four beams recorded 'up' velocities are the same) which is normally a reasonable assumption in oceans, rivers and lakes (Teledyne, 2011). Usefully, an ADCP can calculate the 'error velocity' in its two estimates of vertical velocity thus providing a means to evaluate the assumption of horizontal homogeneity and/or data quality. If a single beams vertical velocity is different to the other beams measurements, error velocity increases. This can be used to detect whether the flow is inhomogeneous (and turbulent), if the ADCP is malfunctioning or if obstacles in the water are present which are interfering with the acoustic signals, such as underwater structures or fauna (Teledyne, 2011). With distance from the sensor head, spatial resolution decreases as the beams diverge. Beams are typically orientated at an angle of 20 ° meaning that beam spread increases with depth and the assumption of horizontal homogeneity weakens. This, therefore, means that bed-mounted ADCPs looking up are most suitable for measuring turbulence near the bed whilst surface mounted ADCPs looking down are most suited to measuring turbulence near the surface.

3.3.2.3 Typical ADCP Data Output

ADCPs collect data from 'pings' emitted by each transducer at a frequency commonly around 300 to 1200 kHz depending on the device. The returning signals are then averaged into 'ensembles' of binned vertical velocity typically at a rate of around 1 - 2 Hz (Parsons *et al.*, 2012). Multiple ensembles make up a 'transect' of flow through time and depth. If the ADCP remains in a fixed and static position (looking up from the bed or down from an anchored vessel/platform), a transect is simply a time series of flow through depth. If the ADCP is towed across a channel using a vessel, the transect will provide a cross-section of vertical flow (which is the more commonly used definition of a transect by river researchers

and is regularly used to estimate discharge (Wall *et al.*, 2006; Buijsman and Ridderinkhof, 2007; Parsons *et al.*, 2012)).

ADCPs collect a large amount of data whilst operating and require specialised computer software to convert raw acoustic measurements into coherent current velocity data to be used by the researcher (Parsons *et al.*, 2012). Some studies, such as Osalusi *et al.* (2009b), used the individual beam coordinates to determine the variance between opposite beams in order to derive turbulence metrics. This technique is most suitable for bed-mounted devices which are not likely to pitch and roll whilst recording, as opposed to vessel-mounted surveys which are likely to rotate due to surface instabilities in fast flows and waves. Teledyne RD recommend that the most useful way to derive mean, turbulence strength and intensity measurements in real-time from static vessel-mounted ADCPs is to use software (such as WinRiver II). Internal calculations can resolve the velocity magnitude of flow for each bin by taking into account the ADCPs rotation (pitch, roll and heading) and translation (vessel velocity). Most ADCPs contain inclinometers or vertical gyros to measure pitch and roll and flux-gate or gyro compasses to determine heading. A combination of built-in 'bottom-tracking' and attached vessel global positioning system (GPS) can accurately determine such translation.

WinRiver II automatically identifies the type of ADCP being used and applies appropriate default processing settings based on a number of situational inputs, such as estimated maximum water density, depth and current velocity. The inbuilt calculation process within WinRiver II generates 'earth-referenced current velocities' based on the ships GPS system, vector track and speed over ground (VTG), which are the most realistic estimates of observable flow that can be outputted from a vessel-mounted ADCP (Teledyne, 2011). The accuracy of this estimation is helped by minimal movement such that pitch and roll do not exceed ±15 ° (Teledyne, 2008). This, therefore, means that ADCPs looking down from small vessels should not be operated in high wave activity as this will dramatically vary the rotation of the attached vessel leading to errors. Large tilt angles will result in depth cell mapping as opposite beams collect data at different depths away from the transducer resulting in depth cell reduction. The accuracy of uncorrected data for ship-mounted ADCP rotation was found to be around 1 cm^{-1} by Kosro (1985) which is similar to the bias error.

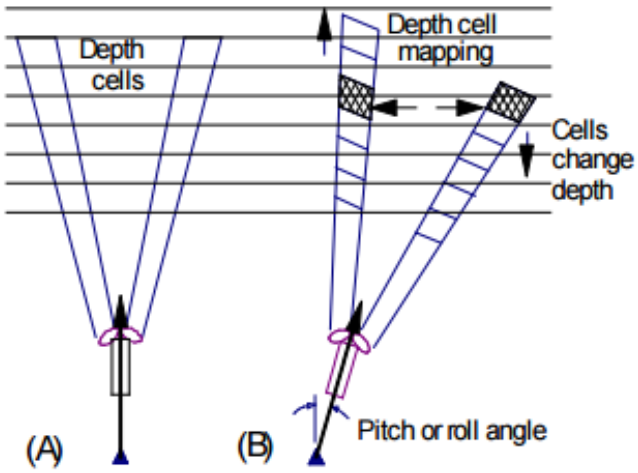

Figure 42: Illustration of depth cell mapping due to instrument rotation (Teledyne, 2011).

3.3.2.4 Typical ADCP Data Quality

Like all instrumentation, ADCPs are susceptible to some degree of measurement error and bias. ADCPs average multiple pings from four-beams into an ensemble because single ping velocity errors are too large to meet most measurement requirements (typically between 1 ms^{-1} and 0.5 ms^{-1}); therefore, the variance method, which uses the difference between opposite beams to calculate variance, could be exposed to these errors (Teledyne, 2011). Averaging a greater number of pings can reduce so-called 'random' errors by a factor of the square root of the number of pings but cannot reduce instrument 'bias' (typically 0.1 ms^{-1}). Averaging over longer periods reduces the random error but at some point further averaging will not reduce error further than the bias error (Teledyne, 2011). The extent of random error can depend on either internal factors (ADCP frequency, depth cell size and ping rate) or external factors (turbulence, internal waves and ADCP motion) (Teledyne, 2011). This, therefore, means that measuring flows with greater turbulence would lead to increased random error too. Bias error involves temperature, mean current speed, signal/noise ratio and beam geometry and cannot be easily identified or removed (Teledyne, 2011).

Lu *et al.* (2000) suggest that researchers attempting to measure turbulence metrics should not use ADCP data where local wave conditions exceed a significant wave height of 0.2 m as Koretenko *et al.* (2013) explain that waves induce velocity variances equal to or an order of magnitude larger than associated turbulent velocity variations, thus contaminating 'calm' turbulence results. In addition, surface mounted ADCPs lowered from boats will be significantly affected by tilt errors induced by pitch and roll of the boat by waves. This, therefore, limits the use of most ADCP surveys to calm conditions, which is of course a major limitation to measuring tidal flows in non-sheltered sites and for investigating wave-current interaction through depth.

3.3.2.5 Limitations of ADCPs

The acoustic frequency of an ADCP affects its range, resolution and random noise which forms the 'trade-off triangle'; each variable is interdependent as changing one affects the other two (Figure 43). For example, the lower the frequency of the ADCP, the greater the profiling range but the coarser bin resolution and increase in Doppler noise (Bouferrouk *et al.*, 2016). Budi *et al.* (2014) argue that ADCPs do not have 'sufficient spatial and temporal resolution to characterise turbulence within the inertial and viscous sub-ranges' and thus prefer to use ADVs to measure turbulence in tidal currents due to a 'higher data output rate and smaller sampling volume'. Whilst this is true, ADVs cannot measure flow through depth and whilst they may have a higher temporal frequency they cannot provide as much data about the vertical distribution of the flow as lower frequency ADCPs. Nystrom *et al.* (2002) found that turbulence intensities were likely to be overestimated by ADCPs within laboratory settings compared to ADVs because of increased random noise and lower resolution.

Figure 43: The ADCP 'trade-off triangle' between Range, Random Noise and Resolution (Teledyne, 2011).

ADCPs are limited by their intrinsic standard error because of Doppler noise, which essentially limits their temporal and spatial resolution (Teledyne, 2011). Doppler noise is created by random and non-random Doppler-shift measurement errors which means that the majority of ADCP measurements are bin-averaged to reduce the effects of standard error; this fundamentally limits their use in higher frequency turbulence or wave-current studies which rely on knowing the variance about the mean flow velocity at high temporal frequencies (>1 Hz). Doppler noise also results in a trade-off between larger range bins with low standard error or shorter range bins with high standard error. Due to the Janus configuration of the four-beams, the area in which flows are averaged increases with distance from the ADCP meaning that the length scale at which turbulence can be measured also increases with distance (Black *et al.*, 2015; Bouferrouk *et al.*, 2016). In many UK tidal stream development sites water depths range between 20 and 80 m meaning that the beam separation distance can be significant away from the ADCP. Velocity fluctuations of eddies smaller than twice the beam spread may not be robustly recorded or suffer

aliasing between bins (Black *et al.,* 2015). However, within shallow estuaries, such as the Humber, this effect will be significantly reduced, as the beam spread distance should not exceed the longest coherent length scales.

All ADCP transects, whether static or in motion, must use a 'blanking distance' close to the transducer and at the bed/surface (Teledyne, 2011). This is done to avoid contaminated bins from ringing or flow interference from surface or bottom structures, including the ADCP itself (Black *et al.*, 2015). Software such as WinRiver II can calculate this distance as a percentage of the total depth, typically around 6 %, meaning that the entire vertical water column cannot be measured using an ADCP (though it is unlikely that TSTs would be have swept areas that cover this region of the water column). Due to their reliance on acoustic signals travelling undisturbed through the water column, they are also susceptible to interference from nearby flora and fauna, which can block and reflect sound waves, thus limiting their use in vegetated or highly populated flows. ADCPs also cannot monitor the surface elevation at high temporal or spatial frequency without a dedicated, fifth, vertical beam. This means that most bed-mounted ADCPs cannot monitor waves simultaneously with currents (Bouferrouk *et al.,* 2016). Acoustic wave and current devices (AWACs) appear to be able to do this but the components that measure waves cannot be operated at the same time as the acoustic Doppler current measuring components meaning that data are not simultaneous and therefore unsuitable for accurate wave-current studies.

The 1200 kHz and 600 kHz models of Teledyne Workhorse ADCPs are commonly used in the literature when sampling mean flows and large-scale turbulence in rivers and estuaries due to their sampling rate and typical depth range. Table 8 shows the technical specifications and limitations of each ADCP. Whilst the ping rate is relatively low for analysing some properties of turbulence, such as the turbulence spectra, these frequencies have been used to measure statistical metrics such as the turbulence strength, which is used within this analysis.

Sensor	**Beam Angle**	**Smallest Bin Depth**	**Typical Depth Range**	**Ping Rate**	**Velocity Accuracy relative to ADCP**	**Compass Type**
1200 kHz	20 °	0.25 m	12 m	~1 Hz	0.03 ms^{-1}	Fluxgate
600 kHz	20 °	0.5 m	50 m	~2 Hz	0.03 ms^{-1}	Fluxgate

Table 8: Technical limitations of the 1200 kHz and 600 KHz models of Teledyne ADCPs (Teledyne, 2011).

3.4 Site Selection

3.4.1 The Humber Estuary

The Humber Estuary has some of the greatest tidal stream characteristics in the UK with strong, turbulent currents up to 2.5 ms^{-1} (according to admiralty charts), Spring tidal ranges in excess of 7 m, whilst also being sheltered from the severe wave conditions encountered in more exposed sites such as in northern Scotland. Nevertheless, wave conditions in the Humber regularly exceed those which are considered 'calm' on the Beaufort wind scale thus allowing an opportunity to investigate the research objectives. Whilst the Humber has been used to test full-scale TSTs in the past, academic publications of *in situ* measurements of flow and turbulence are presently absent from the literature at sites with the greatest tidal streams. Instead, investigations within the Humber have tended to focus on sediment flux within the inner and outer estuary, where tidal flow speeds are significantly reduced (Uncles and Stephens, 1999; Townend and Whitehead, 2003; Uncles *et al.*, 2006). Others have focused on hydrology and flood defence schemes due to the estuaries susceptibility to storm surges (Law *et al.*, 1997; Barham *et al.*, 1999; Skinner *et al.*, 2015). Therefore, this research is the first academic work to collect *in situ* tidal stream time series data for analysis at sites with potential for tidal stream power in the Humber Estuary.

3.4.1.1 Spatial Context

The Humber Estuary is the largest estuarine system in the British Isles with a total catchment area of 26 000 km^2, 20 % of the area of England (Uncles *et al.*, 2006) (see section 3.4.2 and Figure 45 for a map of the Humber Estuary). The estuary can be approximately divided into three sections: the inner, middle and outer estuary. The inner estuary begins at the confluence of the rivers Trent and Ouse, which provide the vast majority of freshwater input resulting in an average 250 m^3s^{-1} discharge into the North Sea (HUMCAT, 2002; Uncles *et al.*, 2006).

The boundary between the middle and outer estuary fluctuates depending on the seastate but is generally around the Port of Immingham where conditions are considered coastal. Mean water depth naturally varies along the channel from the inner estuary (5 m) to the outer estuary (8 m), whilst also varying due to the artificially dredged shipping channel in the middle and outer estuary where depths can reach up to 16 m to accommodate large shipping and cruise vessels.

3.4.1.2 Tidal Regime

During Spring tides the Humber is considered hypertidal (tidal range >6 m and generally well-mixed (Archer, 2013)) with the second largest tidal range in the UK (>7 m) and tidal current velocities up to 2.5 ms^{-1} (Hardisty *et al.*, 1996). These high tidal characteristics occur because of the estuaries unique position in relation to the North Sea amphidromic points (Easton *et al.*, 2012) and the channel's funnelling and thus amplifying shape. The Humber tides are dominated by the M_2 amphidromic point in the eastern-central North Sea (Doodson and Warburg, 1941). The tide generally progresses in a southerly direction along the coast of Holderness and enters the estuary mouth some 6 hours before high water at Dover (Hardisty, 1990 and Hardisty *et al.,* 1996). The tide takes about 3 hours to progress up the estuary from Spurn Head to the Ouse-Trent confluence and higher order harmonics are generated during this progression.

Nguyen (2008) explains that the Humber can be classified as an 'amplified' estuary. This is because the tidal range increases in the upstream direction as the narrowing of the channel, or 'convergence', has a greater effect than the loss of energy by friction. Conversely, as suggested by Dyer (1995), an 'ideal' estuary would balance the effects of convergence and friction, thus generating a constant tidal range along the whole estuary. At a distance along an amplified estuary, frictional forces eventually match and subsequently exceed the convergence effect, resulting in tidal dampening and tidal range reduction. The greatest tidal ranges and thus the strongest tidal flows, then, tend to occur in the middle estuary close to the city of Hull, making it an attractive area for tidal stream power development.

The Humber is particularly sediment-laden due to its large catchment area and proximity to the rapidly eroding Holderness coast, which is made of particularly loose material, such as boulder clay, deposited during the last ice age. Consequently, many of the bedforms and sand banks in the inner estuary are highly dynamic and change with each tidal cycle. Complex, density driven flows are generated in the inner estuary where warmer fresh river water mixes with colder, saltier seawater, generating micro-scale turbulence throughout the water column (Skinner *et al.*, 2015). Turbulence from the bed is also generated because of friction between the flow and bed roughness. The bed roughness drag coefficient is, therefore, between 0.0022 and 0.0061 because of the bed material ranging from mud to rippled sand as given by Dyer (1995) and Soulsby *et al.* (1993) in Hardisty (2009). Subsequent deployments of the Valeport DWR device in the inner estuary were unsuccessful as the intertidal sandbanks there are so dynamic that the device became fully submerged within the bed material over just a single tidal cycle. This of course meant

that the EMCM data was unusable though the pressure transducer still returned accurate estimates of water depth through the Spring-Neap cycle.

3.4.1.3 Wave Regime

There are two resulting wave regimes within the Humber: swell waves generated in the North Sea to the east and locally generated waves within the estuary itself. The most frequently occurring and strongest onshore winds at the mouth of the estuary are from the north and east whilst the inner and middle estuary are dominated by the prevailing south-westerly winds (Shellard, 1976). The mean annual days of gale (DOG: wind speed in excess of 34 knots for several minutes) increase from 2.5 at Hull to 23.7 at Spurn Head suggesting that upstream sites are less windy that downstream sites (Shellard, 1976). North Sea waves are larger than those generated within the estuary due to a much longer fetch and stronger winds; these are most closely recorded at the Dowsing Light Ship, approximately 25 km south-east of the estuary mouth. The 50 year return values for the significant wave height (H_S) here is 8.23 m for the winter maximum which reduces to 7.41, 6.91 and 5.35 for the Autumn, Spring and Summer respectively (Shellard, 1976). Results of wave rider buoys off Holderness are reported by Bacon and Carter (1988) which suggest a 50 year return for H_S of 6 m. Waves within the estuary are locally generated and, therefore, substantially smaller in the order of 1-2 m during localised storms though wave heights generally increase downstream from Hull to Spurn.

3.4.1.4 Tidal Stream Power Developments in the Humber Estuary

The unique geography of the Humber Estuary has attracted a number of tidal stream power developments, most notably are the prototype demonstration devices, Pulse Stream 100 and Neptune Proteus (Figure 44). In May 2009, Pulse Tidal deployed the 100 kW "Pulse-Stream 100" demonstration device in the outer estuary. The design used oscillating hydrofoils which swept up and down exploiting the shallow water tidal currents in both Flood and Ebb directions. Neptune Renewable Energy installed the "Neptune Proteus" in the middle estuary near Kingston-Upon-Hull in 2012 (Hardisty, 2012). The device used a vertical axis Darrius turbine to exploit and accelerate the strong tidal currents that occur in the middle estuary.

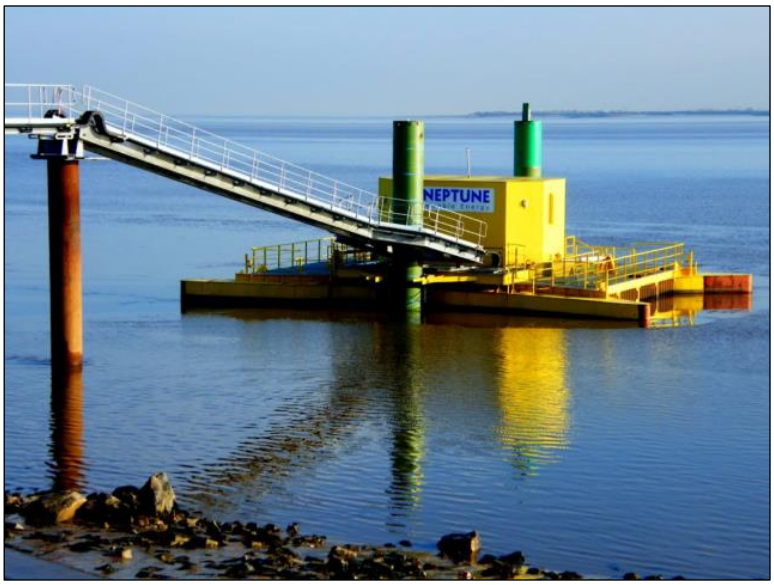

Figure 44: Prototype TSTs, Pulse Stream 100 (Top) and Neptune Proteus (Bottom), deployed in the Humber Estuary (HullValley, 2012; PulseTidal, 2016).

Both devices tested innovative approaches that aimed to exploit tidal streams in relatively shallow water whilst keeping complex machinery above the surface for more cost-effective O&M. Whilst this has economic benefits, the TSTs were positioned close to the water's surface meaning that they will have been affected by surface wave activity, though still much less than the waves experienced in less sheltered sites.

The Humber Local Enterprise's Strategic Economic Plan 2014-2020 (Humber LEP, 2014) acknowledges that there is significant potential for tidal stream power generation within the 'Energy Estuary' over the longer term, most likely when the industry matures and becomes more commercially viable. At present, there is no published literature that quantitatively assesses the potential of the Humber Estuary for modern tidal stream developments, despite its known strong flows, commercial endorsement and maintenance infrastructure via Hull Docks. There is significant scope for arrays of small-scale floating TSTs along the estuary, powering local businesses in close proximity to the banks of the Humber or feeding into the national grid. In the future, utilising this technology could be as commonplace as businesses investing in on-site onshore wind turbines (like Croda Chemicals in Hull) or rooftop solar PV. The estuary also has potential for a prototype testing area in which new designs could be tested in strong flows whilst being sheltered from the very strong storms experienced at other test facilities such as at the European Marine Energy Centre (EMEC) in the Pentland Firth.

3.4.2 Fieldwork Locations

Figure 45 displays the location of the Humber Estuary within the UK and highlights the largest settlements along the estuary for reference. It shows the location of the three main fieldwork locations. The boxes surrounding each of these locations are the boundaries of the subsequent higher-resolution bathymetric maps of each site. Numerous sites were only accessible along the estuary using a rigid inflatable boat (RIB) which was used extensively during all fieldwork. The boat and crew availability, stage of the lunar tidal cycle, stage of the semi-diurnal tidal cycle (in terms of daylight) and weather conditions were important factors in choosing fieldwork dates. All fieldwork started and ended at the slipway at Hessle Foreshore.

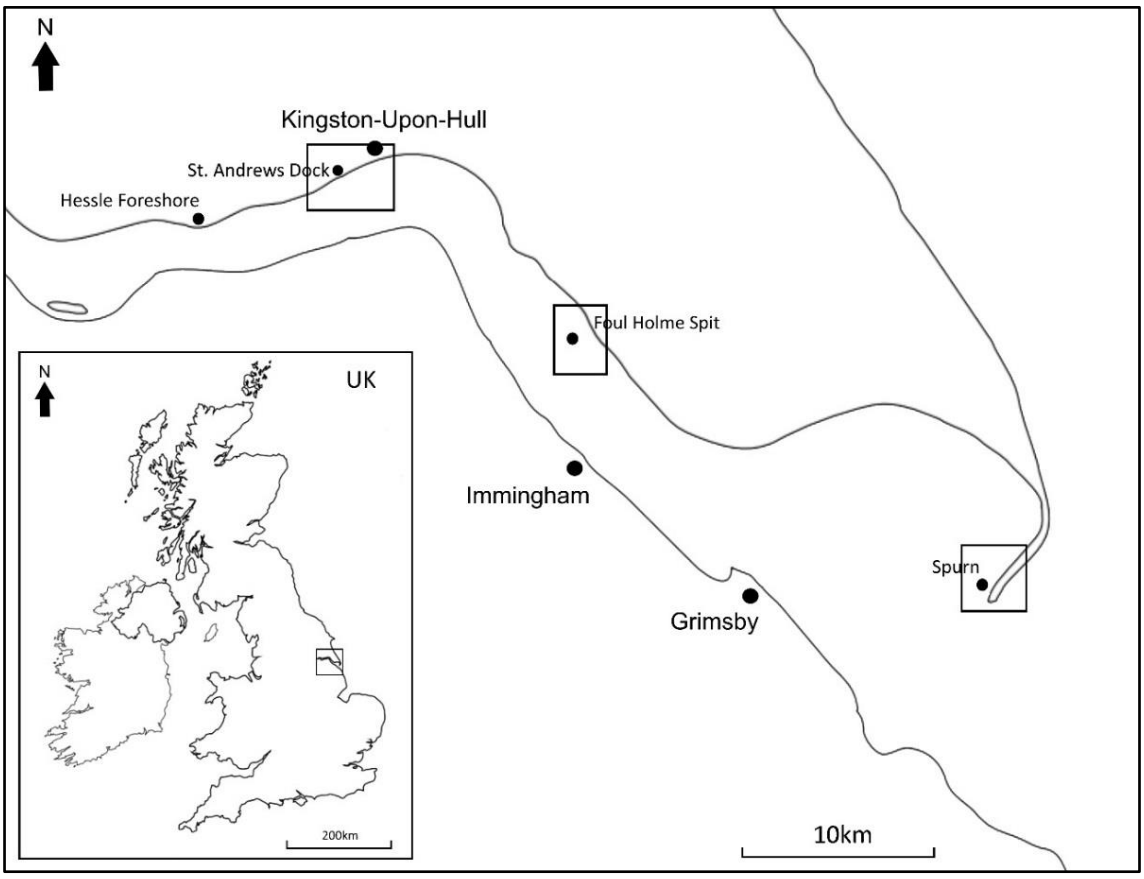

Figure 45: Map of the Humber Estuary and fieldwork locations.

3.4.2.1 Spurn (DWR Pilot)

Many of the bedforms and sand banks in the inner estuary are highly dynamic and are, therefore, unsuitable for long deployments of bed-mounted instruments, as they are likely to become buried under deposited sediment within a short space of time; similarly to the reported case of a bed-mounted ADCP becoming buried in the Dee estuary by Simpson *et al.* (2004). Sand banks in the middle and outer estuary are less dynamic and generally maintain their shape month to month. Most sand banks are particularly difficult to reach by road but a variety of sites on the estuary can be accessed proficiently by RIB; though, without a crane there was no means to safely deploy and recover seabed-mounted instruments in water below chart datum. This meant that a site for a deployment of a seabed directional wave recorder had to meet the following criteria:

- The site had to be dry at a very low water during a Spring tide. This would allow a deployed DWR to remain submerged and record throughout the following Spring-Neap cycle before it then being recovered at a suitably low water of a following Spring tide.
- Due to health and safety precautions, the site also had to be predominantly sand as opposed to mud, which is difficult to move in, and had the potential to swallow the device.
- As a result of the busy port industry in the area and numerous sub-bed pipelines, ABP (Associated British Ports) must also permit all potential obstructions placed within the estuary and issue a 'Notice to Mariners' which again limits the sites available for sea-bed mounted devices for extended durations.

It was agreed with ABP that a sheltered site on the estuary side of Spurn would be used as a pilot deployment of the device. This pilot aimed to test a sampling regime and deployment setup for a future deployment in a more suitable location. Methodologies were also considered to deploy the kit at a fixed position above the bed and closer to the surface at high water, in order to position the device at a possible hub height of a floating TST. This was envisioned to be upon a ladder fixed to a jetty or tidal marker within the Middle estuary. However, after a recce of the Humber in the RIB, no suitable fixed position was available and without the availability of a tidal tripod (as used by Thomson (2011) and McCaffrey *et al.* (2015)) no method to deploy the DWR higher in the flow was possible.

The site chosen for the pilot deployment is shown in Figure 46. There is a steep drop off into the dredged channel to the south of Spurn Point which is used by commercial vessels. To the north-west, there is a vast expanse of sand and mud known as

Spurn Bight, which dries at the low water of a Spring tide. A sandy location at the water's edge of the low water of a Spring tide was used for the deployment. This was also very close to the tidal gauge situated at the pilot jetty of Spurn Point allowing for comparisons with estimates from TotalTide.

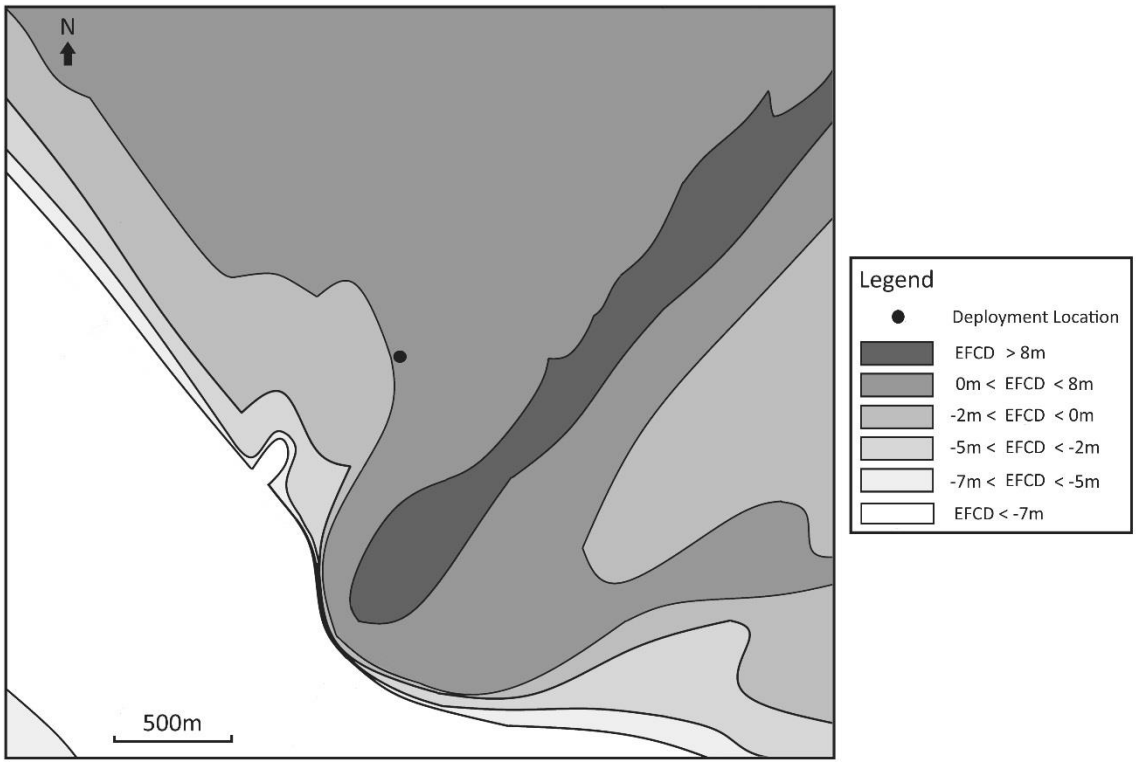

Figure 46: Location of the pilot deployment at Spurn. Bathymetry is illustrated as elevation from chart datum (EFCD).

3.4.2.2 Foul Holme Spit (DWR)

After the pilot deployment, three sites were identified within the middle and outer estuary as being more suitable for a longer deployment to capture suitable simultaneous measurements of currents and waves. The first was Burcom Sand, close to the site of the previously deployed Pulse Stream 100 TST; however, during a recce it was discovered that it did not fully emerge at low water (as the most recent nautical charts suggested it would) and that it was particularly rocky (making a landing from the RIB unsafe). The second was Haltom Flat, a large intertidal sand bank west of the main channel close to Saltend. This site emerged at low water but the deployment was eventually denied by ABP due to potential interference with underlying gas pipelines. The third site was Foul Holme Spit, a short spit of sand on the northern bank that extends out into the main channel from Foul Holme Sands, 2 km north from the Port of Immingham. The spit is predominantly made up of rippled sand and extends far enough into the estuary to capture wave-current interaction free from shoaling. The site was permitted by ABP and the fieldwork was

carried out on the next suitable Spring low water. The Port of Immingham contains a tidal gauge used to estimate tidal heights throughout the estuary, which meant that accurate predictions of tidal height and estimates of flow velocity and direction could be obtained relatively close to the site for comparisons with observed results. The port also contains a weather station; therefore, readings for atmospheric pressure, wind speed and direction were collected throughout the deployment to compare meteorological parameters with observed results.

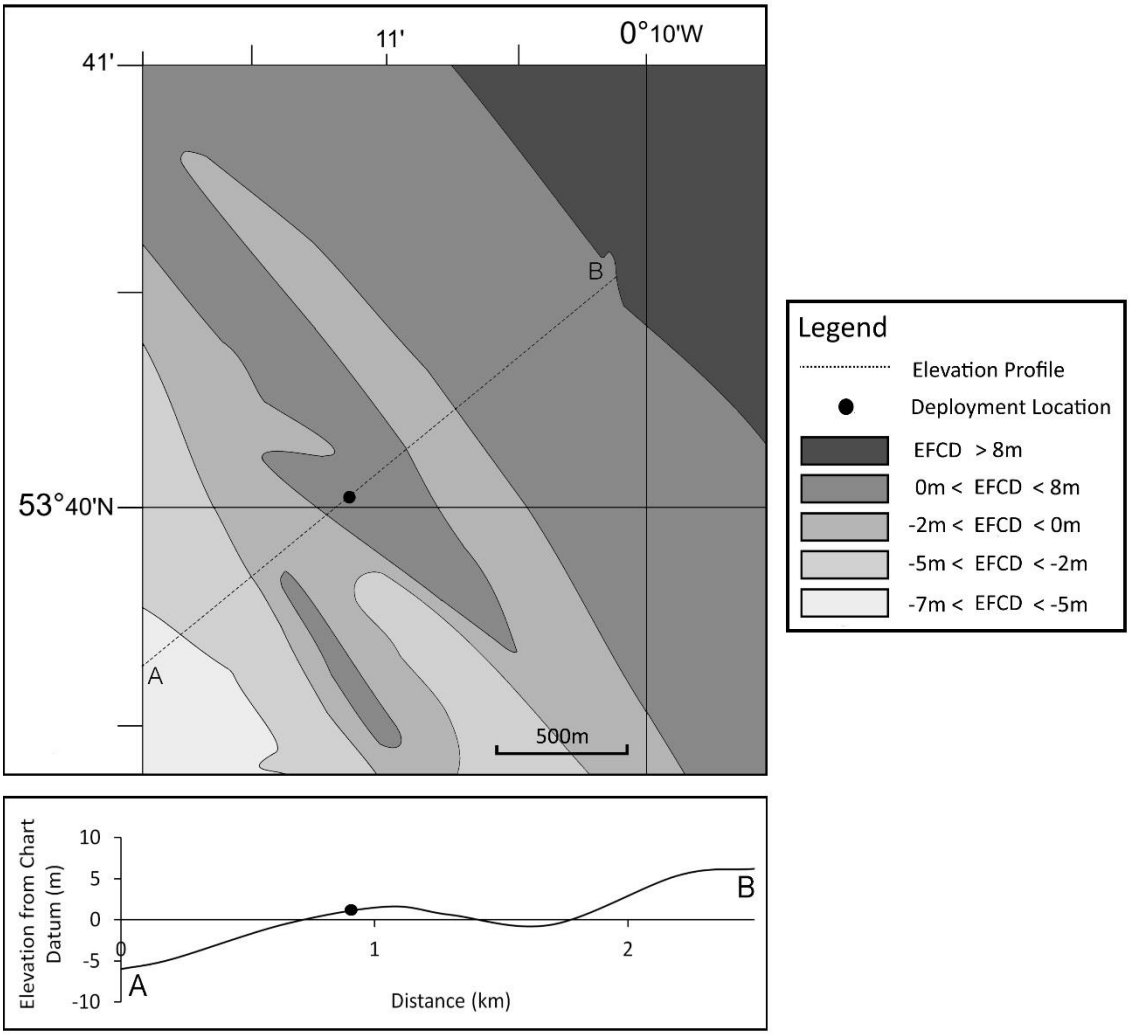

Figure 47: Location of the deployment at Foul Holme Spit. Bathymetry is illustrated as elevation from chart datum (EFCD).

3.4.2.3 St. Andrews Dock (ADCP)

The chosen ADCP static survey site was located in the deep-water channel close to the now derelict St. Andrews Dock. This location was previously identified as a possible site for the Neptune Proteus TST demonstrator device in 2012 due to:

- Estimated strong velocities of around 2 ms^{-1}
- Proximity to industry and electricity substations
- Distance away from the main shipping routes

The site is within the 'Northern Channel', which flows on the outward bend of the large meander between Hull and Immingham. South of this channel is a large sand bank known as Hull Middle and south of that is another deep channel known as 'Skitter Channel' which is used by large vessels (Figure 48).

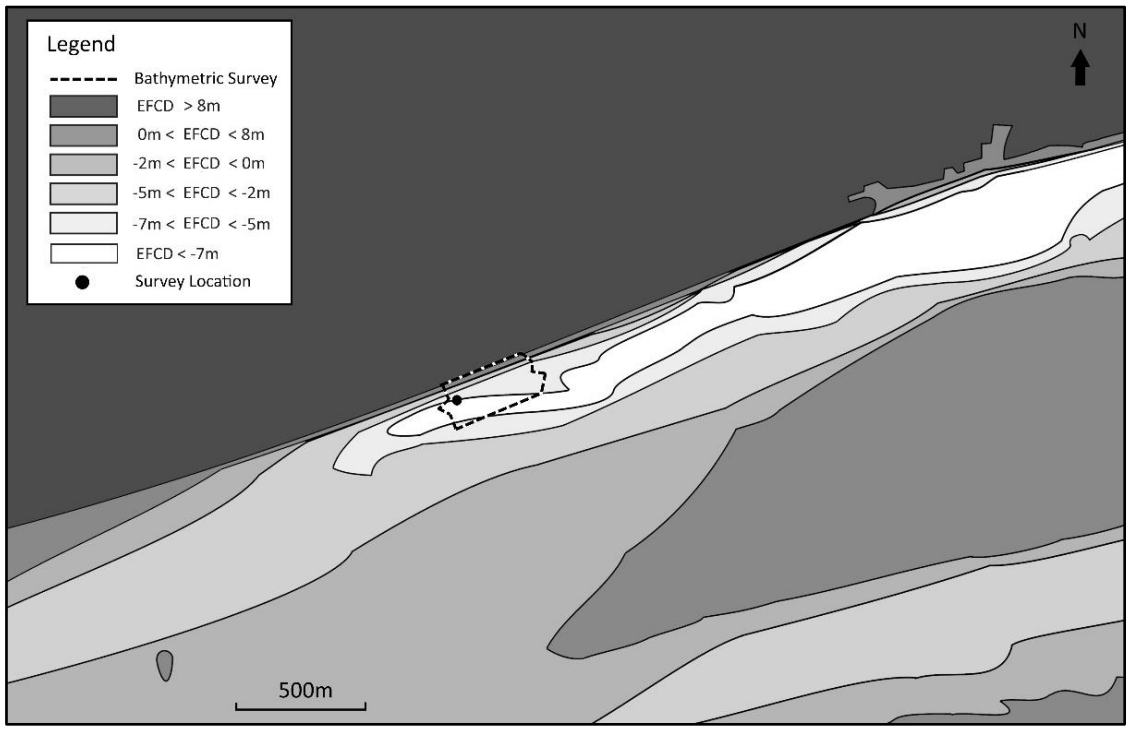

Figure 48: Map of survey location based on 2015 admiralty charts. Bathymetry is illustrated as elevation from chart datum (EFCD).

During the planning of the Neptune deployment, ABP carried out bathymetric surveys of both the St. Andrews Dock and River Hull sites using multi-beam echo sounders (Figure 49). The survey profile shows a steep drop off from the shoreline to the deep channel of about 7 m depth below chart datum. Beyond this step, the bed is relatively flat for 150 m varying only 0.3 m in depth in places. There is no evidence of large-scale geomorphological features such as dunes or upstream boulders generating localised eddies or back-flow in the measured area (as was identified in the site monitored by Jeffcoate *et al.*

(2015)). Beyond the initial bathymetric surveys, no *in situ* velocity data were ever collected here making it an ideal place to collect data in order to model the mean and turbulent flow regimes at the site with the view that it may be used to verify the suitability of the site for a future tidal stream development.

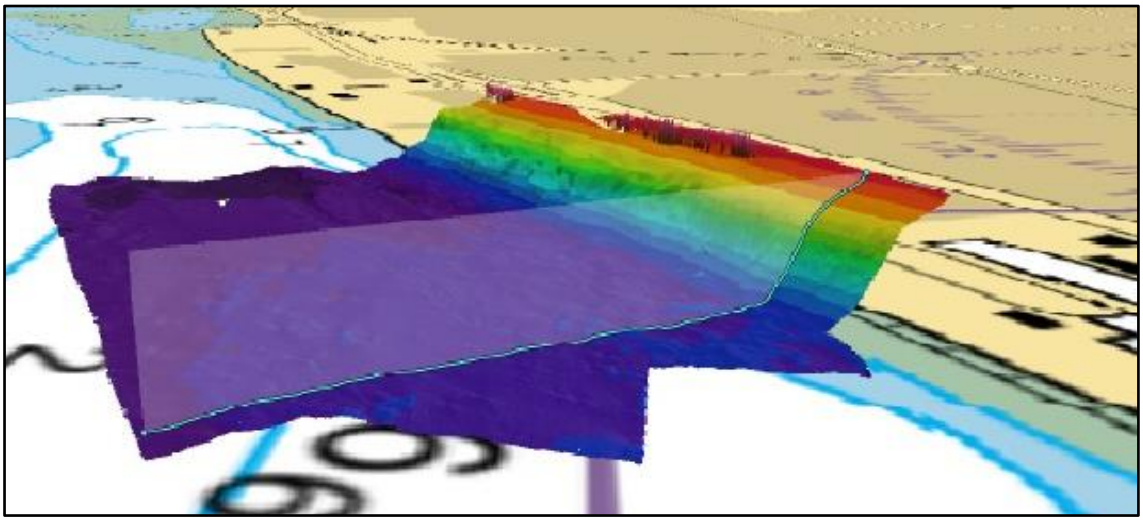

Figure 49: Bathymetric survey by ABP at St. Andrews Dock (Edited from ABP, 2012).

3.5 DWR Fieldwork

3.5.1 Introduction

The main aim of the DWR deployments was to collect high-frequency tidal stream flow data to investigate the relationships between mean flow velocity, turbulence strength and intensity at a point in both calm and stormy conditions to meet Objectives 1 and 2. Two separate deployments of the Valeport MIDAS Directional Wave Recorder (DWR) are described here in detail. This includes a pilot deployment at a sheltered site at Spurn Point and a longer deployment further upstream at Foul Holme Spit of which the following results, analysis and discussion chapters are concerned. This section ends by describing the methods used in post-processing the collected raw data.

3.5.2 Pilot Deployment and Recovery at Spurn Point

3.5.2.1 Introduction

The sand promontory at the mouth of the Humber (Spurn Point) was chosen as a site to run a pilot deployment of the DWR device. This tested a methodology for deploying the device within a sheltered site over a Spring-Neap-Spring cycle to ensure the device recorded as programmed and that the anchoring methodology held the device in place. The method involved deploying the device on the seabed close to the water's edge during the low water of a Spring tide and leaving it to record in sampling bursts for 18 days (Figure 50). This ensured the device remained submerged during the following Neap tides, even at low water. This was the only way to guarantee the device was submerged at the greatest number of samples throughout a Spring-Neap-Spring cycle without using a larger boat with a crane to deploy in deeper water.

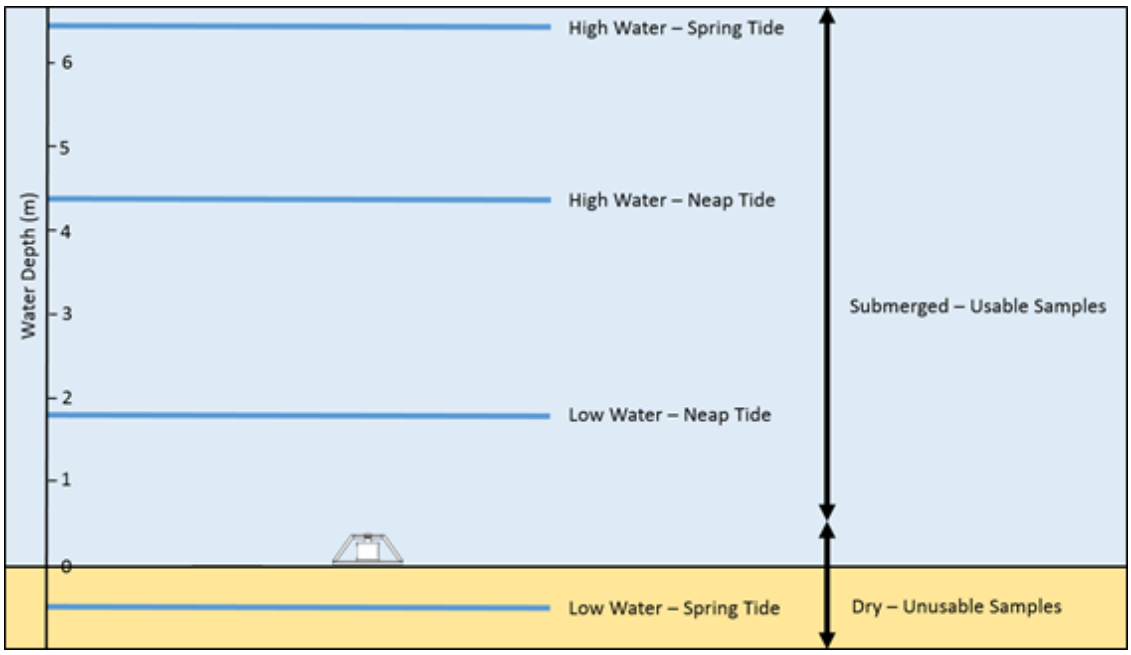

Figure 50: Diagram of water depth above deployed DWRs during stages of the tide.

3.5.2.2 Identifying suitable deployment date

TotalTide was used to identify the start of a Spring-Neap-Spring cycle where the device could be placed close to chart datum at low water and remain submerged throughout Neap tides until the following Spring tides where it could then be recovered. The low water of the tidal cycle during 4th March meant that when the device was deployed at the water line it was approximately 1 m above chart datum. The red line, therefore, gives a prediction of the devices position above chart datum throughout the deployment and thus all recorded water depths would be based on being recorded at this height.

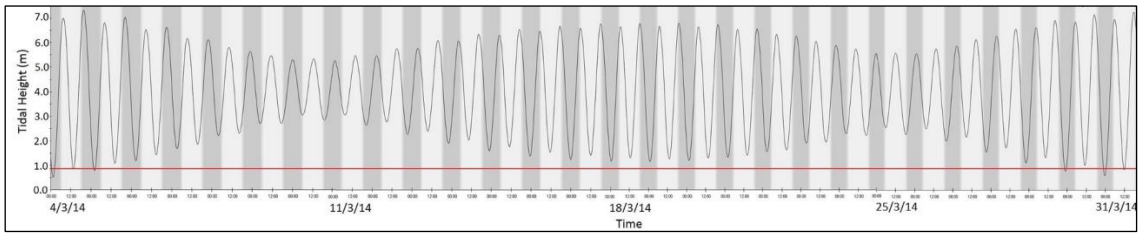

Figure 51: TotalTide prediction of tidal height throughout the deployment at Spurn Point between 4th and 31st March.

3.5.2.3 Sampling Strategy

As the device was going to be deployed for around 30 days, the maximum battery and memory life were desired whilst still recording at a suitably high sampling rate, duration and interval. Therefore, the maximum of 32 1.5 V alkaline D-cells were inserted into the base of the device (Figure 52). Lithium batteries with longer battery lives that can also be recharged could also be used but are significantly more expensive and were not available at the time.

Figure 52: Battery configuration of the Valeport MIDAS DWR using 32 1.5 V alkaline D-cells.

A sampling rate of 4 Hz was decided to be sufficient in order to observe the profiles of individual waves in the Humber Estuary, which has low period waves (~1-4 seconds). This is similar to the rates used by other wave-current studies using EMCMs such as Lambrakos *et al.* (1988), Soulsby and Humphrey (1990), and Powell *et al.* (2000). The higher rate of 8 Hz was tempting for increased temporal resolution but this would have halved the overall measurement duration meaning that had the first half been calm and the second half stormy important wave-current interaction events would have been missed. The EMEC standards (EMEC, 2009) suggest waves are measured at 5 Hz but the device only operates in powers of two. Therefore, as 4 Hz was closer to 5 Hz than 8 Hz a longer deployment was decided to be more desirable than higher frequency samples. A tidal burst interval of 10 minutes and a wave burst interval of 20 minutes for a duration of 1024 samples meant that the on-board memory would last 18 full days, enough to cover a Spring-Neap-Spring cycle. By recording in short sample bursts the sampled time series data were considered stationary and would not need to be detrended, as McCaffrey *et al.* (2015) suggests. All available parameters were checked as "Save" and "Output" as suggested in the manual (Valeport, 2008).

3.5.2.4 Deployment and Recovery of Device at Spurn

Due to the breach in the road caused by a storm surge at Spurn Point in December 2013 the only access to the deployment site was via boat. A RIB was used to transport the device and four crew from the nearest available launching site at Hessle Foreshore to Spurn, approximately 40 km downstream (Figure 53). At Spurn Point the device was positioned at the waterline at low water. Anchors were attached by chain at each corner of the steel frame and positioned 5 m away to keep the device and the sensor head level throughout the deployment. Steel pigtail rods were also inserted into a number of holes on the base of the device to further secure it in place. A marker buoy was attached by rope in order to alert mariners to the devices position thus avoiding collisions or nearby trawling. Thirty days later the device was recovered from Spurn Point during the low water of a Spring tide equivalent in range to the one in which it was deployed. The device had not moved at all and all anchors were recovered successfully. The rope of the marker buoy was snagged on an anchor meaning the buoy was most probably submerged at high water.

Figure 53: Photographs of: The RIB being lowered into the Humber Estuary from Hessle Foreshore beneath the Humber Bridge, the DWR deployed at Spurn Point and the device after being successfully recovered.

3.5.2.5 Limitations of the Pilot Deployment

The stored binary data were downloaded using WaveLog Express. Due to selecting the 'Output' setting in the sampling set up screen prior to deployment, the device had attempted to post-process the data whilst deployed and as a result had only collected data during the first 21 hours under calm conditions, thus rendering it useless to further analyses in terms of the research objectives. Also, from the 63 samples that had recorded, it became evident from the tidal summary files that the direction of flow was approximately 90 ° greater than expected, which suggested that tidal flows were moving onshore-offshore as opposed to downstream-upstream, which could not be correct. Outputted wave direction was as expected given the local wind direction. As the device failed to record for the expected number of samples the device had to be tested and calibrated in a controlled environment to determine whether it was the device or the software generating this error and to determine why the tidal direction was 90 ° out. The DWRs dimensions meant that it was too large to fit within the channel of the flume at the University of Hull but it could fit within the water tanks beneath (Figure 54).

Figure 54: Testing the flow direction output of MIDAS DWR in uni-directional flume.

New batteries were fitted, and a new sampling regime was configured which did not have the 'Output' option selected (as advised by Valeport). The device was placed in the tanks below the departmental flume and a hosepipe was used to create a uni-directional flow of water with arbitrary velocity. The flow was directed from the west (270 °) but the device later outputted a summary file stating a tidal flow direction of 180 °. Valeport were

contacted and after confirming that the device itself was not faulty, via a number of component checks, a fault was eventually identified within the Wavelog Express software code by the developer. A new version of Wavelog Express was subsequently rolled out that fixed the issue.

This pilot study, therefore, highlighted the trepidations of using state-of-the-art instrumentation, as it was clear that the device and bespoke software had not been adequately tested prior to sale. It was also revealed that the deployment methodology was a success in that the device remained in position, though the marker buoy would have to be modified to prevent it from snagging in future deployments.

3.5.3 Foul Holme Spit Deployment and Recovery

3.5.3.1 Introduction

A more suitable location upstream from Spurn was identified for a second deployment (Foul Holme Spit), where stronger tidal currents and larger waves were likely to interact. This deployment utilised two available, identical devices to act as redundancy should one fail but also to be used to compare and validate results. This section will describe the changes made to the pilot methodology and describe the deployment and recovery process.

3.5.3.2 Redesign of Deployment Methodology

Due to a number of minor issues that occurred during the pilot deployment and with the next intended deployment in a more energetic site with expected stronger flows and larger waves, the deployment design was subtly modified (Figure 55). A second, identical, device was incorporated into the design as a back-up should one of them not record as intended (as occurred in the pilot deployment). A larger marker buoy with a flashing light was purchased, as required by ABP for upstream deployments, and attached to the devices by a 10 m chain instead of rope. A screw anchor was positioned in the centre of the design and used to secure the buoy to the centre of the deployment layout. Four, 2 m chains were then fastened and pulled taught from the screw anchor and connected to the corners of each steel frame closest to the centre-point. The corners furthest from the centre were connected to 5 m chains that were pulled taught and connected to Danforth anchors, as opposed to grapple anchors, in order to prevent snagging the buoy or other debris. This design was envisioned to fasten the devices even more securely to the bed than in the pilot deployment and minimise device tilt, which could lead to errors.

Figure 55: New deployment design laid out on grass incorporating two DWRs and marker buoy.

3.5.3.3 Identifying Suitable Deployment Date

As with the pilot deployment, TotalTide was used to identify a particularly strong Spring tide in which to deploy the devices as close to chart datum as possible. This would ensure the maximum number of useable submerged samples. The deployment was anticipated, then, to be performed on 13th August 2014 with a subsequent recovery on 11th September 2014, weather permitting. Wind speeds were too high to deploy safely on the 13th August 2014; therefore, the device was actually deployed a day later but recovered on the foreseen date. Finding the balance between recording strong flows during increased wave conditions within appropriate depths of water meant that a longer recording duration was necessary to measure a period of increased wave activity. The battery configuration of the device significantly limited deployment duration. Whilst a storm was more likely to be captured during Winter or Spring months, when wind speeds are often increased, there was also the requirement for calm days during the right tidal conditions in order to carry out the fieldwork safely using the RIB. It was then considered that if the August deployment captured a good range of calm and increased wave activity then it would be used for analysis. If the wave data were too calm, a further deployment would be carried out during the following Winter or Spring, though at a greater risk of fieldworks being cancelled due to unsuitable weather conditions during deployment and recovery windows.

3.5.3.4 Priming Devices with Revised Sampling Regime

The device was again fitted with 32x 1.5 V fresh alkaline D-cell batteries. The sampling rate remained the same as in the pilot study except that the 'Output' option was left unchecked meaning that the device would not post-process the sampling data *in situ* and would only store raw binary data (to later be translated by the software). Again, the device estimated a memory life of 18 days and a battery life of 34 days at this configuration, ensuring sampling throughout a Spring-Neap-Spring cycle. The instrument clock for both devices was synchronised to the PC's time and a delayed start-time was programmed to ensure both devices would start recording synchronously only when deployed. This guaranteed maximum-recorded data given the limited battery life and memory.

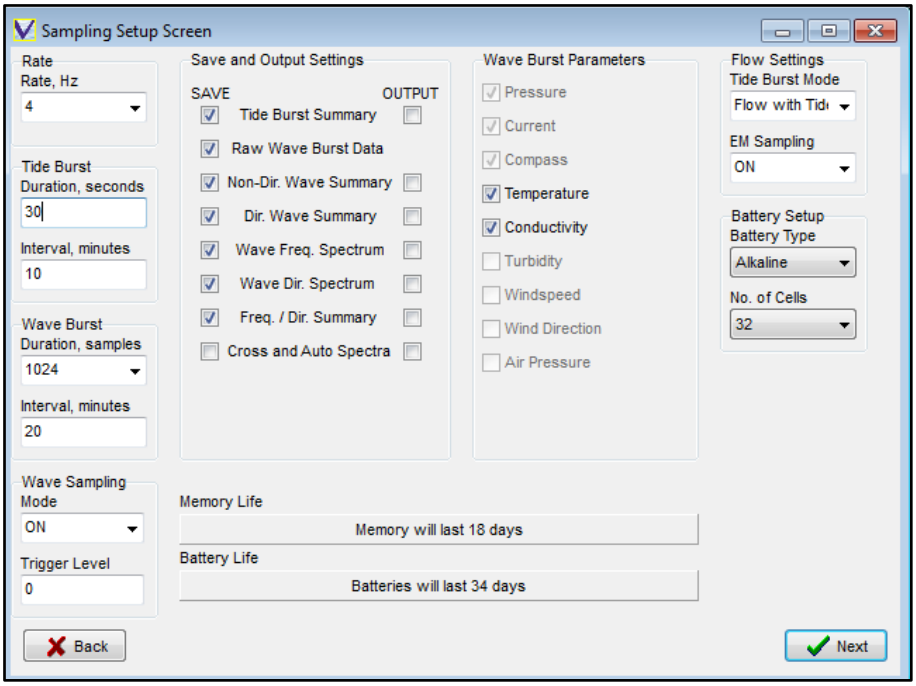

Figure 56: Valeport Wavelog Express sampling setup screen displaying deployment criteria used at Foul Holme Spit.

3.5.3.5 Deployment and Recovery of Devices at Foul Holme Spit

Foul Holme Spit extends from the bank into the channel meaning that it can be accessed via road, though it was not feasible to carry/transport the instruments over the harsh terrain to the water's edge; therefore, the RIB was again used to transport all equipment and crew from Hessle to the site approximately 24 km downstream. The devices were deployed in the same configuration as in (Figure 55). Devices were positioned about 0.5 m above the low water line as the slope of the sandbar close to the waterline was relatively steep and may have caused tilt errors. The bed was very flat mainly consisting of rippled sand.

Figure 57: Devices deployed at Foul Holme Spit.

Upon recovery, it was discovered that both devices had successfully remained in position. However, the chain from the marker buoy had become snagged on one of the devices EMCM sensor head and one of the pigtail pins and had caused the steel frame to rotate into the sand, thus creating significant tilt and potential errors (Figure 58). From this point on, the device that remained correctly orientated was named Device 1 and the device that had sunk into the sand was named Device 2.

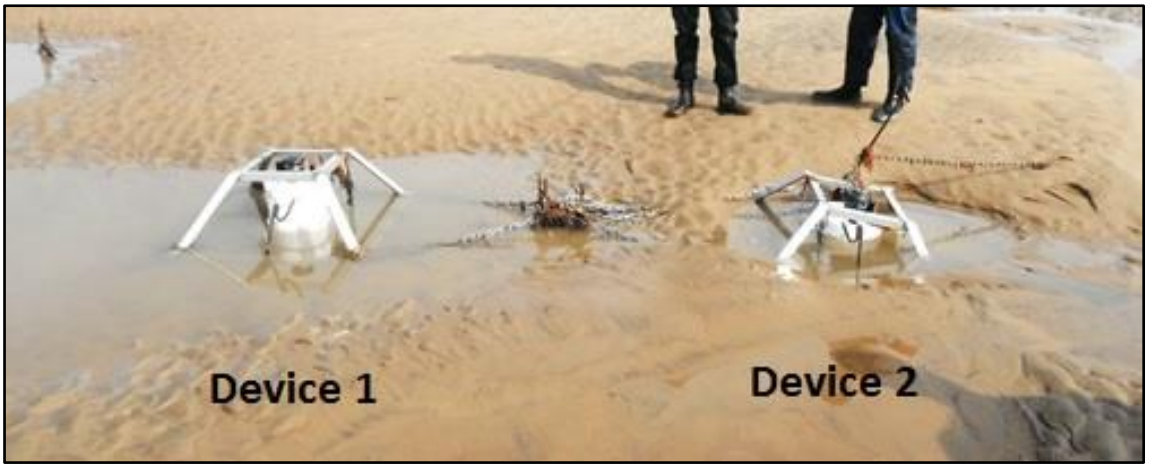

Figure 58: Devices recovered from Foul Holme Spit after 29 days.

3.5.3.6 Meteorological Data

During the deployment duration, local weather data was monitored and recorded at Immingham Dock just 2 km south using 'World Weather Online' which outputted 3-hour averages of atmospheric pressure, wind speed, direction and temperature. These data were used to anticipate which days were likely to have increased wave activity during the deployment but were not suitable for accurately calculating expected wave parameters.

3.5.4 Data Processing, Validation and Analysis

3.5.4.1 Data Processing

Both devices were connected to Wavelog Express and the data were downloaded and translated from binary to text. It was discovered that on this deployment both devices had successfully recorded flows as planned. This process generated raw data files of each wave burst, summary files of each tidal and wave burst, spreading files, directional spectra and non-directional spectra. In order to generate surface recreation files and wave spectra, the raw files that had been generated in the translation had to be post-processed using the 'Open Raw Files to Post-Process' function. The generated summary files, raw files and surface recreation files can all be viewed as time series within the WaveLog Express software. However, the data visualisation options are limited. Therefore, all data were imported into Excel for further post-processing and visualisation (Figure 59).

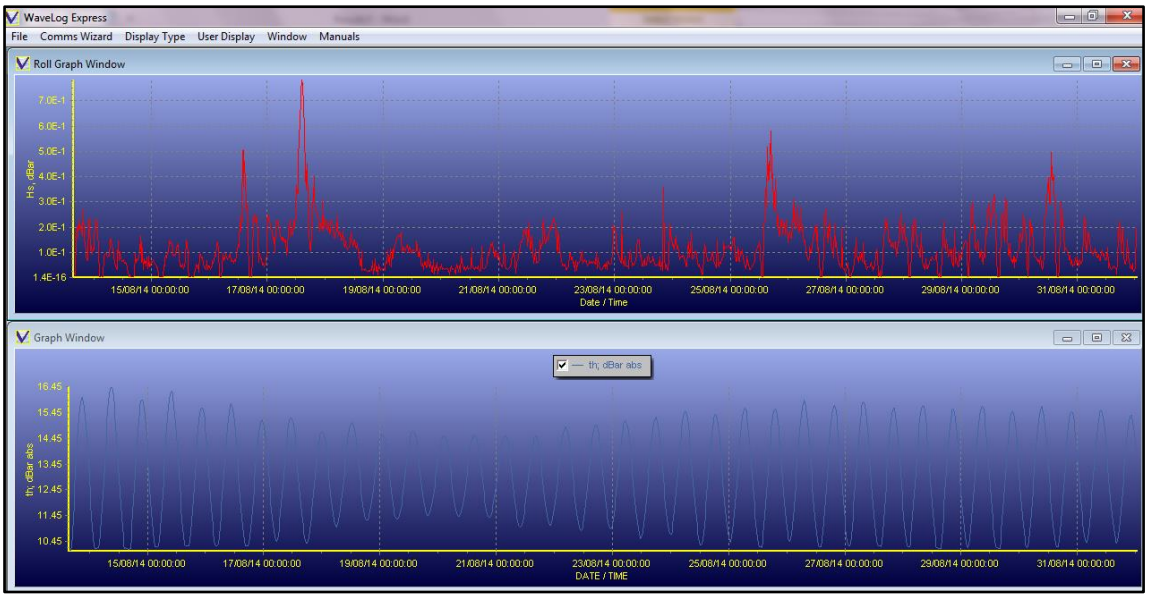

Figure 59: Summary tidal and wave files viewed in WaveLog Express.

3.5.4.1.1 Cleaning the Summary Files

Whilst the majority of the collected summary files contained expected figures, some files contained spurious values and therefore required cleaning.

During the Spring tides, the device emerged briefly at low water. The tidal and wave sample bursts during this period were identified by sudden drops in recorded conductivity within the tidal burst summary files as the sensor dried out. The values for tidal and wave parameters during these durations contained erroneously high results which were removed from the dataset thus generating lacunas during some Spring low waters.

Some wave parameters also contained erroneously high results such as wave periods above 60 seconds. These errors occurred during periods of low wind speed and high water which suggests the device could not generate a reasonable prediction of wave period and thus gave an erroneous result; these were subsequently removed from the dataset.

Tidal current velocity outputs were all positive; therefore, for a better representation of the sinusoidal Spring-Neap pattern, Ebb currents were made negative.

3.5.4.1.2 Cleaning the Raw Wave Burst Files

Outside of dry periods, or very calm conditions, just four bursts were identified as containing erroneous flow data (wave bursts 125, 262, 263 and 264). These bursts contained sporadic values in both *u* and *v* velocities that skewed calculations of the mean and standard deviation of flow (see section 3.5.4.3). These bursts had accelerations between velocity data well above reasonable values. The greatest accelerations were close to gravitational acceleration (9.81 ms^{-2}), which could not have occurred naturally given the context. Outlying velocity data were removed from the four wave bursts if their value was above two standard deviations of the mean. This method appeared suitable for burst 264 as only 43 data points were considered outliers (out of 1024). However, for bursts 125, 262 and 263 the majority of data were considered too noisy for treatment as around one third of data had erroneous accelerations between measurements, thus significantly reducing the number of data points used to calculate the standard deviation and mean. These three bursts were subsequently removed from any further analysis. It is thought that the device was either bio-fouled (covered in seaweed) or entangled in the marker buoy chain during these bursts, as all preceding and subsequent bursts appeared to be free from similar errors. Black *et al.* (2015) found that seaweed snagging and collisions caused anomalous, large-amplitude spikes in data from an ADV but states that there is no accepted standard for dealing with such anomalies.

3.5.4.2 Data Validation

A number of validation methods were used to test the validity of the Valeport devices data. As two devices were used, the output files from each device were tested against one another. The devices were positioned very close together and recorded at exactly the same time suggesting that all data collected by the devices would be very similar and, therefore, have a very strong linear relationship between identical variables. As one of the devices was found to have tilted during the deployment it was hypothesised that there would not be a linear relationship between variables such as tidal mean flow because of the errors induced

by the tilted EMCM sensor. The data retrieved from Device 1 was subsequently tested against modelled data generated within TotalTide at the Immingham tidal station. Although the device was positioned 2 km away and recorded close to the bed it was hypothesised that there would still be a reasonably good relationship between the modelled and observed data. The results of these validation tests are presented in sections 4.2.1 and 4.2.2.

3.5.4.3 Data Analysis

In order to test the relationships between turbulence strength, intensity and mean current velocity for Objective 1, the standard deviation and mean average of each of the raw wave burst data files were calculated using an Excel Macro. To model the influence of surface waves on these relationships for Objective 2, the turbulence spectrum was derived from the wave burst files using a Fast Fourier Transform and visualised using ggplot2 within RStudio.

Two methods of regression were used to test the relationships between mean current velocity and turbulence metrics. Linear regression was used to test the 'straight-line' relationship between the dependent variable (turbulence strength/intensity) and independent variables (mean current velocity, surface wave metrics). The goodness of fit was tested using the R^2 coefficient of determination and statistical significance tested using the p-value which are commonly used statistical methods. Where R^2 value was not strong and the relationship appears curved power regression was used to determine if a better goodness of fit exists. These methods provide coefficients and constants for simple models that could be used by the tidal power industry to predict turbulence at sites where only the mean current velocity can be estimated. If relationships are not evident higher order multinomial regression methods can be used to determine more complex relationships though previous data provided in the literature suggests that these may not be necessary.

3.6 ADCP Fieldwork

3.6.1 Introduction

The main aim of the ADCP static surveys at St. Andrews Dock was to model the relationships between mean flow and turbulence metrics through depth between semi-diurnal tidal cycles for Objective 3. Two types of ADCP were used with a RIB to measure flows across Ebb and Flood cycles during a Spring tide and a Neap tide. Tidal flows had previously been observed to peak approximately halfway between high and low water at this location. As vessel-mounted ADCPs require calm conditions in order to obtain accurate binned data, all surveys were conducted during periods of very low wind speed to avoid interference from surface wave activity. The following section provides further details of the fieldwork methodology including date selection, setting up the ADCP, carrying out the survey and data processing and analysis.

3.6.2 Date Selection

The dates chosen to survey relied on four criteria; stage of the tide, hours of daylight, weather conditions and boat/crew availability. It was important to monitor the flows during both the Spring tides and Neap tides to analyse a broad range of tidal heights and flow velocities. These dates also had to coincide with calm weather conditions (as ADCPs do not give good results when waves cause the instrument to excessively tilt) and because of the length of time the crew would have to endure increased wave activity. It was also important that the tides coincided with daylight for navigation purposes and crew availability; for health and safety, there had to be a minimum of two crew on-board with the relevant qualifications to skipper the boat at all times. Admiralty TotalTide was used to predict tidal heights throughout April and May, which revealed suitable dates and times for fieldwork. Weather forecasts were monitored and a number of suitable days in regards to tidal stage were unsuitable because of anticipated high winds. This ultimately resulted in Spring tides being surveyed between 09:00 and 19:00 during 19th April 2015 and Neap tides being surveyed between 09:00 and 20:00 during 13th May 2015.

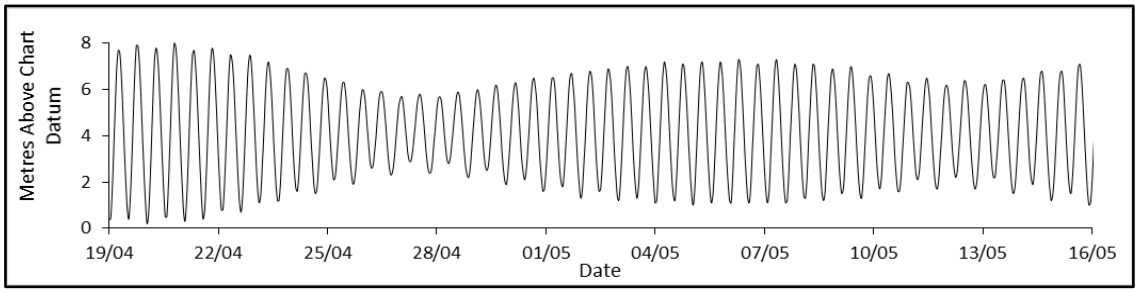

Figure 60: Predicted tidal heights at nearby site using TotalTide.

3.6.3 ADCP Setup

Two types of ADCP were used during the fieldwork (due to availability). During the surveying of the Spring tides a Teledyne Workhorse 1200 kHz ADCP was used whilst during the Neap tides a Teledyne Workhorse 600 kHz ADCP was used. Both devices were deemed suitable for the site dimensions; however, the 600 kHz appeared to perform better in the sediment-laden flows than the 1200 kHz.

On both survey days, the available ADCP was connected to the boat on the port side using scaffolding poles which could pivot into transit and recording positions (Figure 61). In its recording position (beam 3 facing incoming flow) the sensor head was positioned perpendicular to, and approximately 1 m below, the water surface. This meant that it was positioned away from any flow conditions induced by the boat or short-period surface waves.

Figure 61: Photograph of vessel-mounted ADCP setup in the field.

The ADCP was powered and controlled from a custom-built power box, a schematic of which is presented in Figure 62. The box was designed as a portable, waterproof case that housed all of the components needed to perform the ADCP survey. It contained a laptop installed with WinRiver II, a USB external monitor, an uninterruptable power supply (UPS), an inverter, a consumer unit, a 4-port COM replicator and a 4-way USB 3.0 hub. The setup was powered by an automotive battery which, when fully charged, lasted approximately 9 hours under default configuration. Batteries could be swapped easily without losing power to the laptop or ADCP because of the UPS. As the laptop and internal devices were not waterproof, the box was designed to work both open and closed. In the event of rain or spray from waves, the lid could be closed and the laptop screen would switch to the waterproof external monitor allowing continued observations. Apertures in the side of the box allowed for ventilation when closed and as a hole to pass necessary wires through. The ADCP was connected to both the laptop and the power supply whilst the GPS feed from the boat was connected to the COM replicator through one of the vents.

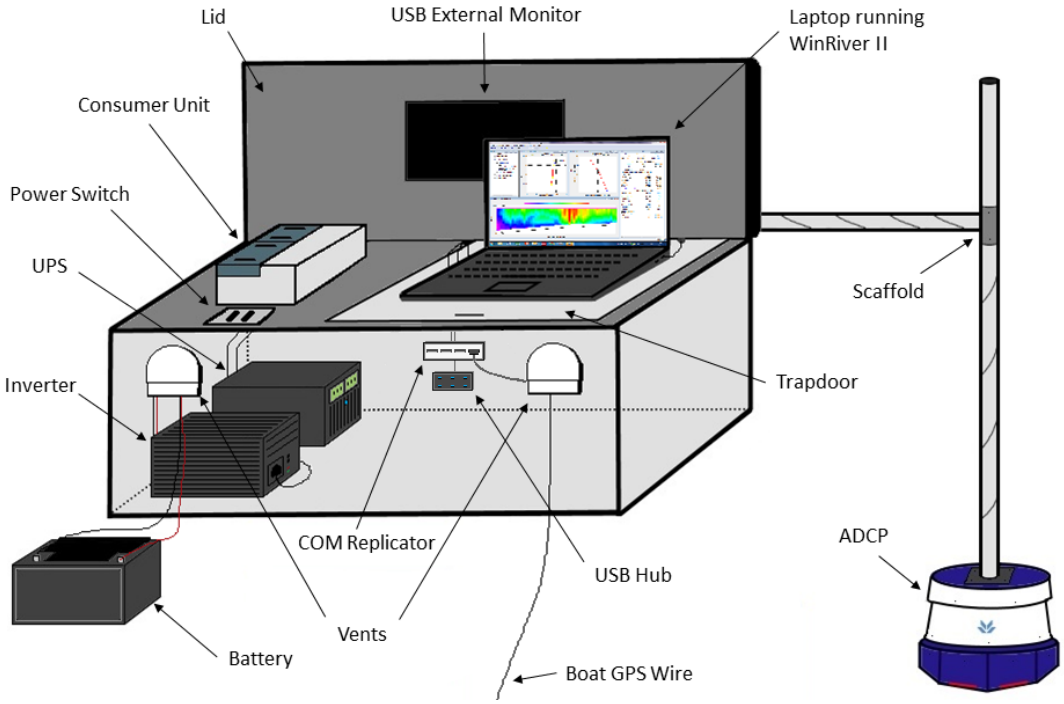

Figure 62: Custom-made power box schematic used to power and control the ADCP from the RIB.

WinRiver II was used to control the ADCP sampling configuration, real-time data collection and post-processing to earth-velocity coordinates. Wave mode 12 (WM12) data collection configurations were used on both occasions with required basic input values such as maximum expected water speed (3 ms^{-1}), maximum expected water depth (15 m) and the depth of the sensor head below the surface (1 m). Bin depths and ensemble

sampling frequency were left as defaults but both were unique to each type of ADCP (0.25 m and 2.33 Hz for 1200 kHz and 0.5 m and 1.075 Hz for 600 kHz) (Teledyne, 2007).

3.6.4 Surveying

One of the difficulties with multiple static vessel-mounted ADCP surveys is positioning the vessel in the same exact spot for each transect. Due to the long duration of the survey, the crew had to have a break halfway through which meant that at slack water the boat would go ashore and come back an hour later and get back into position once the tide had turned but before flow velocities began to accelerate. The problem with keeping a boat in position and accurately dropping a very long anchor chain to the bed meant that the boat was not in the exact same spot for each survey, as Table 9 shows. Due to the bathymetric survey showing a relatively homogenous bed and the fact that the beam spread at the extent of the ADCP configuration is around 2.5 to 5 m (depending on water depth) it was deemed that the transects approximately measured the same location each time.

	Time	Northings	Westings
Spring Ebb	09:00 - 13:00	53 ° 43.7126	0 ° 21.7719
Spring Flood	15:00 - 19:00	53 ° 43.6932	0 ° 21.7722
Neap Flood	09:30 - 13:30	53 ° 43.7163	0 ° 21.7990
Neap Ebb	15:30 - 20:00	53 ° 43.7206	0 ° 21.7516

Table 9: Time and location of each ADCP static survey.

The Spring Ebb flow was surveyed between 09:00 and 13:00 (Figure 63). The boat was then piloted to nearby steps at low water so the crew could have a break between 13:15 and 14:45. The boat was piloted back to approximately the same site and the Spring Flood flow was surveyed between 15:00 and 19:00.

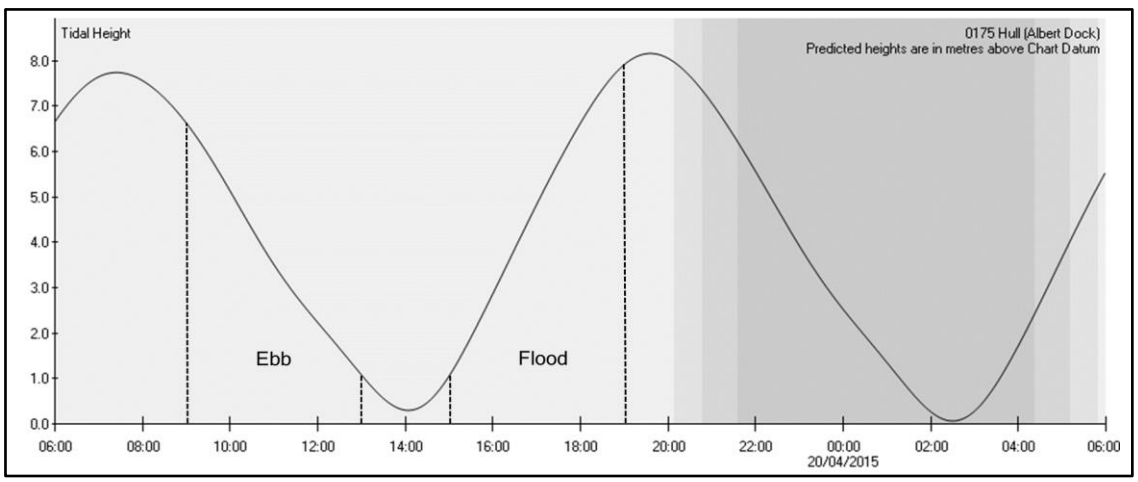

Figure 63: TotalTide prediction of Spring tidal heights at Hull (Albert Dock).

The Neap Flood flow was surveyed between 09:30 and 13:30 (Figure 64). The boat was piloted to nearby steps so the crew could have a break between 13:45 and 15:15. The boat was piloted back to the same site and the Neap Ebb flow was surveyed between 15:30 and 20:00. The boat was eventually piloted back to Hessle foreshore and left the water at 20:30.

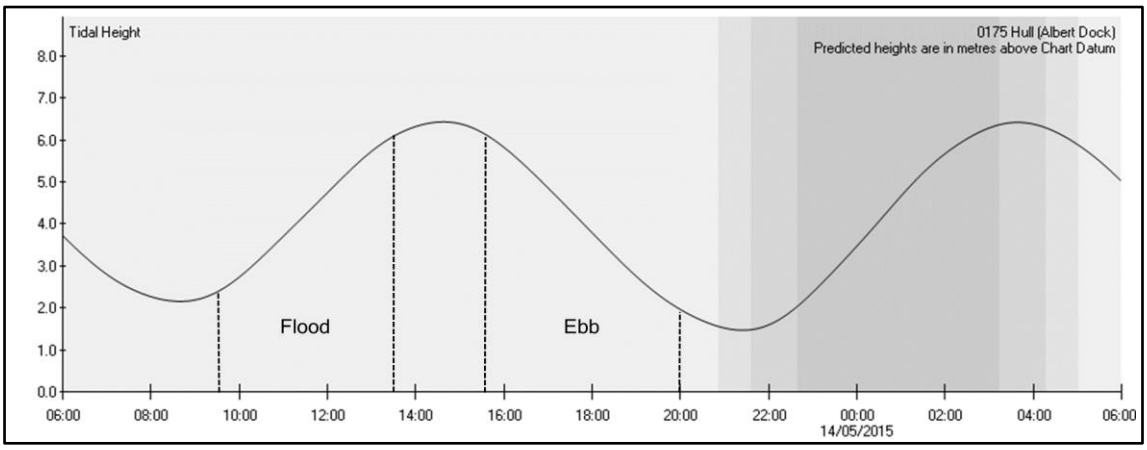

Figure 64: TotalTide prediction of Neap tidal heights at Hull (Albert Dock).

During the first transect (on 19th April) the ADCP collected many 'bad bins' during the first hour which resulted in numerous missing ensembles. From between 09:00 and 10:00 the ADCP did not collect any useable data and, therefore, the ADCP was stopped and checked for fouling and faulty connections. It was restarted at 10:00 and it began collecting a suitable number of ensembles after around 10 minutes. The reason for this interruption is assumed to be that the 1200 kHz could not accurately determine flow velocities through the high sediment density present at the start of the Spring Ebb flow. The bottom tracker could not accurately identify the bottom due to not penetrating the whole water column. The 1200 kHz performed much better during the Spring Flood and the 600 kHz performed almost faultlessly during both the Neap Ebb and Flood tides.

3.6.5 Data Processing, Analysis and Visualisation

3.6.5.1 Data Processing

WinRiver II was used to process and observe the live ADCP output data, but further analysis and presentation options with the software are limited. This meant that the output data had to be exported to and post-processed within Excel and Matlab, which have numerous additional viisualisation and analysis capabilities. The ADCP output data contained many different calculated variables but for the present analysis just four variables were chosen to be exported into an ASCII file which can be exported to other software:

Earth Velocity Magnitude (Ref: VTG), Water Speed (Ref: VTG), Flow Direction (Ref: VTG) and Beam Average Depth.

3.6.5.2 Data Analysis

Matlab code was used to stationarise the time series data from the ASCII files of each transect so that statistically stationary estimates of the mean and standard deviation could be calculated. It was determined that mean velocities and standard deviations remained constant over intervals of 5-minutes, as has been commonly determined by other tidal stream researches (see appendix of McCaffrey *et al.*, 2015). The turbulence intensity was calculated for each 5-minute average at each bin depth. Depth-averaged values for current velocity, turbulence strength and turbulence intensity were then calculated.

3.6.5.3 Data Visualisation

In order to present the time series of current velocity, turbulence strength and turbulence intensity through depth heat maps were generated in Matlab as is the most commonly used method of ADCP data visualisation within recent literature (see Ogalusi *et al.*, 2009 and McCaffrey *et al.*, 2015). These figures contained x-axes of time, y-axes of depth and z-axes of either current velocity, turbulence strength or turbulence intensity using coloured scales. The bottom-tracking values of maximum depth were also plotted illustrating the areas not measured by the ADCP at the surface and at the bed (approximately 1 m).

3.7 Conclusion

This chapter has provided a detailed description of the fieldwork methodologies employed within this thesis, in order to collect appropriate, highly sought-after, *in situ,* tidal and wave data and to meet the three thesis objectives. The Humber Estuary has been shown to be an appropriate site for the fieldwork due to its tidal characteristics, wave climate and practical accessibility. The fieldwork broadly involved the deployment of two DWRs to measure turbulence and wave-current interaction at a point, which involved a pilot deployment at Spurn and a subsequent deployment at Foul Holme Spit. Following this, four static ADCP surveys using vessel-mounted ADCPs collected flow data from a potential tidal stream development site close to St. Andrews Dock to measure turbulence through depth.

The problems with instrumentation experienced during these fieldworks add to the long list of reported issues when collecting *in situ* measurements from difficult marine environments as Easton *et al.* (2012) and Morgan (2014) explain (which is likely to be longer than the published literature would suggest). Leaving a bed-mounted device

recording out of sight for a long period without knowing if it is recording appropriate data is of course a problematic method but, so long as the devices are tested and calibrated beforehand, the risk of this occurring is minimised. In the DWR's case, it was faults within the bespoke software that led to a pilot deployment that yielded unusable data. This ultimately improved the second deployment of the DWRs at Foul Holme Spit, which collected a very robust, detailed and wide-ranging simultaneous wave-current dataset. The issues with the 1200 kHz ADCP during the first survey remain unsolved but it did not affect a long duration of the survey and all subsequent surveys collected 'good' bin data. The following chapter discusses the results of the fieldwork.

4 Results

4.1 Introduction

This chapter presents and describes the data collected by both the directional wave recorder (DWR) and acoustic Doppler current profiler (ADCP) devices prior to the analysis of relationships between variables to meet the three thesis objectives discussed in the following analysis chapter.

The results of the deployment of two DWRs at Foul Holme Spit between 13th August and 11th September 2014 are presented in section 4.2. Results of the preceding pilot deployment are omitted from this chapter for the reasons detailed within the methodology (see section 3.5.2). The available meteorological data from the nearby Port of Immingham is reported first including atmospheric pressure, temperature, wind speed and direction. WaveLog Express was used to process the data collected by the DWRs into summary data files of tidal and wave sampling bursts. A comparison between summary data files outputted by both of the devices is then considered and discussed. It was clear that Device 2 contained numerous samples with spurious data throughout the deployment and a comparison between the devices' datasets showed that, after the third semi-diurnal tidal cycle, data began to vary significantly between datasets. Only the summary data files from Device 1 are thus presented and subsequently compared with modelled results generated by TotalTide. The DWR monitored a range of oceanographic variables including conductivity, temperature, pressure, current velocity, tidal flow direction, and significant wave height, zero crossing period, peak frequency, wave energy and wave direction. Variables such as conductivity and temperature were used to help filter out any erroneous data collected during low water when the sensor head of the EMCM emerged, thus generating lacunas in the time series. OriginPro was used to generate stacked graphs of the meteorological data and the tidal and wave summary data files to visualise the simultaneous results on single x-axes through time. Whilst the device outputted summary files of separate tidal and wave bursts, a final stacked graph shows the calculated mean streamwise current velocity, turbulence strength and turbulence intensity parameters calculated from the raw data, as discussed in the methodology.

The results of the four static surveys at St. Andrews Dock are then presented in section 4.3. WinRiver II was used to collect and process the individual beam data from the ADCPs into ensemble averages throughout the Spring Ebb, Spring Flood, Neap Flood and Neap Ebb tides. The earth referenced velocity magnitude and direction were calculated by the software which took into account the rotation of the vessel and the orientation of the

ADCP to North based on the VTG GPS reference. Acoustic backscatter (ABS) data were also evaluated for erroneously strong signals indicating the presence of flora, fauna or underwater structures but no evidence of any was detected; therefore, the ABS data has not been included for the sake of brevity. Transects are presented in chronological order and contain values of average water depth obtained via bottom-tracking; this highlights the regions of flow that cannot be accurately measured by the ADCP (the blanking distance) at the surface and at the bed. WinRiver II does not allow its internal graphing capabilities to be exported as suitable image formats; therefore, screenshots are provided of the ensemble data. Matlab was then used to stationarise these data into 5-minute averages of which velocity profiles, streamwise mean current velocity, turbulence strength and turbulence intensity were subsequently derived. Velocity profiles occurring during slack water, accelerating flow, peak flow and decelerating flow are represented in blue, green, red and yellow respectively. This was done in order to illustrate how flow varies with depth through each tidal cycle. These visualisations are presented similarly to the graphs produced of velocity profiles in the Severn Estuary collected by vessel-mounted ADCP in Mason-Jones *et al.* (2013). Areas deemed slack water (<0.8 ms^{-1} by MacEnri *et al.* (2013)) and above requisite Spring tidal velocities (>2.0 ms^{-1} by Fairley *et al.* (2013)) are also included. Relevant blanking distances are also identified at the bed and near the surface. The results of the four surveys are thoroughly described in chronological order.

This chapter concludes by comparing the results of the DWR and ADCP fieldwork with results presented in the literature (section 4.4).

4.2 Results of the DWR Fieldwork

4.2.1 Meteorological Data from the Port of Immingham

Online weather data including atmospheric pressure, temperature, wind speed and direction were collected from a weather station located at the Port of Immingham, which was 2 km south of the deployment location at Foul Holme Spit. These data were collected in order to identify and correlate storm activity during the deployment period before the data was retrieved from the deployed device. The available data contained averages taken every three hours, which is a lower interval frequency than the device sampled at (20 mins) but was the only nearby resolution of data that was available.

Figure 65 shows that the atmospheric pressure ranged between 1001 mbar and 1019 mbar during the deployment. Three distinct periods of low pressure (between 1000 mbar and 1005 mbar) during 13/08, 15/08 and 17/08 indicate increased wind speeds and thus increased wave activity. Wind speeds above 25 kph were recorded on three separate days, 17/08, 26/08 and 29/08 thus suggesting there may be slight to moderate wave activity during these dates due to an estimated Beaufort scale of 4. Wind speeds on the 17/08 peaked at 34 kph, which coincided with a period of low pressure enforcing this assumption. The Beaufort scale at this wind speed is five with expected wave heights of 1.2 - 2.4 m (though this would be dependent on wind direction and fetch). The average wind direction between 13/08 and 24/08 came from the west before shifting towards easterlies between 24/08 and 28/08 then back towards westerlies for the remainder of the deployment. Easterlies meant that there was an increased probability of swell waves from the North Sea entering the estuary, resulting in longer period waves than those locally generated in the limited fetch of the channel.

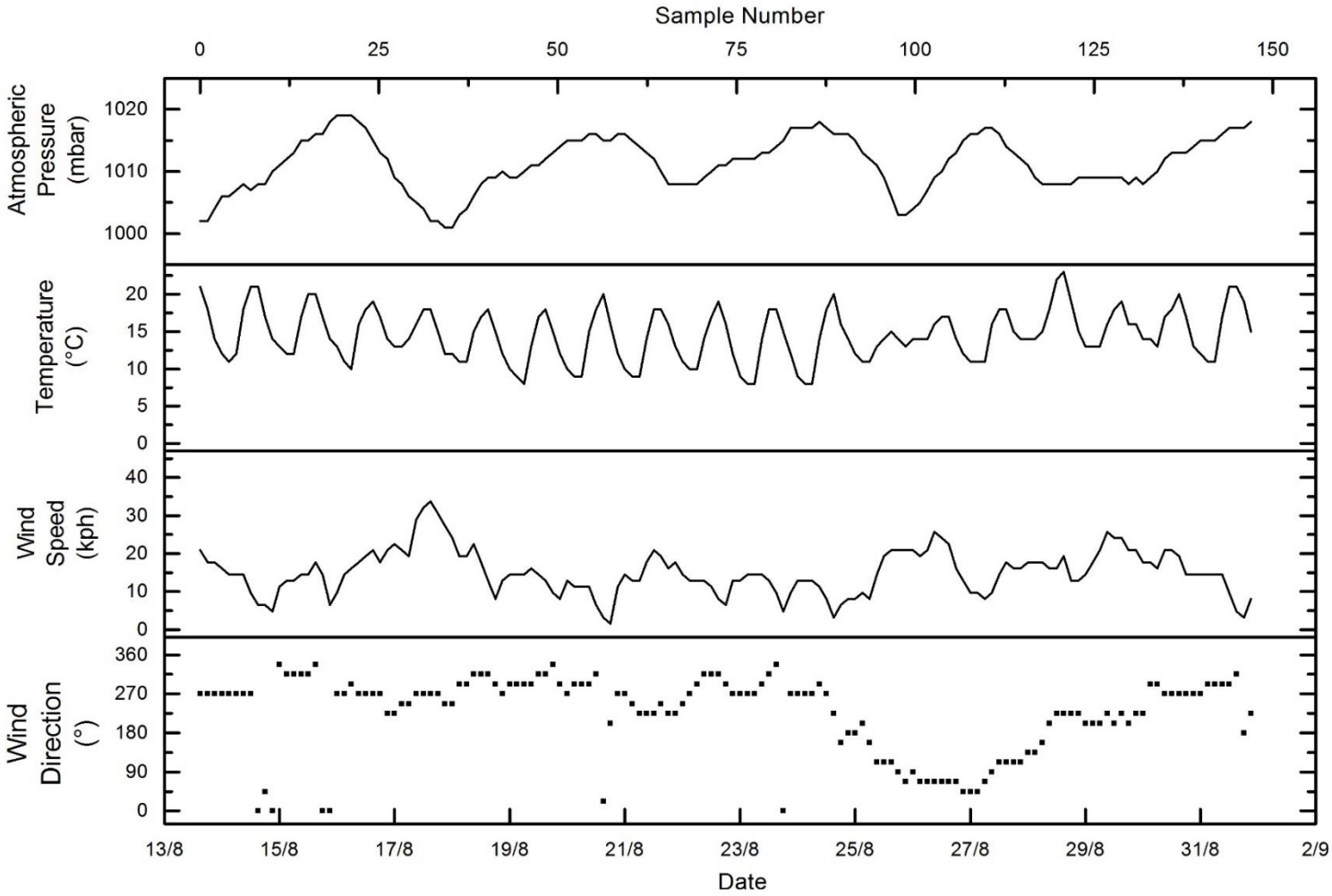

Figure 65: Meteorological data from the Port of Immingham weather station.

4.2.2 Comparison between both Device's Summary Data

As discussed in section 3.5.1, two devices were available for deployment. They were set up with identical sampling regimes and placed in close proximity. This allowed for a direct comparison between recorded measurements in order to demonstrate variability in parameters between devices and identify parameters that may be susceptible to discrepancies and errors. Upon recovery, it was observed that Device 1 had remained in position whilst Device 2 had rotated approximately 20 ° onto its side because of the marker buoy chain wrapping around the EMCM sensor-head. It was, therefore, necessary to compare the collected datasets to determine which device had the most reliable data to analyse further and to estimate when the chain may have begun affecting results.

The water depth was calculated by subtracting 10 dbar from the mean pressure values within in each tidal burst sample's summary file. Figure 66 directly compares Device 1's water depth measurements with the second device. A near perfect linear relationship with an R^2 of 0.9997 demonstrates that both devices successfully measured very similar pressure readings, regardless of the second device's tilt. The y-intercept of 0.0298 indicates that Device 2 was likely positioned around 3 cm lower than Device 1 on the sandbank. This relationship suggests that either devices measurement of water depth could be used confidently for further analysis.

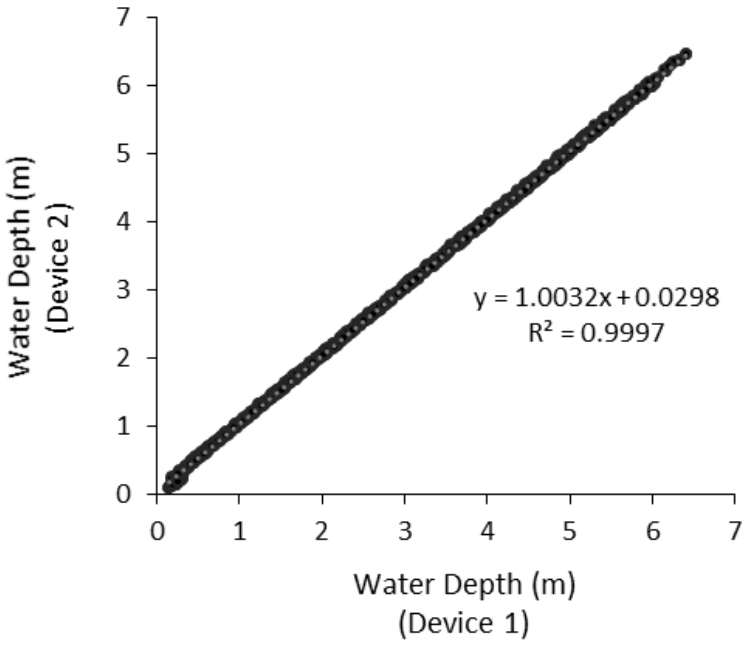

Figure 66: Comparison of water depth estimates between Devices 1 and 2.

The tidal flow estimates were calculated as the mean of the resultant EMCM 'tidal bursts' which lasted 30 seconds. Figure 67 demonstrates that, unlike water depth, tidal flow measurements have a weaker relationship between datasets due to an R^2 of 0.6758. There is a variation of around 0.2 ms^{-1} about x=y and a considerable number of samples with outlying results suggesting that Device 2 was at times over-estimating tidal flow by up to 150 %. There is also evidence to suggest that Device 2 may not have been tilted for the entire duration of the deployment as the majority of results still take on a linear relationship through x=y; therefore, the relationship between the first three Flood and Ebb tides measured were compared in Figure 68 and Figure 69. It can clearly be seen that in the first two Ebb and Flood tides there is a much stronger relationship between measurements than observed in the third Flood and Ebbs tides where the relationship is much weaker. This, therefore, suggests that the chain wrapped around Device 2 after the second Ebb tide and began causing it to tilt and generate inaccurate measurements of tidal current velocity. Nevertheless, even though both of the devices were positioned very close to each other, there is no evidence to suggest that their proximity affected the downstream device (which of course switched between Flood and Ebb tide). Also, their mean velocities were never exactly the same thus emphasising the difficulty in measuring and accurately modelling tidal flows.

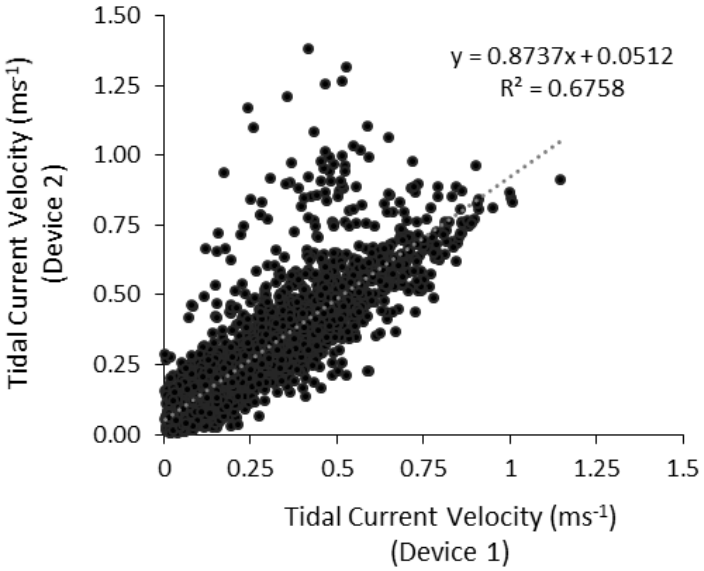

Figure 67: Comparison of tidal current velocity estimates between Device 1 and 2.

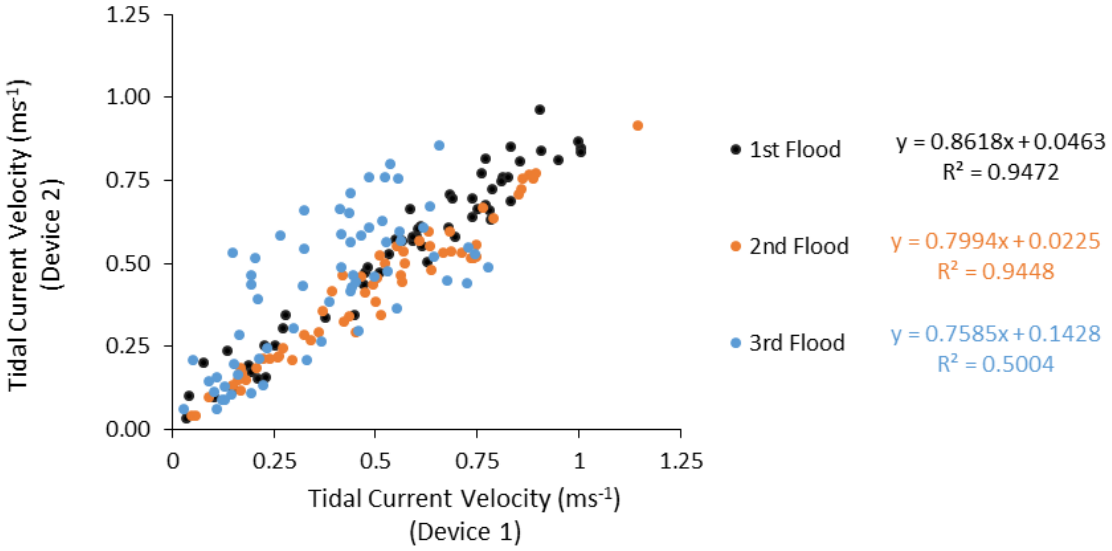

Figure 68: Comparison between tidal current velocity estimates of Device 1 and 2 during the first three Floods.

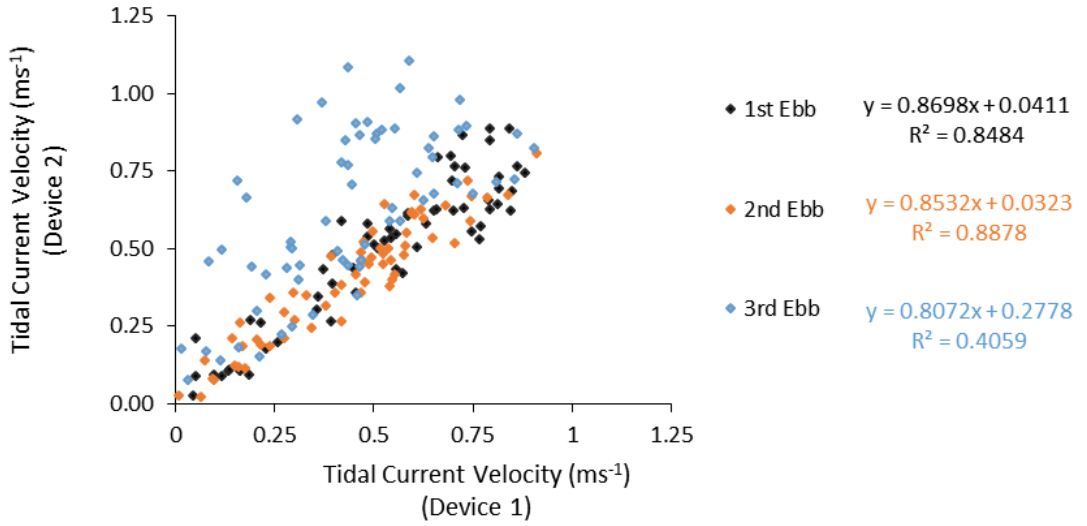

Figure 69: Comparison between tidal current velocity estimates of Device 1 and 2 during the first three Ebbs.

As the majority of the wave parameters were resolved by the pressure transducer (which was proved to have a good relationship between devices), which records independently from the EMCM (which was proved to have a weaker relationship between devices), it was assumed that there would be a good relationship between each devices estimates of the significant wave height and zero-crossing period. Figure 70 shows a comparison between significant wave height estimates between Devices 1 and 2. An R^2 value of 0.7466 indicates a strong relationship but the relationship is much weaker than that for the water depth. The maximum recorded significant wave heights (close to 0.8 m) are reasonably close to the line of best fit but heights between 0.1 and 0.5 m are overestimated by Device 2 by up to 0.3 m. Figure 71 shows a similar comparison using the estimates of the zero-crossing period. An R^2 of 0.6827 indicates that zero-crossing periods varied between devices more so than the significant wave height. However, this parameter is more

susceptible to inaccuracies because the device calculates values during very calm conditions when wave periods are likely to be less than 1 second and thus below the accuracy of the device.

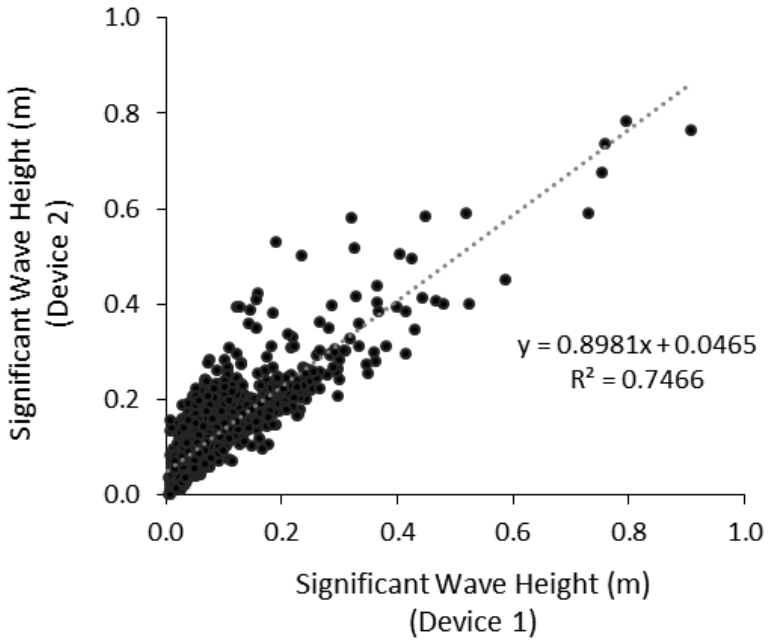

Figure 70: Comparison of significant wave height estimates between Device 1 and 2.

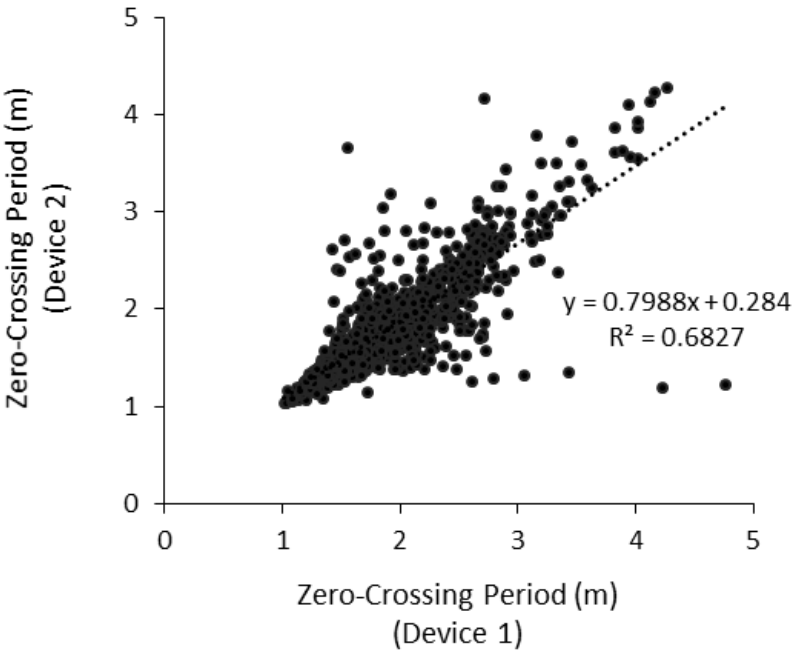

Figure 71: Comparison of zero-crossing period estimates between Device 1 and 2.

4.2.3 Foul Holme Spit Summary Files (Device 1)

4.2.3.1 Introduction

The following section describes the parameters recorded throughout the duration of the deployment by Device 1 (13/08 - 01/09). A description of the device's recording instruments and the way in which each summary parameter is derived was previously given in section 3.3.1.3. It is worth bearing in mind that the tidal burst data sampled at 10-minute intervals for just 30 seconds thus producing 2644 separate bursts whereas the wave burst data sampled in 20 minute intervals but for 4 minutes producing 1322 separate bursts. This, therefore, meant that half the tidal bursts are actually the first 30 seconds of every wave burst. Throughout, evidence for periods of increased wave activity is noted in order to inform the choice of samples taken for further analysis. The section concludes by discussing which samples were selected for in-depth analyses of their raw data.

4.2.3.2 Tidal Burst Data

Each of the tidal burst parameters are presented in Figure 72 and discussed separately in the following sections.

4.2.3.2.1 Conductivity

The conductivity of water is linearly related to the salinity of water and is, therefore, a useful metric to help understand whether or not the device was submerged or had broke the surface during low water. Samples containing zero conductivity were identified and used to remove erroneous results produced from other parameters during these periods. Salinity was expected to increase during the Flood tide as saltier North Sea water flowed into the estuary and subsequently decrease during Ebb tide as seawater flowed out of the estuary. The periodic rise and fall in salinity match the rise and fall of the water depth, as expected. There are obvious troughs that occur during the early Spring tides (13/08 - 16/08) and the later Spring tides (24/08 - 30/08) with values of zero which indicate that the device emerged at low water. Minimum values (ignoring zero values) throughout the deployment period remained relatively constant at 27 $mScm^{-1}$, whilst maximum values oscillated in unison with tidal height. During Spring tides values of conductivity peaked at 38 $mScm^{-1}$ whereas during Neap tides values peaked at just 33 $mScm^{-1}$. This, therefore, suggests that the deployment location became more saline during Spring tides than at Neap tides.

4.2.3.2.2 Temperature

Average water temperature decreased from 18 to 15 °C over the first 14 days before increasing to 16 °C during the final 4 days of recording. As with conductivity, fluctuations from the mean suggest the device emerged during the low waters of a Spring tide but remained submerged through the entirety of the Neaps, as planned. When compared to the collected weather data, the periodic fluctuations in temperature closely match the local air temperature. Fluctuations greater than the mean occurred during daylight suggesting that the air temperature was greater than the water temperature whilst the fluctuations smaller than the mean occurred during the night suggesting that the air temperature was actually colder than the water temperature.

4.2.3.2.3 Water Depth

The water depth followed a very clear Spring-Neap-Spring pattern and the lowest values of water depth coincided with low conductivity. As expected (from the predictions of TotalTide), the greatest tidal range occurred straight after deployment during the first Springs (6.4 m on 13/08) confirming the site can be described as hyper-tidal (tidal range >6 m (Archer, 2013)). The smallest tidal range occurs mid-Neap (4 m on 19/08) where even at low water the device remained submerged at a depth of 1.5 m. There is an observed semi-diurnal inequality (up to 40 cm) during Springs and as low as 10 cm during Neaps.

4.2.3.2.4 Tidal Current Velocity Magnitude and Direction

The tidal current velocity follows a similar Spring-Neap-Spring pattern to water depth, though with a phase shift, as maximum tidal flow occurs between high and low water. All positive velocity values followed a direction of approximately 315 ° (upstream) indicating that they are Flood currents, whereas negative velocity values had an approximate direction of 135 ° (downstream) suggesting that they are Ebb currents. Flood currents peak within the first recorded tidal cycle at 0.9 ms^{-1}, whereas Ebb currents peak during the third recorded tidal cycle at 1.2 ms^{-1}. Neap currents peak at values close to one-third of Spring values. It can generally be seen that peak Ebb currents are within 10 - 20 % faster than peak Flood currents. There appear to be slight variations in flow direction during peak flow, which is particularly evident during the Ebb flood on 17/08.

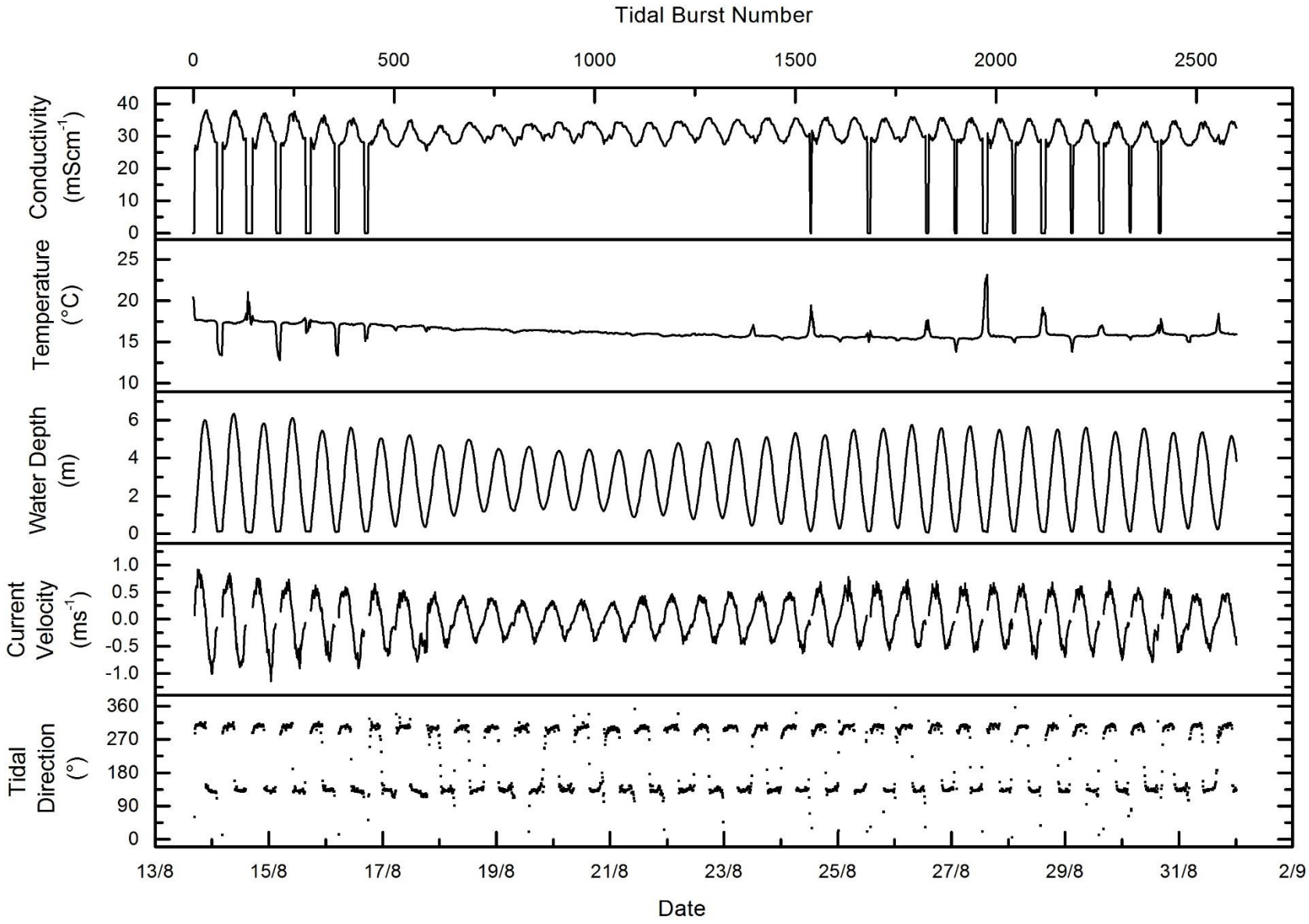

Figure 72: Tidal burst summary data from Device 1.

4.2.3.3 Wave Burst Data

4.2.3.3.1 Significant Wave Height

Figure 73 shows the calculated significant wave height of each wave burst during the deployment. It can be seen that four distinct peaks are observable on 16/08, 17/08, 25/08 and 30/08. Increased wave height is of course a good indicator of increased wave activity. The greatest significant wave height recorded was observed on 17/08 at 0.78 m. This also exactly matched the timing of the peak wind speed of the deployment (22 kph) (Figure 65). Whilst this is a relatively low value for a significant wave height at offshore sites, it is considerable for an estuarine environment and indicative of increased localised wind speeds. The other three peaks are lower than on 17/08, with peaks ranging between 0.5 m and 0.6 m. Some days saw very low wave heights. The evenings of 18/08 and 19/08 have values as low as 0.04 m which coincides with very low wind speed (0 - 5 kph) (Figure 65). The relationship between wind speed and wave height does not appear linear as some periods of increased wind speed have very low wave heights. For example, midday 16/08 has relatively high wind speeds at 13 kph yet low wave heights between 0.1 m and 0.2 m. It must be noted, however, that the observed wave height data are at much higher temporal frequency than the weather data and is, therefore, more difficult to match up.

4.2.3.3.2 Zero-Crossing Period

It can generally be seen that the zero-crossing period increases from 1.5 seconds at low water, up to 3 seconds at high water except from between 25/08 and 26/08 where periods at high water exceed 4 seconds. These dates have previously been identified as a period of increased wave activity from the significant wave height data; however, the other storm periods identified do not contain peaks in zero-crossing period data. This period also contains waves that propagated from 135 ° suggesting that these waves may have originated offshore and could be storm swell, which usually contains longer period waves. The period during 17/08, which contained the greatest significant wave height recorded, shows the smoothest rise and fall of periods from the whole dataset yet does not peak higher than in calm conditions during the Neaps.

The period of a wave is generally related to its fetch and should not change when the wave moves into shallower water (only its wavelength should decrease). It can, therefore, be seen from the estimates of zero-crossing period that the period follows a semi-diurnal oscillation similar to that observed in the water depth. This is thought to be because of the greater fetch available within the estuary at high water, which allows waves

to be generated over a greater distance. This phenomenon is not commonly noted in relevant literature but could be an interesting research topic to pursue in future work as it could determine whether or not tidal stream turbines (TSTs) are more likely to be affected by longer periods waves at high water than low water (see section 5.6).

4.2.3.3.3 Peak Frequency

The peak frequency data contained a lot of noise because the majority of the observed dataset was relatively calm and the device struggled to predict a peak frequency from spectral analysis of the calmest surface recreation files. The only reasonable data occurred during the previously identified dates with increased significant wave height. For example, during 17/08 the peak frequency appears to be a close reciprocal of the zero-crossing period with peak frequencies of around 0.4 Hz occurring during the peak in significant wave height.

4.2.3.3.4 Wave Energy

Wave energy is a function of the significant wave height and, therefore, closely matches the peaks previously identified; however, it exaggerates them because of the square function making it clear where wave energy is maximised.

4.2.3.3.5 Wave Direction

The peak wave direction of each sample burst occurred between 90 ° and 315 °, closely matching the directional distribution of the wind direction (Figure 65). During the period of the most increased wave energy density (17/08) there appears to be a narrower band of directions suggesting that sustained winds generated waves that flowed in the direction of the wind whilst during calm periods waves were generated from a wider range of directions. This again occurs during the spike in wave energy density during 25/08 where wave direction trends towards 135 ° whilst wind direction also shifts to around 90 ° (Figure 65). As the device was positioned on the northeast bank, it is no surprise that no waves came from this direction and that all waves came from between 95 ° and 300 °. The wave directions with the largest count of occurrences came from between 195 ° and 255 ° degrees.

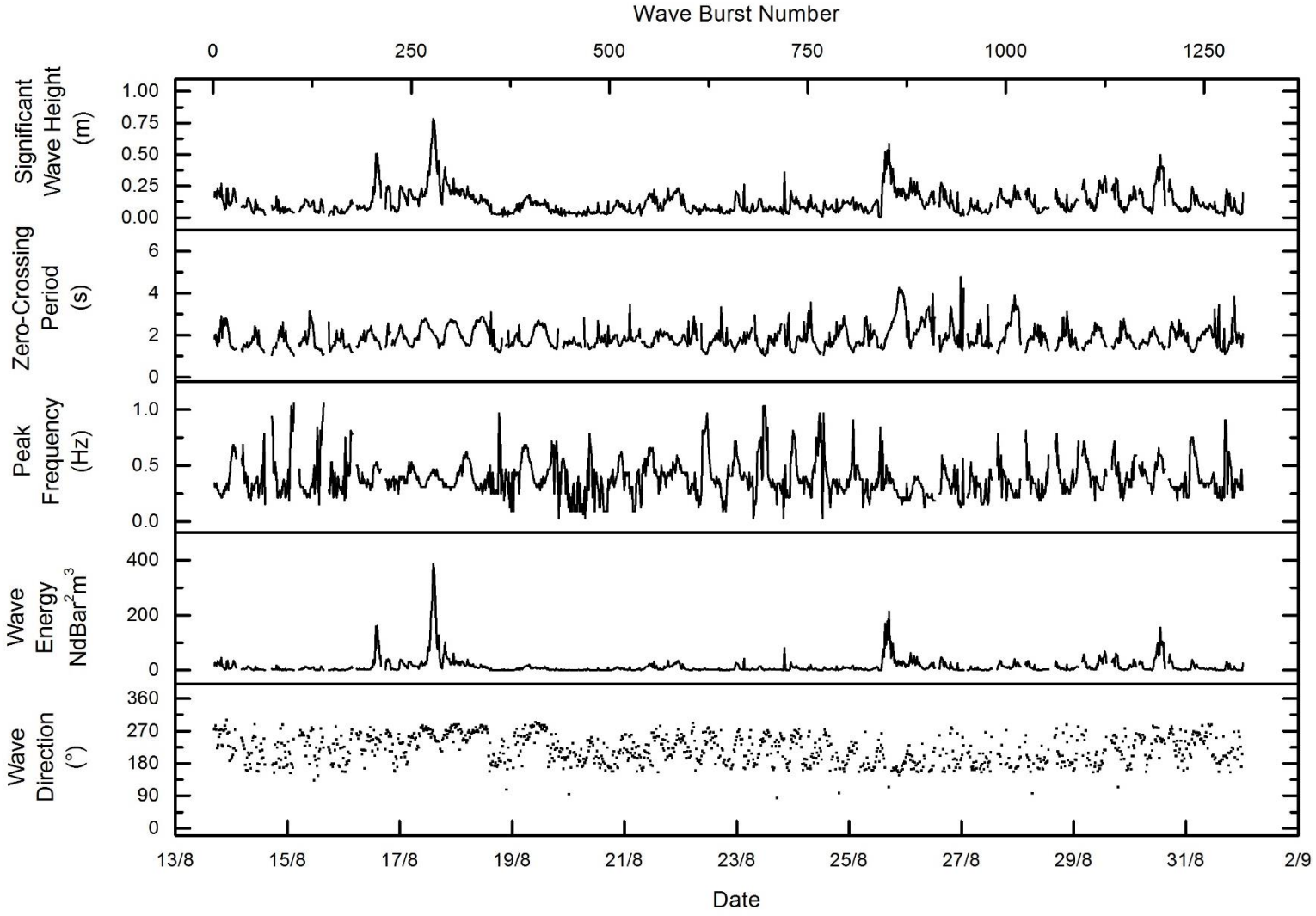

Figure 73: Wave burst summary files from Device 1.

4.2.3.3.6 Tidal Flow and Wave Directionality in Perspective

Figure 74 shows the direction, significant wave height and zero-crossing period of each wave burst. It is obvious that the majority of wave bursts contained low wave heights and propagated from between 150 and 300 °. Longer period waves are found at the edges of this band around 150 and 300 °. In order to gain perspective of tidal and wave directionality in context with the deployment location, Figure 75 shows the directional summary data as an occurrence radar centred upon the deployment co-ordinates. Tidal direction can be described as rectilinear and bi-directional as the majority of occurrences follow a distinct upstream or downstream direction almost parallel to the banks, whilst the majority of waves appear to have originated locally from the west and south-west and possibly offshore from the south-east.

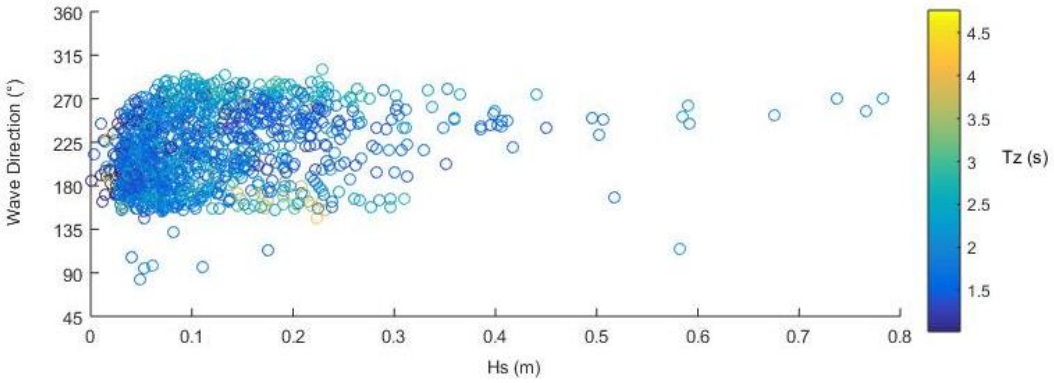

Figure 74: Comparison of significant wave height, zero-crossing period and wave direction at Foul Holme Spit throughout deployment.

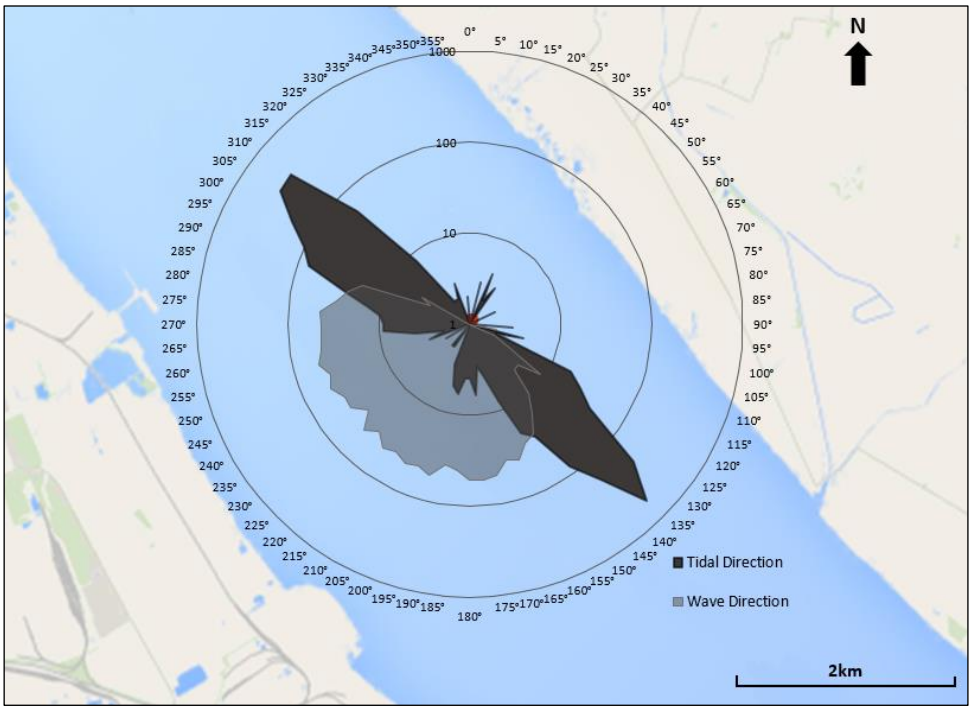

Figure 75: Tidal and wave direction occurrence radar overlaying Foul Holme Spit deployment site.

Figure 76 shows the same wave directional data as presented in Figure 75 except it also contains the rectilinear direction of tidal flow either upstream or downstream. From this it is easy to visualise which samples had waves moving in-line with the tidal currents, though without the time series of tidal currents (which over-complicates the graph) it is not possible to determine whether they were matching or opposing the tidal flow; this is more easily done on an individual sample basis.

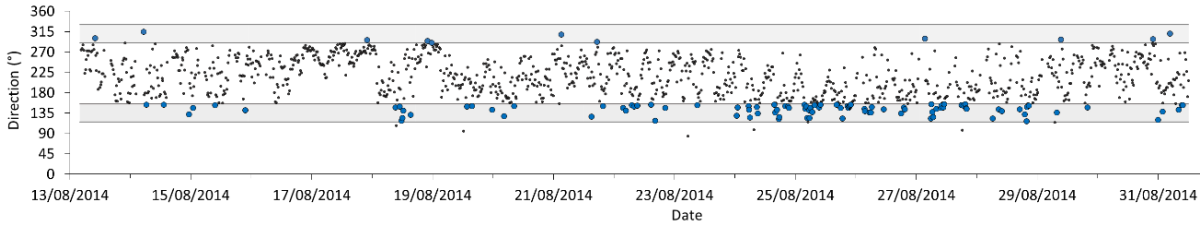

Figure 76: Comparison between wave and tide direction in the style of Lewis et al. (2014).

4.2.4 Comparisons between Device 1's Summary Data and TotalTide Predictions of Water Depth and Current Velocity

TotalTide was used to model water depths and tidal currents close to the deployment site in order to compare it to the observed data. The main tidal station in the Humber (and the east coast of England) is at the Port of Immingham, just 2 km south of the Foul Holme Spit deployment site (this is also where the meteorological data were taken from). Tidal height and current data were modelled at Immingham using TotalTide for the duration of the deployment and compared to the recorded *in situ* data collected by Device 1. This demonstrates the predictive capabilities of TotalTide for water depths and the poor predictive capabilities for tidal currents for a relatively close site to a tidal station.

4.2.4.1 Water Depth

The observed and modelled water depth data are presented in Figure 77. The time series follow a very similar, in-phase, Spring-Neap-Spring pattern. The main difference is that the modelled data suggests high waters and low waters are all 1 - 1.5 m greater than the observed results except from during the first few tidal cycles where the low water modelled data are just 0.5 m greater. This difference is most likely because the device was not deployed at chart datum, and was actually located approximately 1 m higher up the sand bank to make it easier to recover at the subsequent Spring tide.

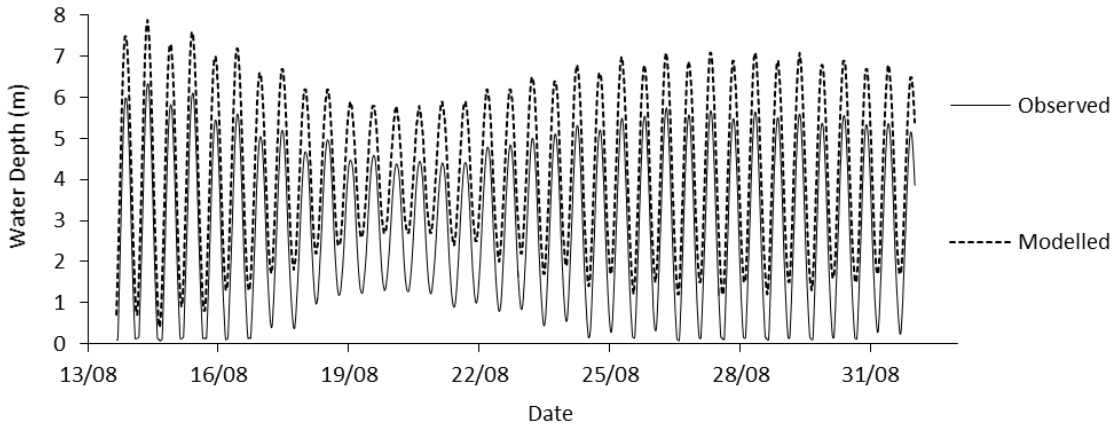

Figure 77: Time series comparison between the observed and modelled water depths.

The modelled and observed values were plotted against one another to determine their relationship. Figure 78 shows an almost perfect linear relationship with a regression of 0.9936 indicating a very strong positive correlation between the modelled data and the observed calculation of water depth. The y-intercept of -1.1375 suggests that 1.14 m was the precise height above chart datum that the device was deployed at, thus generating the observed offset.

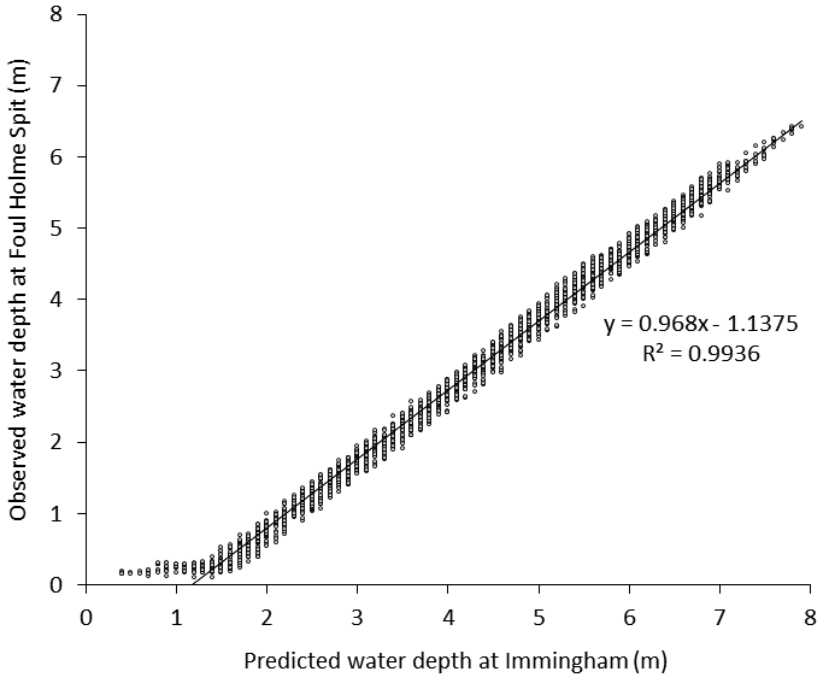

Figure 78: Correlation between the observed and modelled water depths.

4.2.4.2 Tidal Current Velocity

The observed and modelled tidal current data over the recording duration are presented in Figure 79. The modelled peak currents at Immingham are significantly larger than those observed at the measurement height at Foul Holme Spit yet both series show the expected Spring-Neap-Spring pattern. Modelled current velocities are 2 - 3 times larger than the observed current velocities which is likely because the modelled data are a prediction of the depth-averaged current velocity whilst the EMCM sensor-head measured a constant height of 0.4 m above the bed, which will be at the lower end of the velocity profile and, therefore, slower as a result of shear. A strong semi-diurnal inequality is predicted throughout the deployment though there is a disparity in some cases about when this occurs in the observed series. In the first Spring cycles and the Neap cycles, both the observed and predicted currents show stronger Flood tides than Ebb; however, during the second Spring cycles a number of cycles actually show stronger Ebb currents than Flood currents. The observed currents do not oscillate as smoothly as the predicted currents or the observed tidal heights and instead have periods of variability around peak flow.

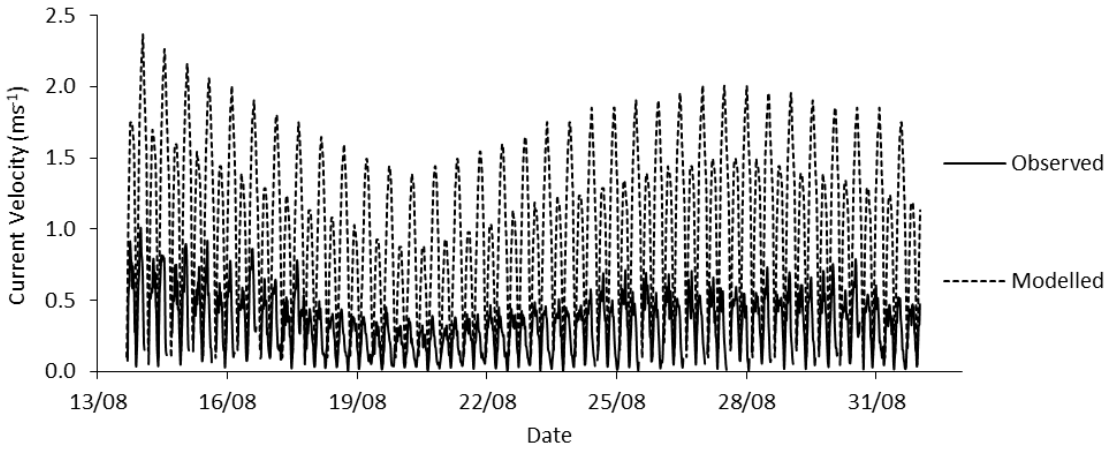

Figure 79: Time series comparison between modelled and observed tidal current velocities.

When plotted against one another the relationship between observed and modelled current velocities is much weaker than for water depth, with an R^2 value of 0.3295 (Figure 80). This does not necessarily mean that either the model or the recorded measurements are incorrect it simply demonstrates the variability in tidal streams through spatial scales; in this case it is most likely the variation through depth because of shear and because of the variation in bathymetry between Foul Holme Spit and Immingham.

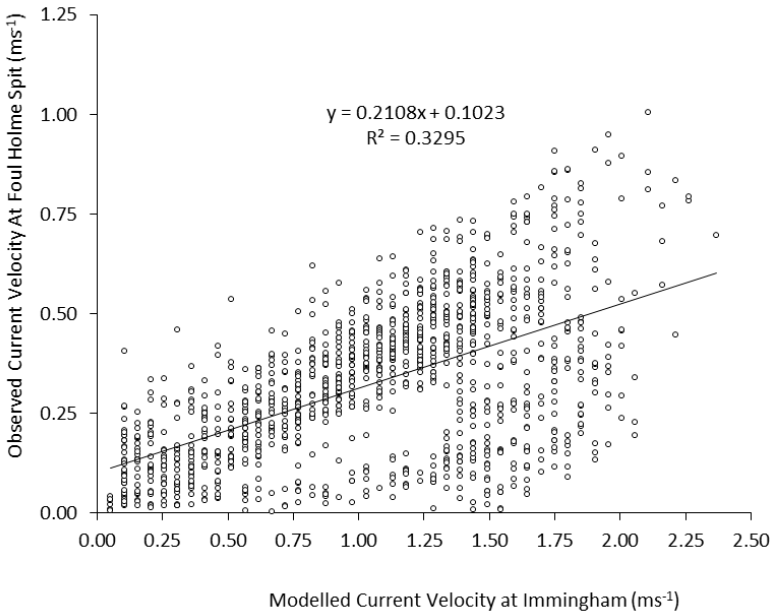

Figure 80: Correlation between modelled and observed tidal current velocities.

4.2.5 Data Used in the Analysis

The data used in the analysis chapter are presented as a time series in Figure 81. These include the summary data outputted in the wave bursts from the pressure transducer (water depth, significant wave height and zero-crossing period) but also data calculated from the EMCM data within the raw data files that were not automatically generated by the Wavelog Express software (streamwise mean current velocity, turbulence strength and turbulence intensity). Finally, in order to estimate the variance induced by wave orbital motion near the bed, the Soulsby exponential approximation was calculated based on the water depth, significant wave height and zero-crossing period of each sample respectively. The accuracy of this estimate is represented using *t*. Where *t* was greater than 0.4 the estimate was said to be an overestimation of greater than 40 %; therefore, these estimates were removed. Only samples that were >2 m water depth were included in order to avoid the non-linear effects of the surf zone (Aubrey, 1989) and inaccuracies in taking the resultant of *u* and *v* when wave orbital velocities actually caused reversal in the flow thus affecting the streamwise mean. The effects of waves on turbulence intensity in the surf zone may be of interest to sedimentologists but has no real application to tidal stream power and, therefore, these data are not explored further.

As the device is limited to recording near the bed using the present methodology, the recorded mean current velocities were much lower than those observed by MacEnri *et al.* (2013) (who measured at an undefined hub height, estimated to be around 10 m from the bed) because of the effects of shear velocity profiles. The turbulence strength appears to follow the Spring-Neap-Spring pattern of the mean current velocity whilst the

turbulence intensity occasionally peaks during low mean velocity (and low turbulence strength) but is otherwise around 10 to 20 %. From these time series, it is unclear whether or not the turbulence intensity is significantly modified under the four main previously identified periods of increased wave activity. Even if there were obvious increases, the significant wave height and the zero-crossing period would not directly affect a change in turbulence metrics as it would actually be the related induced orbital velocities that decrease exponentially with depth that would. The Soulsby exponential approximation is the closest published solution available for estimating this affect using both spectral wave parameters and the water depth (though its intended use is for in the open ocean with no mean flow). It can be seen that the approximation does peak during peaks in significant wave height but, as it also takes into account the water depth, it suitably demonstrates that smaller wave heights can still have equivalent influence in shallow water depths. This is evident in that many of the peaks in orbital motion occur at the lowest water depths even when wave heights are considered low, particularly during the last few days. Figure 82 demonstrates this effect using 3D surface plots of the modelled U_{RMS} values at given significant wave heights, zero-crossing periods and water depths. The first three graphs show typical water depths and met-ocean conditions found in the Humber Estuary and demonstrates how, as water depth increases, the same sized surface wave parameters have lower modelled near-bed U_{RMS} values. The fourth graph shows typical water depths and wave climate found in the Pentland Firth demonstrating how a severe storm in the Pentland Firth could generate the same near bed U_{RMS} value as a localised storm in the much shallower Humber Estuary, reaching up to around 1 ms^{-1}. Due to the exponential decay of wave-induced orbital velocities, it is expected that wave-induced velocities nearer the surface are potentially much greater and could cause serious loading problems to turbines positioned within wave base such as floating and buoyant designs or bed-mounted designs in shallow waters or with relatively high wave climates. It is, however, exceedingly difficult to record these near-surface velocities using fixed position methodologies in areas of high tidal range, as the depth from the surface will inevitably change through the tidal cycle.

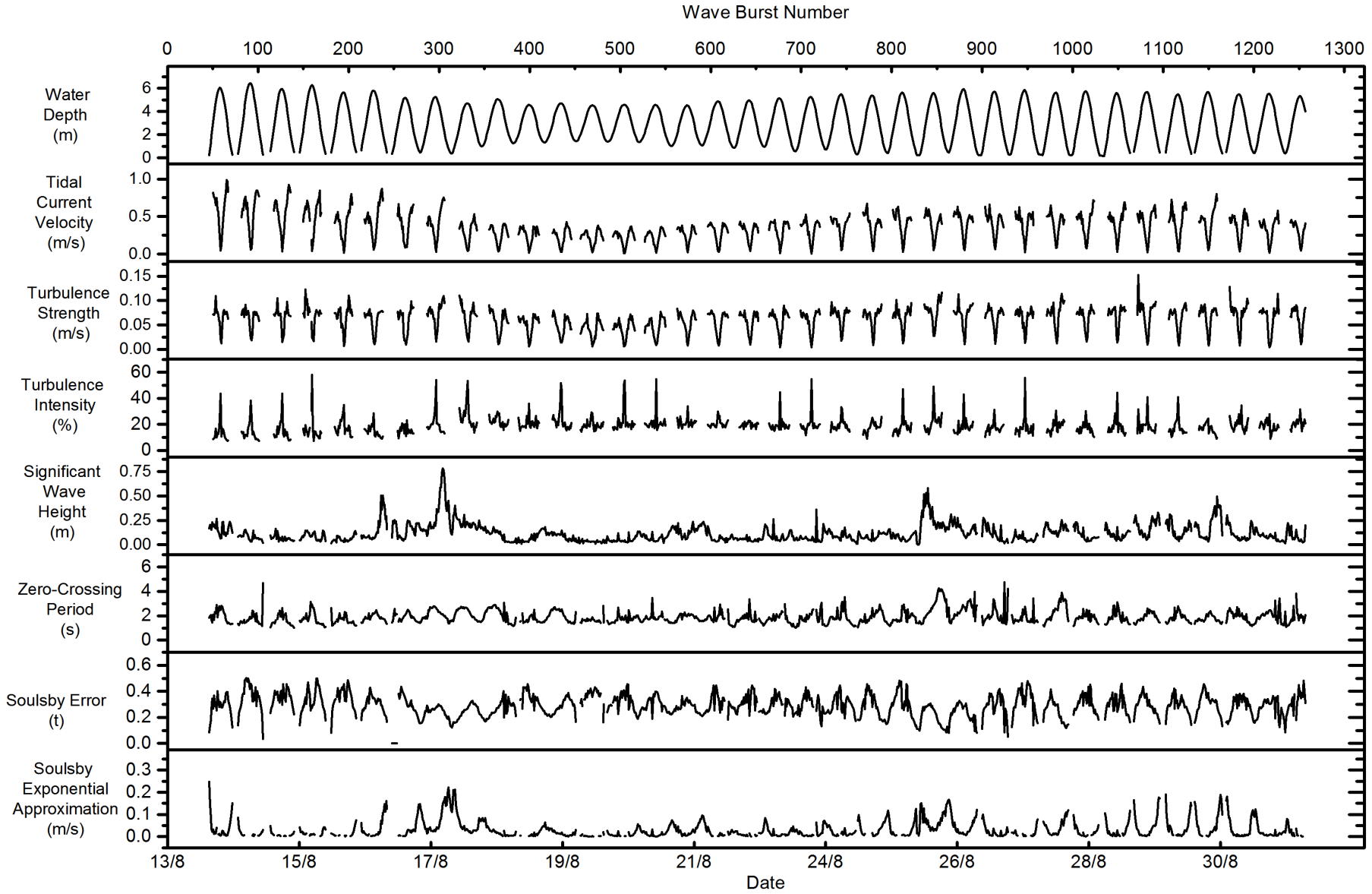

Figure 81: Time series of tidal and wave data relevant to the analysis from device 1 as well as the modelled values of the Soulsby exponential approximation.

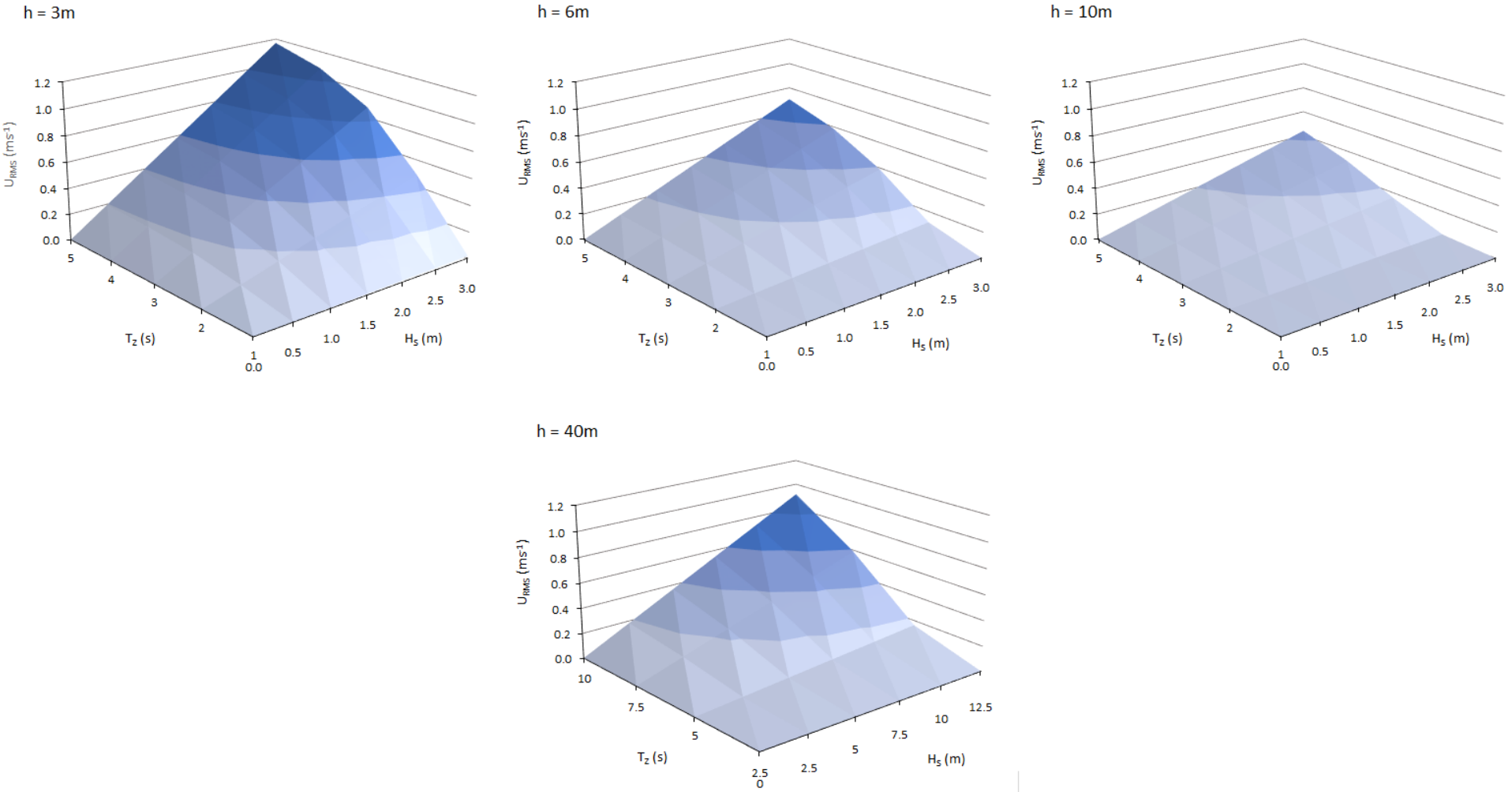

Figure 82: Modelled wave-induced U_{RMS} values at given significant wave heights, zero-crossing periods and water depths

4.2.6 Summary of the DWR Fieldwork

The deployment of Valeport MIDAS DWRs at Foul Holme Spit in the Humber Estuary collected one of the most comprehensive wave-current datasets ever collected from a hyper-tidal estuary. A range of current velocities, water depths and surface wave parameters were collected with four distinct periods of increased wave activity identified. Whilst one of the devices suffered fouling by the marker buoy chain (Device 2) the other device (Device 1) returned suitable data for further analyses. The problem with having to locate the device near the bed meant that wave-current interaction could only be explored in lower flow velocities due to velocity shear and low wave-induced velocities due to the exponential decay of these velocities from the surface. Nevertheless, the mean streamwise velocities and surface wave parameters recorded were still greater than some published wave-current studies and are, therefore, very useful.

By comparing observed and modelled estimations of water depths and currents from two relatively close sites within the Humber Estuary it is clear that whilst water depths can be very well predicted using harmonic analysis over a large spatial area, tidal current predictions are comparatively poor. The reason for this is that they are more susceptible to a range of dynamic variables that water depths are not, such as variation with depth, because of shear, bed roughness and, potentially, meteorological influences such as surface waves.

By calculating and comparing the turbulence strength, turbulence intensity and wave-induced orbital velocity component as a time series, it is evident that the turbulence strength appears to be related to the spring-neap-spring pattern observed within the mean current velocity whilst large increases in turbulence strength induced by surface wave activity are less clear.

4.3 Results of the ADCP Fieldwork

4.3.1 Static Surveys during a Spring Ebb and Flood tide

As detailed in the methodology, a 1200 kHz ADCP was used during the Spring tide static surveys. Ensembles with 0.25 m bin depths were generated at around 1 Hz with a top blanking distance of 1.11 m. The first transect, which began just after slack water, contained only 'bad bins' (unreliable data). Therefore, the transect was stopped and the ADCP checked. After half an hour, the transect was restarted and 'good bins' (reliable data) began to be collected. The measurements eventually made during the second transect throughout the Spring Ebb were, however, littered with bad ensembles and erroneous estimates of depth from the bottom tracker; Table 10 shows that over 13 % of ensembles calculated during this transect were considered bad. The cause of this intermittency remains unknown as the ADCP should have been capable of operating within the site conditions given its technical specifications. Comparatively, the measurements made during the Spring Flood were much improved, as only 10 ensembles out of 16 350 were considered bad.

Stage	Duration of transect (secs)	Number of ensembles in transect	Number of bad ensembles in transect
Spring Ebb	12 534	13 519	1 859
Spring Flood	15 160	16 350	10

Table 10: Ensemble information for the Spring static ADCP surveys.

The earth velocity magnitude and direction during the Spring Ebb are presented in Figure 83. During the first half an hour of the transect the maximum water depth fluctuated around 14 m and gradually decreased to 8 m at low water at 13:00. A second period of depth fluctuation was observed between 11:30 and 12:10. It is possible that this fluctuation could have been the result of a moving bed or instrument tilt due to waves but as conditions were calm and the fluctuations were not consistent throughout peak flow it was unlikely that either of these possible explanations are correct. Flow velocities increase up to a maximum at 10:50; with velocities up to 1.75 ms^{-1} occurring at mid-depth, around 1.5 ms^{-1} at the surface and 1.25 ms^{-1} at the bed. After this, flows follow a more typical velocity profile with velocities >1.5 ms^{-1} at the surface and a clear region of slower velocities <1 ms^{-1} nearer the bed. Flow direction was generally consistent with depth and varied between 60 and 80 °, which was expected given the channels orientation.

The earth velocity magnitude and direction during the Spring Ebb are presented in Figure 84. This transect contained the fastest and most sustained flows of the static survey

undertaken. During the first 30 minutes, the transect was started but the boat had to be repositioned due to being anchored too far from the Spring Ebb survey location. Only slack water was recorded during this time; therefore, it should generally be ignored. The following 30 minutes exhibited rapid acceleration in flow with more structured velocity profiles and flows up to 1.5 ms^{-1}. Beyond 16:00, flows generally ranged between 1.75 and 2.3 ms^{-1} at the surface and 1.25 ms^{-1} and 1.75 ms^{-1} at the bed for 2.5 hours. These near-surface flows indicate that the site would be suitable for tidal stream power developments according to the threshold discussed in Fairley *et al.* (2013). Flows began to decelerate after 18:15 and slowed to around 1.25 ms^{-1} at all depths at 19:00. The flow direction (beyond the first 30 minutes) fluctuated in a much narrower band than during the Spring Ebb between 245 and 255 ° with no evidence of flow reversal or large eddies, as experienced by Jeffcoate *et al.* (2015).

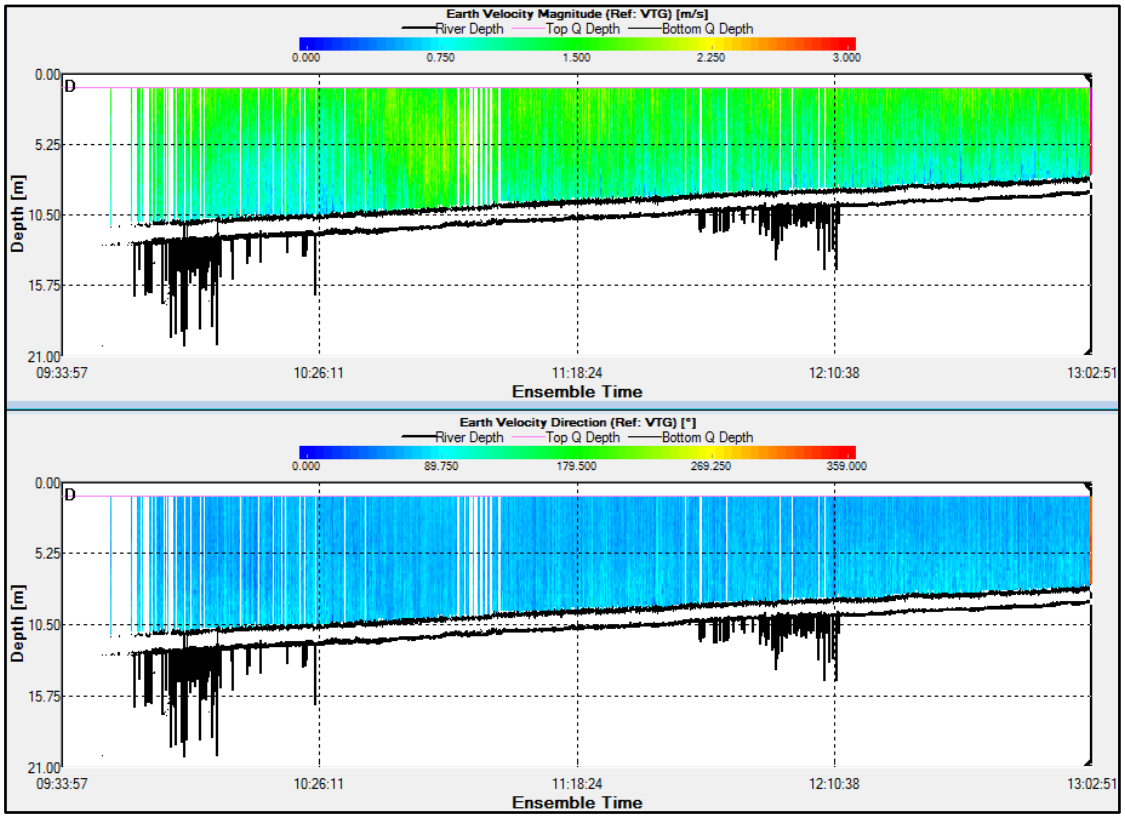

Figure 83: Earth velocity magnitude and direction during the Spring Ebb tide at St. Andrews Dock.

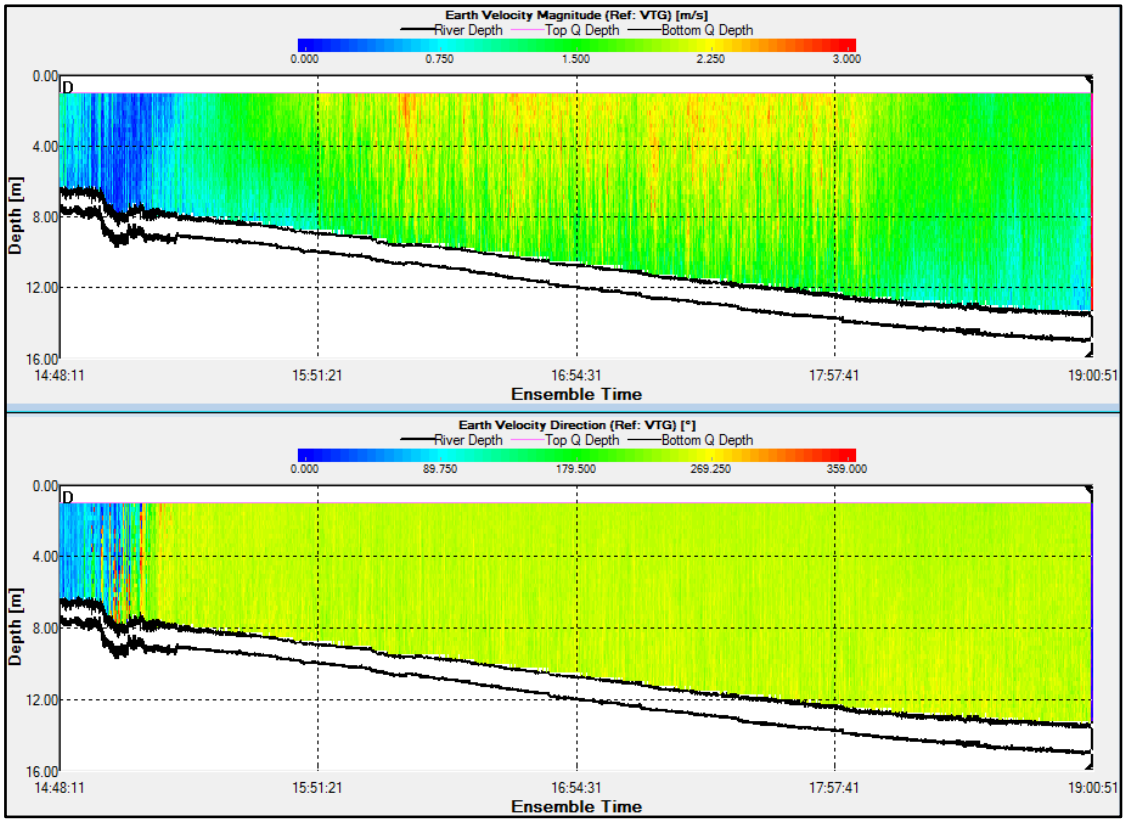

Figure 84: Earth velocity magnitude and direction during the Spring Flood tide at St. Andrews Dock.

4.3.1.1 Spring Ebb Velocity Profiles, Mean Streamwise Current Velocity, Turbulence Strength and Turbulence Intensity

Figure 85 shows how velocity profiles were similar during slack, accelerating and decelerating periods and that peak flow velocity profiles were highly sheared with the lowest velocities at the bed around 1 ms^{-1} and around 1.6 ms^{-1} at the surface. Figure 86 shows the 5-minute averaged streamwise earth velocity magnitude data, which generally follows the description already provided in section 4.3.1. The time-averaged turbulence strength data collected during the Spring Ebb survey are presented in Figure 87. Throughout this transect there does not appear to be any clear structure or pattern to the turbulence strength within the water column as the highest standard deviations are not observed at the fastest averaged velocities. During the first 30 minutes there are many different values ranging between 0 and 0.3 ms^{-1} though this is likely a combination of slack water and the boat settling into positon within the flow. Whist the time-averaged peak flow occurred around 10:45 the peak in turbulence strength did not occur until around 11:30. Whilst there appeared to be limited observable relationships between mean current velocity and turbulence strength, more structure to the flow is noticeable when the turbulence intensity is calculated (Figure 88). Generally, there are higher turbulent intensities (up to 25 %) close to the bed where flow velocities are lowest and turbulence is relatively constant through depth. Conversely, turbulence intensities are lowest at the surface (around 10 %) where current velocities are greatest and turbulence strength is marginally lower. Very low turbulence strength and intensity values are occasionally given at the bottom-most bins; these are likely erroneous values given because of depth-cell mapping with data that does not adequately fit into the bottom bin depth and should, therefore, be ignored.

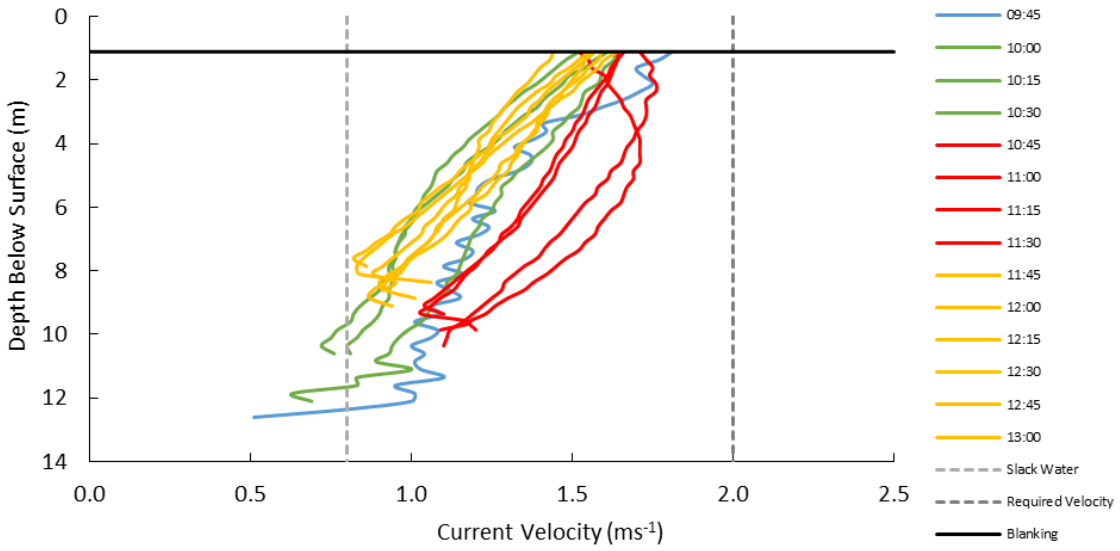

Figure 85: Streamwise current velocity profiles during Spring Ebb (5 minute averages at 15 min intervals).

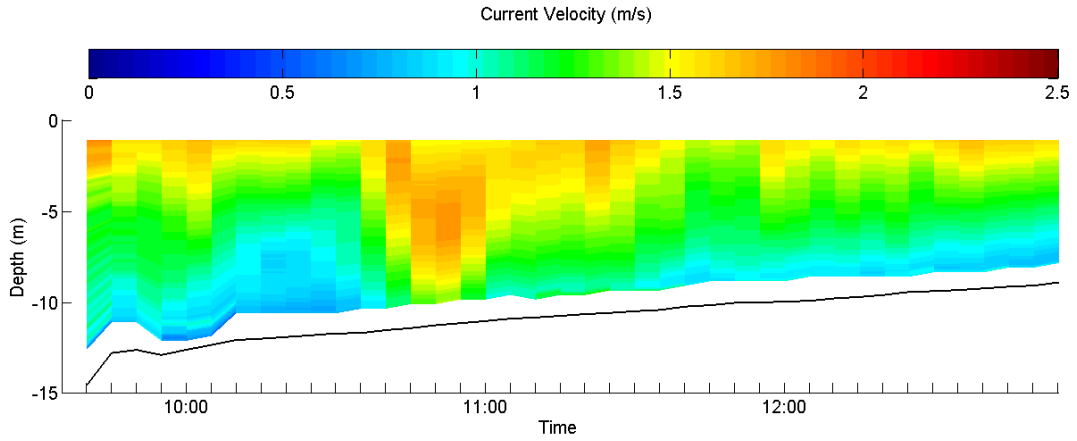

Figure 86: Spring Ebb streamwise current velocity data through depth and time (using a 5-minute average).

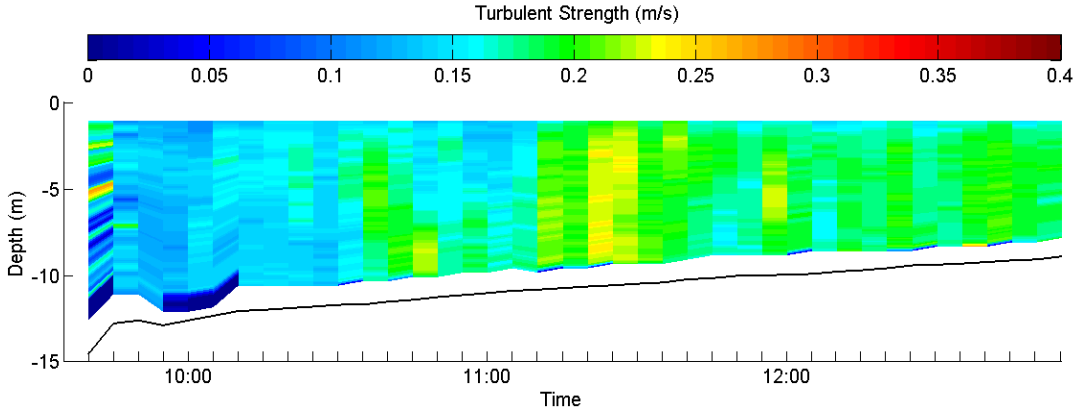

Figure 87: Spring Ebb turbulence strength data through depth and time (using a 5-minute average).

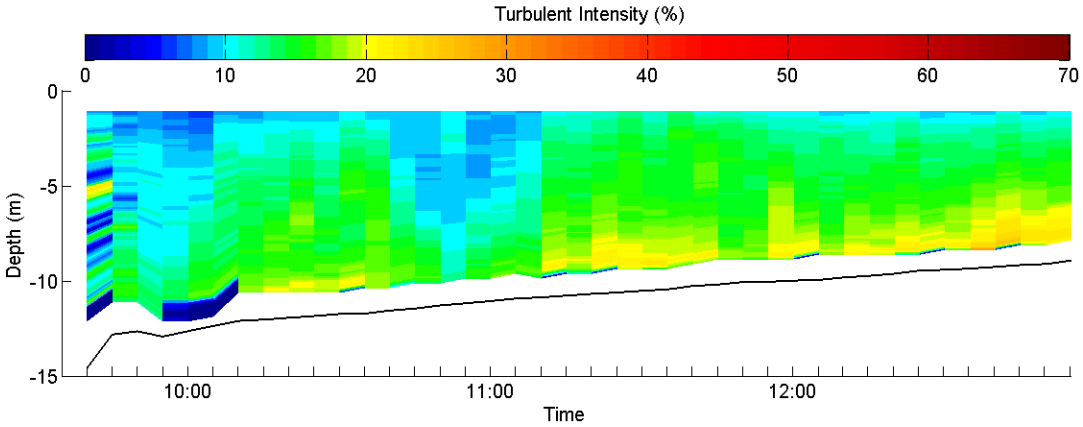

Figure 88: Spring Ebb turbulence intensity data through depth and time (using a 5-minute average).

4.3.1.2 Spring Flood Velocity Profiles, Mean Streamwise Current Velocity, Turbulence Strength and Turbulence Intensity

Figure 89 shows that slack water had some concave down profiles whilst the majority of the other profiles included were typically concave up. One of the decelerating profiles had higher velocities at a mid-depth than at the surface or the bed. The peak flow velocity profiles contained velocities above 2.0 ms^{-1} to a depth of around 6 m which only varied around 0.2 ms^{-1} during 1.75 hours and had profiles which closely fit the $1/7^{th}$ power law with near perfect regressions of $R^2 = 0.9946$ (Figure 90). In Figure 91, the 5-minute averaged streamwise earth velocity magnitude data generally follows the description already provided in section 4.3.1. The Flood velocities were greater than the Ebb velocities through depth and time at each stage of the tidal cycle. The time-averaged turbulence strength data collected during the Spring Flood tide are presented in Figure 92. Although low mean velocities were observed during the first 30 minutes there was high turbulence strength up to 0.28 ms^{-1}, but as flow velocities were low here it is considered that the increased standard deviation is a result of the boat settling into position before flows accelerated. The following 30 minutes contained low turbulence strength, around 0.1 ms^{-1}. There is a rapid increase at 16:00 where the turbulent structure becomes more ordered with low turbulence around 0.1 ms^{-1} at the surface and higher values up to 0.28 ms^{-1} nearer the bed. This ordered structure persists for the duration of the fastest mean velocities and decreases as mean velocities begin to decelerate at 18:30. In the first half an hour, when current velocity was lowest and turbulence strength was high, turbulence intensity was at its maximum with values between 20 and 70 % at all depths (Figure 93). Once current velocities accelerated beyond 1 ms^{-1} (after 15:30) a noticeable turbulence intensity profile is discernible. Generally, the bottom third of the water column has a turbulence intensity around 15 %, the middle third has an intensity of around 10 % whilst the top third has turbulent intensities between 2 and 10 %. In the final 30 minutes, the current velocity decreased, as did the turbulence strength, but the turbulence intensity maintained this distinct vertical profile.

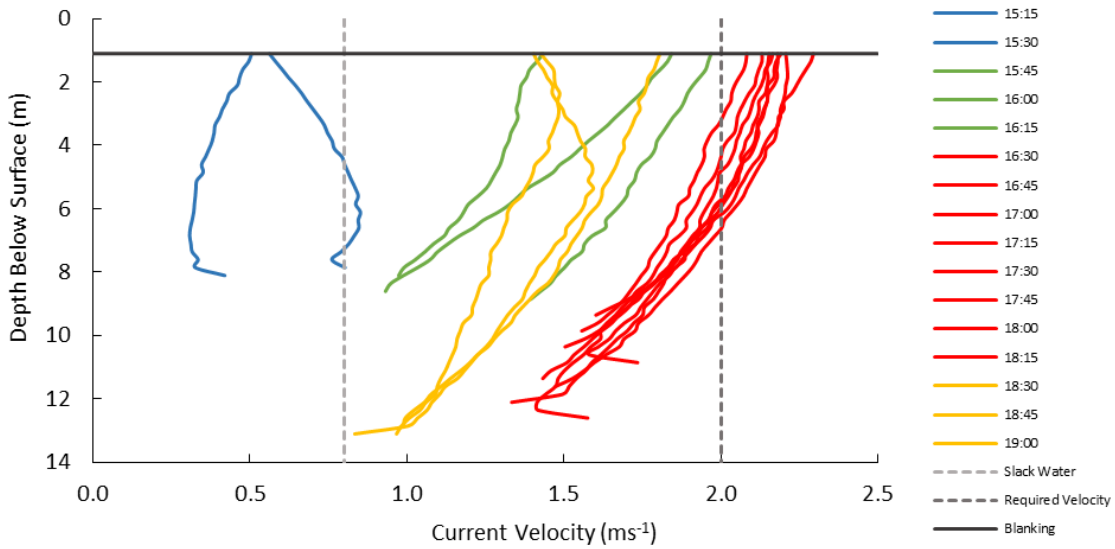

Figure 89: Spring Flood streamwise current velocity profiles (5-minute averages at 15 min intervals).

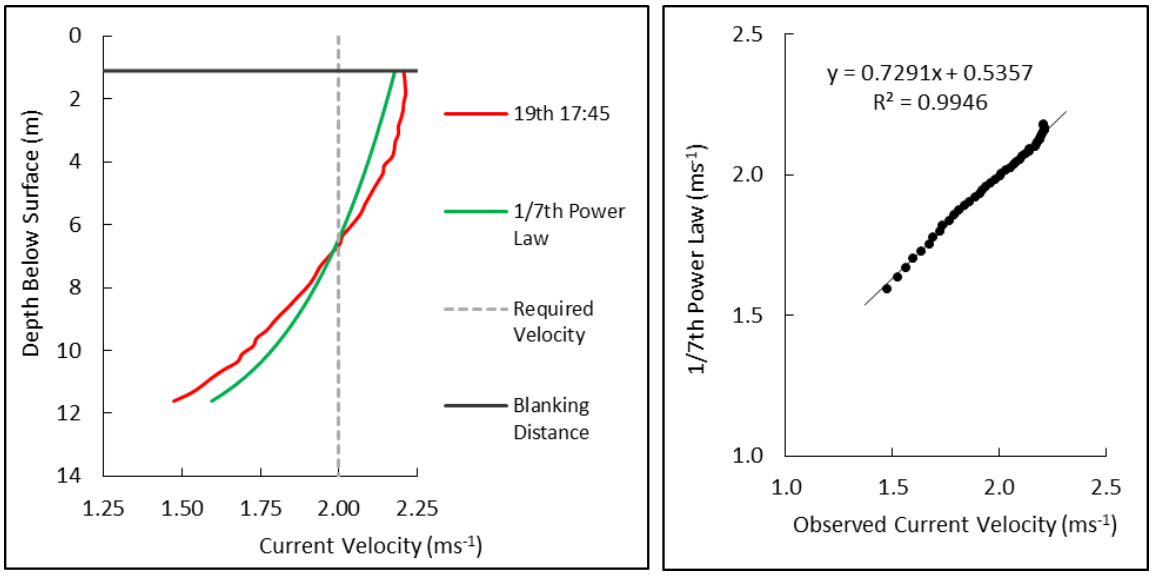

Figure 90: Peak Spring Flood flow fit to 1/7th power law.

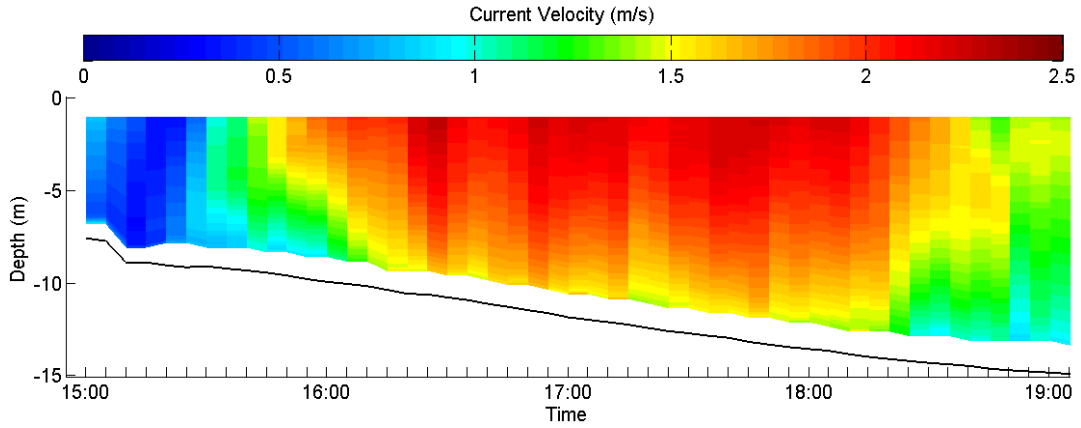

Figure 91: Spring Flood streamwise current velocity data through depth and time (using a 5-minute average).

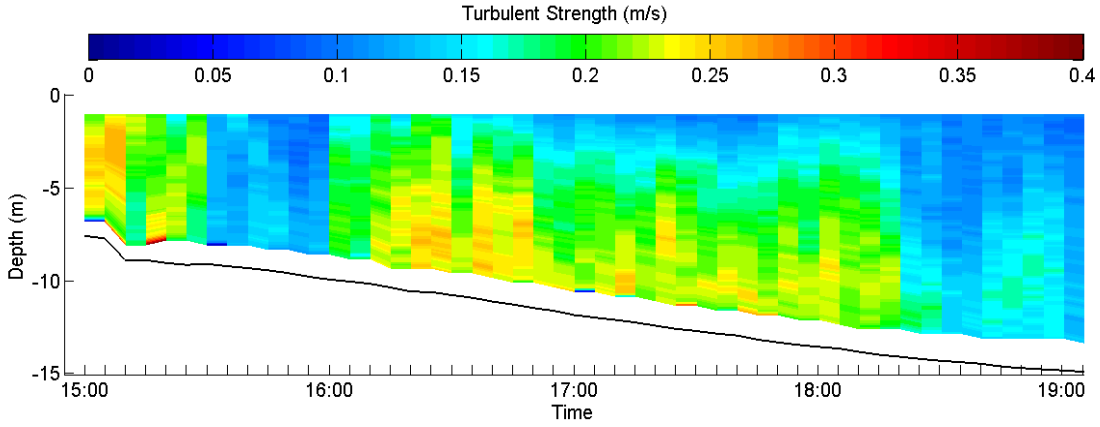

Figure 92: Spring Flood turbulence strength data through depth and time (using a 5-minute average).

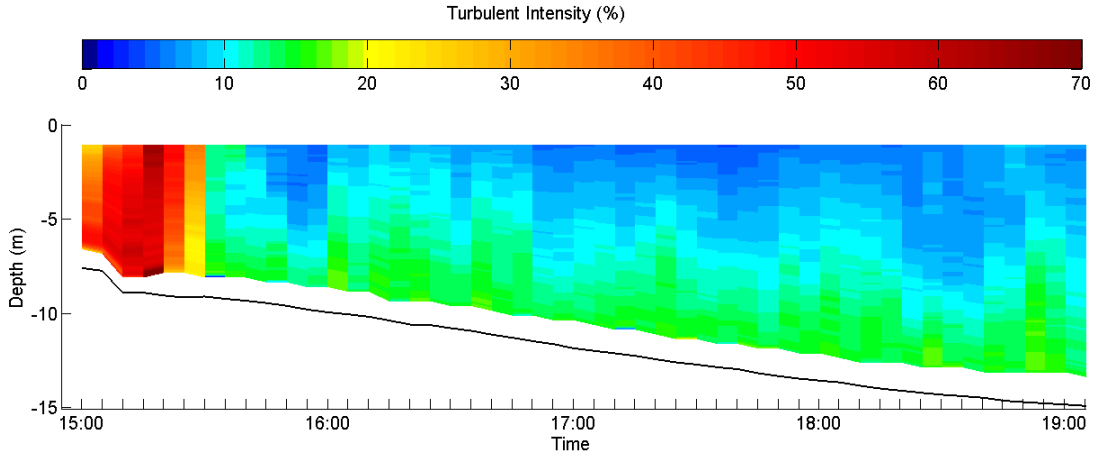

Figure 93: Spring Flood turbulence intensity data through depth and time (using a 5-minute average).

4.3.2 Static Surveys during a Neap Flood and Ebb tide

A 600 kHz ADCP was used during the Neap tide static surveys. This meant that ensembles with 0.5 m bin depths were generated at around 2 Hz with a top blanking distance of 1.36 m. Table 11 shows that the 600 kHz ADCP performed particularly well on both the Neap Flood (15 bad ensembles out of 27676) and Neap Ebb (0 bad ensembles out of 30784) surveys.

Stage	Duration of transect (secs)	Number of ensembles in transect	Number of bad ensembles in transect
Neap Flood	14 374	27 676	15
Neap Ebb	15 985	30 784	0

Table 11: Ensemble information for the Neap static ADCP surveys.

The earth velocity magnitude and direction during the Neap Flood are presented in Figure 94. Flow velocities were generally much slower than during the Spring Flood transects, as was to be expected, with a maximum current velocity of 1.7 ms^{-1} occurring close to the surface between 11:50 and 12:30. During the first hour, velocities gradually increased from 0.75 ms^{-1} near the bed to 1.2 ms^{-1} at the surface. At around 11:00 the flow took on a more typical velocity profile with the fastest flows close to the surface and decreasing with depth. This transect would have benefitted in being approximately an hour longer to capture the deceleration in flow prior to the next slack water as the flow is still around 1.25 ms^{-1} at 13:20. The flow direction fluctuated between 236 and 262 ° during the first half an hour before steadying between 245 and 255 ° for the remainder of the transect.

The earth velocity magnitude and direction during the Neap Flood are presented in Figure 95. The majority of the transect had a well-formed velocity profile, with the fastest flows at the surface and velocities decreasing towards the bed. During the first 2.5 hours flow velocities were relatively slow, ranging from 1.2 ms^{-1} close to the surface and <0.25 ms^{-1} close to the bed. There is a distinct acceleration in current velocity at 17:55 with a near-surface increase to 1.4 ms^{-1} and a subsequent near bed increase to 0.9 ms^{-1} that lasted for 1 hour. Flow velocities then decelerate beyond 19:00 but do not reach slack water velocities before the transect was stopped at low water.

It is, therefore, clear that the Neap flows were out of phase with the water depth by around 1 hour as the transect durations were based on the predicted water depth given by TotalTide but the Neap flows continued beyond expected slack waters at high and low

water respectively. During the Spring tides the flow velocities were found to be in phase with the predicted water depth and thus survey duration.

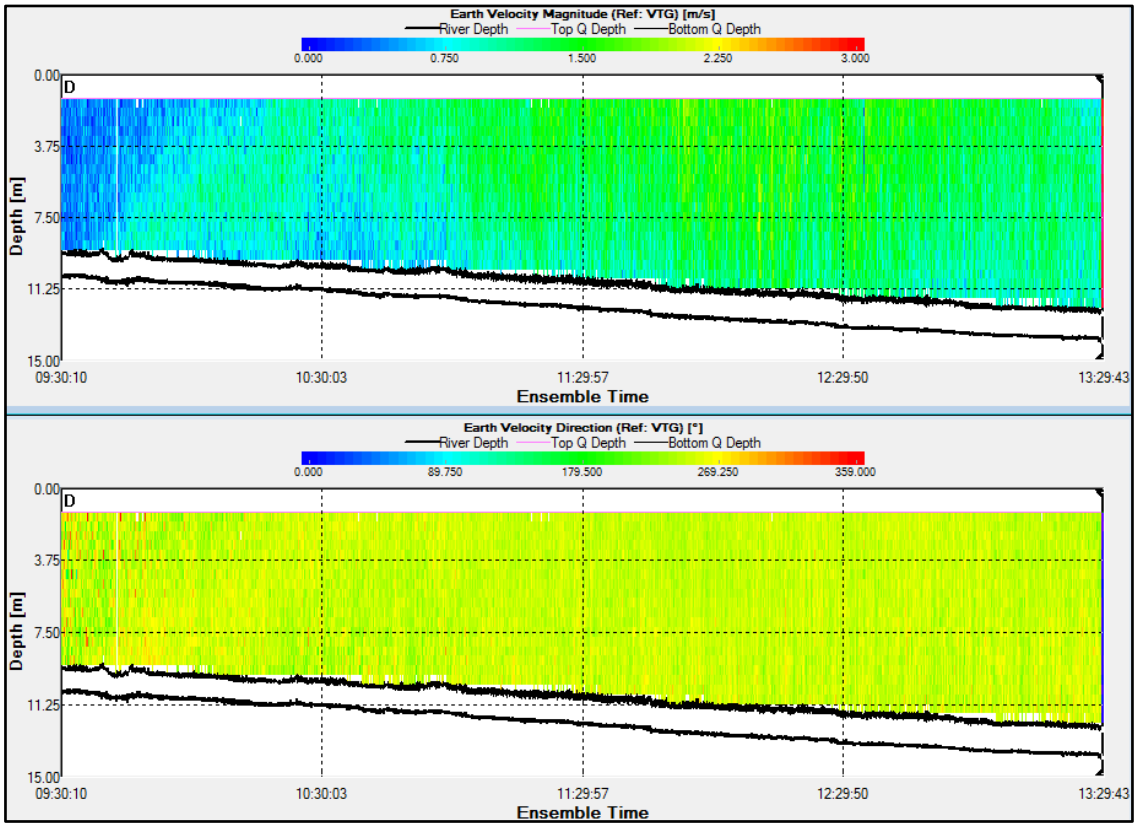

Figure 94: Earth velocity magnitude and direction during the Neap Flood tide at St. Andrews Dock.

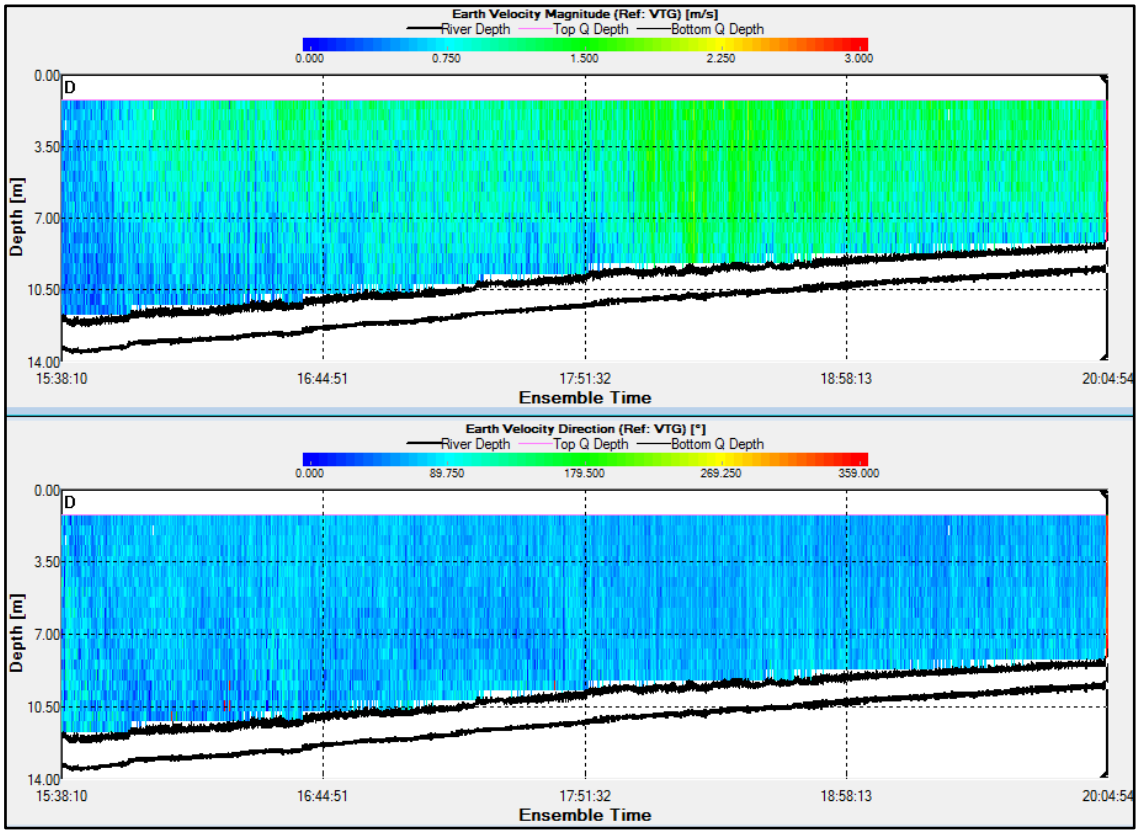

Figure 95: Earth velocity magnitude and direction during the Neap Ebb tide at St. Andrews Dock.

4.3.2.1 Neap Flood Velocity Profiles, Mean Streamwise Current Velocity, Turbulence Strength and Turbulence Intensity

Figure 96 contains a number of velocity profiles that have relatively high velocities at mid-depth compared to the surface and bed suggesting that 5 minutes may not be long enough to characterise these peak velocity profiles. Figure 97 shows the 5-minute averaged streamwise earth velocity magnitude data, which generally follows the description already provided in section 4.3.2. The time-averaged turbulence strength data collected during the Neap Flood tide are presented in Figure 98. During the lower current velocities present in the first hour there are unstructured turbulence strengths of around 0.15 ms^{-1}. However, at the same time as the maximum current velocities (11:50 to 12:30), the turbulence strength increased to its maximum of up to 0.28 ms^{-1}. Beyond peak flow, the turbulence strength decreased. During the first hour, the turbulence intensity mostly resembles the first hour of the current velocity data with high turbulent intensities up to 40 % in slower velocities and 15 % in slightly faster velocities (Figure 99). Once the Flood flow accelerates and the standard velocity profile forms, the turbulence intensity becomes more structured with higher turbulent intensities up to 25 % occurring close to the bed and lower turbulence intensities around 12 % occurring close to the surface.

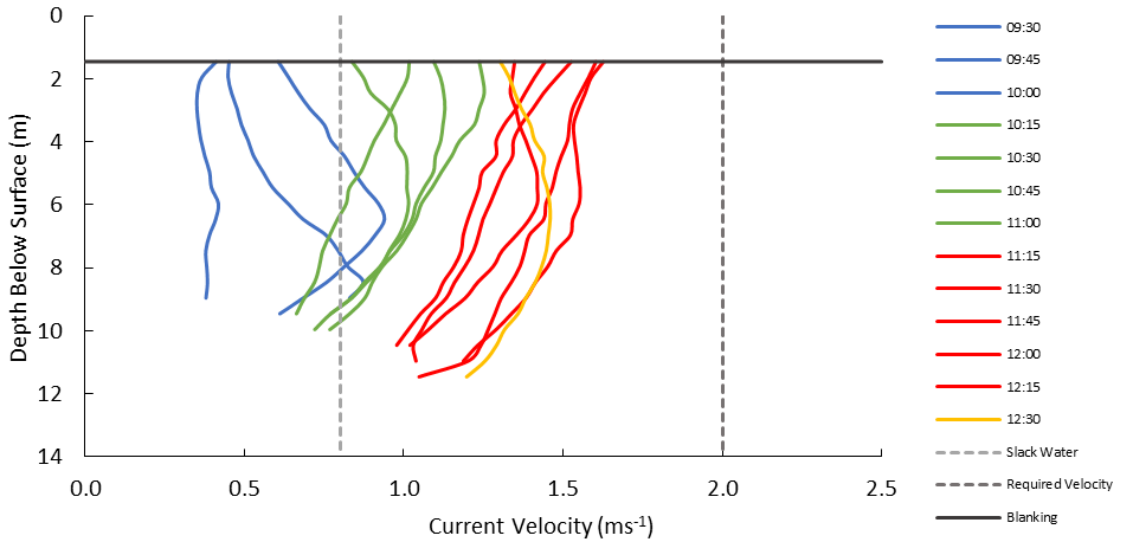

Figure 96: Streamwise current velocity profiles during Neap Flood (5-minute averages at 15-minute intervals).

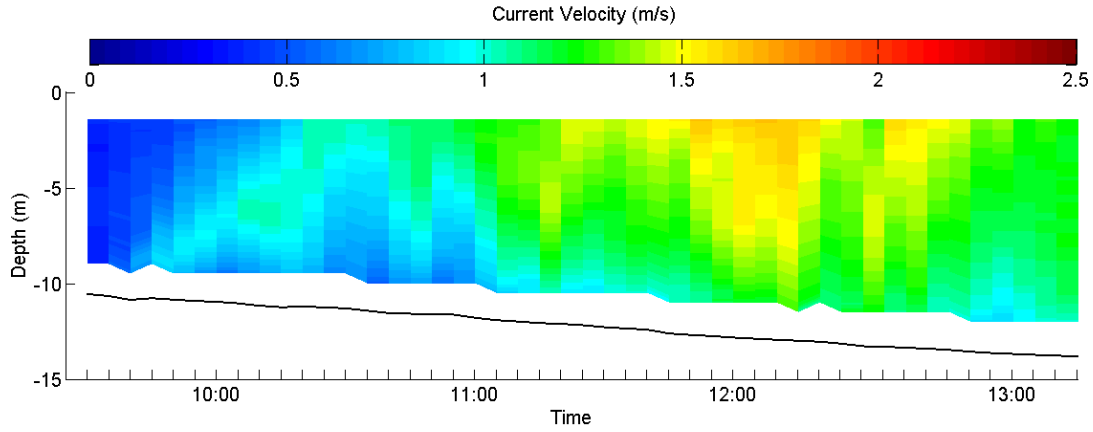

Figure 97: Neap Flood streamwise current velocity data through depth and time (using a 5-minute average).

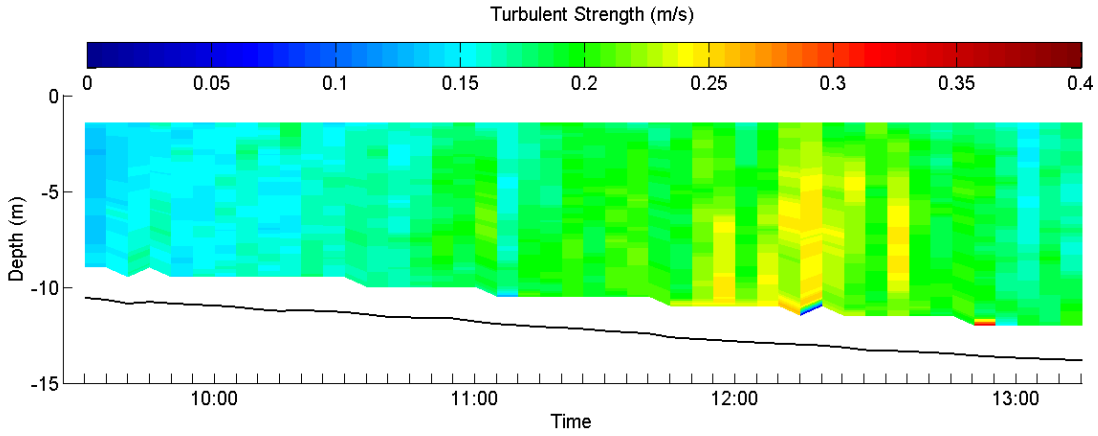

Figure 98: Neap Flood turbulence strength data through depth and time (using a 5-minute average).

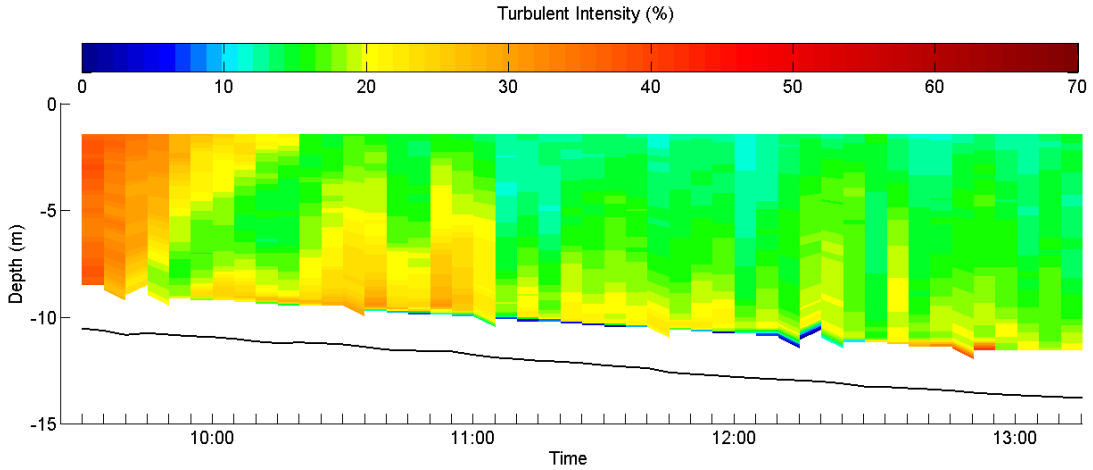

Figure 99: Neap Flood turbulence intensity data through depth and time (using a 5-minute average).

4.3.2.2 Neap Ebb Velocity Profiles, Mean Streamwise Current Velocity, Turbulence Strength and Turbulence Intensity

Figure 100 presents more typical velocity profiles but at lower overall velocities than the other three surveys. At the lowest bin of a number of profiles, an increase in velocity is observed; however, this is likely due to errors in depth-cell mapping where the blanking distance was probably not long enough. Figure 101 shows the 5-minute averaged streamwise earth velocity magnitude data, which generally follows the description already provided in section 4.3.2. The time-averaged turbulence strength data collected during the Neap Ebb tide are presented in Figure 102. Turbulence strength did not appear to vary much with depth throughout the duration of the survey. During the 2.5 hour period of slow velocities at the beginning of the transect turbulence strength ranged between 0.15 ms^{-1} and 0.2 ms^{-1}. Between 17:55 and 18:20 (when velocities were at a maximum) turbulence strength increased to between 0.2 and 0.3 ms^{-1}. As flow velocities decelerated, turbulence strength stayed relatively constant at 0.2 ms^{-1}. As the current velocity time series had a well-developed velocity profile and the turbulence strength remained constant through depth, the turbulence intensity time series followed a now familiar pattern, with higher turbulent intensities up to 40 % near the bed and decreasing with height above the bed to 15 % close to the surface (Figure 103). Between 17:55 and 18:20 (when velocities and turbulence strength were at a maximum), the turbulence intensity at a mid-depth was consistent with the near-surface value of 15 %.

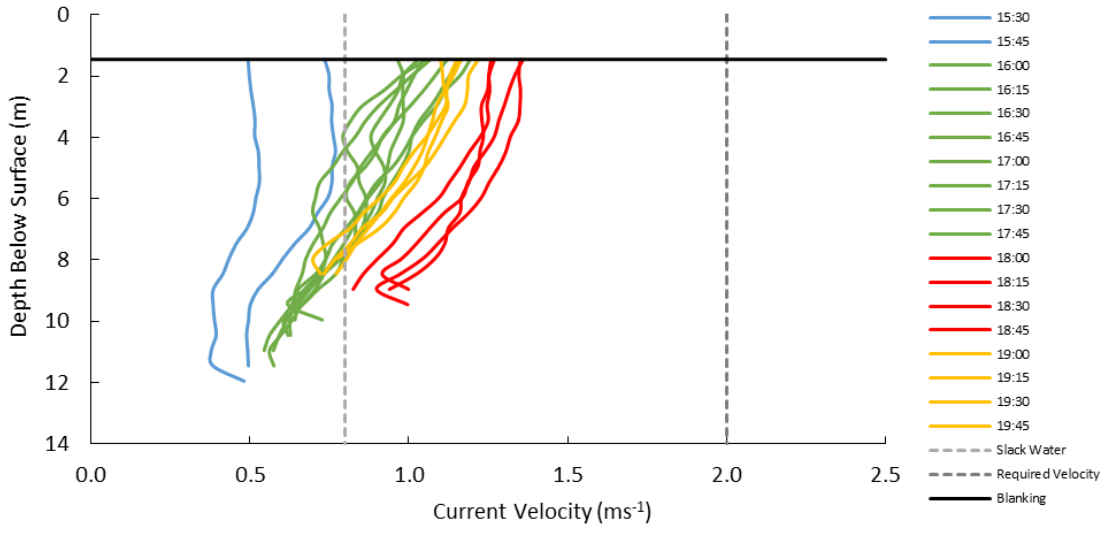

Figure 100: Streamwise current velocity profiles during Neap Ebb (5-minute averages at 15 minute intervals).

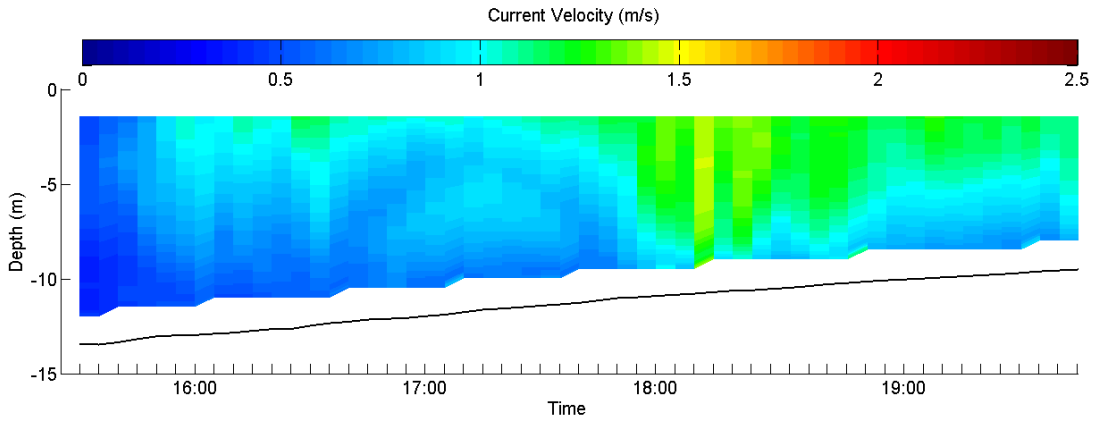

Figure 101: Neap Ebb Streamwise current velocity data through depth and time (using a 5-minute average).

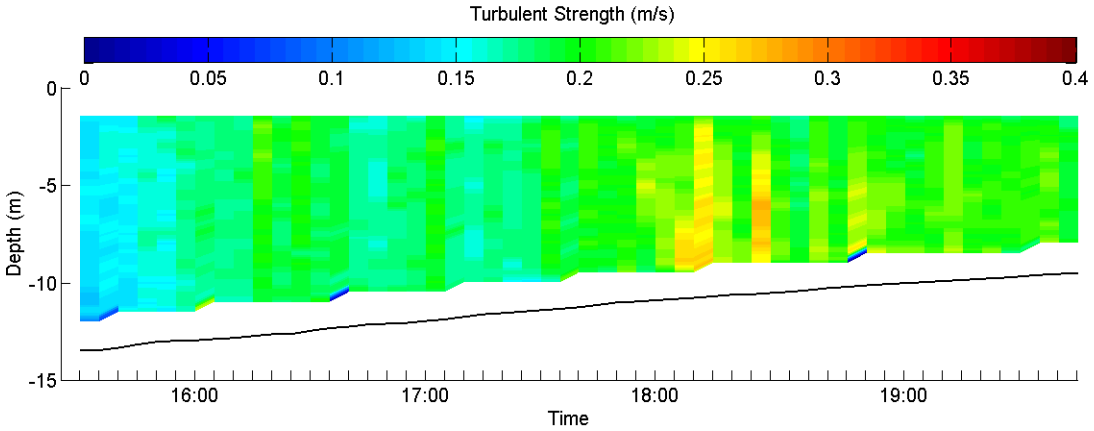

Figure 102: Neap Ebb turbulence strength data through depth and time (using a 5-minute average).

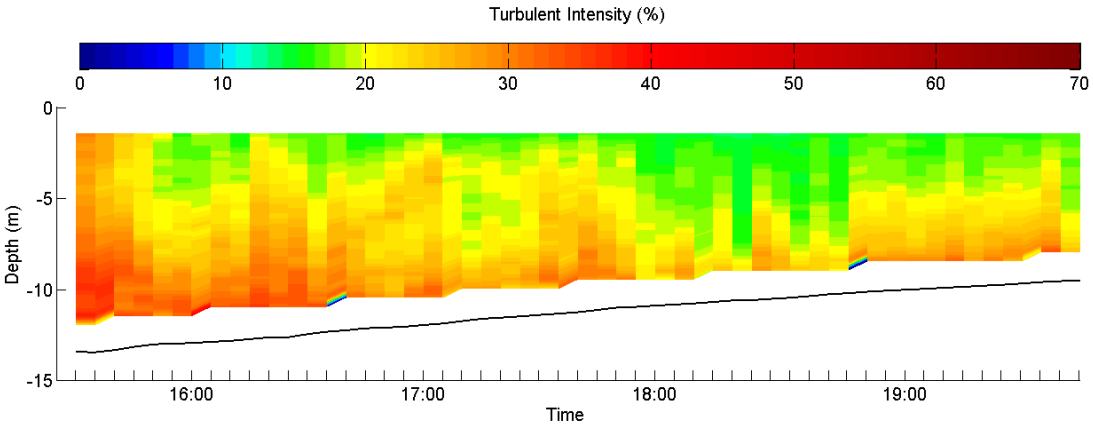

Figure 103: Neap Ebb turbulence intensity data through depth and time (using a 5-minute average).

4.3.3 Understanding the Vertical Distribution of Turbulence Intensity

Analysing such relationships through depth, *in situ*, is complicated by the fact that the water depth changes throughout the tidal cycle meaning that the measurement depth is constantly changing along with the current velocity. At the St. Andrews Dock site, depth-averaged flows in excess of 1.5 ms^{-1} are observable during peak flow. Lesser velocities (1 to 1.5 ms^{-1}) actually occur twice during a semi-diurnal tidal cycle as they occur during accelerating and decelerating periods (either side of peak flow) and each period has considerably different average water depths. Figure 104 compares the average water depth and depth-averaged current velocities between the four tidal cycles. It can be seen that during each tidal cycle, similar current velocities occur at varying depths because of the changing tidal height throughout each tidal cycle. The effect is most pronounced during the Flood tidal cycles, which means that it is likely that the depth of water and not simply current velocity also affects the turbulence intensities vertical distribution.

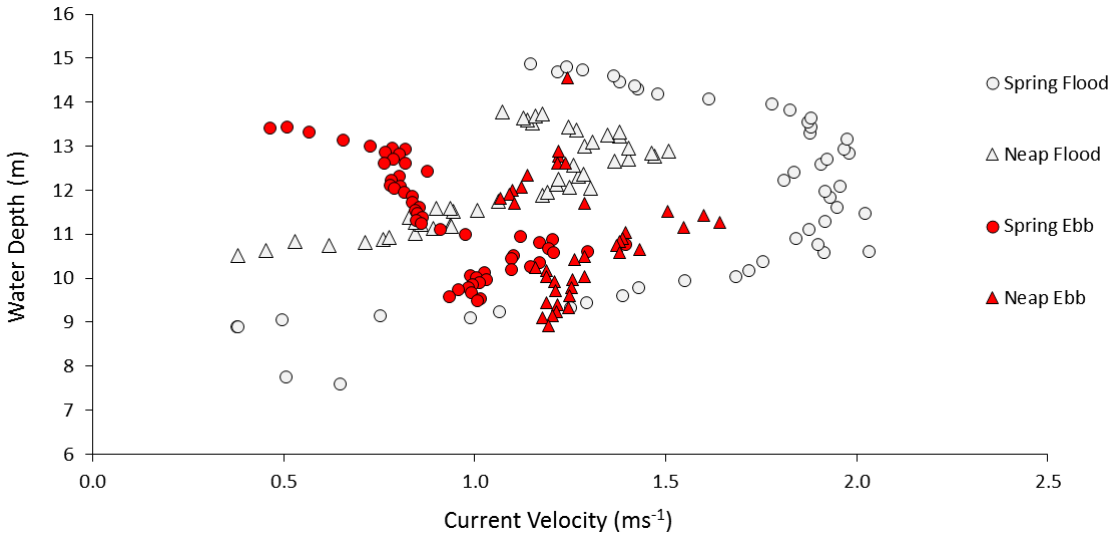

Figure 104: Comparison of simultaneous water depth and current velocity between tidal cycles.

Figure 105 demonstrates this by comparing the tidal current velocity with the turbulence intensity measured at every bin during the Spring Flood survey whilst also highlighting bin depth. It clearly shows that the bins with the lowest turbulence intensity (5 to 8 %) occurred close to the surface and that the highest turbulence intensities (12 to 18 %) were recorded in the deepest waters measured. It also shows that at, for example, 1.5 ms^{-1} there is a distinct variation in turbulence intensity through depth with values close to 6 % measured near the surface whilst values between 13 and 18 % are found in depths greater than 10 m. Two obvious diagonal groupings (from left to right) are divided by a space with

few data. This is considered to be a divide between the peak flow (right) and the accelerating and decelerating flows (left). The absence of data in between is thought to be because of the rapid increase in turbulence strength and thus turbulence intensity at 16:00 and subsequent rapid decrease at 18:20. Figure 106 displays similar data for the Neap Flood. It can be seen that a similar pattern exists whereby the lowest turbulence intensities are found in the near-surface flow and turbulence intensity increases as depths increase.

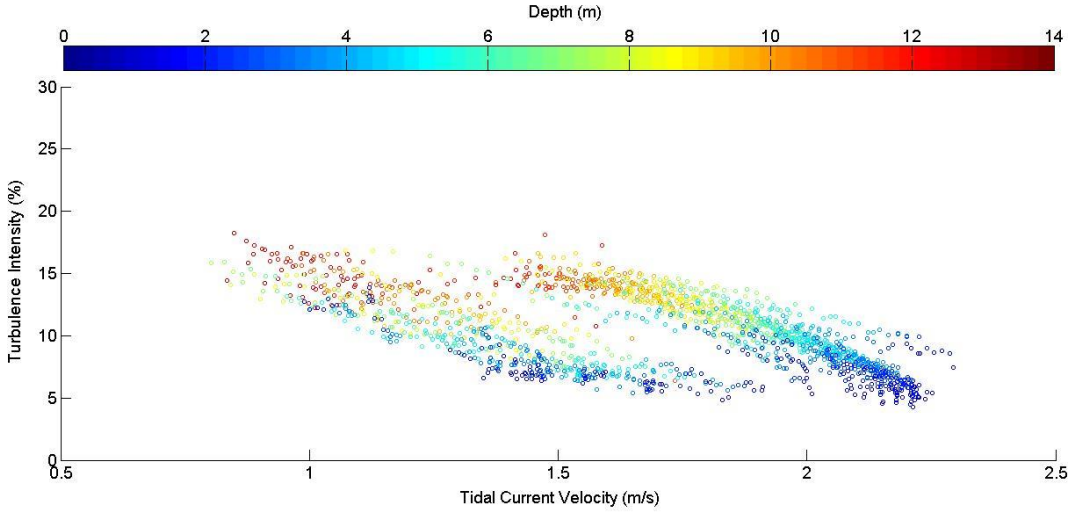

Figure 105: Comparison of tidal current velocity, turbulence intensity and depth during the Spring Flood between 15:35 and 19:00.

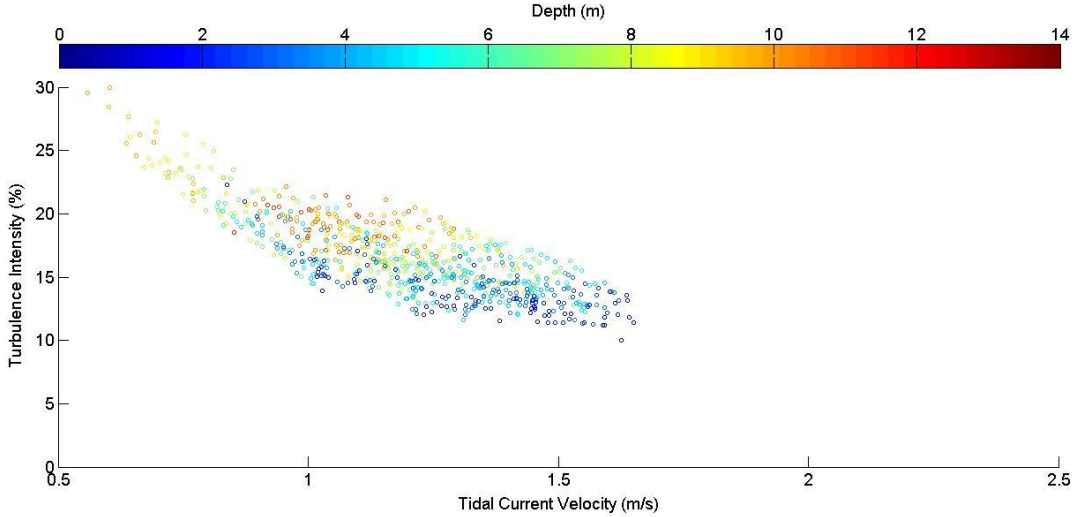

Figure 106: Comparison of tidal current velocity, turbulence intensity and depth during the Neap Flood between 10:15 and 13:15.

4.3.4 Summary of the ADCP Fieldwork

Overall the static vessel-mounted ADCP surveys produced very reliable results in which the vast majority of ensembles were considered 'good' by WinRiver II's internal quality checks. The Spring Ebb survey contained a large number of bad ensembles, which remain unexplained. It was found that the Spring Flood data contained the fastest peak velocities of the four surveys and that the Flood tides were generally faster than the Ebb tides across both Spring and Neaps. Generally, turbulence strength was found to increase during peak velocities and did not vary much with depth, though, as velocity varied with depth close to the $1/7^{th}$ power law, turbulence intensity was found to be higher nearer the bed than at the surface as well as being higher at shallower depths either side of peak flow. A simultaneous bed-mounted ADCP deployment at the same site would have been desirable in order to validate the vessel-mounted data but this was simply not possible yet could be incorporated into future experiments.

4.4 Comparison of Results with the Literature

Important parameters derived from papers that present relevant *in situ* data are directly compared to the results of this research in Table 12. The literature are presented in chronological order and further divided between fieldwork instrumentation (ADCP, ADV or EMCM) and focus on tidal and/or wave measurements. Papers included in Table 12 report turbulence strength and intensity over a sample duration between 5 and 20 minutes and a sampling frequency between 1 and 4 Hz (with the exception of two ADV deployment, which measured between 10 and 32 Hz). The fieldwork conducted in this thesis used durations and frequencies that fell between theses ranges allowing for direct comparisons. Typically, point measurements are made at a height above the bed close to the anticipated hub height of a bed-mounted TST (often ~5 m). A number of ADCP methodologies were able to measure over a wider range of depths (typically between 0.5 and 20 m above the seabed). When looking at the height above bed/water depth ratio (z/h) it becomes clear that although this research measured in shallower water depths and much closer to the bed than a TST hub height the measurement height is proportional to the measurements of other papers, thus allowing direct comparisons.

Papers tend to report turbulence intensity more frequently than turbulence strength. Generally, turbulence intensity measured at peak flow velocity ranges between 6 and 15 %, as was measured during both of the fieldworks conducted as part of this research. The data reported by MacEnri *et al.* (2013) contain by far the greatest peak flow measurements (3.9 ms^{-1}) and also the lowest turbulence intensity value (6 %).

The wave heights recorded during the DWR fieldwork were generally much lower than other reported wave-current interaction papers that measured at exposed sites with significant wave heights greater than 1.5 m. Whilst Boufferouk *et al.* (2016) had a lower peak flow and a higher turbulence intensity at peak flow value than the DWR results, it is hard to draw any significant conclusions from this comparison as they used a significantly different methodology to measure through depth. Therefore, a significant number of reported, *in situ*, wave-current research using the same methodology in different locations is needed before direct comparisons between sites will have any further meaning.

Reference	Location	Measure	Instrumentation	Deployment methodology	Deployment duration (days)	Sampling frequency (Hz)	Sampling duration (mins)	Measurement height from seabed (z) (m)	Water depth (h) (m)	*Height depth ratio (z/h)*	*Peak flow ($\bar{U}$)* (ms^{-1})	Turbulence strength at peak flow (U_σ) (ms^{-1})	Turbulence intensity at peak flow (I_T) (%)	Significant wave height (Hs) (m)
Osalusi *et al.*, 2009	Fall of Warness, UK	Tidal	600 kHz ADCP	Bed-mounted	7	2	17	5	42	0.12	1.5	-	11	-
Thomson *et al.*, 2012	Puget Sound, USA	Tidal	- kHz ADV	Bed-mounted	4.3	32	5	4.7	22	0.21	1.7	-	9	-
Thomson *et al.*, 2012	Puget Sound, USA	Tidal	600 kHz ADCP	Bed-mounted	17	2	5	3.2 - 20.6	22	0.15 - 0.94	1.7	-	11	-
Milne *et al.*, 2013	Sound of Islay, UK	Tidal	- kHz ADV	Bed-mounted	15	4	5	5	55	0.09	2.5	0.32	13	-
MacEnri *et al.*, 2013	Strangford Narrows, UK	Tidal	EMCM	Fixed to TST	-	1	10	14	24	0.58	3.9	0.2	6	-
Gunawan *et al.*, 2014	East River, USA	Tidal	10 MHz ADV	Bed-mounted	16	10 & 20	5	4.25	-	-	2.4	0.28	12	-
Jeffcoate *et al.*, 2015	Strangford Lough, UK	Tidal	600 kHz ADCP	Vessel-mounted	48	2	4	0.5 - 16.3	9.6 - 15.8	0.27 - 0.97	2.1	-	16	-
Filipot *et al.*, 2015	English Channel, UK	Tidal and Wave	600 kHz ADCP	Bed-mounted	3	2	20	-	43	-	1.5	0.25	-	1.5 - 3
Bouferrouk *et al.*, 2016	Bristol Channel, UK	Tidal and Wave	300 kHz ADCP	Bed-mounted	11	2	17	6.2 - 36	40	0.16 - 0.9	0.9	-	15	0.5 - 3.3
Hardisty and Jennings, TBC	Humber Estuary, UK	Tidal and Wave	DWR (EMCM)	Bed-mounted	18	4	4	0.4	0 - 6	0.05 - 0.15	1.1	0.08	8	0 - 0.8
Hardisty and Jennings, 2016	Humber Estuary, UK	Tidal	1200 and 600 kHz ADCP	Vessel-mounted	2	1 & 2	5	0.5 - 13.5	7 - 14	0.03 - 0.97	2	0.27	10	-

Table 12: Comparison of relevant literature and thesis results.

4.5 Conclusion

This chapter described and explained the results generated from the ADCP and DWR fieldwork. These results are used in the following analysis and discussion chapter to meet the three thesis objectives. Prior to regression analysis, all results appear to suggest that turbulence strength increases in relation to the mean current velocity and that neither water depth nor wave-current interaction appear to have a significant influence on this relationship. As a result, turbulence intensity decreases with increased mean current velocity, in agreement with the literature. These relationships are quantitatively modelled in the following sections.

5 Analysis and Discussion

5.1 Introduction

This chapter analyses the results of the directional wave recorder (DWR) and acoustic Doppler current profiler (ADCP) fieldwork in order to better understand and to model turbulence strength and intensity at a point ignoring wave-current interaction (Objective 1), at a point including wave-current interaction (Objective 2) and through depth ignoring wave-current interaction (Objective 3) (see Table 13). Previous literature has presented figures that describe such relationships yet rarely attempt to empirically model or compare such relationships; these are the key contributions made to the field within this thesis. When modelling at a point, a distinction is made between inter-tidal and intra-tidal analysis where inter-tidal refers to data taken over multiple Flood and Ebb tides (i.e. over a Spring-Neap cycle) and intra-tidal refers to data within a single tidal phase (i.e. a single Flood or Ebb tide lasting approximately 6 hours). Within each Objective section, the most relevant literature that supports or opposes the objective findings are discussed and the implications of such findings on tidal stream power EYAs are demonstrated.

Measure	**Ignoring Wave-Current Interaction**	**Including Wave-Current Interaction**
At a point	Objective 1 (section 5.2)	Objective 2 (section 5.3)
Through depth	Objective 3 (section 5.4)	Recommendations (section 5.6)

Table 13: Structure of the analysis chapter

Following these sections, a summary of the key findings is made (section 5.5). The model results from the Humber are quantitatively compared with published literature made elsewhere. Because the model results share numerous similarities with other sites it is then argued that the models created here can be used by the tidal stream power industry to estimate turbulence metrics as a function of mean current velocity and depth at a site prior to development. Next, an evaluation of the methodology is provided to identify key strengths and limitations in order to inform the final section that explores recommendations for future work (section 5.6).

5.2 Analysis and Discussion of Objective 1:

Model the relationship between turbulence strength, intensity and mean current velocity at a point, ignoring wave-current interaction.

5.2.1 Introduction

As discussed in the literature review, a number of authors have recently presented figures which describe the relationship between turbulence strength, intensity and mean current velocity at a point within strong tidal streams (see for example MacEnri *et al.* (2013) (Figure 21), Gunawan *et al.* (2014) (Figure 19) and McCaffrey *et al.* (2015) (Figure 18)). These observed relationships have yet to be empirically modelled. An empirical approximation of turbulence, when given a streamwise mean current velocity, would be useful for tidal EYAs as this could be used to anticipate TST performance and fatigue at various locations. Here, the results of the DWR fieldwork in the hypertidal Humber Estuary are used to model these relationships empirically at a point. Section 5.2.2 first focuses on modelling turbulence strength then section 5.2.3 focuses on modelling turbulence intensity. The influence of wave-current interaction on these models is ignored in Objective 1 but explored in Objective 2.

5.2.2 Modelling the Relationship between Turbulence Strength and Mean Current Velocity at a Point, Ignoring Wave-Current Interaction

In Chapter 4, Figure 81 identified that the mean current velocity and the turbulence strength appeared to be correlated through time as both closely followed the typical Spring-Neap-Spring pattern. Figure 107 shows the relationship between streamwise mean current velocity and turbulence strength in water depths greater than 2 m (to avoid the non-linear effects of the surf zone) during both Flood and Ebb tide throughout the 18-day deployment at Foul Holme Spit. Lines of best fit have been left off this graph as various regression techniques are later used to quantify these relationships in Table 14 and Table 15. A strong positive correlation is evident between mean current velocities of 0 and 0.45 ms^{-1} which appears to be linear. Beyond 0.45 ms^{-1} this correlation diminishes and turbulence strength appears to level off at a value between 0.06 and 0.11 ms^{-1}. There does not appear to be a significant difference between this correlation during the respective Flood and Ebb data.

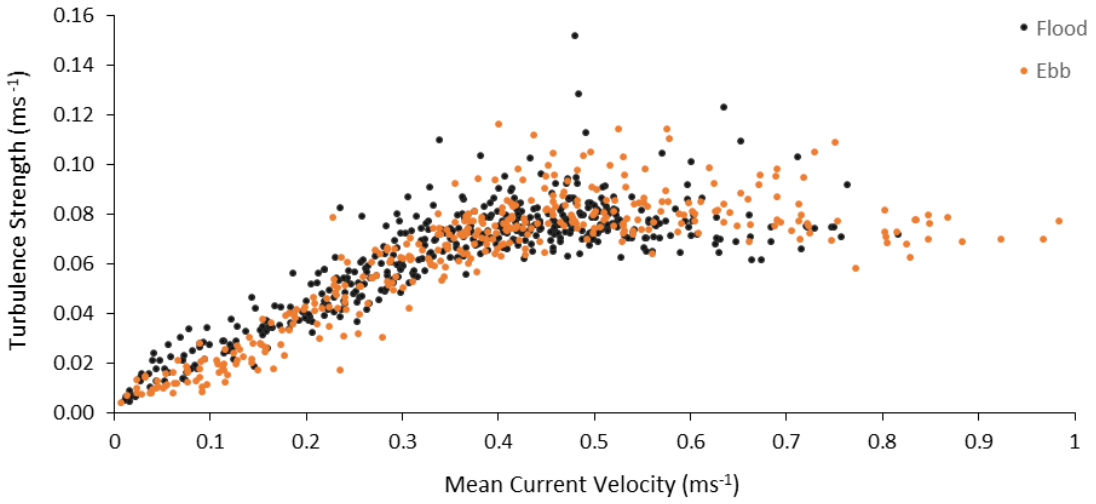

Figure 107: Relationship between mean current velocity and turbulence strength throughout Flood and Ebb tides.

5.2.2.1 Inter-tidal Linear Regression

In Table 14, linear regression analysis is used to test the inter-tidal relationships between mean current velocity, $\bar{U}$, and turbulence strength, $U\sigma$, over the whole deployment (All), and separately for the Flood and Ebb tides following Equation 23

$$U_\sigma = a + b\,\bar{\mathrm{U}} \tag{23}$$

Where a is the intercept and b is the gradient. In Table 14, N represents the number of data points used in the linear regression. The linear relationships are statistically significant at the 95% confidence interval with p-values less than 0.05. Therefore, the null hypothesis of there being no statistically significant relationship can be rejected. When taking into account 'All' wave burst samples, an R^2 of 0.6232 suggests a strong linear relationship with a slightly stronger linear relationship found in the Flood samples (R^2 = 0.6451) than during the Ebb samples (R^2 = 0.6176).

	N	a	b	R^2	P-Value
All	812	0.0252	0.1014	0.6232	0.0000
Flood	437	0.0247	0.1073	0.6451	0.0000
Ebb	375	0.0241	0.0986	0.6176	0.0000

Table 14: Linear regression analysis of the whole deployment (All), Flood and Ebb tide between streamwise mean current velocity and turbulence strength.

5.2.2.2 Inter-tidal Power Regression

Because of the curve in the inter-tidal relationship between turbulence strength and streamwise mean current velocity, linear regression is not the most suitable statistical test to apply to this dataset. Power regression suggests that a relationship, in the form

$$U_\sigma = \alpha \bar{U}^\beta \tag{24}$$

presents higher R^2 values as opposed to the equivalent linear models. Table 15 shows that R^2 values are much greater than in Table 14 with a maximum of 0.8721 in the case of the Flood data. The power relationships are statistically significant at the 95% confidence interval with p-values less than 0.05. Therefore, the null hypothesis of there being no statistically significant relationship can be rejected. Values of α and β are relatively consistent between these three tests suggesting that flow direction does not have a significant effect on this relationship at this particular site, as illustrated by Figure 107. The inter-tidal α value for 'All' samples is 0.1298 and the β value is 0.7154. These values are later used to test against the ADCP data (section 5.4.3) and results from relevant literature (section 5.5.1).

	N	α	β	R^2	P-value
All	812	0.1298	0.7154	0.8510	0.0000
Flood	437	0.1279	0.6683	0.8721	0.0000
Ebb	375	0.1307	0.7657	0.8543	0.0000

Table 15: Power regression analysis of the whole deployment (All), Flood and Ebb tide between streamwise mean current velocity and turbulence strength.

5.2.2.3 Intra-tidal Power Regression

Whilst the previous tests have focused on the inter-tidal relationship between mean current velocity and turbulence strength over the 18-day Spring-Neap-Spring cycle it is important to understand how the intra-tidal relationship between streamwise mean current velocity and turbulence strength changes at a higher frequency, for example, over each semi-diurnal tidal cycle through Flood and Ebb. As power regression produced the statistical test with the highest R^2 value, power relationships were determined for each consecutive Flood and Ebb tidal phase of which the α, β, and R^2 values are presented as time series in Figure 108. The values of α varied throughout the deployment between 0.09 and 0.25, whilst values of

β varied between 0.4 and 1.2. R^2 values varied between 0.62 and 0.99 indicating that a high percentage of the data fit the power model. During the Neap tides (tidal cycles 20 - 40) there was little fluctuation between α, β and R^2 values; however, during the Spring tides there appeared to be more obvious fluctuations between consecutive tidal cycles indicating that there was subtle, yet mostly consistent, differences between Flood and Ebb cycles. There also appears to be a strong linear relationship between α and β values following

$$\beta = 4.0914\alpha + 0.1773$$

with an R^2 value of 0.6185.

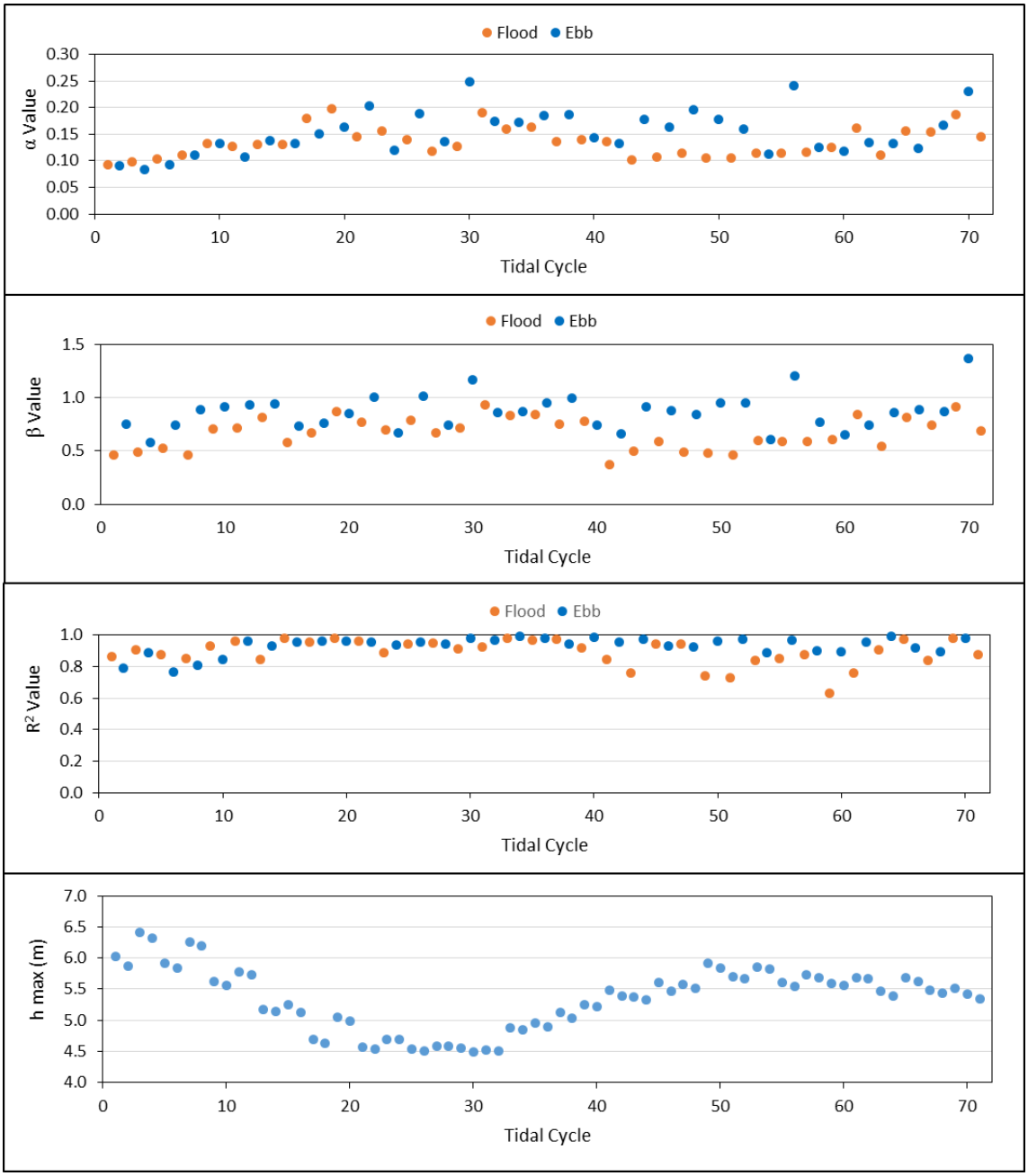

Figure 108: a, β, R² and a vs β values calculated for every Flood and Ebb tidal cycle during the DWR deployment.

Since it has been demonstrated that the α and β values can be used to model the relationship between mean current velocity and turbulence strength the intertidal variation throughout the deployment remains poorly understood. The calculated α and β values were tested against three variables independent of the mean current velocity to identify further correlations (Figure 109). Firstly, the maximum water depth, *h*, during each tidal cycle was calculated to capture the effects of the Spring-Neap tides. Then, the average significant wave height, H_S, and zero-crossing period, T_Z, throughout each cycle were calculated and tested against the respective α and β values. It is clear from linear regression analysis that correlation between these variables and both the α and β values is very weak, with the water depth having the greatest negative correlation with an R^2 of just 0.2724.

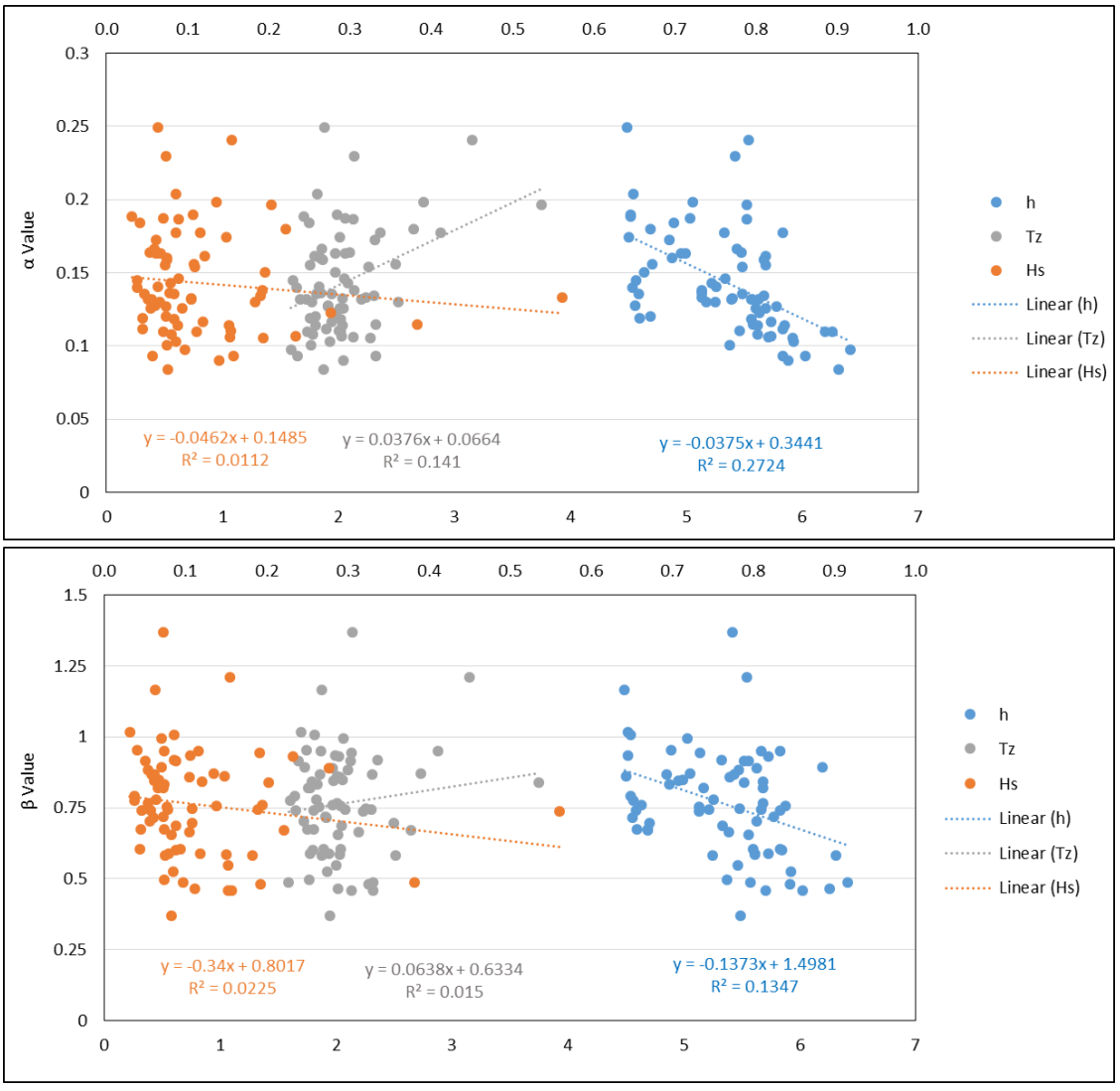

Figure 109: Relationship between water depth, significant wave height and zero-crossing period and values of α and β.

5.2.2.4 Summary of Findings

From this analysis it was determined that the inter-tidal relationship between streamwise mean current velocity and turbulence strength can be modelled with high R^2 values (0.8721) using power regression where α is 0.13 and β is 0.72. There did not appear to be a significant difference between values of α and β between Flood and Ebb flow directions. Power regression on intra-tidal relations found that α an β values can empirically model the relationship between mean current velocity and turbulence strength, though an analytical solution to predicting α and β values remains to be solved as water depth and surface wave parameters do not seem to have a significant influence on α and β.

Hence, it is considered that upstream bathymetry and bed roughness coefficients (which were not measured) may have changed during the duration of the deployment thus causing different levels of turbulence strength occurring at the measuring location, which in turn altered the values of α and β through time. This potential effect should be explored in further research; either in laboratory flumes or via *in situ* observations (see section 5.6.4 for a detailed recommendation for further research).

5.2.3 Modelling the Relationship between Turbulence Intensity and Mean Current Velocity at a Point, Ignoring Wave-Current Interaction

The streamwise mean current velocity is plotted against the turbulence intensity in Figure 110. A familiar observed relationship emerges (see Figure 17, Figure 18, Figure 20, Figure 22 and Figure 23) whereby there is high scatter at low velocities (0 - 0.1 ms^{-1}, 8 - 58 %), medium scatter at mid-velocities (0.1 - 0.8 ms^{-1}, 10 - 35 %) and low scatter at higher velocities (>0.8 ms^{-1}, 6 - 11 %). Like the equivalent test using turbulence strength in Figure 107, there are no significant differences between Flood and Ebb data.

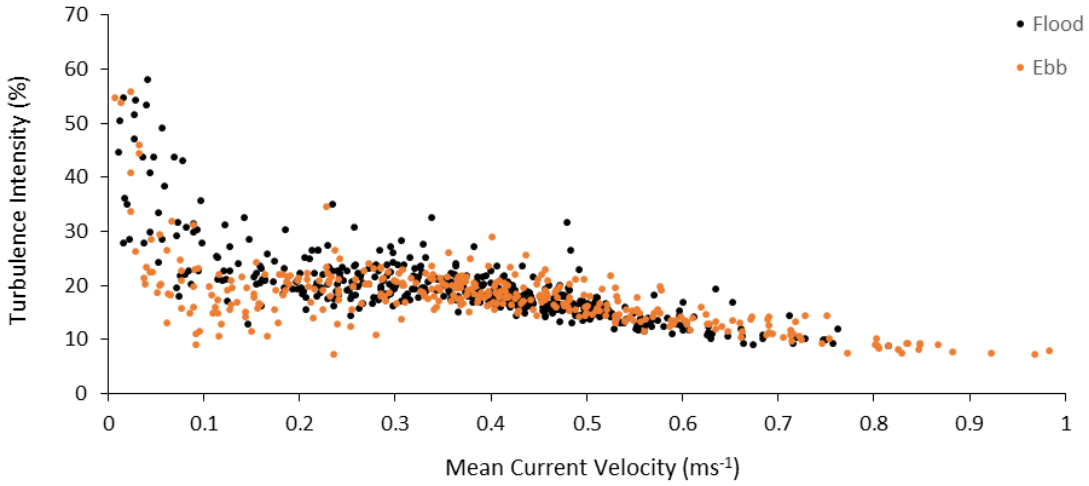

Figure 110: Relationship between mean current velocity and turbulence intensity throughout Flood and Ebb tides.

5.2.3.1 Inter-tidal Power Regression

In order to empirically model this relationship it can be seen that a linear regression is not appropriate due to the curved relationship observed, particularly between 0 and 0.35 ms^{-1}; therefore, the relationship can again be modelled using power regression in the form:

$$I_T = \gamma \bar{U}^{\delta} \quad (25)$$

Table 16 shows that this model produces R^2 values that are generally lower than the model used for turbulence strength (Table 15) with 0.5482 for 'All' tidal cycles and 0.4112 and 0.662 for Flood and Ebb respectively. The power relationships are statistically significant at the 95% confidence interval with p-values less than 0.05. Therefore, the null hypothesis of there being no statistically significant relationship can be rejected. The γ value for 'All' is 14.315 and the δ value is -0.2316.

	N	γ	δ	R^2	P-value
All	812	14.315	-0.2316	0.5483	0.0000
Flood	437	15.276	-0.134	0.4112	0.0000
Ebb	375	13.4202	-0.3264	0.662	0.0000

Table 16: Power regression analysis of the whole deployment (All), Flood and Ebb tide between streamwise mean current velocity and turbulence intensity.

5.2.3.2 Intra-tidal Power Regression

It is important to understand how these relationships change between Flood and Ebb tidal cycles; therefore, Figure 111 shows how the values γ and δ varied throughout the measured duration of the deployment. Values for γ varied between 8 and 24 with some irregular oscillations whilst δ values varied between 0.57 and 0.38 with some irregular oscillations that coincide with the oscillations present in the γ time series. R^2 values vary throughout the deployment between 0 and 1. The reason for very low R^2 values in some of these regressions is that if the turbulence intensity is very low (<10 %) during low velocities (<0.2 ms^{-1}) the power trend does not exist and R^2 values fall. It is, therefore, important to measure turbulence intensities in low velocities as well as high velocities in order to obtain this trend. The correlation between γ and δ values appears much weaker than observed in the equivalent turbulence strength analysis.

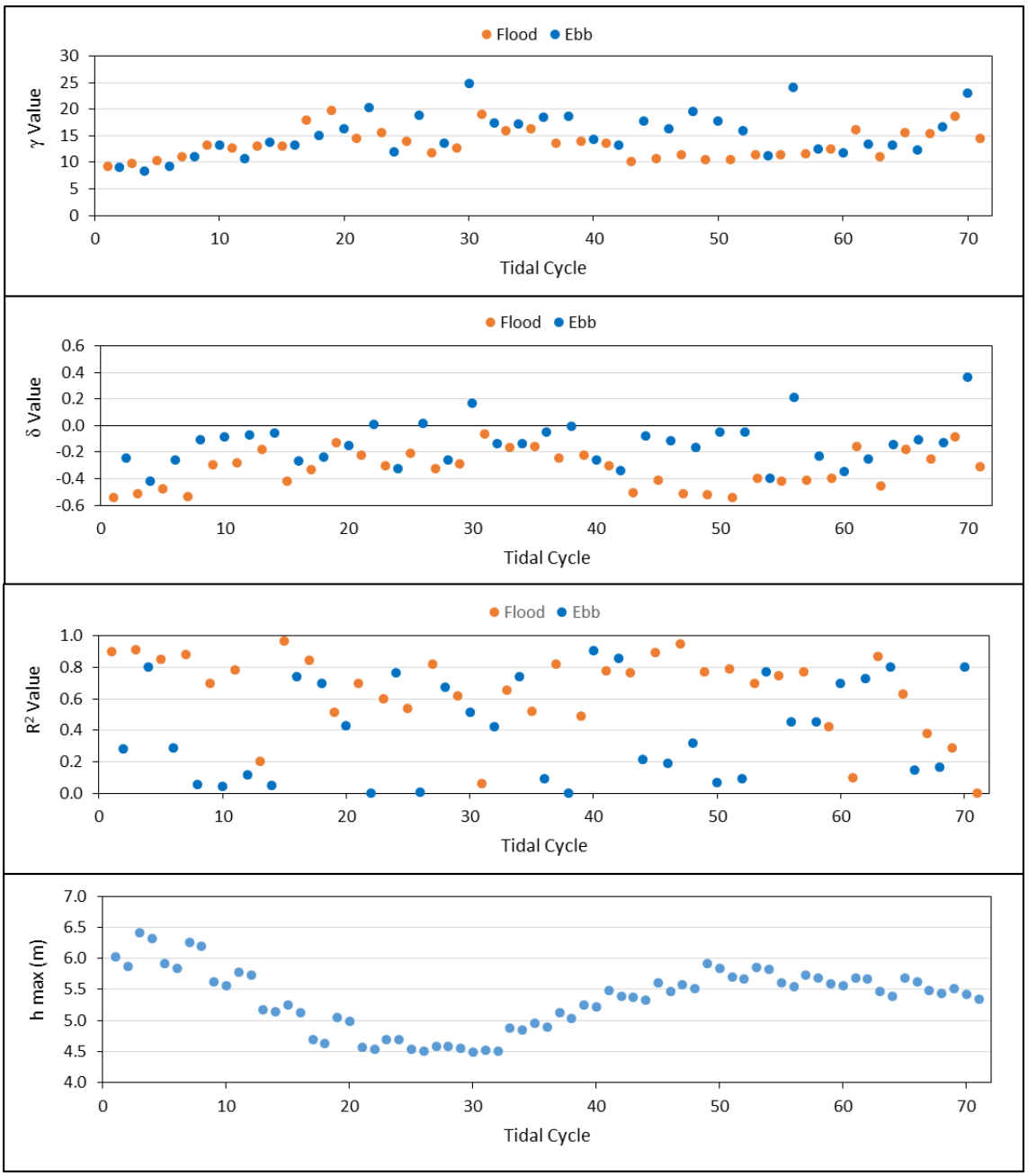

Figure 111: γ, δ, R² and γ vs δ values calculated for every tidal cycle during the DWR deployment.

As the power trends did not produce very high R^2 values it was considered that the same confounding variables (as tested in Figure 109) may exist and were therefore tested in Figure 112. Much like in the turbulence strength data, no obvious relationships between these variables and the modelled values were observed. This is because α and γ are very highly correlated whilst β and δ are not as highly correlated.

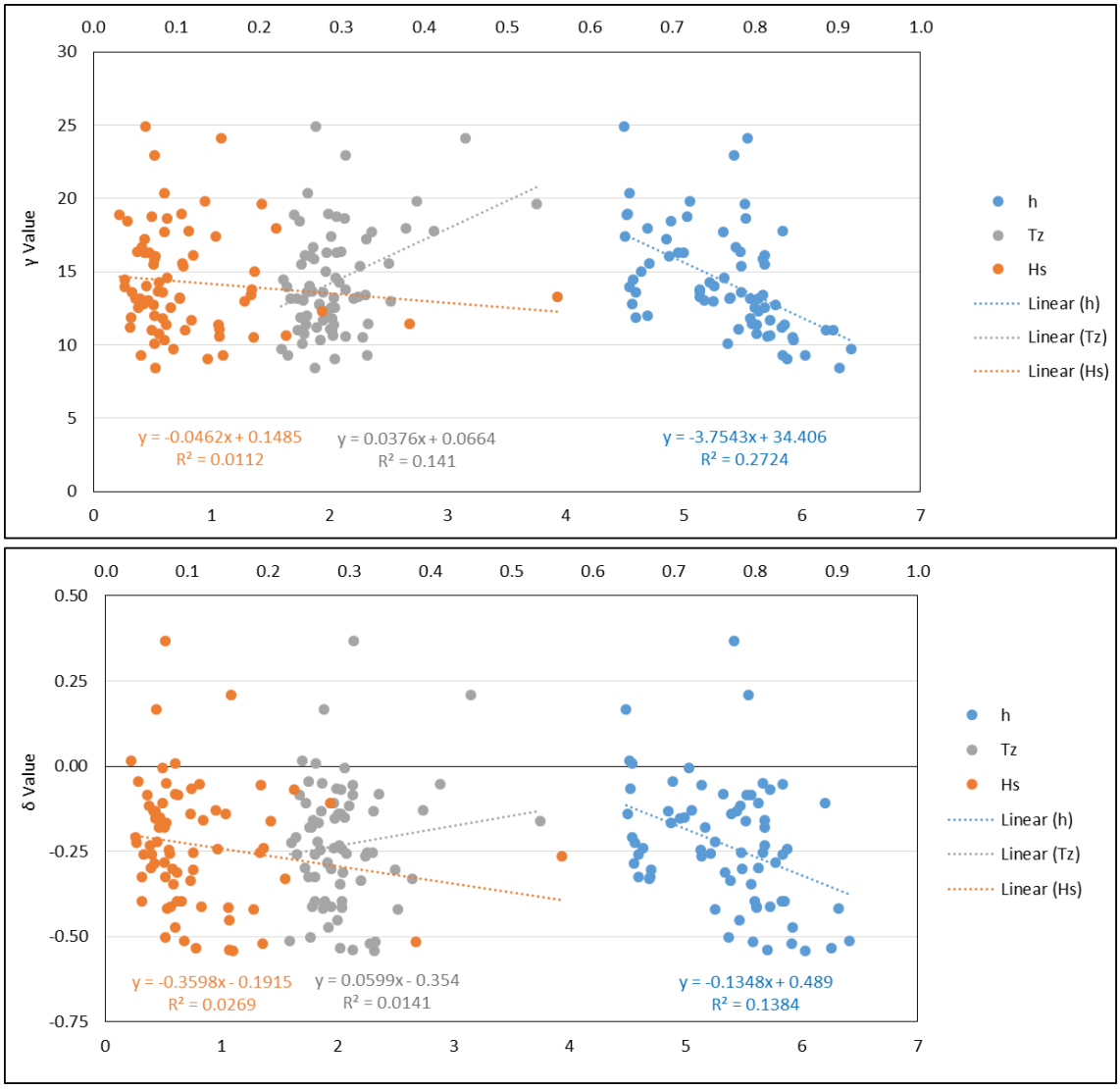

Figure 112: Relationship between water depth, significant wave height and zero-crossing period and values of γ and δ.

5.2.3.3 Summary of Findings

The relationship between streamwise mean current velocity and turbulence intensity contained within the wave burst data from the DWR followed a strong power relationship in the form of Equation 25. This relationship was generally much weaker than observed in Objective 1 and did not appear to be affected by flow direction, water depth or surface wave activity.

5.2.4 Discussion of Objective 1

The inter-tidal models (Figure 107 (Table 15) and Figure 110 (Table 16)) revealed that the DWR dateset shares similarities in terms of velocity range and general relationships with figures presented in MacEnri *et al.* (2013) (Figure 21), Gunawan *et al.* (2014) (Figure 19) and McCaffrey *et al.* (2015) (Figure 18). Where these papers simply presented their results, this work applied an empirical best fit using power regression to predict turbulence strength and intensity as a function of mean current velocity and empirical coefficients. The inter-tidal models were repeated for Flood and Ebb tides but there was little difference in coefficient values. This was in contrast to the similar figure of mean current velocity vs turbulence strength presented in Gunawan *et al.* (2014) (Figure 20) of which a significant difference in the relationship between mean current velocity and turbulence strength is observed between Flood and Ebb tides, which they explained by differing upstream bathymetry between Flood and Ebb tides. This, therefore, suggests that the upstream bathymetry at Foul Holme Spit (which of course shifts with the tidal direction) generates relatively similar coherent structures in flow during Flood and Ebb tides, which are observable when measuring at 4 Hz.

The intra-tidal models revealed that during each consecutive Flood and Ebb tides the relationship between mean current velocity, turbulence strength (Figure 108) and intensity (Figure 111) could be modelled using power regression. For turbulence strength values of α and β fluctuated between Flood and Ebb throughout the deployment duration but linear regression between these values, water depth, significant wave height and zero-crossing period revealed very little correlation thus suggesting their variation through time may be because of a confounding variable not measured within the fieldwork, such as upstream bathymetry (Figure 109). Similarly, fluctuations between γ and δ had very weak correlations with water depth, significant wave height and zero-crossing period.

Both the inter-tidal and intra-tidal models showed that the turbulence strength and intensity can be modelled as a function of mean current velocity at a point, however fluctuations in the empirically derived coefficients throughout the deployment could be analytically explained by other monitored variables. These models are used in later sections to compare to ADCP data through depth and results taken from the literature.

Due to using an EMCM, instead of an ADV, the DWR could not measure flow in three dimensions. This prohibited the observation and modelling of stress metrics and anisotropy, which other papers such as McCaffrey *et al.* (2015) attempted. Due to the similarities between Figure 18 and Figure 110 it could be assumed that anisotropy increases in the same direction as McCaffrey *et al.* (2015) determined. They also found that

turbulence intensities had a similar range of scatter in mean current velocities of 0 to 0.5 ms^{-1} and found that turbulence intensities did not become constant near a value of 10 % until around 1.2 ms^{-1}. This is most likely because their ADV was positioned higher in the boundary layer and thus monitored higher flow velocities.

5.3 Analysis and Discussion of Objective 2:

Model the relationship between turbulence strength, intensity and mean current velocity at a point, including wave-current interaction.

5.3.1 Introduction

As explained in the literature review, surface waves induce velocities into the water column, which oscillate at frequencies dependent on the height and period of the local wave spectra (Holthuijsen, 2007). These oscillations are hypothesised to increase the turbulent fluctuation about the mean current velocity in tidal streams. This would increase the standard deviation and thus increase both the turbulence strength and intensity above what can be modelled in calm conditions. However, wave-current interaction has largely been ignored from previous *in situ* observations of tidal turbulence and has yet to be modelled within the context of tidal stream power energy yield assessments. This section first compares the models calculated within section 5.2 with new models that are calculated based on DWR wave bursts with increased wave activity. The Soulsby Exponential Approximation is tested on *in situ* data, for the first time, to determine its usefulness in predicting wave-induced velocities in tidal streams (2.4.2). Finally, wave bursts with calm and stormy conditions are compared in order to determine the effect of wave-current interaction on the turbulence spectrum to build on the conceptual model presented within Soulsby and Humphrey (1990) (see section 2.4.3.3).

5.3.2 Modelling the Relationship between Turbulence Strength, Intensity and Mean Current Velocity at a Point, Including Wave-Current Interaction.

Whilst power regression determined a strong relationship between mean current velocity and turbulence strength the lack of a perfect R^2 value and clear spread of results meant that confounding variables might exist for more accurately predicting turbulence strength and intensity through time such as surface wave parameters.

5.3.2.1 Inter-tidal Power Regression during Increased Wave Activity

Using the hypothesis that wave-induced velocities increase fluctuations about the mean, which in turn increases the standard deviation and thus turbulence strength, it can be shown that data containing increased wave-activity do not necessarily have the greatest turbulence characteristics at all given mean current velocities. Figure 113 and Figure 114 show the same data and relationships as Figure 107 and Figure 110 for turbulence strength and turbulence intensity respectively with any wave bursts that contained significant wave heights greater than 0.2 m highlighted in red. The models are identical at mean current velocities between 0.3 ms^{-1} and 0.6 ms^{-1} with slightly higher turbulence strength and intensity values between 0 and 0.3 ms^{-1} and slightly lower turbulence strength and intensity values between 0.6 and 1 ms^{-1}. The greatest outliers from the power models occur at around 0.47 ms^{-1} with significantly greater turbulence strength values than the line of best fit. These are compared to calm bursts at the same mean current velocity and water depth in section 5.3.3.

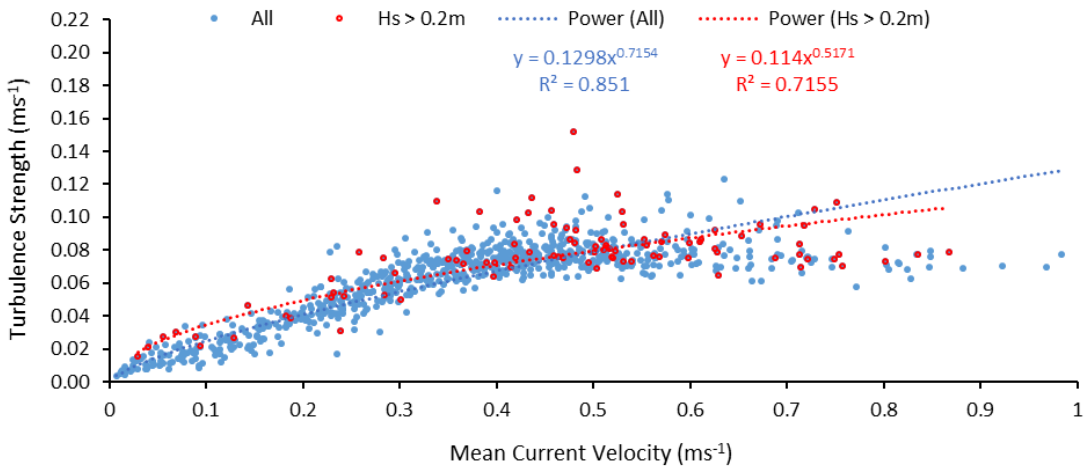

Figure 113: Relationship between mean current velocity and turbulence strength with bursts containing significant wave heights greater than 0.2 m highlighted in red.

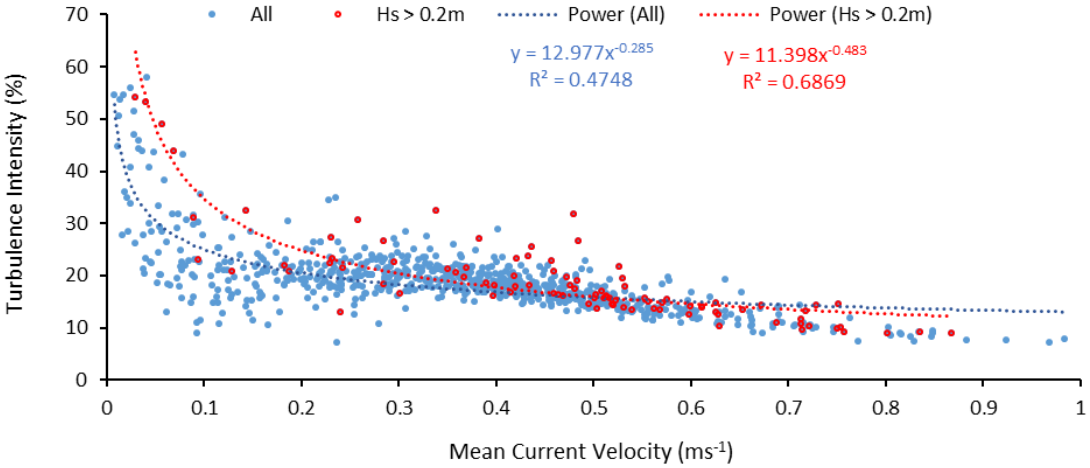

Figure 114: Relationship between mean current velocity and turbulence intensity with bursts containing significant wave heights greater than 0.2 m highlighted in red.

5.3.2.2 Testing the Soulsby Exponential Approximation on *In Situ* Data

Figure 115 plots the Soulsby exponential approximation of wave-induced velocity (using Equation 20) against the relative observed mean current velocity during each wave burst. This identified when increases in fluctuation about the mean should have occurred based on the recorded surface wave parameters and water depth at the site. At low velocities, there was low modelled wave-induced variance but at higher velocities there was significantly increased modelled variance; up to 0.16 ms^{-1} at around 0.71 ms^{-1}. This scale of additional variance due to waves is not clearly observed in Figure 107 and suggests that the approximation either overestimated the wave-induced variance measured by the device or that because the wave-induced variance was not significantly greater than the turbulence-induced variance the turbulence strength did not perceptibly increase. This could, therefore, mean that wave-induced variance will only increase the turbulence strength if its induced motion is significantly greater than the turbulence strength present in otherwise calm conditions at given velocities. This observation is further investigated in section 5.3.3 through a comparison of calm and stormy turbulence spectra.

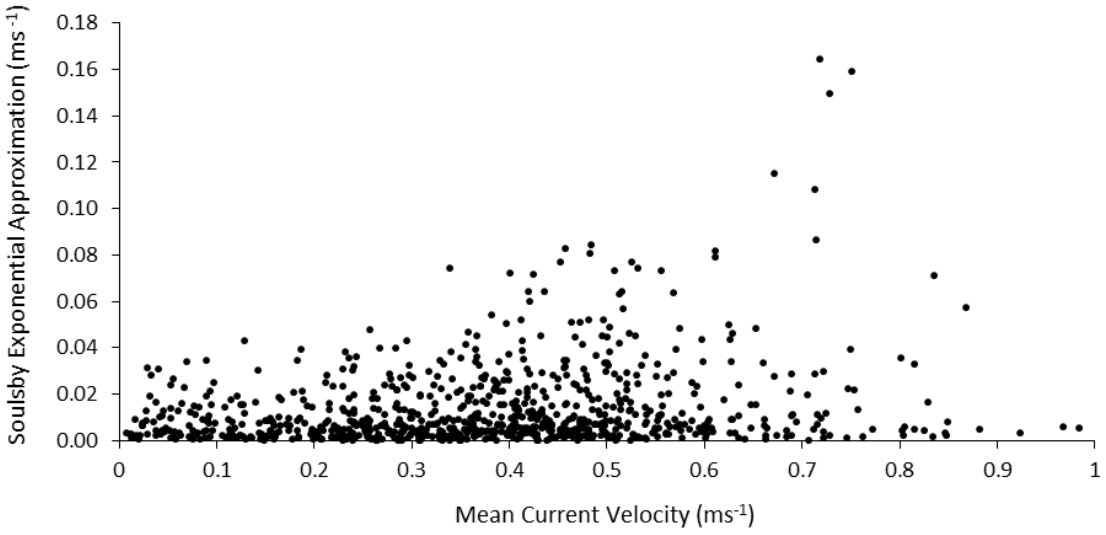

Figure 115: The calculated Soulsby exponential approximation at relevant mean current velocities.

Multiple linear regression was used to determine whether further independent variables could more effectively explain the change in turbulence strength throughout the deployment. Table 17 shows the results of a multiple linear regression analysis that took into account the mean current velocity and the Soulsby exponential approximation as independent variables. It determined that the relationships were significant (p-value < 0.05) for each relationship and that the R^2 value increased by around 0.03 for 'All', Flood and Ebb respectively. Whilst this is a slight improvement on the initial linear regression analysis, it does not fully explain the change in turbulence strength through time meaning that other

confounding variables may exist or the relationship may be better described using non-linear regression techniques.

	N	Independent Variable	R^2	P-Value
All	812	Streamwise mean current velocity	0.6482	0.0000
		Soulsby exponential approximation		0.0000
Flood	437	Streamwise mean current velocity	0.6765	0.0000
		Soulsby exponential approximation		0.0000
Ebb	375	Streamwise mean current velocity	0.6440	0.0000
		Soulsby exponential approximation		0.0000

Table 17: Multiple linear regression analysis of the whole deployment (All), Flood and Ebb tide between streamwise mean current velocity, the Soulsby exponential approximation and turbulence strength.

5.3.2.3 Summary of Findings

The section showed that the wave bursts containing increased wave activity (designated as having significant wave heights greater than 0.2 m) did not have significantly greater turbulence strength or intensity values in comparison to bursts at the same mean current velocity in calm conditions. The Soulsby exponential approximation was used to estimate the wave-induced velocity about the mean current velocity however these additional fluctuations could not be observed in the inter-tidal relationships. This is likely to be because the wave conditions were not great enough or propagating parallel enough to be observable above the turbulence fluctuations present during calm conditions and the wave-induced signal is lost in the noise of the turbulence. In the following section this signal is observed by comparing the turbulence spectra.

5.3.3 Modelling Wave-Current Interaction in the Turbulence Spectrum

Soulsby and Humphrey (1990) present a conceptual model of which energy induced by surface waves can be visualised within the turbulence spectrum. Clark *et al.* (2015b) suggest that different scales of turbulence will have impacts on different parts of a TST, therefore understanding how wave-current interaction affects models of turbulence strength and the turbulence spectrum is a significant research area which remains relatively unexplored. Here, the Soulsby exponential approximation is again used to estimate wave-induced velocity within each burst.

Table 18 compares summary data of two wave bursts (numbers 173 and 284) recorded by the DWR at Foul Holme Spit. Each sample has relatively similar water depths (3.16 m, 2.96 m) and relatively high mean current velocities (0.72 ms^{-1} and 0.73 ms^{-1}), yet the major differences were the surface wave parameters recorded. Wave burst 173 had a very low significant wave height (0.07 m) and zero-crossing period (1.45 s) whereas wave burst 284 had a relatively high significant wave height (0.78 m) and zero-crossing period (2.15 s). Significant differences in turbulence strength and thus turbulence intensity are also observed between samples, with the turbulence strength higher by 0.03 ms^{-1} in the increased wave activity sample meaning the turbulence intensity was higher by 3.96 %. The Soulsby exponential approximation was also compared and showed that during the calm wave burst (173) it predicts a wave-induced standard deviation of 0 ms^{-1}, as expected, whilst it predicts a standard deviation of 0.15 ms^{-1} for wave burst 284 given the increased wave parameters. It is clear that the Soulsby exponential approximation was overestimated in this case considering the total standard deviation in wave sample 284 was just 0.11 ms^{-1}. Nevertheless, the approximation was designed to be used when the mean current velocity is 0 ms^{-1} (and in the absence of turbulence) and no alternative approximation is available for a combined wave-current flow. The approximation is also designed to be used when the wave direction and tidal flow direction are exactly aligned, though in this wave burst the interaction occurred at a 43 ° angle, potentially reducing the wave-induced velocity in the streamwise direction.

Figure 116 shows the time series of current velocity and surface elevation over the four-minute wave bursts. Like in Table 12, data from wave burst 173 are coloured black and data from wave burst 284 are coloured red whilst the means of each are represented in blue. The most obvious difference is the large variation in surface elevation between the wave bursts, with the elevation in wave burst 284 showing clear wave grouping. These groupings appear to coincide with grouped oscillations in the current velocity data. Figure

117 presents the data that are displayed as a time series in Figure 116 in the frequency domain after a fast Fourier transform (FFT). By first focusing on wave burst 173 it can be seen that the pressure energy, PE, (as outputted by WaveLog Express) is minimal and that the power spectral density of the velocity signal (as used within other tidal research, such as Filipot *et al.* (2015)) is greatest at low frequencies and reduces with increased frequency. Using log scales presents this relationship in a form that can be tested against Kolmogorov's well known $f^{-5/3}$ inertial subrange relationship. In this case, the $f^{-5/3}$ rule applies between $10^{-0.25}$ and $10^{0.1}$ Hz. Comparatively, wave burst 284 contains a spike in both pressure energy and power spectral density between 0.4 and 0.6 Hz, which suggests that the surface pressure energy can give a good indication of when and how strong the wave-induced increase in power spectral density will be. Therefore, the peak frequency outputted by the device may provide the best indication of where in the frequency domain this spike will occur. In the logged axes, it is clear that this spike causes the $f^{-5/3}$ relationship to occur over an extended frequency range from $10^{-0.45}$ and $10^{0.2}$ Hz. These data, therefore, support the conceptual graph presented in Soulsby and Humphrey (1990) but with much more localised capture of the surface wave spectral parameters.

Wave Burst Number	Date (mm/dd/yyyy)	Time (hh:ss)	Mean Current Velocity ($\bar{U}$) (ms^{-1})	Turbulence Strength (U_σ) (ms^{-1})	Turbulence Intensity (I_T) (%)	Tidal Current Direction (°)	Water Depth (h) (m)
173	16/08/14	01:20	0.72	0.08	10.45	134	3.16
284	17/08/14	14:20	0.73	0.11	14.41	133	2.96

Wave Burst Number	Date (mm/dd/yyyy)	Time (hh:ss)	Significant Wave Height (H_S) (m)	Maximum Wave Height (H_{MAX}) (m)	Zero-Crossing Period (T_Z) (s)	Peak Frequency ($Pk\ F$) (H_Z)	Wave Direction (°)	Wave Energy (E) ($NdBar^2m^{-3}$)	Soulsby Exponential Approximation (U_{RMS}) (ms^{-1})
173	16/08/14	01:20	0.07	0.1	1.45	0.53	183	2.74	0
284	17/08/14	14:20	0.78	1.23	2.15	0.44	270	386.19	0.15

Table 18: Tidal and wave parameters of calm and increased wave activity samples.

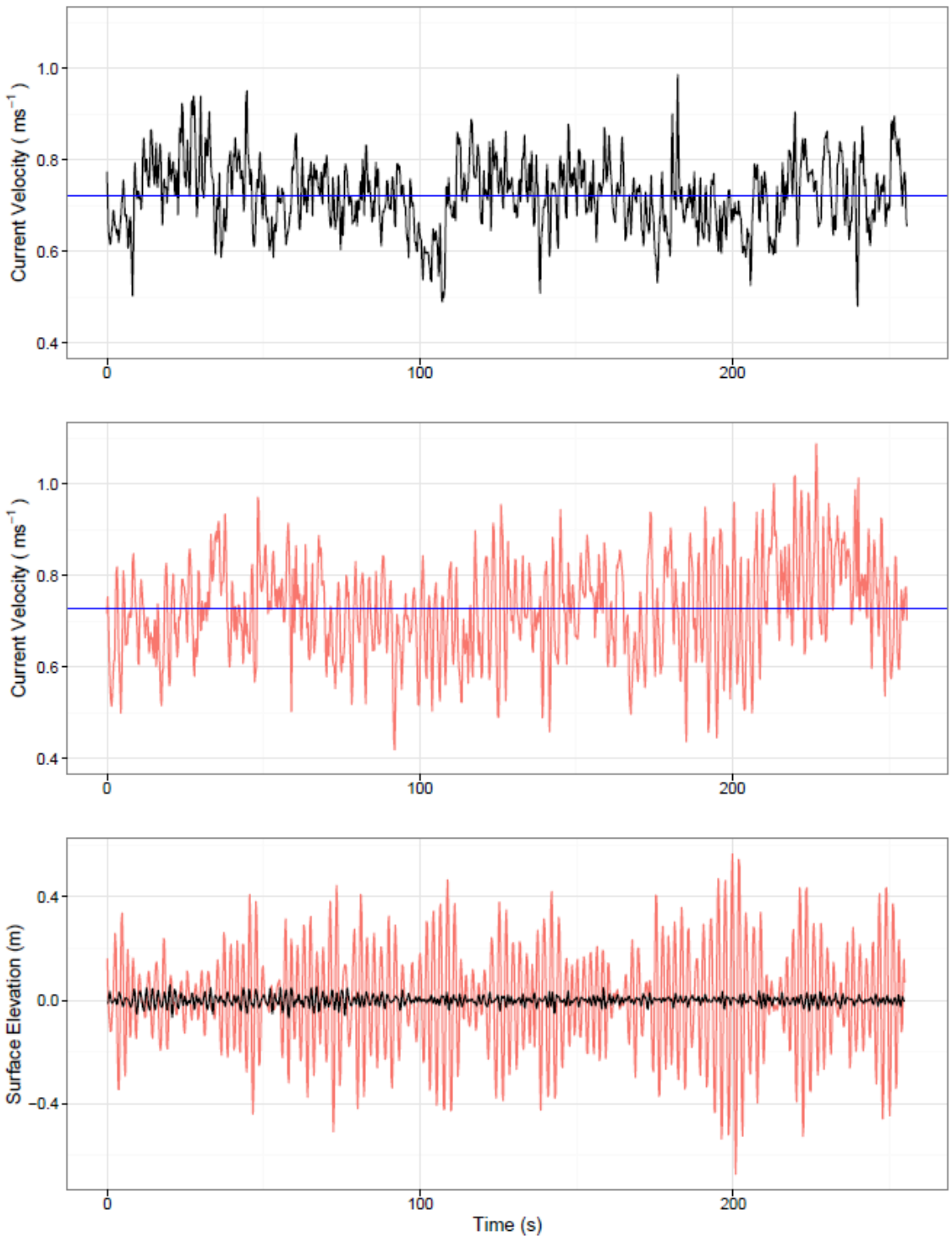

Figure 116: Comparison of current velocity and surface elevation measured during wave bursts 173 and 284.

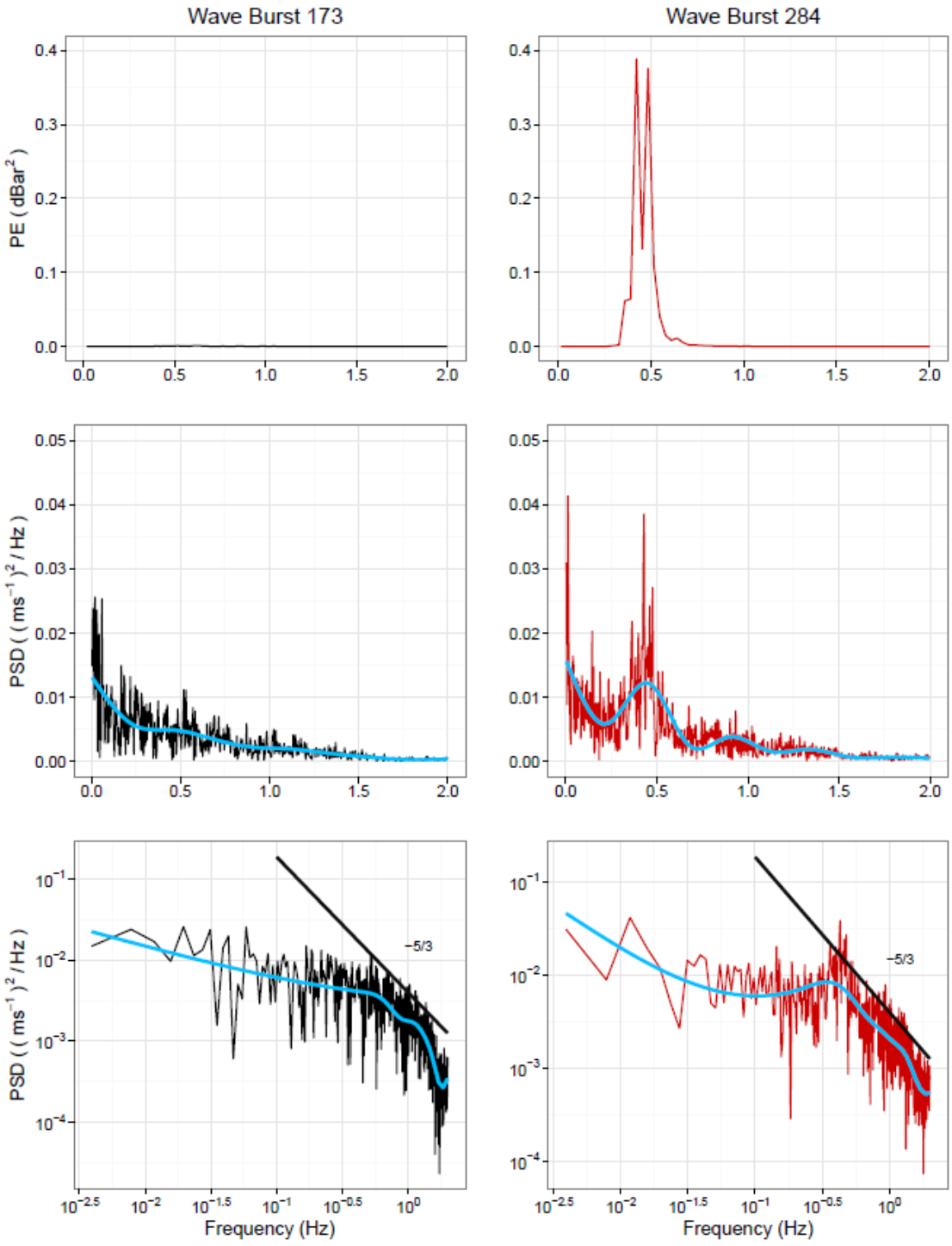

Figure 117: Comparison of pressure energy and power spectral density calculated during wave bursts 173 and 284.

5.3.3.1 Summary of Findings

This section demonstrated that the turbulent fluctuations about the mean have different characteristics between calm and stormy conditions. Whilst only small difference can be observed in the turbulence strength between these two wave bursts their turbulence spectra shows that wave-induced velocities increase the energy present at the peak period of the local surface wave spectra.

5.3.4 Discussion of Objective 2

The first section of Objective 2 compared the models of the relationships between turbulence strength, intensity and mean current velocity calculated in Objective 1 to a new model that only included wave bursts with significant wave heights greater than 0.2 m to determine if there were statistical differences between the power models. It was shown that wave bursts containing increased wave activity did not contain higher turbulence strength or turbulence intensity values than other wave bursts recorded at similar mean current velocities. The Soulsby exponential approximation was then used to estimate how much wave-induced velocities should have contributed to the standard deviation about the mean of each wave burst. Multiple linear regression was used to determine whether including these approximations in the linear models from Objective 1 could improve their R^2 values and thus predictive capability but the model's R^2's did not increase significantly.

The second section of Objective 2 directly compared two wave bursts in order to compare turbulent fluctuations in calm and stormy conditions. Soulsby and Humphrey (1990) suggested that a high-frequency time series of combined wave and turbulent flow could be broken down into its constituent parts using spectral analysis and found that in a sample burst with expected high waves, a peak in the turbulence energy spectrum was found at the peak frequency of surface gravity waves. However, their experiment was flawed by the failure of the pressure transducer on their STABLE frame so could not accurately determine the local wave spectra rendering their conclusions conceptual (see Figure 33). Similar data were presented by Hannay *et al.* (1994) yet these papers were concerned with the effects of wave-current interaction on sedimentology. A recent paper by Filipot *et al.* (2015) revived this theory and linked wave-current interaction to marine energy yield assessments by attempting to measure the phenomenon using bed-mounted ADCP. However, their results were not described in appropriate detail and it was not clear at what depth their figure detailing turbulence spectra was made.

This work provides new empirical, *in situ*, data through the novel use of a DWR in the Humber Estuary to further knowledge of wave-current interaction in tidal streams in

order to suggest how this phenomenon should be accounted for in tidal stream power EYAs. By comparing two wave bursts (173 and 284) that had similar tidal characteristics and different surface wave parameters it can be seen that wave-induced velocities increase the power spectral density of the turbulence spectrum in tidal flows close to the frequency of the peak frequency of the wave spectra. The analysis presented in section 5.2.3.3 supports the conceptual model provided in Soulsby and Humphrey (1990) in which wave-induced velocities increase the power spectral density of the turbulence spectrum in tidal flows close to the frequency of the peak frequency of the wave spectra. Whilst turbulence spectrums are commonly presented in the tidal stream power literature, very few have presented turbulent spectra in the presence of surface wave activity, as most *in situ* measurements have been collected below expected wave base. This work collected the first simultaneous wave-current dataset from a hyper-tidal estuary and has been analysed within the context of tidal stream power by using conceptual models previously only used in sedimentology studies.

Increasing the power spectral energy at certain frequencies as a result of surface waves will likely affect the scales of turbulence that have been identified as affecting the performance and fatigue of TSTs in Clark *et al.* (2015b). For example, relatively small waves have been identified in this study and the increases in energy at such frequencies are likely to increase the effects attributed to 'small-scale eddies' (see section 2.3.1). As such, larger waves than those that occur in the Humber Estuary are expected to increase the power spectral density at lower frequencies and increase the effects of mid and large-scale eddies. Therefore, the interaction between larger waves and strong tidal streams, which occurs in more exposed sites such as the Pentland Firth, must be the focus of future related research to have a more direct application to the industry.

5.4 Analysis and Discussion of Objective 3:

Model the relationship between turbulence strength, intensity and mean current velocity through depth, ignoring wave-current interaction.

5.4.1 Introduction

A number of authors have recently presented figures which describe the relationship between turbulence strength, intensity and mean current velocity through depth in calm conditions at tidal stream development sites (see Thomson *et al.* (2012) (Figure 17), MacEnri *et al.* (2013) (Figure 21), Gunawan *et al.* (2014) (Figure 19) and McCaffrey *et al.* (2015) (Figure 18). These results are often presented yet rarely modelled. Empirical models that can predict turbulence strength and intensity based on the streamwise mean current velocity through depth could be very useful within tidal stream power EYAs. The variation of turbulence metrics through depth and time could be crucial when considering the vertical position of a TST in the water column and for inputting more realistic constants into numerical simulations of turbulence.

Models that can estimate depth-averaged turbulence metrics based on depth-averaged current velocities could be used to evaluate a wide geographical area as depth-averaged mean current velocities can be quickly estimated using tools such as TotalTide.

Here, the results of the ADCP fieldwork in the Humber Estuary are used to first model the relationship between depth-averaged current velocity and turbulence intensity and secondly to model the relationship between turbulence strength and mean current velocity through depth.

5.4.2 Modelling the Relationship between Turbulence Intensity and Depth-Averaged Current Velocity

This section explores the relationship between depth-averaged current velocity (except blanking distances), $\bar{U}_d$, and the depth-averaged turbulence intensity, I_{Td}. Any relationships between these values could be used to improve numerical models by estimating the depth-averaged turbulence intensity at a site when given a mean current velocity that can be calculated from models such as TotalTide. This analysis is novel and has not yet been attempted in the reviewed literature. As in section 5.2.3, the model for

$$I_{Td} = \varepsilon \, \bar{U}_d{}^{\zeta} \tag{26}$$

depth-averaged turbulence intensity follows the form:

$\bar{U}_d$ and I_{Td} are empirically modelled during Spring and Neap tides in Figure 118. At lower velocities (<1 ms^{-1}) I_{Td} is generally higher during the Spring Flood than in the Neap Flood. At velocities greater than 1 ms^{-1} the turbulence intensity is greater in the Neap Flood than in the Spring Flood. The data for Spring Flood were fit with a power trend line following the equation $I_{Td} = 17.215 \, \bar{U}_d{}^{-1.001}$ with an R^2 value of 0.7982 and for Neap Flood following the equation $I_{Td} = 17.923 \, \bar{U}_d{}^{-0.641}$ with an R^2 value of 0.8851. The main difference between Spring and Neap Flood currents is the water depth present at each current velocity.

$\bar{U}_d$ and I_{Td} are empirically modelled during Spring and Neap tides in Figure 119. The data for Spring Ebb were fitted with a power trend line following the equation $I_{Td} = 15.01 \, \bar{U}_d{}^{-0.501}$ with an R^2 value of 0.0997 and for Neap Ebb following the equation $I_{Td} = 20.05 \, \bar{U}_d{}^{-0.519}$ with an R^2 value of 0.805. The Spring Ebb data does not have a strong power relation due to its low R^2 value; this is because no velocities below 1 ms^{-1} were collected as the ADCP failed to record accurately during the 1st hour of the transect. Again, the main difference between Spring and Neap Ebb currents is the water depth present at each current velocity.

As it has been shown that each of the four surveys follow a distinct pattern, Figure 120 combines every $\bar{U}_d$ and I_{Td} data point and uses power regression to calculate a combined empirical model following the equaution $I_{Td} = 17.75 \, \bar{U}_d{}^{-0.94}$ with an R^2 of 0.791.

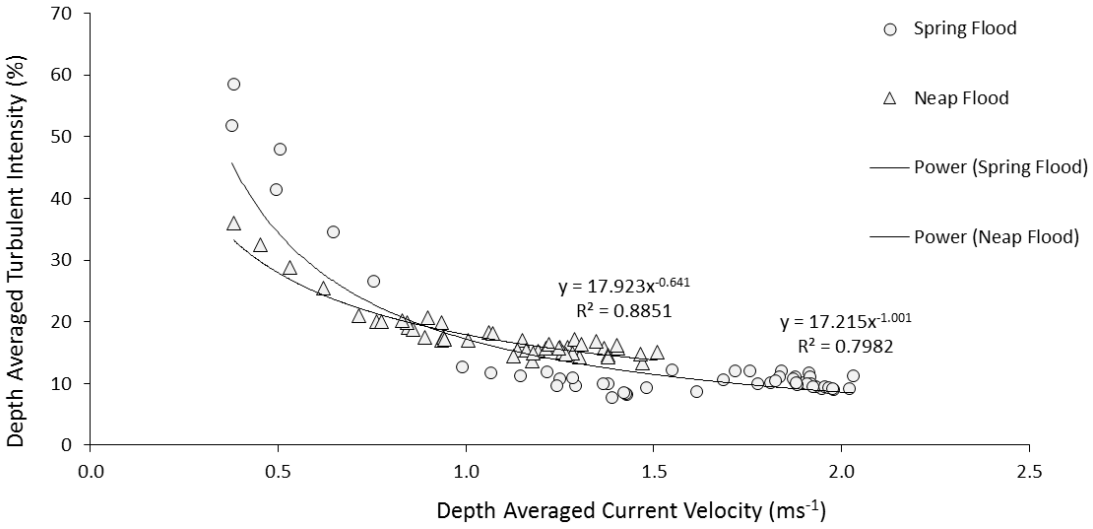

Figure 118: Depth-averaged Flood current velocity against turbulence intensity during Spring and Neap tides.

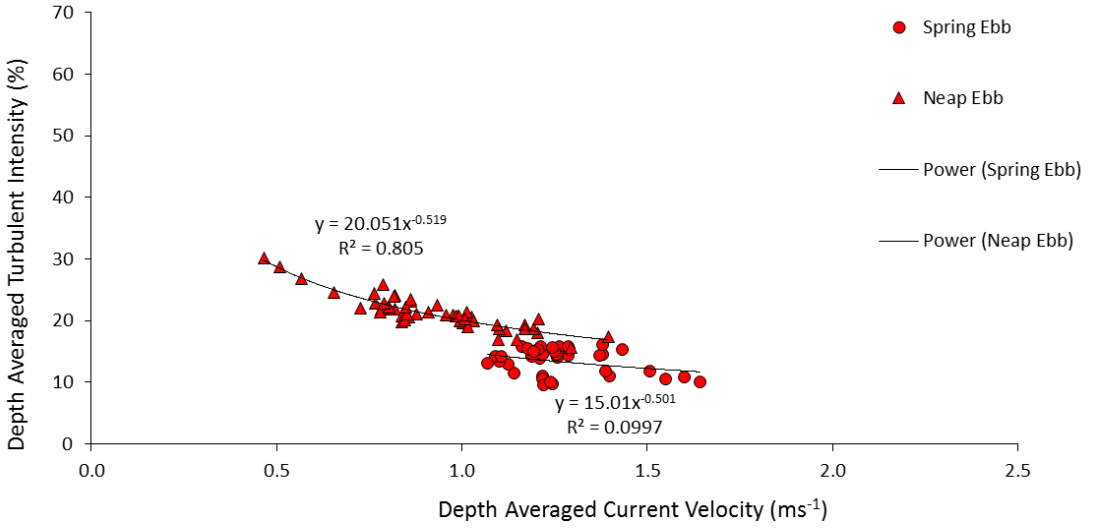

Figure 119: Depth-averaged Ebb current velocity against turbulence intensity during Spring and Neap tides.

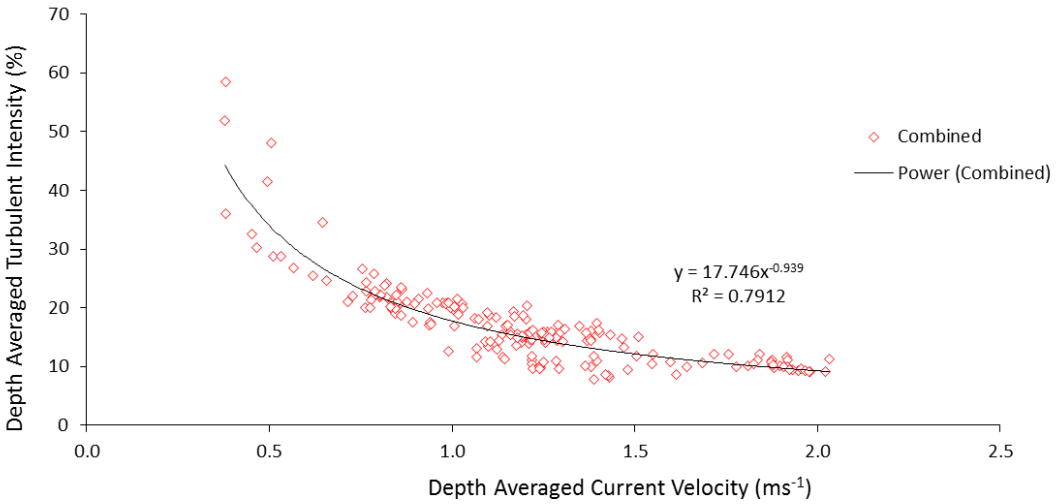

Figure 120: Power model of combined depth-averaged ADCP results.

5.4.2.1 Summary of Findings

Figure 120 shows that the inter-tidal relationship between streamwise mean current velocity and turbulence intensity can be modelled using depth-averaged values using power regression where ε is 17.75 and ζ is -0.94 with an R^2 value of 0.7912. High values of depth-averaged turbulence intensity, I_{Td}, occurred during low depth-average mean current velocities, $\bar{U}_d$, and low values during high current velocities, at around 10 %. This relationship is very similar to that displayed in Figure 23, however, Jeffcoate *et al.* (2015) only monitored Flood tides and only across the swept area of a floating TST; therefore, this analysis expands this knowledge by comparing Flood and Ebb tides but also Spring and Neap tides. It is considered that any differences between tidal cycles will be because of the variations in flow direction, velocity, upstream roughness and water depth.

5.4.3 Modelling the Relationship between Turbulence Strength and Mean Current Velocity through Depth

The vertical distribution of the turbulence strength through time was discussed in chapter 4. The ADCP data are used here to test the relationship between streamwise mean current velocity and turbulence strength through depth. The empirical formula derived in section 5.2 is then tested against the ADCP results.

Figure 121 shows the relationship between streamwise mean current velocity and turbulence strength throughout the Spring Flood cycle whilst Figure 122 shows the same relationship but during the Neap Flood cycle. There is not an easily identifiable trend during the Spring Flood data whilst the Neap Flood data appears to follow the same power regression observed in the DWR point data, albeit with a much lower R^2 value of 0.4267. Despite these much weaker relationships, the turbulence strength is around the same values for the DWR data suggesting that the α and β values identified in the DWR analysis could be used to approximate turbulence strength values from any given streamwise mean velocity value at a given depth. This theory was tested in Figure 123 and Figure 124 using the values of $\alpha = 0.1298$ and $\beta = 0.7154$ to model values of turbulence strength and plot the difference between the modelled and observed values. In the Spring Flood data (Figure 123), this method returned values that were within ± 0.2 ms^{-1} throughout the survey, which were generally overestimated near the bed and underestimated nearer the surface. The same was observed in the Neap Flood data though the majority of data were within ± 0.1 ms^{-1}.

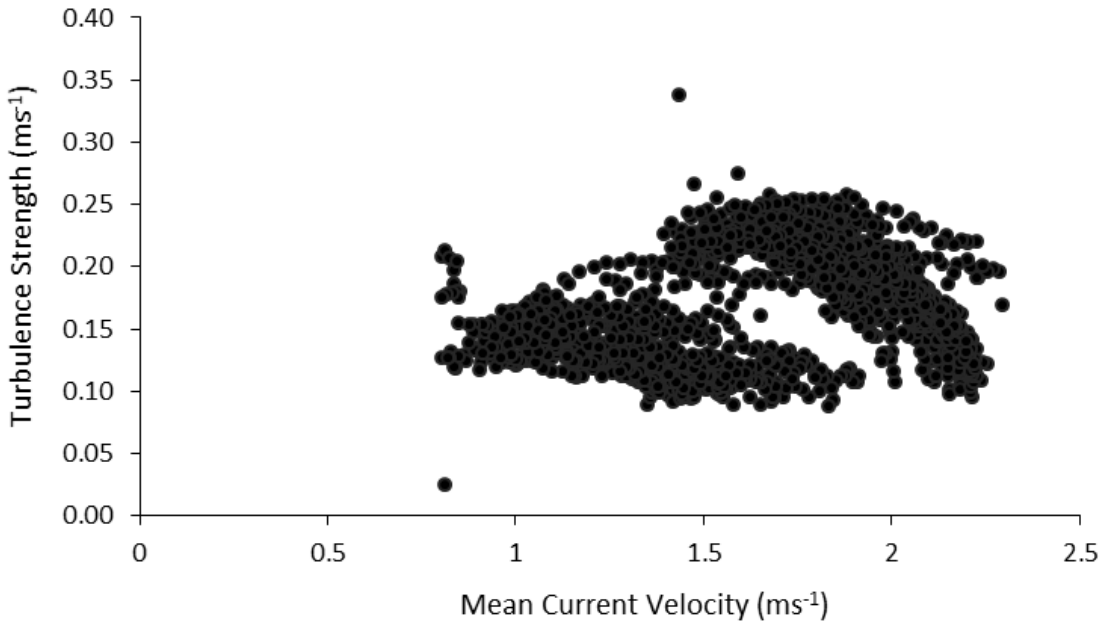

Figure 121: Relationship between mean current velocity and turbulence strength throughout the Spring Flood ADCP survey.

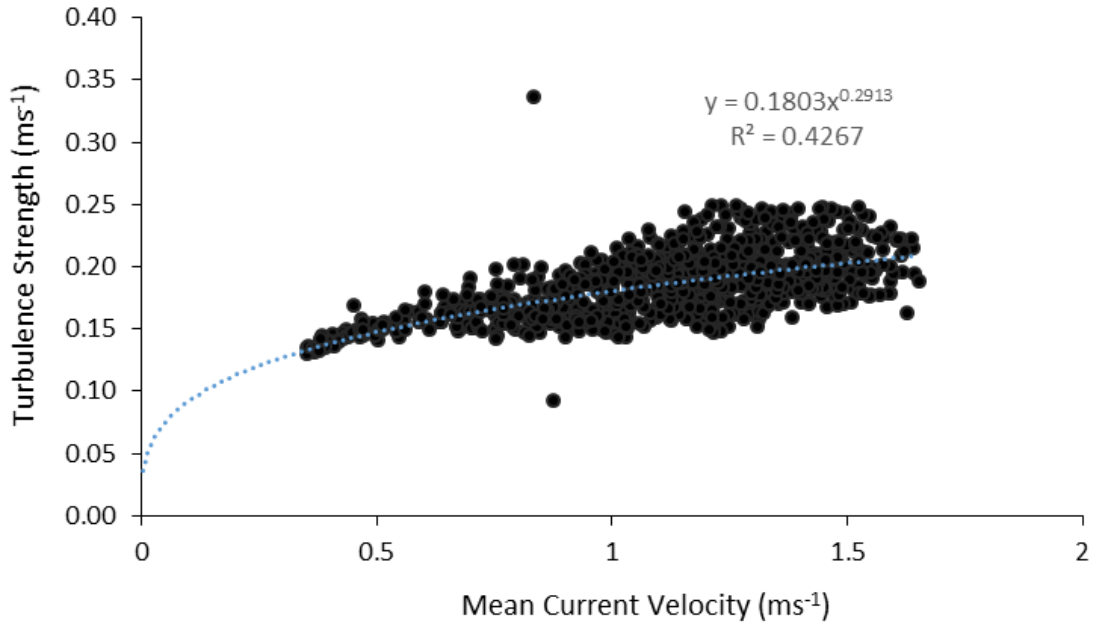

Figure 122: Relationship between mean current velocity and turbulence strength throughout the Neap Flood ADCP survey.

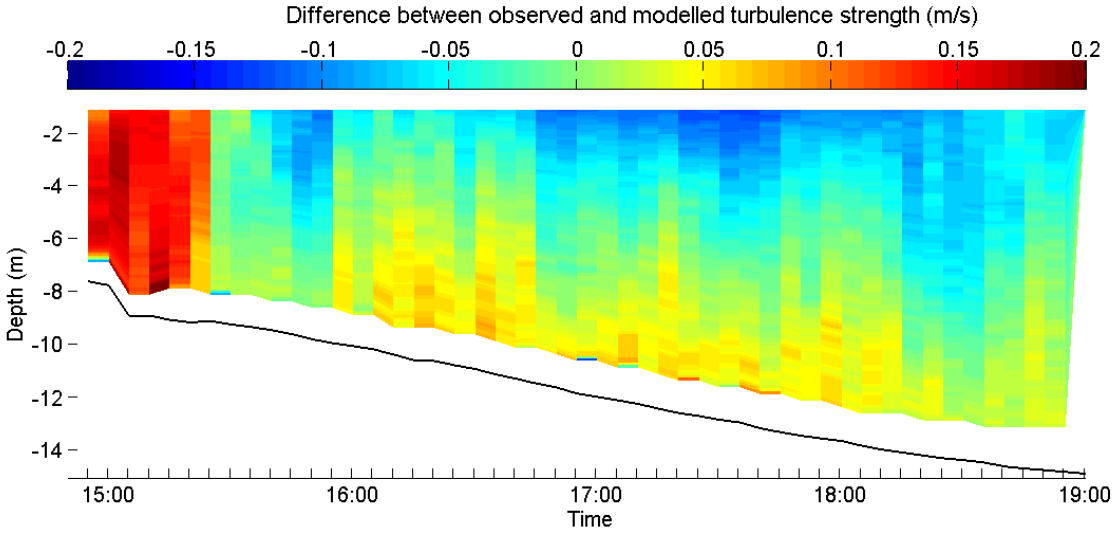

Figure 123: Difference between observed and modelled turbulence strength during the Spring Flood ADCP transect.

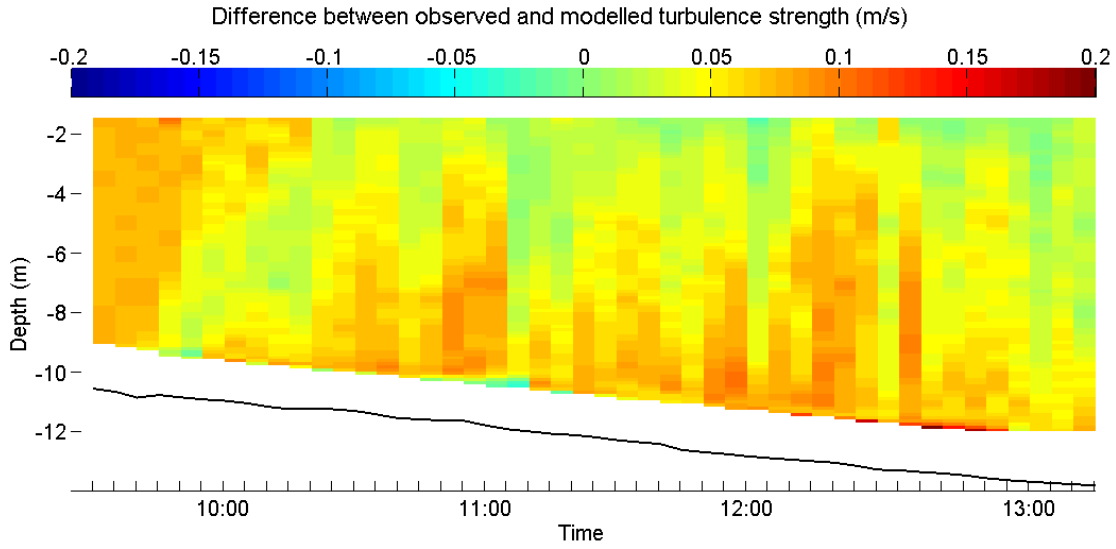

Figure 124: Difference between observed and modelled turbulence strength during the Neap Flood ADCP transect.

As the Neap Flood data were more closely related to the models output, the observed and modelled values were directly tested in Figure 125. This figure clearly identifies that, whilst a number of samples were exactly modelled (by appearing on the x=y line), the majority of samples had higher modelled values than observed, though this could be calibrated further using the trend line (red).

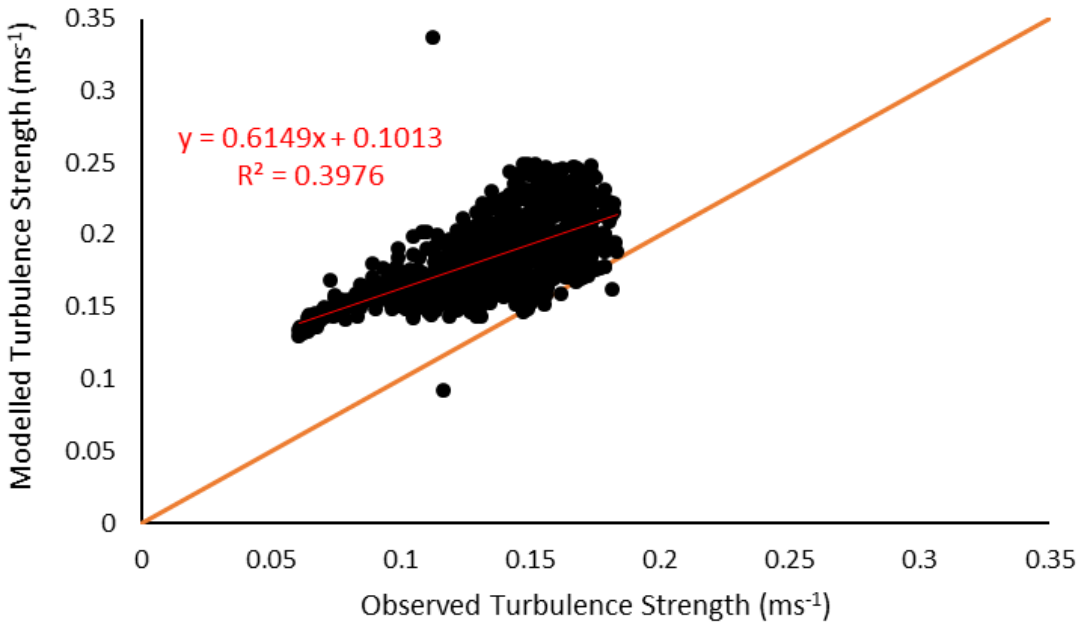

Figure 125: Observed turbulence strength data against modelled turbulence strength data during the Neap Flood ADCP Survey.

5.4.3.1 Summary of Findings

From this analysis it was determined that the power model used to explain the relationship between streamwise mean current velocity and turbulence strength from the DWR fieldwork can be used to model the turbulence strength through depth given streamwise mean current velocities (provided by the ADCP fieldwork). A better fit was identified with the Neap Flood data than the Spring Flood data and this may be because the Neap Flood survey used a 600 kHz ADCP that sampled at twice the rate of the 1200 kHz ADCP used in the Spring surveys thus capturing a more accurate representation of the turbulence strength. The linear relationship between the observed and modelled data followed $y=0.6149x+0.1013$ with a R^2 of 0.3976. Whilst this is a relatively weak correlation, the DWR model can still predict the turbulence strength through depth to within 0.1 ms^{-1}, which could be useful to tidal stream power developers. Data from many more sites would be needed to further calibrate and validate this model but this initial analysis shows that the model has potential to be applicable universally.

5.4.4 Discussion of Objective 3

The ADCP fieldwork data contained strong power relationships between the depth-averaged mean current velocity, $\bar{U}_d$, and the depth-averaged turbulence intensity, I_{Td}, which has only been briefly used by Jeffcoate *et al.* (2015) to assess the relationship over the hub diameter of a floating tidal stream turbine (TST). Knowledge that these relationships existing throughout the full water column could be used to compare prospective sites in the future to determine sites with the lowest turbulence intensity at peak flow. This relationship has not been explored within the reviewed literature but could be useful for tidal stream power EYA in that numerous models produce estimates of mean current velocities but could also predict an approximation of turbulence intensity in the form of Equation 26.

The ADCP fieldwork collected data that were used to plot mean current velocity vs turbulence strength graphs (Figure 121 and Figure 122) which share similarities with graphs presented in Filipot *et al.* (2015) (Figure 35). Whilst ADCP transects of fast flowing rivers and estuaries are relatively common, most focus on lateral transects focused on estimating discharge and very few record at a static point to measure flow through depth and time. This methodology, therefore, enabled the calculation of turbulence strength through depth and time at a prospective tidal stream power development site, thus furthering knowledge of this relationship through depth. Generally, it was found that turbulence strength increases with depth from the surface and that it increases with the mean current velocity, though the relationship was not as strong as was the case in the DWR fieldwork.

5.5 Summary of Findings and Implications

5.5.1 Comparison of Models to Literature

The models developed within this research are here compared to the results of relevant literature. Figure 126 directly compares the peak flow and associated turbulence strength presented in the literature (from Table 12). It shows that results from different geographical locations appear to follow the empirical equation generated by the research as the power curve of these data points very closely matches the $U_\sigma = 0.13\ \bar{U}^{0.72}$ model for turbulence strength. Whilst a much larger sample size of different locations is required to validate this theory it is an interesting observation which established a hypothesis that this rule is potentially universal and also that research into this relationship from other sites is important in the future to investigate this further.

Figure 127 compares the peak flow and associated turbulence intensity presented in the literature (Table 12). It shows that results from different geographical areas appear to follow the empirical equation generated by this research as the power curve of these data points (of which there are four more than in Figure 126) closely matches the curve of the $I_T = 14.3\ \bar{U}^{-0.23}$ model for turbulence intensity but is around 2 % lower at all peak flow velocities. This is an interesting observation that suggests this model could also be universal but may require calibration and further data points in order to be validated.

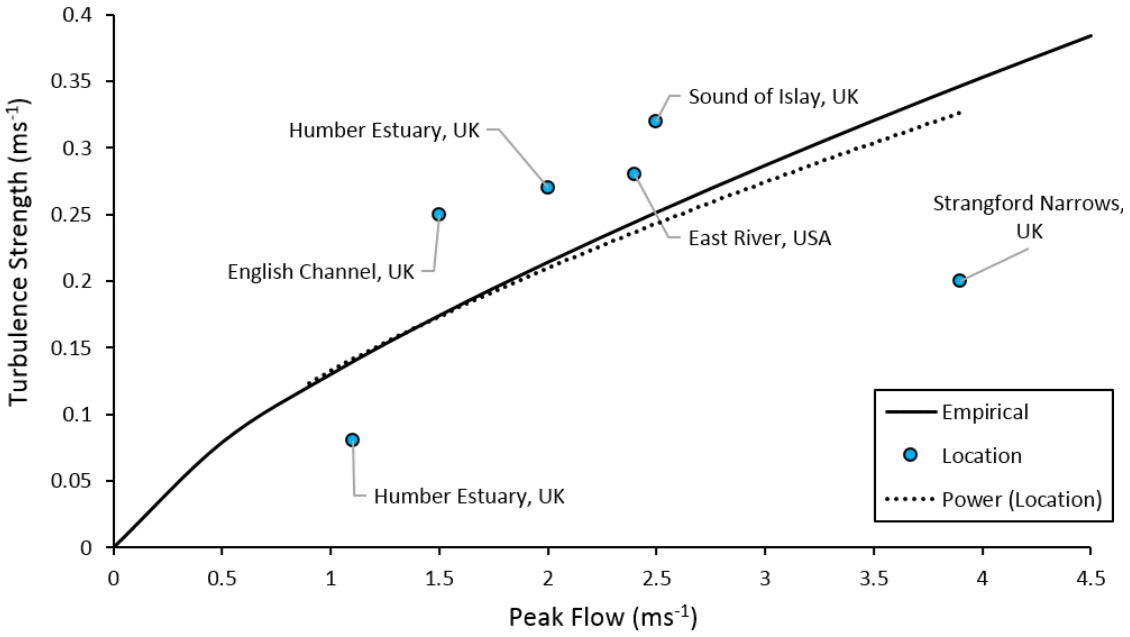

Figure 126: Comparison of turbulence strength empirical model and power trend between peak flow data presented within the literature.

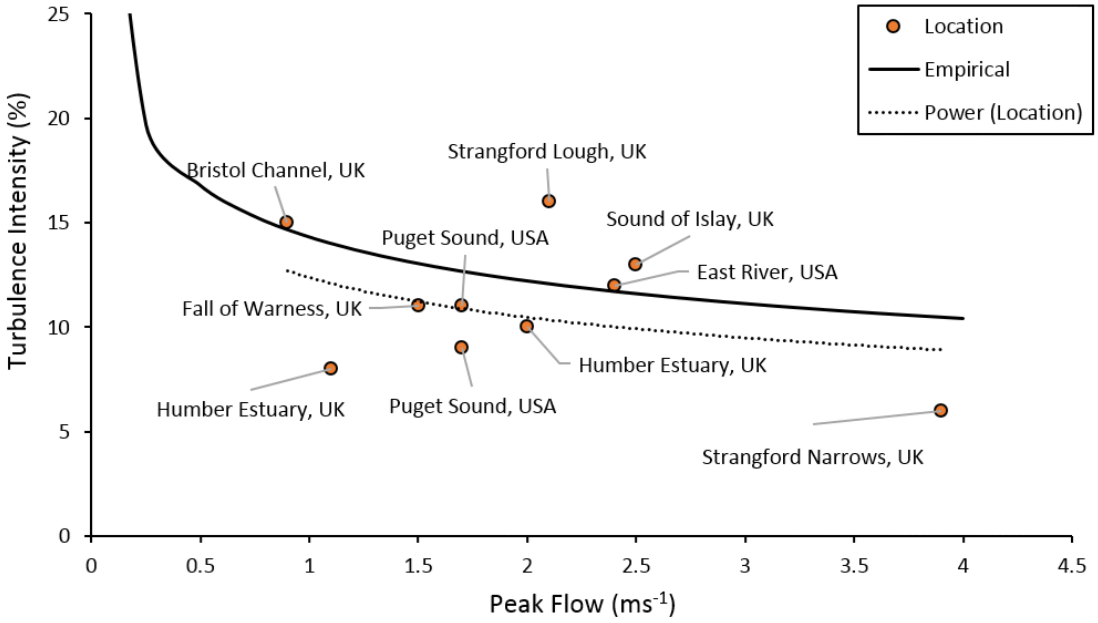

Figure 127: Comparison of turbulence intensity empirical model and power trend between peak flow data presented within the literature.

5.5.2 Example Usage of a Model to Predict Turbulence Strength in Tidal Stream Power Energy Yield Assessments

When presenting any mean average of a dataset the standard deviation should also be presented to show the spread of the data. Previous EYAs have typically only used the mean streamwise current velocity (averaged over around 5 - 20 minutes) in order to predict the available power at prospective tidal stream power sites. However, this research has shown that the turbulence strength can be modelled in terms of the mean streamwise current velocity and would, therefore, be useful to include within more inclusive tidal stream power EYAs as such:

$$P = \tfrac{1}{2}\,\rho\,A\,(\bar{U} \pm U_\sigma)^3 \tag{27}$$

The coefficients identified by the DWR dataset through All tidal cycles, where $\alpha = 0.13$ and $\beta = 0.72$, were used to predict the turbulence strength at a given mean current velocity such that:

$$U_\sigma = 0.13\,\bar{U}^{\,0.72} \tag{28}$$

Figure 128 thus demonstrates how the available power within a tidal flow may be affected by the inclusion of the turbulence strength. As velocities increase, the cubic effect creates an increasing range of available power that is asymmetric as illustrated by the difference between $\bar{U} + U_\sigma$, $\bar{U} - U_\sigma$ and $\bar{U}$. This asymmetry is negligible between 0 and 1 ms^{-1} but increases to 0.7 kW at 3 ms^{-1}.

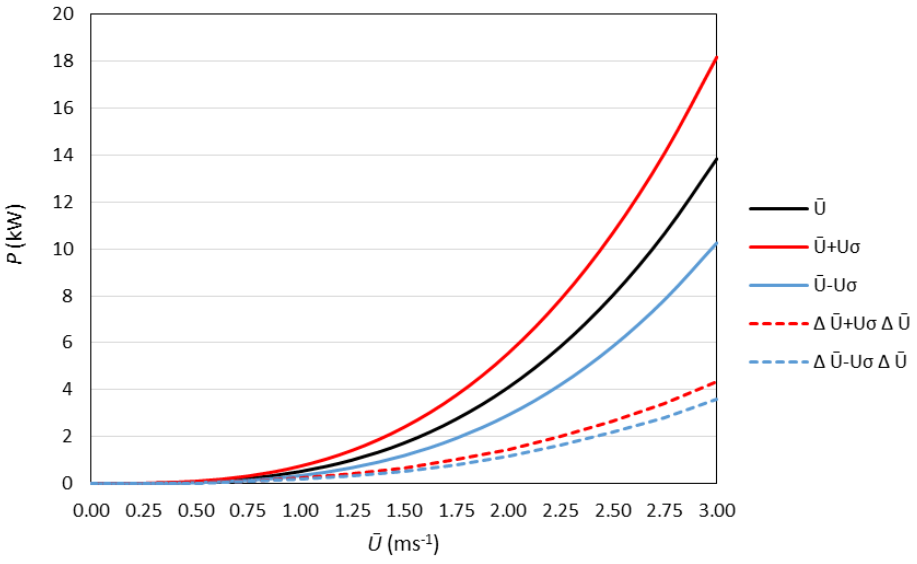

Figure 128: Effect of including turbulence strength within tidal stream power EYA.

5.6 Evaluation and Recommendations for Future Work

Whilst the collected data proved to be of suitable use to meet the thesis objectives, the fieldwork methodology could be iteratively improved should the fieldwork be repeated. The following sections go into detail about what worked well and what could be improved for both the DWR and ADCP fieldwork methodologies. Additionally, areas of investigation have emerged that could further develop and progress this work. As these could not be completed within the timeframe and scope of the thesis' aim and objectives, they are here presented as recommendations for further work.

5.6.1 Evaluation of the DWR Fieldwork Methodology and Recommendations for Improvements

Foul Holme Spit proved to be a suitable fieldwork location as it was easily accessible by RIB, was away from public or shipping interference, experienced strong tidal flows, was in a section of the Humber that resembled a long straight channel and did not drastically change its morphology during the deployment duration. With the knowledge gained from the pilot deployment at Spurn Point, the DWR sampled almost flawlessly as pre-programmed at Foul Holme Spit. As discussed in the results, a number of wave sample bursts contained erroneously high velocity measurements, the cause of which were unknown and had to be removed from the dataset as they could not be meaningfully filtered. Having a second device to compare flow velocity and surface wave parameters throughout the duration of the deployment would have been ideal to validate the results. However, as previously discussed, the data from the device that worked proved to reveal relationships that were comparable to the literature. It was determined in the results section that neither device interfered with one another and that if the methodology were repeated it is likely that both devices would record as planned should the marker buoy be positioned so that it did not foul either device.

A significant limitation of the DWR fieldwork, in comparison to other similar deployments, was that the device measured at a height above the bed that was lower than any TST turbine rotor would be realistically positioned. As explained, this was for practicality reasons and, as the field in which this research aims to contribute is still establishing the basic principles of these relationships, this study was envisioned as a preliminary step before the methodology can be developed to position the device higher in the water column, as has been the case with recent ADV studies. However, as Table 12 showed, the z/h ratio at which the DWR measured was similar to other literature. Sites were identified for a subsequent deployment; such as on the ladder of a tidal marker tower

downstream of Foul Holme Spit, however permission was denied by ABP. Recommendations as to how this could be achieved are discussed in section 5.6.3.

The DWR device sampled at a rate of 4 Hz, which proved to be high enough to measure the surface wave parameters in the Humber Estuary and high enough to accurately measure turbulence throughout the inertial subrange (see section 5.3). As discussed in the literature review, many other studies have measured at 4 Hz (or very close to) as it is around this frequency that the most important effects of turbulence and waves on TSTs will occur. In order to increase the chances of collecting a good range of calm and stormy conditions, the methodology should be repeated in the winter months when significant wave heights are generally increased. If chances of storm activity were increased this would allow the DWR to sample at its maximum rate (8 Hz) and be deployed for half the time.

It would be useful to compare the DWRs results to a collocated ADV. Simultaneously deploying an ADV sampling at a higher rate than the DWR could validate the turbulence spectra and record the flow in three-dimensions allowing the calculation of turbulence anisotropy. This would enable a more detailed comparison with previous literature that used ADVs to measure turbulence metrics at a point and would be able to contribute further knowledge by also measuring the effect of wave-current interaction on turbulence anisotropy.

5.6.2 Evaluation of the ADCP Fieldwork Methodology and Recommendations for Improvements

The site chosen to monitor mean current velocity and turbulence through depth using the ADCPs was suitable as it was a prospective tidal stream power development site, was easily accessible and was away from the main shipping channels, thus allowing uninterrupted surveys. Therefore, if the fieldwork was repeated this location could again be used.

It was determined that the 600 kHz ADCP performed best in the conditions of the Humber Estuary and revisions to the methodology would, therefore, include this ADCP over the 1200 kHz, which, for example, produced many bad bins during the Spring Ebb survey. The increased temporal frequency of the 600 kHz is also a more important factor than the decreased spatial frequency, within this context. Again, due to practicality, these surveys were carried out as and when these particular ADCPs were available but future methodologies should aim to use the same instrument to eliminate instrument bias.

A significant limitation to this methodology was that the crew inevitably had to have a break between tidal cycles meaning that slack water data were not obtained at the

start and the end of each transect. The relationship between depth-averaged mean current velocity and depth-averaged turbulence intensity remained consistent at lower velocities yet the lowest velocities were not measured due to these breaks. These breaks also meant that the vessel had to be repositioned at an exact co-ordinate before each transect though this proved difficult to accurately achieve due to dropping an anchor into a soft bed at a considerable depth. A bed-mounted methodology would inevitably improve this though this would again require the use of a vessel with a crane, which was unavailable at the time. Whilst (in this case) vessel-mounted surveys had the advantage of being cheaper, they are also potentially susceptible to weather conditions and may have had to be abandoned should the weather forecasts been inaccurate. Due to the limitations of instrument and crew availability, just four surveys could be made. In order to re-test the relationships observed in the research many more surveys should be taken at the same site and at others to determine how the empirical model changes in different water depths and over different bed roughnesses.

A bed-mounted deployment of the ADCP would be able to collect a much longer time series of flows through depth. This would require deployment from a larger vessel, divers and require permission from ABP. A fixed-bed deployment would also present the opportunity to utilise the variance method to calculate turbulence intensity in three dimensions and determine how anisotropy changes through depth and time over a tidal cycle.

5.6.3 Recommendations for Measuring Turbulence and Wave-current Interaction Higher in the Water Column

It would be interesting to measure combined wave-current flow at a point higher in the water column in order to measure faster flows in the free stream with potentially higher wave orbital velocities than those observed in the DWR fieldwork. Positioning the DWR device at this height would require a tidal tripod, which would require a more stringent risk assessment and larger deployment vessel than the methodology employed within this thesis. ADCPs remain the only method to monitor the vertical water column without physically obstructing the flow but their temporal and spatial resolution limits their application to only the largest of turbulent length and time scales whereas ADVs and EMCMs can operate at much more appropriate temporal scales but are limited to single point measurements. Therefore, methods to position ADVs and EMCMs at the optimal vertical height from the bed or hub height of a TST (which may be any height given advances in floating and buoyant platforms) are necessary. Thomson *et al.* (2011; 2012) suggest using a

combination of floats and chains to position ADVs higher in the water column (Figure 129) though they have yet to publish any evidence that this methodology has been attempted. It is highly likely that the ADVs used in this methodology would tilt and rotate considerably during peak flow thus complicating the analysis of three-dimensional flow. This setup could also be very expensive to build, deploy and maintain. It would also require permission from local shipping authorities, which could be difficult to obtain. Recent innovations such as the Rockland Scientific NEMO Turbulence mooring system provides a floating platform for ADV instrumentation enabling the measurement of turbulence at a point throughout the water column (Rockland Scientific, 2016). Such innovations should certainly be considered in future experiments to solve the problem of measuring at high-frequency higher in the water column.

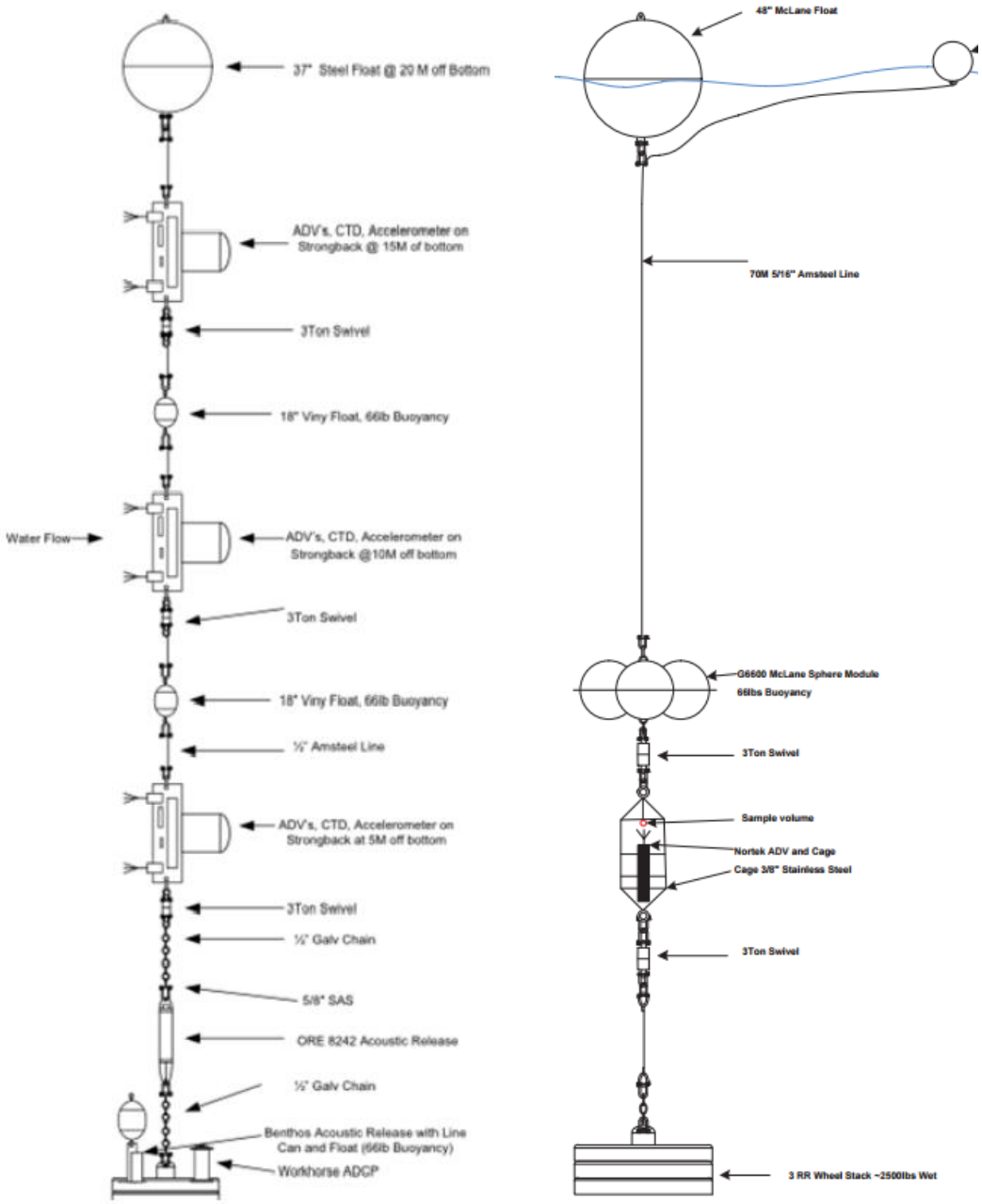

Figure 129: Diagrams of proposed methodologies to measure turbulence through depth in fast tidal streams by Thomson et al. (2011; 2012).

5.6.4 Recommendations for Experiments to Analyse the Impact of Bathymetry on Turbulence and TST performance.

By characterising the relationship between streamwise mean current velocity, turbulence strength and turbulence intensity new coefficients have been identified, though could not be analytically defined by the tested variables. Future studies of these relationships must also make note of these coefficients so that they can be more confidently explained. Increased knowledge of why these coefficients occur, in order to describe such relationships, could be vital to predicting turbulence metrics at future tidal stream power sites. It is here hypothesised that the upstream bathymetry or bed roughness is the likely cause of the change in α and β values; therefore, any future deployment should attempt to survey the changes in upstream bathymetry of the deployment location.

This could be done by vessel-mounted multi-beam surveys (as used by ABP to produce Figure 49) but would need to be carried out repeatedly in order to capture change throughout the full Spring-Neap-Spring cycle. This effect could be more cost effectively tested within a laboratory flume by simulating a tidal cycle and changing the upstream bed roughness whilst measuring the streamwise mean current velocity and turbulence strength. These flume experiments could also include a downstream prototype TST in order to measure the performance during bathymetry change leading to turbulence strength change.

5.6.5 Recommendation to Analyse the Effect of Increased Fetch on Wave-current Interaction in hyper-tidal Estuaries.

When measuring waves in the Humber Estuary it became apparent that wave heights and periods were generally lower at low water than at high water. In hyper-tidal estuaries, the surface area of water can significantly increase from low water to high water, thus increasing the potential fetch of locally generated waves. It would therefore be useful to simulate the generation of locally generated waves at different stages of the tide to predict the height and period of waves at given winds speeds during various stages of the tide. This could be done similarly to Lewis *et al.* (2014) using CFD models with an increased focus on the differences between fetch at low and high water at hyper-tidal locations. This could then be used to improve tidal energy yield assessments to help predict which areas will be sheltered from the longest fetches and thus the greatest wave activity.

6 Conclusion

This thesis has made significant contributions of knowledge towards the interdisciplinary research field concerning the exploitation of the tidal stream resource. Though the tidal stream resource is predicted to be vast, converting this plentiful, renewable source of energy to electricity has proved to be an enormous scientific and engineering challenge. Whilst the tidal stream resource can be considered predictable (in terms of the background deterministic streamwise mean current velocity) the relationships between the streamwise mean current velocity, the turbulence strength, intensity, and wave-induced motion have, in recent years, become an industry-driven field of research. The literature review identified research gaps concerning *in situ* measurements and modelling such relationships within the context of tidal stream power. Whilst some recent studies have begun to present figures illustrating relationships between the streamwise mean current velocity and turbulence metrics (strength and intensity) none have gone as far as modelling the observed relationships or attempting to explain why these relationships exist. Additionally, these relationships had not yet been measured or analysed within wavebase as surface wave activity will induce orbital velocities, which could influence turbulence metrics and/or spectra. As many prospective tidal stream power development sites are expected to be exposed to significant surface wave activity this emerged an important research gap to fill.

In situ data were collected during two fieldwork campaigns within the Humber Estuary during 2014 and 2015. These locations were chosen due to having strong predicted tidal flows in excess of 2 ms^{-1} and relative shelter from instrument damaging storm swell. Whilst the interaction between strong tidal streams and storm swell would have ideally been investigated, a trade-off between possibility and practicality must be made. The risk of expensive instrument loss within environments in which this interaction regularly occurs was deemed much higher and unfeasible considering the available budget and novelty of the research objectives.

An 18-day deployment of two Valeport MIDAS directional wave recorders (DWR) at Foul Holme Spit in 2014 collected a primary dataset of which relationships between streamwise mean current velocity, turbulence and wave-current interaction were modelled and analysed at a point throughout a Spring-Neap-Spring cycle, for the first time. Static, vessel-mounted acoustic Doppler current profiler (ADCP) surveys close to St. Andrews Dock in 2015 collected four transects across Spring Flood, Spring Ebb, Neap Flood and Neap Ebb of which relationships between streamwise mean current velocity and turbulence metrics were similarly modelled and analysed through depth.

The analyses revealed distinct relationships between the mean current velocity, turbulence strength and turbulence intensity at a point, which are comparable to recently published results (Osalusi *et al.*, 2009a and 2009b; Thomson *et al.*, 2010a, 2010b, 2011, 2012; Gunawan *et al.*, 2014; MacEnri *et al.*, 2013; McCaffrey *et al.*, 2015).

For Objective 1, the inter-tidal relationship between streamwise mean current velocity and turbulence strength is modelled at a point using power regression, where α is 0.13 and β is 0.72 with a high R^2 value of 0.8721. The inter-tidal relationship between streamwise mean current velocity and turbulence intensity is modelled at a point using power regression where γ is 14.315 and δ is -0.2316 with a lower R^2 value of 0.5482. These values were used to directly compare to results from other geographic locations and a power regression between these data had almost exactly the same values suggesting that these models could be used universally.

For Objective 2, the same models as derived in Objective 1 are tested on the data points with the greatest wave-activity. There was very little difference in these models suggesting that wave-induced velocities did not significantly influence the model coefficients, though the waves measured within this fieldwork were relatively small. The exponential approximation of wave-induced velocity, proposed by Soulsby (2006), was tested and shown to be inappropriate for estimating wave-induced velocities at this scale. A comparative spectral analysis between DWR sample bursts determined that spikes in the turbulence spectra can be attributed to surface wave parameters, thus validating the conceptual model proposed by Soulsby and Humphrey (1990). Spikes in the turbulence spectra due to wave-induced velocities could increase the energy within small-scales of turbulence beyond what would be expected in calm conditions, which have been attributed to structural fatigue in Clarke *et al.* (2015b).

For Objective 3, a newly defined empirical relationship between depth-averaged mean current velocity and turbulence intensity is modelled using power regression where ε is 17.75 and ζ is -0.94 with an R^2 value of 0.7912. This could be useful as an input to future numerical models to predict turbulence intensity at a site. The models derived in Objective 1 were tested and used to estimate the turbulence strength through depth and exhibited strong predictive capability within the order of 0.1 ms^{-1}. A better fit was identified with the Neap Flood data than the Spring Flood data and this may be because the Neap Flood survey used a 600 kHz ADCP that sampled at twice the rate of the 1200 kHz ADCP used in the Spring surveys, thus capturing a more accurate representation of the turbulence strength. The linear relationship between the observed and modelled data followed $y=0.6149x+0.1013$ with a R^2 of 0.3976. Whilst this is a relatively weak correlation, the

DWR model can still predict the turbulence strength through depth to within 0.1 ms^{-1}, which could be very useful to tidal stream power developers. Data from many more sites would be needed to further calibrate and validate this model but this initial analysis shows that the model has potential to be applicable universally.

As with any scientific study, the methodology could be iteratively improved. The main improvements would include increasing the recording frequency of the electro-magnetic current meters (EMCMs) and acoustic Doppler current profilers (ADCPs) to more accurately determine the turbulence spectra at higher wave numbers though, at present, the state of the art instrumentation is limited. This would also increase the number of measurements included within each regression analysis to further increase statistical signifiance and confidence. It is also increasingly important to measure these interactions in the most likely prospective development sites, such as the Pentland Firth, where tidal flows and wave parameters are greater and more likely to reflect the most extreme environment tidal turbines will face. Further data can be used to compare to the results presented here to validate the derived empirical models.

The tidal stream power industry in which this knowledge may be applied is still developing and has diversified considerably in recent years. Whilst the wave power industry has seemingly stalled in terms of development, the tidal stream power industry has continued to develop its technology and will continue to benefit from *in situ* research such as this.

7 Bibliography

ABP. (2012). *Neptune Bathymetric Survey, William Wright Dock, Hull, River Humber*. Report 25th May 2012. ABP.

Adcock, T. A. A., Draper, S., Houlsby, G. T., Borthwick, A. G. L. and Serhadlıoğlu, S. (2014). The Available Power in the Pentland Firth. *Proc. Roy. Soc. A*, 469 (2157), pp. 1-21.

Afghan, I., McNaughton, J., Rolfo, S., Apsley, D. D., Stallard, S. and Stansby, P. (2013). Turbulent Flow and Loading on a Tidal Stream Turbine by LES and RANS. *International Journal of Heat and Fluid Flow*, 43, pp. 96-108.

Ahmed, M. R., Faizal, M., Prasad, K. and Lee, Y. (2010). Exploiting the orbital motion of water particles for energy extraction from waves. *Journal of Mechanical Science and Technology*, 24(4), pp. 943-949.

Andrews, J. and Jelley, N. (2013). *Energy Science: Principles, Technologies and Impacts*. Oxford University Press.

Anis, A. and Moum, J. N. (1995). Surface Wave-Turbulence Interactions: Scaling $\epsilon(z)$ near the Sea Surface. *J. Phys. Oceanogr.*, 25, pp. 2 025-2 045.

Antunes do Carmo, J. S. (2012). Turbulent Boundary Layer Models: Theory and Applications. In: H. W. Oh. ed., *Advanced Fluid Dynamics*, Intech.

Archer, A. W. (2013). World's Highest Tides: Hypertidal Coastal Systems in North America, South America and Europe. *Sedimentary Geology*, 284, pp. 1-25.

Ashall, L. M., Mulligan, R. P. and Law, B. A. (2016). Variability in Suspended Sediment Concentration in the Minas Basin, Bay of Fundy, and Implications for Changes due to Tidal Power Extraction. *Coastal Engineering*, 107, pp. 102-115.

ATC. (2016). Andritz Hydro GMBH. [online]. Available from: http://www.atc.or.at/en/industry/andritz-hydro/ [Accessed 26/02/16].

Atlantis Resources Ltd. (2014). Global Resource. [online]. Available from: http://atlantisresourcesltd.com/marine-power/global-resources.html/ [Accessed 26/12/2014].

Aubrey, D. G. (1989). Measurement Errors for Electromagnetic Current Meters. In: R. J., Seymour. ed., *Nearshore Sediment Transport*, Springer.

Babanin, A. V. and Haus, B. K. (2009). On the Existence of Water Turbulence Induced by Nonbreaking Surface Waves. *J. Phys. Oceanogr.*, 39, pp. 2 675-2 679.

Babanin, A. V., Onorato, M. and Qiao, F. (2012). Surface waves and wave-coupled effects in lower atmosphere and upper ocean, *Journal of Geophysical Research*, 117, pp. 1-10.

Barham, P. Winn, P. and Young, R. (1999). The Development of a Tidal Defence Strategy for the Humber Estuary. *Proceedings of the 33rd MAFF Conference of River and Coastal Engineers*, MAFF, London.

Barltrop, N., Varyani, K. S., Grant, A. D., Clelland, D. and Pham, X. P. (2007). Investigation into Wave-Current Interactions in Marine Current Turbines. *Proceedings of the Institution of Mechanical Engineers, Part A: Journal of Power and Energy*, 221 (2), pp. 233-242.

Barman, K., Debnath, K. and Mazumder, B. S. (2016). Turbulence between Two Inline Hemispherical Obstacles under Wave-Current Interactions. *Advances in Water Resources*, 88, pp. 32-52.

Belu, R. and Koracin, D. (2013). Statistical and Spectral Analysis of Wind Characteristics Relevant to Wind Energy Assessment Using Tower Measurements in Complex Terrain. *Journal of Wind Energy*, 2013, pp. 1-12.

Binh, L. V., Ishihara, T., Phuc, P. V. and Fujino, Y. (2008). A Peak Factor for Non-Gaussian Response Analysis of Wind Turbine Tower. *Journal of Wind Engineering and Industrial Aerodynamics*, 96, pp. 2 217-2 227.

Black and Veatch and Carbon Trust. (2005). *Phase II UK Tidal Stream Energy Resource Assessment*. Issue to TCT 3, 44.

Black Rock Tidal Power. (2016). *Technology*. [online]. Available from: http://www.blackrocktidalpower.com/technology/ [Accessed 26/02/16].

Black, K., Ibrahim, J., Helsby, R., McKay, J., Clark, T., Pearson, N., Moore, R. and Hernon, J. (2015). Turbulence: Best practices for Measurement of Turbulent Flows: A Guide for the Tidal Power Industry. *Technical Report*, MRCF-TiME-KS9a. ITPower.

BlueTEC. (2016). *Texel: BlueTEC Modular Demo*. [online]. Available from: http://www.bluewater.com/new-energy/texel-project/ [Accessed 26/02/16].

Blunden, L. S. and Bahaj, A. S. (2005). Initial Evaluation of Tidal Stream Energy Resources at Portland Bill, UK. *Renewable Energy*, 31, pp. 121-132.

Bouferrouk, A., Hardwick, J. P., Colucci, A. M. and Johanning, L. (2016). Quantifying Turbulence from Field Measurements at a Mixed Low Tidal Energy Site. *Renewable Energy*, 87, pp. 478-492.

Bowden, K. F. and Fairbairn, L. A. (1952a). A Determination of the Frictional Forces in a Tidal Current. *Phil. Trans. A*, 244, pp. 371-392.

Bowden, K. F. and Fairbairn, L. A. (1952b). Further Observations of the Turbulent Fluctuation in a Tidal Current. *Proc. Roy. Soc. A*, 214, pp. 335-392.

Bowden, K. F. and Fairbairn, L. A. (1956). Measurements of Turbulent Fluctuations and Reynolds Stresses in a Tidal Current. *Proc. Roy. Soc. A*, 237, pp. 422-438.

Bowden, K. F. and Fairbairn, L. A. (1962). Measurements of Turbulence near the Sea Bed in a Tidal Current. *Journal of Geophysical research*, 67 (8), pp. 3 181-3 186.

Bowden, K. F. and Proudman, J. (1949). Observations of the Turbulent Fluctuations of a Tidal Current, *Proc. Roy. Soc.*, 199, pp. 311-327.

Bowden, K. F. and Howe, M. R. (1963). Observations of Turbulence in a Tidal Current. *Journal of Fluid Mechanics*, 17 (2), 271-284.

Boyle, G. (2012). *Renewable Energy: Power for a Sustainable Future*. 3rd Edition. Oxford.

Bricheno, L, M., Wolf, J. and Aldridge, J., (2015). Distribution of Natural Disturbance due to Wave and Tidal Bed Currents around the UK. *Continental Shelf Research*, 109, pp. 67-77.

Budi, G., Vincent, S. N. and Cilby, J. (2014). Tidal Energy Site Resource Assessment in the East River Tidal Strait, near Roosevelt Island, New York, New York. *Renewable Energy*, 71, pp. 509-517.

Buijsman, M. C. and Ridderinkhof, H. (2007). Long-term Ferry-ADCP Observations of Tidal Currents in the Marsdiep Inlet. *Journal of Sea Research*, 57, pp. 237-256.

Casella, L. (2015). Performance Analysis of the First Method for Long-term Turbulence Intensity Estimation at Potential Wind Energy Sites. *Renewable Energy*, 74, pp. 106-115.

Chamarro, L. and Porte-Agel, F. (2009). A Wind-Tunnel Investigation of Wind-Turbine Wakes: Boundary-Layer Turbulence Effects. *Boundary-Layer Meteorology*, 132, pp. 129-149.

Charnock, H. (1959). Tidal Friction from Currents near the Seabed. *GeoPhys. J. R. Astronomical Soc*, 2, pp. 215-221.

Chatfield, C. (1984). *The Analysis of Time Series: An Introduction*. Chapman and Hall.

Clark, T. (2015). A Framework for Classifying Turbulence and its Effects. *EWEA Resource Assessment 2015*, Helsinki.

Clark, T., Black, K., Ibrahim, J., Hernon, J., White, R., Minns, N., Roc, T. and Fisher, S. (2015a). *Turbulence: Best Practices for Data Processing, Classification and Characterisation of Turbulent Flows: A Guide for the Tidal Power Industry*. Technical Report, MRCF-TiME-KS9b. ITPower.

Clark, T., Roc, T., Fisher, S. and Minns, N. (2015b). *Turbulence and Turbulent Effects in Turbine and Array Engineering. A Guide for the Tidal Power Industry*. Technical Report, MRCF-TiME-KS10. ITPower.

Davidson, P. (2012). *Turbulence: An Introduction for Scientists and Engineers*. Oxford University Press.

De Jesus Henriques, T. A., Tedds, S. C., Botsari, A., Najafian, G., Hedges, T. S., Sutcliffe, C. J. and Poole, R. J. (2014). The Effects of Wave-Current Interaction on the Performance of a Model Horizontal Axis Tidal Turbine. *International Journal of Marine Energy*, 8, pp. 17-35.

Dey, S. (2012). *Fluvial Hydrodynamics: Sediment Transport and Scour Phenomena*. Springer.

Dohmen-Janssen, C. M., Kroekenstoel, D, F., Hassan, W. N. and Ribberink, J, S. (2002). Phase Lags in Oscillatory Sheet Flow: Experiments and Bed Load Modelling. *Coastal Engineering*, 46, pp. 61-87.

Doodson, A. T. and Warburg, H. D., (1941). *Admiralty Manual of the Tides*. H. M. Stationary Office, London.

Draper, S., Adcock, T. A. A., Borthwick, A. G. L. and Houlsby, G. T. (2014). Estimate of the tidal stream power resource of the Pentland Firth. *Renewable Energy*, 63, pp. 650-657.

Duarte, B. A. F., Ramos, I. C. R. and Santos, H. A. (2012). Reynolds Shear-Stress and Velocity: Positive Biological Response of Neotropical Fishes to Hydraulic Parameters in a Vertical Slot Fishway. *Neotropical Ichthyology*, 10 (4), pp. 813-819.

Durgesh, V., Thomson, J., Richmond, M. C. and Polagye, B. L. (2014). Noise Correction of Turbulent Spectra Obtained from Acoustic Doppler Velocimeters. *Flow Measurement and Instrumentation*, 37, pp. 29-41.

Dyer, K. R. (1995). Sediment Transport Processes In Estuaries. In: Perillo, G. M. E. ed, *Geomorphology and Sedimentology of Estuaries*. Elsevier: Amsterdam, pp. 423 449.

Easton, M. C., Woolf, D. K. and Bowyer, P. A. (2012). The dynamics of an energetic tidal channel, the Pentland Firth, Scotland. *Continental Shelf Research*, 48, pp. 50-60.

Edmunds, M., Malki, R., Williams, A. J., Masters, I. and Croft, T. N. (2014). Aspects of Tidal Stream Turbine Modelling in the Natural Environment Using a Coupled BEM-CFD Model. *International Journal of Marine Energy*, 7, pp. 20-47.

EMEC. (2009). *Assessment of the Tidal Energy Resource*. [online]. Available from: http://www.emec.org.uk/assessment-of-tidal-energy-resource/ [Accessed 18/6/14].

EMEC. (2014). *Marine energy*. [online]. Available from: http://www.emec.org.uk/marine-energy/ [Accessed 18/6/14].

EMEC. (2015). *Blog: Integrated Data Collection in Hostile Environments*. [online]. Available from: http://www.emec.org.uk/blog-integrated-data-collection-in-hostile-environments/. [Accessed 04/01/2015].

EoEarth. (2011). *Oceans and Sea, Amphidrome*. [online]. Available from: http://www.eoearth.org/view/article/150033/ [Accessed 01/09/15].

Fairley, I., Evans, P., Wooldridge, C., Willis, M. and Masters, I. (2013). Evaluation of Tidal Stream Resource in a Potential Array Area via Direct Measurements. *Renewable Energy*, 57, pp. 70-78.

Faudot, C. and Dahlhaug, O. (2012). Prediction of Wave Loads on Tidal Turbine Blades. *Energy Procedia*, 20, pp. 116-133.

Fernandez-Rodriguez E., Stallard, T. J. and Stansby, P. K. (2014). Experimental Study of Extreme Thrust on a Tidal Stream Rotor due to Turbulent Flow and with Opposing Waves. *Journal of Fluid and Structures*, 51, pp. 354-361.

Fernando, P. C., Guo, J. and Lin, P. (2011a). Wave-Current Interaction at an Angle 1: Experiment. *Journal of Hydraulic Research*, 49(4), pp. 424-436.

Fernando, P. C., Guo, J. and Lin, P. (2011b). Wave-Current Interaction at an Angle 2: Theory. *Journal of Hydraulic Research*, 49(4), pp. 437-449.

Filipot, J., Prevosto, M., Maisondieu, C., Boulluec, M. L. and Thomson, J. (2015). Wave and Turbulence Measurements at a Tidal Energy Site. *The 2015 IEEE/OES 11th Current, Waves and Turbulence Measurement Workshop (CWTM)*, Florida, USA.

Fulford, J. M., Thibodeaux, K. G. and Kaehrle, W. R. (1994). Comparison of Current Meters used for Stream Gaging. *Proceedings of the Symposium on Fundamentals and Advancements in Hydraulic Measurements and Experimentation*. Buffalo, NY, USA.

Galloway, P. W., Myers, L. E. and Bahaj, A. S. (2014). Quantifying Wave and Yaw Effects on a Scale Tidal Stream Turbine. *Renewable Energy*, 63, pp. 297-307.

Garrett, C. and Cummins, P. (2005). The Power Potential of Tidal Currents in Channels. *Proc. Roy. Soc.*, A, pp. 2 563-2 572.

Gaurier, B., Davies, P., Deuff, A. and Germain, G. (2013). Flume Tank Characterisation of Marine Current Turbine Blade Behaviour under Current and Wave Loading. *Renewable Energy*, 59, pp. 1-12.

Ghaffari, P., Azizpour, J., Noranian, M., Chegini, V., Tavakoli, V. and Shah-Hosseini, M. (2011). Estimating Suspended Sediment Concentrations using a Broadband ADCP in Mahshahr Tidal Channel. *Ocean Sci. Discuss.*, 8, pp. 1 601-1 630.

Glazzard. (2009). *TA0727 : St Andrew's Dock, Hull.* [online]. Available from: http://www.geograph.org.uk/photo/1219153 [Accessed 10/09/2015]

Golovanov, N., Lazaroiu, G. C., Roscia, M. and Zaninelli, D. (2013). Power Quality Analysis in Renewable Energy Systems Supplying Distribution Grids. *International Conference on Renewable Energies and Power Quality (ICREPQ'13),* Bilbao, Spain.

Gooch, S., Thomson, J., Polagye, B. and Meggitt, D. (2009). Site Characterisation for Tidal Power. *OCEANS 2009, MTS/IEEE Biloxi - Marine Technology for Our Future: Global and Local Challenges*. Mississippi, USA.

Gordon, C. M. and Dohne, C. F. (1973). Some Observations of Turbulent Flow in a Tidal Estuary, *Journal of Geophysical Research*, 78 (12), pp. 1971-1978.

Gourgue, O., Baeyens, W., Chen, M. S., de Brauwere, A., de Brye, B., Deleersnijder, E., Elskens, M. and Legat, V. (2013). A Depth-Averaged Two-Dimensional Sediment Transport Model for Environmental Studies in the Scheldt Estuary and Tidal River Network.
Journal of Marine Systems, 128, pp. 27-39.

Grant, H. L., Stewart, R. W. and Moilliet, A. (1961). Turbulence Spectra from a Tidal Channel. *Journal of Fluid Mechanics*, 12(2), pp. 241-268.

Groeneweg, J. and Klopman, G. (1998). Changes in the Mean Velocity Profiles in the Combined Wave-Current Motion Described in GLM Formulation. *Journal of Fluid Mechanics*, 370, pp. 271-296.

Gross, T. F. and Nowell, A. R. (1983). Mean Flow and Turbulence Scaling in a Tidal Boundary Layer. *Continental Shelf Research*, 2, pp. 109-126.

Gunawan, B., Neary, V. S. and Colby, J. (2014). Tidal Energy Site Resource Assessment in the East River Tidal Strait, Near Roosevelt Island, New York City, New York. *Renewable Energy*, 71, pp. 509-517.

Guo, J. (2002). Simple and Explicit Solution of the Wave Dispersion Equation. *Coastal Engineering, 45*, pp. 71-74.

Gyongy, I., Bruce, T. and Bryden, I. (2014). Numerical Analysis of Force-Feedback Control in a Circular Tank. *Applied Ocean Research*, 47, pp. 329-343.

Hardisty, J. (1989). Morphodynamics and Experimental Assessments of Wave Theories and Intermediate Water Depths. *Earth Surface Processes and Landforms*, 14, pp. 107-118.

Hardisty, J. (1990). *Beaches: Form and Process*. Springer Science and Business Media.

Hardisty, J. (2007). *Estuaries: Monitoring and Modelling the Physical System*. John Wiley and Sons.

Hardisty, J. (2009). *The Analysis of Tidal stream Power*. John Wiley and Sons.

Hardisty, J. (2012). The Tidal Stream Power Curve: A Case Study. *Energy and Power Engineering*, 4, pp. 132-136.

Hardisty, J. and Jennings, R. (2016). The Parameterisation of Turbulence in the Marine Environment. *Journal of Marine Engineering and Technology*. Online, pp. 1-7.

Hardisty, J. and Rouse, H. L. (1996). The Humber Observatory: Monitoring, Modelling and Management for the Coastal Environment. *Jnl. Coastal Res.*, 12, pp. 683-690.

Hashemi, M. R., Neill, S., Robins, P. E., Davies, A, G. and Lewis, M, J. (2015). Effects of Waves on the Tidal Energy Resource at a Planned Tidal Stream Array. *Renewable Energy*, 75, pp. 626-639.

Heathershaw, A. D. and Langhorne, D. N. (1988). Observations of Near Bed Velocity Profiles and Seabed Roughness in Tidal Currents Flowing Over Sandy Gravels. *Estuarine Coastal and Shelf Science*, 26, pp. 459-482.

Holmes, P. (2001). *Coastal Processes: Waves*. CDCM Professional Training Programme, 2001

Holtappels, M. and Lorke, A. (2011). Estimating Turbulent Diffusion in a Benthic Boundary Layer. *Limnol. Oceanogr.: Methods*, 9, pp. 29-41.

Holthuijsen, L. H. (2007). *Waves in Oceanic and Coastal Waters*. Cambridge University Press.

Humber LEP. (2014). *Strategic Economic Plan 2014-2020*. Humber Local Enterprise Partnership.

Hunt, J. N. (1979). Direct Solution of Wave Dispersion Equation. *J. Waterw., Port, Coastal Ocean Div., Am. Soc. Civ. Eng.*, 105 (4), pp. 457-459.

IEC61400-21. (2008). *Wind Turbines Part 21: Measurement and Assessment of Power Quality Characteristics of Grid Connected Wind Turbines*. IEC.

Jeffcoate, P., Starzmann, R., Elsaesser, B., Scholl, S. and Bischoff, S. (2015). Field Measurements of a Full-Scale Tidal Turbine. *International Journal of Marine Energy*, 12, pp. 3-20.

Jones, N. L. and Monismith, S. (2008). The Influence of Whitecapping Waves on the Vertical Structure of Turbulence in a Shallow Estuarine Embayment. *J. Phys. Oceanogr.*, 113, pp. 1-13.

Kemp, P. H. and Simons, R. R. (1982). The Interaction between Waves and a Turbulent Current: Waves Propagating with the Current. *Journal of Fluid Mechanics*, 116, pp. 227-250.

Kemp, P. H. and Simons, R. R. (1983). The Interaction between Waves and a Turbulent Current: Waves Propagating Against the Current. *Journal of Fluid Mechanics*, 130, pp. 73-89.

Khan, M. J., Bhuyan, G., Iqbal, M. T. and Quaicoe, J. E. 2009. Hydrokinetic Energy Conversion Systems and Assessment of Horizontal and Vertical Axis Turbines for River and Tidal Applications: A Technology Status Review. *Applied Energy*, 86(10), pp. 1 823-1 835.

Knauss, J. A., (1978). *Introduction to Physical Oceanography*. Prentice-Hall.

Kosro, P. M. (1985). *Shipboard Acoustic Current Profiling during the Coastal Ocean Dynamic Experiment*. Ph.D Thesis, Univ. of California, San Diego (La Jolla, Ca, U.S.A.).

Kvale, E. P. (2006). The Origin of Neap-Spring Tidal Cycles. *Marine Geology*, 235(1-4), pp. 5-18.

Lambrakos, K. F., MyrHaug, D. and Slaattelid, O. H. (1988). Seabed Current Boundary Layers in Wave-Plus-Current Flow Conditions. *J. Waterw. Port Coastal Ocean Div. Am. Soc. Civ. Eng.*, 114(2), pp. 161-174.

Law, M., Wass, P. and Grimshaw, D. (1997). The Hydrology of the Humber Catchment. *The Science of the Total Environment*, 194-195, pp. 119-128.

Lewis, M., Neill, S., Hashemi, M. R. and Reza, M. (2014). Realistic Wave Conditions and Their Influence on Quantifying the Tidal Stream Energy Resource. *Applied Energy*, 136, pp. 495-508.

Li, S. W., Tse, K. T., Weerasuriya, A, U. and Chan, P. W. (2014). Estimation of Turbulence Intensities under Strong Wind Conditions via Turbulent Kinetic Energy Dissipation Rates. *Journal of Wind Engineering and Industrial Aerodynamics*, 131, pp. 1-11.

Liu, J. H., Yang, S. L., Zhu, Q. and Zhang, J. (2014). Controls on Suspended Sediment Concentration Profiles in the Shallow and Turbid Yangtze Estuary. *Continental Shelf Research*, 90, pp. 96-108.

Lloyd, T. P., Turnock, S. R. and Humphrey, V. F. (2014). Assessing the Influence of Inflow Turbulence on Noise and Performance of a Tidal Turbine using Large Eddy Simulations, *Renewable Energy*, 71, pp. 742-754.

Lu, Y. (2000). Turbulence Characteristics in a Tidal Channel. *Journal of Physical Oceanography*, 30(5), pp. 855-867.

Lu, Y. and Lueck, R. G. (1999a). Using a Broadband ADCP in a Tidal Channel. Part 1: Mean Flow and Shear, *J. Atmos. Ocean. Technol*, 16, pp. 1 556-1 567.

Lu, Y. and Lueck, R. G. (1999b). Using a Broadband ADCP in a Tidal Channel: Part II: Turbulence. *J. Atmos. Ocean. Technol*, 16, pp. 1 568-1 579.

Lueck, R. G. (2002). Oceanic Microstructure Measurements in the 20th Century, Japan *J. Oceanogr*, 58, pp. 153-174.

Lueck, R. G. (2005). Horizontal and Vertical Turbulence Profilers. In: Helmut. Z. *et al.* ed., *Marine Turbulence, Theories Observations and Models*. Cambridge University Press. Chapter 11. pp. 89-100.

Lust, E. E., Luznik, L., Flack, K. A., Walker, J. M. and Van Benthem, M. C. (2013). The Influence of Surface Gravity Waves on Marine Current Turbine Performance. *Int. J. Mar. Energy*, 3 (4), pp. 27-40.

MacEnri, J., Reed, M. and Thiringer, T. (2013). Influence of Tidal Parameters on SeaGen Flicker Performance. *Philosophical Transactions of the Royal Society*, 371.

MacMillan, D. H. (1966). *Tides*. American Elsevier, New York.

Markus, D., Hojjat, R., Wuchner, R. and Bletzinger, K. U. (2013). A CFD Approach to Modeling Wave-Current Interaction. *International Journal of Offshore and Polar Engineering*, 23, pp. 29-32.

Mason-Jones, A., O'Doherty, D. M., Morris, C. E. and O'Doherty, T. (2013). Influence of a Velocity Profile & Support Structure on Tidal Stream Turbine Performance. *Renewable Energy*, 52, pp. 23-30.

Mazumder, B, S. and Ojha, S. P. (2007). Turbulence Statistics of Flow due to Wave-Current Interaction. *Flow Measurement and Instrumentation*, 18, pp. 129-138.

McCaffrey, K., Fox-Kemper, B., Hamlington, P. E. and Thomson, J. (2015). Characterization of Turbulence Anisotropy, Coherence, and Intermittency at a Prospective Tidal Energy Site: Observational Data Analysis. *Renewable Energy*, 76, pp. 441-453.

McCann, G. N. (2007). Tidal Current Turbine Fatigue Loading Sensitivity to Waves and Turbulence-a Parametric Study. *7th European Wave and Tidal Energy Conference*. Porto, Portugal.

McGovern, D., Ilic, S., Folkard, A., McClelland, S. and Murphy, B. (2009). Turbulence and Shear Stress around Offshore Wind Turbine Pile in Tidal Currents using Particle Image Velocimetry. In: M. Mizuguchi, and S. Sato, ed, *Proceedings of Coastal Dynamics 2009: Impacts of Human Activities on Dynamic Coastal Processes*, 141, World Scientific Publishing: Singapore.

Mclean, S. R. and Smith, D. (1979). Turbulence Measurements in the Boundary Layer over a Sand Wave Field. *Journal of Geophysical Research*, 84(12), pp. 7 791-7 808.

McLelland, S. J. and Nicholas A. P. (2000). A New Method for Evaluating Errors in High-Frequency ADV Measurements. *Hydrol. Process*, 14, pp. 351-366.

McNaughton, J., Afghan, I., Apsley, D. D., Rolfo, S., Stallard, T. and Stansby, P. K. (2013). A Simple Sliding-Mesh Interface Procedure and its Application to the CFD Simulation of a Tidal-Stream Turbine. *International Journal for Numerical Methods in Fluids*, 74, pp. 250-269.

MCT. (2011). *Siemens Invests in Marine Current Turbines*. [online]. Available from: http://www.marineturbines.com/3/news/article/30/siemens_invests_in_marine_current_turbines [Accessed 19/01/2014].

Met Office. (2016). *Beaufort Wind Force Scale*. [online]. Available from: http://www.metoffice.gov.uk/guide/weather/marine/beaufort-scale. [Accessed: 10/02/16].

Meygen. (2016). *About Phase 1*. [online]. Available from: http://www.meygen.com/about-phase-1a/ [Accessed 24/05/16].

Milne, I. A., Day, A. H., Sharma, R. N. and Flay, R. G. J. (2016). The Characterisation of the Hydrodynamic Loads on Tidal Turbines due to Turbulence. *Renewable and Sustainable Energy Reviews*, 56, pp. 851-864.

Milne, I. A., Sharma, R. N., Flay, R. G. J. and Bickerton, S. (2013). Characteristics of the Turbulence in the Flow at a Tidal Stream Power Site. *Philosophical Transactions of the Royal Society*, 371.

Monbet, V., Ailliot, P. and Prevosto, M. (2007). Survey of Stochastic Models for Wind and Sea State Time Series. *Probabilistic Engineering Mechanics*, 22, pp. 113-126.

Morgan, M. (2014). Performing Oceanographic Surveys on Tidal Energy Sites using a Data Buoy. *3rd Oxford Tidal Energy Workshop*.

Mycek, P., Gaurier, B., Germain, G., Pinon, G. and Riveolan, E. (2014). Experimental Study of the Turbulence Intensity Effects on Marine Current Turbines Behaviour. Part I: One Single Turbine. *Renewable Energy*, 66, pp.729-746.

Nautricity. (2016). *CoRMaT*. [online]. Available from: http://www.nautricity.com/cormat/ [Accessed 26/02/16].

Nazarenko, S., Lukaschuk, S., McLelland S., J. and Denissenko, P. (2010). Statistics of Surface Gravity Wave Turbulence in the Space and Time Domains. *J. Fluid Mech*, 642, pp. 395-420.

Nezu, I. and Nakagawa, H. (1993). Turbulence in Open Channel Flow. Taylor and Francis.

Nguyen, A. D. (2008). *Salt Intrusion, Tides and Mixing in Multi-Channel Estuaries*. CRC Press.

NOAA. (2013). *Tides and Currents*. [online]. Available from: https://tidesandcurrents.noaa.gov/faq4.html [Accessed 15/08/2015].

Nova Innovation. (2016). *A Leading Tidal Engineering Company*. [online]. Available from: http://www.novainnovation.co.uk/ [Accessed 30/08/16].

Nystrom, E. A., Oberg, K. A. and Rehman, C. R. (2002). Measurement of Turbulence with Acoustic Doppler Current Profilers - Sources of Error and Laboratory Results. *Hydraulic Measurements and Experimental Methods*. Estes Park, Colorado, USA.

Ojha, S. P. and Mazumder, B. S. (2010). Turbulence Characteristics of Flow Over a Series of 2-D Bed Forms in the Presence of Surface Waves. *Journal of Geophysical Research*, 115.

Okorie, O. P. (2011). *Scale Effects in Testing of a Monopile Support Structure Submerged in Tidal Currents*. PhD thesis. Robert Gordon University. Aberdeen.

ORE Catapult. (2015). *Wave and Tidal Energy Yield Uncertainty: Literature Review*. Report: PN000083-SRT-004.

Osalusi, E., Side, J. and Harris, R. (2009a). Reynolds Stress and Turbulence Estimates in Bottom Boundary Layer of Fall of Warness. *International Communications in Heat and Mass Transfer*, 36, pp. 412-421.

Osalusi, E., Side, J. and Harris, R. (2009b). Structure of Turbulent Flow in EMEC's Tidal Energy Test Site. *International Communications in Heat and Mass Transfer*, 36 (5), pp. 422-431.

Parsons, D. R., Jackson, P. R., Czuba, J. A., Engel, F. L., Rhoads, B. L., Oberg, J. L., Best, J. L., Mueller, D. S., Johnson, K. K. and Riley, J. D. (2012). Velocity Mapping Toolbox (VMT): a Processing and Visualization Suite for Moving-Vessel ADCP Measurements. *Earth Surface Processes and Landforms*, 38, pp. 1 244-1 260.

Peake, S., Everett, B. and Boyle, G. (2012). Introducing Energy Systems and Sustainability. In: Everett, B., Boyle, G., Peake, S. and Ramage, J., ed., *Energy Systems and Sustainability*. Oxford University Press, Oxford.

Perkey, D. and Pratt T. C. (2010). Comparison of SSC Measurements with Acoustic Backscatter Data: West Bay Sediment Diversion, Mississippi River. *2nd Joint Federal Interagency Conference, Las Vegas, NV, June 27 - July 1, 2010*.

Portilla-Yandun, J., Cavaleri, L. and Vledder, G. P. V. (2015). Wave Spectra Partitioning and Long Term Statistical Distribution. *Ocean Modelling*, 96, pp. 148-160.

Powell, H. J., Voulgaris, G., Collins, M. B. and Bastos, A. C. (2000). Wave-Current Interaction Over Bedforms: Observations and Model Predictions. *Marine Sandwave Dynamics. 23 & 24 March 2000 - Lille, France*.

Pulse Tidal. (2016). *Our Technology: Overview*. [online]. Available from: http://pulsetidal.com/our-technology.html. [Accessed 12/07/16].

Ram, K., Narayan, S., Ahmed, M. R., Nakavulevu, P. and Lee, Y. H. (2014). *In Situ* Near-Shore Wave Resource Assessment in the Fiji Islands. *Energy for Sustainable Development*, 23, pp. 170-178.

ReNews. (2014). *Siemens Abandons Tidal Energy*. [online]. Available from: http://renews.biz/79710/siemens-abandons-ocean-energy/ [Accessed 19/01/2014].

ReNews. (2016). *Global marine special report 2016*. ReNews.

Richards, J., Thomson, J., Polagye, B. and Bard, J. (2013). Method for Identification of Doppler Noise Levels in Turbulent Flow Measurements Dedicated to Tidal Energy. *International Journal of Marine Energy*, 3-4, pp. 52-64.

Rockland Scientific. (2016). *Moored Systems*. [online]. Available from: http://rocklandscientific.com/products/moored-systems/ [Accessed 02/09/16].

Rosman, J. H., Hench, J. L., Koseff, J. R. and Monismith, S. G. (2008). Extracting Reynolds Stresses from Acoustic Doppler Current Profiler Measurements in Wave-Dominated Environments. *J. Atmos. Oceanic Technol.*, 25, pp. 286-306.

RWE. (2015). *Renewable Energy*. [online]. Available from: http://www.rwe.com/web/cms/en/284070/rwe-npower/about-us/our-businesses/renewable-energy/ [Accessed 29/10/15].

Sana, A. and Tanaka, H. (2007). Full-Range Equation for the Wave Boundary Layer Thickness. *Coastal Engineering*, 54 (8), pp. 639-642.

Sanchez, M., Carballo. R., Ramos, R. and Iglesias, G. (2014). Energy Production from Tidal Currents in an Estuary: A Comparative Study of Floating and Bottom-Fixed Turbines. *Energy*, 77, pp. 802-811.

Saruwatari, A., Ingram, D. M. and Cradden, L. (2013). Wave-Current Interaction Effects on Marine Energy Converters. *Ocean Engineering*, 73, pp. 106-118.

Schwartz, M. (2006). *Encyclopaedia of Coastal Science.* Springer Science and Business Media.

ScotRenewables. (2016). *Technology*. [online]. Available from: http://www.scotrenewables.com/ [Accessed 26/02/16].

Scottish Energy News. (2016). *Scotland's Atlantis tidal power colossus now spans the Atlantic with feed-in tariff for 4.5MW of Canadian generation*. [online]. Available from: http://www.scottishenergynews.com/scotlands-atlantis-tidal-power-colossus-now-spans-the-atlantic-with-feed-in-tariff-for-4-5mw-of-canadian-generation/ [Accessed 26/02/16].

Shapiro, G. I. (2010). Effect of Tidal Stream Power Generation on the Region-Wide Circulation in a Shallow Sea. *Ocean Sci. Discuss.*, 7, pp. 1 785-1 810.

Sheinman Y. and Rosen, A. (1992). A Dynamic Model of the Influence of Turbulence on the Power Output of a Wind Turbine. *J. Wind Eng. Ind. Aerodyn.*, 39, pp. 329-341.

Shiono, K. and West, J. R. (1987). Turbulent Perturbations in the Conwy Estuary. *Estuarine, Coastal and Shelf Science*, 25(5), pp. 533-553.

Shuiqing, L. and Dongliang, Z. (2016). Gas Transfer Velocity in the Presence of Wave Breaking. *Tellus B.*, 68, pp. 1-16.

Simpson, J. (2005). *Acoustic Doppler Techniques.* In: Z. Helmut, J. Simpson, J. Sundermann. ed., Marine Turbulence, Theories Observations and Models. Cambridge University Press. Chapter 15. pp. 127-138.

Simpson, J. H., Fisher, N. R. and Wiles, P. (2004). Reynolds Stress and TKE Production in an Estuary with a Tidal Bore. *Estuarine, Coastal and Shelf Science*, 60 (4), pp. 619-627.

Skinner, C. J., Coulthard, T. J., Parsons, D. R., Ramirez, J. A., Mullen, L. and Manson, S. (2015). Simulating Tidal and Storm Surge Hydraulics with a Simple 2D Inertia Based Model, in the Humber Estuary, U.K. *Estuarine, Coastal and Shelf Science*, 155, pp. 126-136.

Soulsby, R. L. (1979). Selecting Record Length and Digitisation Rate for Near-Bed Turbulence Measurements. *Journal of Physical Oceanography*, 10, pp. 208-219.

Soulsby, R. L. (1997). *Dynamic of Marine Sands*. Thomas Telford.

Soulsby, R. L. (2006). *Simplified Calculation of Wave Orbital Velocities*. HR Wallingford TR 155.

Soulsby, R. L. and Humphrey, J. D. (1990). Field Observations of Wave-Current Interaction at the Sea-Bed. *Water Wave Kinematics: Advanced Research Workshop*, pp. 413-428.

Soulsby, R. L., Whitehouse, R. J. S. and Marten, K. V. (2012). Prediction of Time-Evolving Sand Ripples in Shelf Seas. *Continental Shelf Research*, 38, pp. 47-62.

Soulsby, R., Hamm, L., Klopman, L. and Myrh, G. (1993). Wave-Current Interaction Within and Outside the Bottom Boundary Layer. *Coastal Engineering*, 21, pp. 41-69.

Stacey, M. T., Monismith, S. G. and Burau, J. R. (1999). Measurements of Reynolds Stress Profiles in Unstratified Tidal Flow. *Journal of Geophysical Research*, 104, pp. 10 933-10 949.

Stallard, T., Feng, T. and Stansby, F. K. (2015). Experimental Study of the Mean Wake of a Tidal Stream Rotor in a Shallow Turbulent Flow. *Journal of Fluid and Structures*, 54, pp. 235-246.

Suara, K., Brown, R.J. and Chanson, H. (2014). Turbulence Measurements in a Shallow Tidal Estuary: Analysis Based On Triple Decomposition. *Proceedings of 19th Australasian Fluid Mechanics Conference,* Melbourne, Australia, 359, pp.1-4.

Sustainable Marine Energy. (2016). *Our Products and Services*. [online]. Available from: http://sustainablemarine.com/technology [Accessed 26/02/16].

Tambroni, N., Figueredo da Silva, J., Duck, R. W., McLelland, S. J., Venier, C. and Lanzoni, S. (2015). Experimental Investigation of the Impact of Macroalgal Mats on the Wave and Current Dynamics. *Advances in Water Resources*, 93, pp. 326-335.

Tatsumi, T. (2000). Turbulence as a Complex Mechanical System. *Applied Energy*, 67, pp. 91-116.

Tatum, S. C., Frost, C. H., Allmark, M., O'Doherty, D. M., Mason-Jones, A., Prickett, P. W., Grosvenor, R. I., Bryne, C. B. and O'Doherty, T. (2015). Wave-Current Interaction Effects on Tidal Stream Turbine Performance and Loading Characteristics. *International Journal of Marine Energy*, 14, pp. 161-179.

Teledyne. (2007). *WinRiver II user's guide*. Rep., N 957-6231-00.

Teledyne. (2011). *Acoustic Doppler Current Profiler Principles of Operation A Practical Primer*. Teledyne RD Instruments.

Teledyne. (2015). *Teledyne RDI's Tech Tips*. [online] Available from: http://www.rdinstruments.com/tips/tips_archive/4beam1202.aspx [Accessed 13/10/15).

Thomson, J., Polagye, B., Durgesh, V. and Richmond, M. C. (2012). Measurements of Turbulence at Two Tidal Energy Sites, Puget Sound, WA. *IEEE Journal of Oceanic Engineering*, 37, 3, pp. 363-374.

Thomson, J., Polagye, B., Richmond, M. and Durgesh, V. (2010a). *Inflow Characterization for Marine and Hydrokinetic Energy Devices FY-2010 Annual Progress Report*. U.S. Department of Energy, Contract DE-AC05-76RL01830.

Thomson, J., Polagye, B., Richmond, M. and Durgesh, V. (2010b). Quantifying Turbulence for Tidal Power Applications. *Oceans Conference 2010*. Seattle, USA. pp. 1-8.

Thomson, J., Polagye, B., Richmond, M. and Durgesh, V. (2011). *Inflow Characterization for Marine and Hydrokinetic Energy Devices FY-2011 Annual Progress Report*. U.S. Department of Energy, Contract DE-AC05-76RL01830.

Thomson, R. E. and Emery, W. J. (2014). *Data Analysis Methods in Physical Oceanography*. 3rd Edition. Newnes.

Thorne, P. D., Hardcastle, P. J. and Soulsby, R. (1993). Analysis of Acoustic Measurements of Suspended Sediments. *Journal of Geophysical Research*, 98, pp. 899-910.

Torrens-Spence, H., Schmitt, P., Mackinnon, P. and Elsaesser, B. (2015). Current and Turbulence Measurement with Collocated ADP and Turbulence Profiler Data. *Current, Waves and Turbulence Measurement (CWTM), 2015 IEEE/OES Eleventh*. pp. 1-8.

Townend, I. and Whitehead, P. (2003). A Preliminary Sediment Budget for the Humber Estuary. *Science of the Total Environment*, 314-316, pp. 755-767.

Tsai, C. H., Doong, D. J., Chen, Y. C., Yen, C. W. and Maa, M. J. (2016). Tidal Stream Characteristics on the Coast of Cape Fuguei in North-western Taiwan for a Potential Power Generation Site. *International Journal of Marine Energy*, 13, pp. 193-205.

Uihlein, A. and Magagna, D. (2016). Wave and Tidal Current Energy - A Review of the Current State of Research beyond Technology. *Renewable and Sustainable Energy Reviews*, 58, pp. 1070-1081.

Uncles, R. J. and Stephens J. A. (1999). Suspended Sediment Fluxes in the Tidal Ouse, UK. *Journal of Hydrological Processes*, 13, pp. 1167-1179.

Uncles, R. J., Stephens, J. A. and Law, D. J. (2006). Turbidity Maximum in the Macrotidal, Highly Turbid Humber Estuary, UK: Flocs, Fluid Mud, Stationary Suspensions and Tidal Bores. *Estuarine, Coastal and Shelf Science*, 67(1-2), pp. 30-52.

Valeport. (2008). *MIDAS DWR & WTR Wave Recorders Operation Manual*. Valeport Limited.

Walker, S. (2013). Barriers to the Development of a 100 MW Tidal Energy Array in the UK. *International Journal of Energy Engineering*, 3, pp. 80-92.

Wall, G. R., Nystrom, E. Y. and Litten, S. (2006). Use of an ADCP to Compute Suspended– Sediment Discharge in the Tidal Hudson River, New York. *Scientific Investigations Report 2006-5055*, U.S. Geological Survey.

West, J., Knight, D. and Shiono, K. (1986). Turbulence Measurements in the Great Ouse Estuary. *J. Hydraul. Eng.*, 112:3, pp. 167-180.

Westerhellweg, A., Canadillas, B. and Neumann, T. (2010). Direction Dependency of Offshore Turbulence Intensity in the German Bight. *10th Wind Energy Conference*, DEWEK 2010.

Wharton, S. and Lundquist, J. K. (2012). Atmospheric Stability Affects Wind Turbine Power Collection. *Environmental Research Letters*, 7, p. 7.

Williams, E. and Simpson, J. H. (2004). Uncertainties in Estimates of Reynolds Stress and TKE Production Rate using the ADCP Variance Method. *Journal of Atmospheric and Ocean Technology*, 21, pp. 347-357.

Williams, J. J., Humphrey, J. D., Moores, S. P. and Clipson, D. (1996). *Analysis of STABLE Data from Deployment 1, Holderness UK, October 1994*. Proudman Oceanic Laboratory Report No, 42.

Wolf, J. and Prandle, D. (1999). Some Observations of Wave-Current Interaction. *Coastal Engineering*, 37, pp. 471-485.

Woodward, J. (2011). *ADCP Measurement of the Blue Nile under High Sediment Conditions* (Mission Report 2007). FAO.

Work, P. A. (2008). Nearshore Directional Wave Measurement by Surface-Following Buoy and Acoustic Doppler Current Profiler. *Ocean Engineering*, 35, pp. 727-737.

World Energy. (2015). *World Energy Trilemma 2015: Priority actions on climate change and how to balance the trilemma*. World Energy Council.